

**Use of Confinement and Additives to Control Inorganic  
Crystallization**

Yunwei Wang

Submitted in accordance with the requirements for the degree of  
Doctor of Philosophy

The University of Leeds  
Faculty of Mathematics and Physical Sciences  
School of Chemistry

March, 2014

The candidate confirms that the work submitted is his/her own, except where work which has formed part of jointly-authored publications has been included. The contribution of the candidate and the other authors to this work has been explicitly indicated below. The candidate confirms that appropriate credit has been given within the thesis where reference has been made to the work of others.

Chapter 3: is based on the paper “*A new precipitation pathway for calcium sulfate dihydrate (gypsum) via amorphous and hemihydrate intermediates* Yun-Wei Wang, Yi-Yeoun Kim, Hugo K. Christenson and Fiona C. Meldrum, ***Chem. Commun.***, 2012,**48**, 504-506”. All the experimental work done is attributable to me, under the supervision of Prof. Fiona Meldrum, except the cryo-TEM and Titration work which was done at Eindhoven University.

Chapter 4: is based on the paper “*Additives stabilize calcium sulfate hemihydrate (bassanite) in solution*, Yun-Wei Wang and Fiona C. Meldrum, ***J. Mater. Chem.***, 2012,**22**, 22055-22062”.

Chapter 5: is based on the paper “*Confinement Leads to Control over Calcium Sulfate Polymorph*, Yun-Wei Wang, Hugo K. Christenson and Fiona C. Meldrum, ***Advanced Functional Materials***, Article first published online: 3 JUN 2013”.

Chapter 7: is based on the paper “*In Situ Study of the Precipitation and Crystallization of Amorphous Calcium Carbonate (ACC)*, Yun-Wei Wang, Yi-Yeoun Kim, Chris J. Stephens, Hugo K. Christenson and Fiona C. Meldrum, ***J. Mater. Chem.***, 2012,**22**, 22055-22062”.

This copy has been supplied on the understanding that it is copyright material and that no quotation from the thesis may be published without proper acknowledgement.

## **Acknowledgements**

I would never have been able to finish my thesis without the guidance of my supervisor, group members, help from friends, and support from my family.

I would like to express my deepest gratitude to my supervisor, Prof. Fiona Meldrum, for her excellent guidance, caring, patience, and providing me with an excellent atmosphere for doing research. I want to thank you to give me opportunity to study in Leeds and for all the help you gave me during my PhD, especially patiently and careful correcting my bad writing!

In addition, I would like to thank all the people from my group. I would like to thank Dr. Yi Yeoun Kim. Thank you for all your help to give the best suggestions during my whole PhD study. And many thanks to Dr Alex Kulak, the good homemade food, snacks and wines. It would have been a lonely lab without him. Furthermore I want to thank my favourite team neighbors, Dr Bram Cantaert and Mr. Johannes Ihli, to chitchat with and start annoying. I also want to thank Anna Schenk and Ciara Mc Nally, the most sweet and pretty girls in our group, and always bring their nice cakes! And of course also Dr. Lukmaan Bawazar, Dr. Bartosz Marzec, Dr. Tony Gong, Dr David Green, Dr. Harvey He, Miss Marie France, Mr. Phillip Lee and Mr William Marchant for their help and interesting talks about all kinds of different subjects.

Furthermore I would like to thank the people from Physics, Dr. Hugo Christenson, Dr. Chris Stephens and Mr. James Campbell. My research and papers would not have been possible without their help!

I also want to thank all the people from the University of Eindhoven, especially Dr. Nico Sommerdijk for his advice and giving me the opportunity to use Cryo-TEM and Titration. Of course also special thanks to Dr. Paul Bomans, Mr. Vladimir Dmitrović and Miss Juliet Li.

Finally, I would like to thank my parents. They were always supporting me and encouraging me with their best wishes.

## **Abstract**

This thesis describes the investigation of the three minerals, calcium sulfate, calcium phosphate and calcium carbonate under two bio-inspired methods, additives and confinement. The first experiment in Chapter 3 investigated the precipitation pathway of calcium sulfate above and under the solubility levels. Two metastable phases were obtained at ambient condition, hemihydrate and amorphous calcium sulfate (ACS), that first revealed hemihydrate can be found in room temperature and the existence of ACS. The transformation of ACS to the most stable phase, gypsum via hemihydrate was also proved under the titration and Cryo-TEM at undersaturated solution. Chapter 4 deals with the investigation of calcium sulfate grown in the presence of additives. These additives which have the profound inhibition effect provide another evidence of the existence of hemihydrate and ACS in the ambient conditions. Neglected before in literature, the morphology change of gypsum and hemihydrate also provide an aggregation-based transformation from hemihydrate to gypsum. Similar results were obtained growing calcium carbonate in confinement allowing formation of amorphous calcium carbonate. The results in Chapter 5 also demonstrated that confinement plays a significant role in the formation not only of the amorphous phase, but also the metastable phase, hemihydrate. Results were obtained in the absence and presence of the additives that lead to stabilize hemihydrate and ACS for more than 24 hours. Precipitation of calcium phosphate in confinement in the absence and presence of the additives used the same method as mentioned in the previous chapter. Similar results were obtained and again demonstrated that confinement and additives play a more significant role in bone formation. The last chapter investigated the crystallization pathway of calcium carbonate under UV-Vis at 2-10 mM concentration solutions with/without additives. The in-situ experiment in Chapter 7 provides a simple method to investigate the influence of concentrations of calcium carbonate solution and additives. Amorphous calcium carbonate nanoparticles were formed at early stage which transformed to stable calcite with time.

## Table of Contents

<b>Acknowledgements.....</b>	<b>iii</b>
<b>Abstract.....</b>	<b>v</b>
<b>Table of Contents.....</b>	<b>vi</b>
<b>List of Tables .....</b>	<b>xi</b>
<b>List of Figures .....</b>	<b>xii</b>
<b>Chapter 1 Introduction .....</b>	<b>1</b>
1.1 Biomineralization: Life and Crystals .....	2
1.2 Crystallization Concepts .....	4
1.2.1 Amorphous Phase and Crystals .....	4
1.2.2 Classical Crystallization .....	5
1.2.2.1 Nucleation.....	6
1.2.2.2 Crystal Growth .....	8
1.2.3 Non-Classical Crystallization.....	10
1.2.3.1 Oriented Attachment .....	10
1.2.3.2 Mesocrystal formation.....	12
1.3 Biological control of crystallization.....	12
1.3.1 Magnesium and Proteins Control Crystal Formation.....	13
1.3.1.1 Magnesium ions.....	13
1.3.1.2 Proteins.....	14
1.3.2 Control of Biomineral growth in Confined volumes .....	14
1.3.2.1 Intracellular Vesicles.....	15
1.3.2.2 Cellular assemblies .....	16
1.3.2.3 Macromolecular frameworks.....	18
1.4. Synthetic Control of Crystal Growth.....	19
1.4.1 Additives control of Crystal Growth .....	19
1.4.1. 1 Simple Ionic Additives .....	22
1.4.1.2 Low Molecular Mass Organic Additives.....	22
1.4.1.3 Polymer additives .....	22
1.4.2 Synthesis in confined reaction spaces.....	23
1.4.2.1. Synthetic Vesicles .....	24
1.4.2.2. Polymer sponges .....	24
1.4.2.3. Droplet Arrays.....	25

1.4.2.4. Track-etch membranes.....	26
1.5.2.5. Crossed-cylinders.....	27
<b>Chapter 2 Experimental Methods.....</b>	<b>29</b>
2.1 Experimental Preparation .....	30
2.2 Crystallization.....	31
2.2.1 General procedure.....	31
2.2.1 Crystallization of CaSO <sub>4</sub> .....	31
2.2.2 Crystallization of Calcium Phosphate (CaP) .....	31
2.2.3 Crystallization of CaCO <sub>3</sub> .....	32
2.3 Characterization Technique .....	32
2.3.1 Scanning Electron Microscopy (SEM) .....	32
2.3.2 Transmission Electron Microscopy (TEM) .....	34
2.3.2.1 High-resolution transmission electron microscopy (HRTEM) .....	34
2.3.2.2 Cryo-TEM Analysis .....	37
2.3.4 Raman spectroscopy .....	39
2.3.5 X-ray Diffraction .....	39
2.3.6 Atomic absorption (AA) .....	40
2.3.7 Infrared spectroscopy (FTIR) .....	40
2.3.8 UV-Vis.....	40
<b>Chapter 3: A New Precipitation Pathway for Calcium Sulfate Dihydrate (Gypsum) via Amorphous and Hemihydrate Intermediates .....</b>	<b>43</b>
3.1 Introduction to Calcium Sulfate.....	45
3.1.1 General Overview of Calcium Sulfate.....	45
3.1.2 Interconversion between the CaSO <sub>4</sub> -xH <sub>2</sub> O Polymorphs .....	49
3.1.3 Crystallization Pathway of Calcium Sulfate .....	51
3.2 Aims of this Project .....	53
3.3 Experimental .....	53
3.3.1 Materials .....	53
3.3.2 Early Stages of Precipitation of Calcium Sulfate .....	53
3.3.3 Titration Experiments.....	54
3.3.4 Characterization Methods .....	55
3.4 Results .....	57
3.4.1 CaSO <sub>4</sub> Precipitation in Bulk Solution.....	57
3.4.2 Early Stages of CaSO <sub>4</sub> Precipitation in Bulk Solution .....	59
3.4.2 Precipitation from Undersaturated Solutions.....	68

3.4.2.1 TEM and Raman analysis .....	68
3.4.2.2 Titration Experiments .....	71
3.4.3 CaSO <sub>4</sub> Precipitation from bound calcium in undersaturated solution .....	77
3.5 Discussion .....	82
3.6 Summary .....	84
<b>Chapter 4: Additives Stabilize Calcium Sulfate Hemihydrate (Bassanite) in Solution .....</b>	<b>86</b>
4.1 Introduction .....	87
4.1.1 Accelerators .....	88
4.1.2 Inhibitor .....	89
4.1.2.1 Carboxyl groups(-COOH).....	89
4.1.2.2 Phosphonate .....	90
4.1.2.3 Sulfonic acid (-SO <sub>3</sub> H).....	90
4.1.2.4 Surface-Active Reagents.....	91
4.1.2.5 Metal Ions .....	91
4.2 Aims .....	92
4.3 Experimental.....	92
4.3.1 Materials .....	92
4.3.2 Precipitation of Calcium Sulfate .....	93
4.3.3 Characterization Methods .....	94
4.4 Results .....	95
4.4.1 Precipitation of Calcium Sulfate in additive-free solution.....	95
4.4.2 Precipitation of Calcium Sulfate in the Presence of PAA .....	96
4.4.3 Effect of the reaction time in the presence of PAA .....	103
4.4.4. Transformation of amorphous to crystalline phases .....	104
4.4.5 Inhibition Efficiency of other Additives .....	106
4.5 Discussion .....	114
4.6 Summary.....	119
<b>Chapter 5: Confinement Leads to Control over Calcium Sulfate Polymorph .....</b>	<b>120</b>
5.1 Introduction .....	121
5.1.1 Effect of Confined Volumes .....	122
5.1.2 Calcium Sulfate Precipitation in Confinement.....	122
5.2 Aims of this Project .....	122
5.3 Experimental .....	123

5.3.1 Materials .....	123
5.3.2 Precipitation of Calcium Sulfate.....	123
5.3.3 Crossed-Cylinder Experiment .....	123
5.3.4 Characterization Methods .....	125
5.4 Results .....	126
5.4.1 CaSO <sub>4</sub> Precipitation in Confinement .....	126
5.4.2 CaSO <sub>4</sub> Precipitation in Confinement in the Presence of Additives .....	135
5.5 Discussion .....	140
5.6 Summary.....	145
<b>Chapter 6: ACP and OCP is Stable in Confinement .....</b>	<b>146</b>
6.1 Introduction to Calcium Phosphate.....	148
6.1.1 Transformation of the Polymorphs of Calcium Phosphate .....	148
6.1.2 Amorphous Calcium Phosphate.....	149
6.1.3 Control crystallization process of calcium phosphate .....	150
6.1.3.1 Calcium Phosphate growth in the presence of Additives .....	150
6.1.3.2 Calcium Phosphate growth in Confinement .....	151
6.2 Aims of this Project .....	152
6.3 Experimental .....	153
6.3.1 Precipitation of Calcium Phosphate .....	153
6.3.2 Crossed-Cylinder Experiment .....	153
6.3.3 Control Experiment.....	154
6.3.4 Characterization Methods .....	154
6.4 Results .....	155
6.4.1 CaP precipitation in bulk solution.....	155
6.4.2 CaP precipitation in Confinement in the absence of PAsp .....	158
6.4.3 CaP precipitation in Confinement in the presence of PAsp .....	163
6.5 Discussion .....	167
6.6 Summary .....	170
<b>Chapter 7: A Turbidity Study of Calcium Carbonate Precipitation .....</b>	<b>172</b>
7.1 Introduction .....	173
7.1.1 Three main crystalline polymorph of Calcium Carbonate .....	174
7.1.2 Amorphous Calcium Carbonate.....	174
7.1.3 Calcium Carbonate in Industry and Biomineralization .....	175

7.1.4 Influence of Metal ions and Organic Molecules in CaCO <sub>3</sub> precipitation .....	176
7.1.4.1 Influence of metal ions on CaCO <sub>3</sub> precipitation .....	177
7.1.4.2 Influence of organic molecules on CaCO <sub>3</sub> precipitation .....	178
7.1.5 Ultraviolet–visible spectroscopy to study the Precipitation of CaCO <sub>3</sub> .....	180
7.2 Aims .....	182
7.3 Experimental.....	183
7.3.1 Materials .....	183
7.3.2 Precipitation of Calcium Carbonate .....	183
7.3.3 Characterization Methods .....	184
7.4 Results .....	185
7.4.1 Precipitation of Calcium Carbonate in Additive-Free Bulk Solution.....	185
7.4.2 Precipitation of CaCO <sub>3</sub> in the Presence of Mg <sup>2+</sup> .....	192
7.4.3 Precipitation of CaCO <sub>3</sub> in the Presence of PAA.....	195
7.5 Discussion .....	199
7.6 Summary.....	203
<b>Chapter 8 Final Conclusion and Future Work .....</b>	<b>205</b>
<b>List of References.....</b>	<b>207</b>

## List of Tables

Table 1.1 Examples of the diversity of biominerals .....	3
Table 3.1 Crystallographic and physical data of the different calcium sulfate phases. ....	46
Table 3.2 Induction periods at various concentrations as a function of time.....	58
Table 3.3 Measured <i>d</i> -spacings of electron diffraction patterns obtained from calcium sulfate particles. ....	60
Table 3.4 Concentrations and percentages of added, bound and free calcium at different time points, as calculated from the titration experiments.....	76
Table 4.1 The additives used in the experiments .....	93
Table 7.1 Time of maximum rate of recovery of light transmission as a function of mole fraction of Mg <sup>2+</sup> for 5 mM and 10 mM Ca <sup>2+</sup> concentrations. ....	194

## List of Figures

Figure 1.5 Common self-assembled structures of lipids.....	16
Figure 1.7 Space delineation using groups of cells in associations .....	17
Figure 1.8 A model of shell mineralization.. .....	18
Figure 1.8 Adsorption of an additive (filled circles) onto a crystal surface lowers its surface energy and, thus, its growth rate. ....	20
Figure 1.9 Sites for impurity absorption on a growing crystal, based on Kossel model.....	21
Figure 1.10 Polymer membrane formed as a replica of a sea urchin plate. ....	25
Figure 1.11 Schematic diagram of the fabrication of the droplet arrays.....	26
Figure 1.12 (a) Calcium carbonate crystals grown within membrane pores. (b) Intra-membrane crystal isolated from the membrane .....	27
Figure 1.13 The crossed-cylinder glasses provide a small volume to growth of crystal .....	28
Figure 2.1 Schematic diagram showing the components of an SEM column.. .....	34
Figure 2.2 Working principle of a Transmission electron microscope. ....	35
Figure 2.3 Schematic diagram showing the components of time-driven dual- beam spectrophotometry. ....	42
Fig 3.1 The crystallographic unit cell of gypsum contains four ‘molecules’ of $\text{CaSO}_4 \cdot 2\text{H}_2\text{O}$ . ....	47
Fig 3.2 The crystallographic unit cell of bassanite, $\text{CaSO}_4 \cdot 0.5\text{H}_2\text{O}$ . ....	48
Fig 3.3 The crystallographic unit cell of anhydrite III, $\text{CaSO}_4$ . ....	49
Fig 3.4 Metrohm® commercial titration setup.. .....	55
Fig 3.5 SEM images of calcium sulfate precipitates produced at different solution concentrations after 1 hour reaction time. ....	57

Figure 3.6 Intensities of transmitted light vs. time for calcium sulfate precipitation at 25 °C from solutions of concentrations, a) 100 mM, b) 80 mM and c) 50 mM .....	58
Figure 3.8 Raman spectra of CaSO <sub>4</sub> particles precipitated from a 50 mM solution.....	62
Figure 3.9 Raman spectra of reference samples.....	62
Figure 3.10 An XRD spectrum of the reference samples .....	63
Figure 3.11 XRD patterns of calcium sulfate precipitated at 50 mM, isolated from solution after 1 minute and then left in air. ....	64
Figure 3.12 TGA spectra of (a) the precipitate isolated from the 50 mM solution after approximately 1 minute and (b) a sample of gypsum.....	65
Figure 3.13 (a) Calcium sulfate dihydrate and (b) calcium sulfate hemihydrate crystals precipitated from the 50 mM solution after 1 hour.....	66
Figure 3.14 (a) Calcium sulfate dihydrate and (b) calcium sulfate hemihydrate crystals precipitated from the 15 mM solution after 1 minute.....	67
Figure 3.15 a) TEM image of amorphous CaSO <sub>4</sub> particles precipitated from a 15 mM solution after 1 min. b) The corresponding EDX spectrum. ....	68
Figure 3.16 a) The selected area electron diffraction pattern of this sample, showing that it is amorphous. b) After 1 min irradiation with the electron beam, crystallisation to CaSO <sub>4</sub> dihydrate (gypsum) occurs. ....	68
Fig 3.17 Precipitates present in a 5 mM calcium sulphate solution, as characterised by TEM and Raman. ....	70
Figure 3.18 a) Titration curve showing the development of [Ca <sup>2+</sup> ] <sub>free</sub> ions (red line) compared to the total amount of [Ca <sup>2+</sup> ] <sub>added</sub> (dashed black line). ....	73
Figure 3.19 An example of the normalization procedure applied to convert the time scale (in seconds) to the time scale where the nucleation point (NP) is normalized to 1.....	74

Fig 3.20 Equal amounts of CaCl <sub>2</sub> (250mM) and Na <sub>2</sub> SO <sub>4</sub> (250mM) solutions were titrated into water. The CryoTEM sample was taken at CaSO <sub>4</sub> concentrations of approximately 13 mM. ....	77
Figure 3.21 a) Titration curve showing the development of [Ca <sup>2+</sup> ] <sub>free</sub> ions (red line) compared to the total amount of [Ca <sup>2+</sup> ] <sub>added</sub> (dashed black line) as a function of time normalized with respect to the NP, with $t = \text{time (s)} / \text{time of NP (s)}$ .....	79
Figure 3.22: Dynamic light scattering (DLS) was performed of by adding 250 mM CaCl <sub>2</sub> solution to 25 ml of 250 mM Na <sub>2</sub> SO <sub>4</sub> .....	80
Figure 3.23. Cryo-TEM images of particles isolated from an experiment in which 250 mM CaCl <sub>2</sub> solution was titrated into 250 mM Na <sub>2</sub> SO <sub>4</sub> solution with an addition rate of 0.1 mL/min.....	81
Figure 4.1. SEM images of calcium sulfate crystals precipitated from 10 mM solutions in the absence of additives.....	95
Figure 4.2 Raman spectra of reference samples (a) calcium sulfate hemihydrate produced after 1 minute and (b) calcium sulfate dihydrate (gypsum) precipitated from a 100 mM solution and isolated after 1 hour. ....	96
Figure 4.3 SEM and TEM images, and electron diffraction patterns of calcium sulfate particles precipitated after 1 hour, in the presence of PAA.....	97
Figure 4.4 TEM images of calcium sulfate crystals precipitated in the presence of 50 µg/ml PAA after 1 hour. The precipitates were a combination of (a) gypsum and (b) hemihydrate. ....	98
Figure 4.5 Raman spectra of CaSO <sub>4</sub> particles precipitated after 1 hour with addition of (a) 100µg/ml PAA, as hemihydrate, (b) 100µg/ml PSS, as gypsum, (c) 200 mM MgCl <sub>2</sub> , as hemihydrate, and (d) 100 µg/ml phosphate, as hemihydrate. ....	99
Figure 4.6 IR spectra of CaSO <sub>4</sub> particles precipitated from 100 mM calcium sulfate solution. ....	100
Figure 4.7 TGA spectra of the precipitate isolated calcium sulfate 100mM solution.....	101

Figure 4.8 XRD patterns of (a) a natural gypsum sample [220] and (b) Hemihydrate as reported in reference[174] (c) gypsum precipitated from a 100 mM solution after 1 hour, (d) calcium sulfate hemihydrate, produced by annealing gypsum at 120 °C for 10 hours, (e) hemihydrate precipitated from a supersaturated solution after 1 min in the absence of additives, and analysed after 1 hour, (f) hemihydrate precipitated in the presence of 100 µg/ml PAA, isolated after 1 hour, and analysed after 1 hour. ....	102
Figure 4.9 SEM and TEM images and electron diffraction patterns of calcium sulfate crystals precipitated in the presence of 200 µg/ml PAA .....	104
Figure 4.10 SEM and TEM images, and electron diffraction patterns of calcium sulfate particles precipitated in the presence of 200 µg/ml PAA .....	106
Figure. 4.11 Scanning electron micrographs of calcium sulfate crystals precipitated spontaneously at the final concentration of 100 mM after 1 hour, 25 °C. ....	108
Figure 4.12 The XRD patterns of calcium sulfate particles precipitated in the presence of (a) PSS 100µg/ml, shown as mixture of hemihydrate and gypsum, * showed the peaks from gypsum (b) 100µg/ml sodium triphosphonate, (c) PAA 100µg/ml, and (d) 200 mM MgCl <sub>2</sub> 6H <sub>2</sub> O, shown as hemihydrate. ....	108
Fig. 4.13 Scanning electron micrographs and TEM of calcium sulfate crystals precipitated spontaneously at the final concentration of 100 mM after 1 hour, 25 °C. ....	109
Figure 4.14 CaSO <sub>4</sub> particles precipitated in the presence of 100 µg/ml sodium triphosphonate, and isolated after 1 hour. ....	110
Fig. 4.15 Scanning electron micrographs of 100 mM calcium sulfate crystals precipitated spontaneously after 1 hour, 25 °C; (a) with addition of MgCl <sub>2</sub> 100 mM, all crystals were hemihydrate, ~200nm in length, (b) with addition of MgCl <sub>2</sub> 200 mM, small size of hemihydrate, ~100 nm in length. ....	112

Figure 4.16: Scanning electron micrographs of calcium sulfate crystals precipitated spontaneously at the final concentration of 100 mM with addition of  $Mg^{2+}$  200 mM, 25 °C, after (a) 1 day, some areas start to transform to gypsum. (b) 3 days, typical gypsum with smooth surface, 50 $\mu$ m in length (c) higher magnification of Fig b..... 112

Figure 4.17 X-ray diffraction spectra of calcium sulfate hemihydrate precipitates (a) from additive-free solution, (b) with 100  $\mu$ g/ml of sodium triphosphate (STP), (c) 100  $\mu$ g/ml PAA and (d) 200 mM  $Mg^{2+}$ ..... 112

Figure 4.18 SEM images of calcium sulfate hemihydrate formed in the presence of 100 $\mu$ g/ml PAA and 200 mM  $Mg^{2+}$  after 1h..... 113

Figure 4.19 Conductivity-time profiles for the spontaneous precipitation of a 100 mM calcium sulfate solution in the absence (solid line) and in the presence of 5  $\mu$ g/ml PAA (dotted line). . ..... 118

Fig 5.1 a) Metal pieces are gradually placed on the top of the holder surface. b) Pieces are added until the surface contact. It is essential. Note: Make sure the surfaces come in contact smoothly and gradually increase the weight so as to not damage the surfaces. .... 124

Fig 5.2 The crossed-cylinder glasses, where r is the radius of cylinder, DCP is the distance from the contact point and SS is the surface separation..... 125

Figure 5.3 SEM image of a) the contact point with scratches and different surface separations of b) 0.5, c) 2 and d) 15  $\mu$ m. The inset SEM images show calcium sulfate precipitates formed at separations around 15  $\mu$ m (I) and around 5  $\mu$ m (II). .... 127

Figure 5.4 SEM image of calcium sulfate particles precipitated in confinement on glass cylinders, showing (a) the contact point, and (b – d) different distances from the contact points (*DCP*), corresponding to surface separations (*SS*) of approx. (b) 0.2  $\mu$ m, (c) 0.5  $\mu$ m and (d) 1.5  $\mu$ m..... 128

Figure 5.5 TEM image of the grid surface in the region of a) contact point with scratches and different surface separations of b) 0.2, c) 0.5 and d) 1.5  $\mu$ m. .... 128

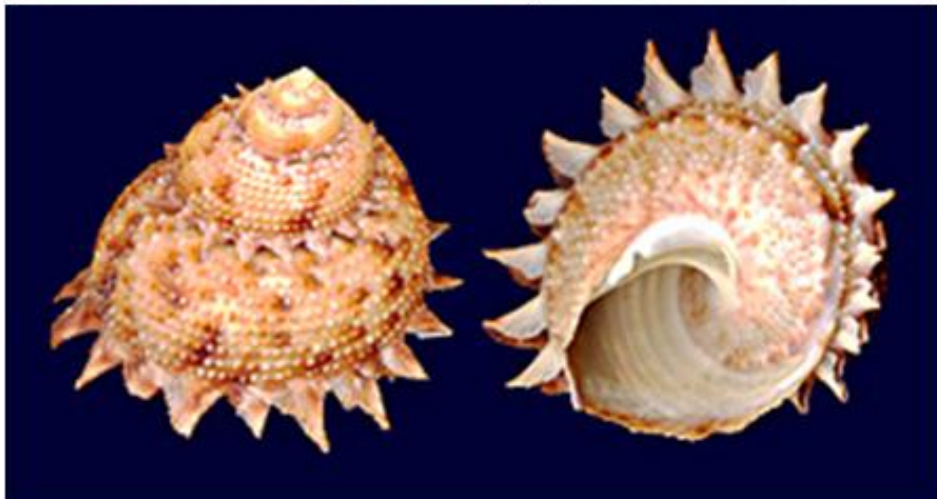
Fig 5.6 SEM images of calcium sulfate crystals precipitated after 1 hour on glass crossed-cylinders. .... 130

Fig 5.7 TEM images of calcium sulfate crystals grown at a final concentration of 100 mM on a TEM grid in the crossed-cylinders system after 1 hour.. ....	131
Fig 5.8 TEM and SEM images of calcium sulfate particle grown at a final concentration of 100 mM of the crossed-cylinders system after 1 hour at a surface separation of 0.2 $\mu\text{m}$ . .....	132
Figure 5.9 SEM images of calcium sulfate particles grown at a final concentration of 100 mM in the crossed-cylinders system after 1 hour. Surface separation = 0.2 $\mu\text{m}$ . It shows a mixture of nanoparticles, approximately 30 nm in the diameter and hemihydrate nanorods. ....	132
Fig 5.10 TEM images of amorphous $\text{CaSO}_4$ particles precipitated after 1 hour from a 100 mM solution at a surface separation of 0.2 $\mu\text{m}$ . .....	134
Figure 5.11 SEM images of $\text{CaSO}_4$ particles precipitated from 100 mM solution in bulk after 1 h in the presence of (a) 100 $\mu\text{g/ml}$ PAA and (b) 10 $\mu\text{g/ml}$ sodium triphosphate.....	135
Fig 5.12 TEM images and corresponding electron diffraction (EDX) patterns of calcium sulfate particles precipitated in confinement in the presence of 100 $\mu\text{g/ml}$ PAA at a surface separation of $\approx 0.5 \mu\text{m}$ after different incubation times. ....	137
Figure 5.13. TEM images of calcium sulfate crystals precipitated after 24 hours on glass crossed-cylinders. ....	138
Fig 5.14 TEM images and corresponding electron diffraction patterns of calcium sulfate particles precipitated in confinement in the presence of 10 $\mu\text{g/ml}$ sodium triphosphate at different surface separations (SS) and incubation times. ....	140
Figure 5.15 Calcium sulfate particles precipitated in the crossed-cylinder system from a solution of concentration 100 mM after 24 h.....	143
Fig 6.1 a) Metal pieces are gradually placed on the top of the holder surface. b) Crossed-cylinder glasses with TEM grid were immersed in CaP solution in a beaker.. .....	154
Figure 6.3 Raman spectrum of CaP produced in bulk solution after 5 hrs at 37 $^\circ\text{C}$ . Analysis of the spectrum showed the produced material was HAP. ....	156

Figure 6.4 The X-ray diffraction pattern of calcium phosphate precipitates obtained in the bulk solution after 5 hrs at 37 °C, corresponding with HAP.....	157
Figure 6.5 TEM images of calcium phosphate precipitates in the presence of PAsp PAsp 10 µg/ml at 37 °C.....	158
Figure 6.6 SEM and TEM images of calcium phosphate precipitates in confinement at 37 °C after 3 days.....	159
Figure 6.7 TEM images of calcium phosphate precipitates in confinement at 37 °C after 3 days at surface separations of 1 µm.....	160
Figure 6.8 SEM and TEM images of calcium phosphate precipitates in confinement at 37 °C after 3 days at surface separations of 0.5 µm.....	161
Figure 6.9 SEM and TEM images of calcium phosphate precipitates in confinement at 37 °C after 3 days at surface separations of 0.2 µm.....	162
Figure 6.10 TEM and SEM images of calcium phosphate precipitates formed in confinement at 37 °C after 1 week in the presence of 10 µm/mL PAsp....	164
Figure 6.11 TEM and SEM images of calcium phosphate precipitates in confinement at 37 °C after 1 week in the presence of 10 µm/mL PAsp.....	165
Figure 6.12 TEM and SEM images of calcium phosphate precipitates in confinement at 37 °C after 1 week in the presence of 10 µm/mL PAsp.....	167
Figure 7.1 Schematic diagram showing the spectrophotometry cuvette.....	181
Fig 7.2 UV-Vis absorption over 200-700 nm, measured for $[Ca^{2+}] = 5$ mM solution 30 s after mixing. A wavelength of $\lambda = 500$ nm was used for the Spectrophotometry measurements. ....	185
Figure 7.3 Percentage transmitted light intensity as a function of time after mixing in solutions of 2-10 mM initial $Ca^{2+}$ concentration. . ....	187
Figure 7.4 The changes of pH as a function of time, for $CaCO_3$ solution concentrations of 2.5 mM (solid line) and 10 mM (dash line).....	188
Figure 7.5 Normalized Raman spectra of $CaCO_3$ precipitates extracted from solutions after varying growth periods.....	190

Figure 7.6	TEM images of CaCO <sub>3</sub> precipitates from solutions of concentration (a) 2.5 mM Ca <sup>2+</sup> after 15 s, (b) 2.5 mM Ca <sup>2+</sup> after 5 min, (c) 3.5 mM Ca <sup>2+</sup> after 15 s, (d) 3.5 mM Ca <sup>2+</sup> after 1 min, (e) 5 mM Ca <sup>2+</sup> after 1 min and (f) 5 mM Ca <sup>2+</sup> after 5 min. ....	191
Fig. 7.7	Percentage transmitted light intensity of [Ca <sup>2+</sup> ]= 5 mM as a function of time in the presence of Mg additives. ....	192
Fig. 7.8	Percentage transmitted light intensity of [Ca <sup>2+</sup> ]= 10 mM as a function of time in the presence of Mg additives. ....	193
Figure 7.9	Time of maximum rate of recovery of light transmission as a function of mole fraction of Mg <sup>2+</sup> for 5 mM and 10 mM Ca <sup>2+</sup> concentrations. ....	195
Fig. 7.10	SEM images of CaCO <sub>3</sub> precipitates from 5 mM calcium carbonate solutions after 20 mins in the presence of PAA.....	196
Fig. 7.11	Percentage transmitted light intensity of [Ca <sup>2+</sup> ]= 5 mM as a function of time in the presence of PAA additives.....	197
Figure 7.12	Time of maximum rate of recovery of light transmission as a function of added amount of poly(acrylic acid) (PAA) for 5 mM and 10 mM Ca <sup>2+</sup> concentrations. . ....	199

## Chapter 1 Introduction



## 1.1 Biomineralization: Life and Crystals

Over the past five decades, a source of inspiration for materials chemistry has been a new area of study for bioinorganic chemistry - the inorganic-based structure of life. This gives rise to inorganic solids deposited in biological systems, such as shells, corals, ivory, bone and enamel, where the process generating these structures is called *biomineralization*.<sup>[1]</sup> Biomineralization is generally divided into two fundamentally different classes, based on the degree of biological control exerted.<sup>[2]</sup> One process, which is characterized by little control over the mineralization, is called “biologically induced mineralization” (BIM). Here, the precipitation of the mineral happens as a result of interactions between the organism and its surroundings, and little or no control is exerted over the mineralization process. A common example is the decoration of bacteria by minerals such as iron and manganese oxides. A bacterial cell can act as a nucleus for apatite crystallization, which can bind metal ions present in the environment.<sup>[3]</sup> In contrast, when the organism exerts a great degree of crystallochemical control over the selected size, morphology, structure, and orientation of the mineral particles, the mineralization process is called “biologically controlled mineralization” (BCM). This process has also been referred to as organic matrix-mediated mineralization<sup>[4]</sup> and boundary-organized biomineralization.<sup>[2]</sup> The best characterized example of BCM is magnetosome formation by the magnetotactic bacteria. These microorganisms carry out BCM in which magnetic crystals appear to have a relatively specific function.<sup>[5]</sup> These biological mechanisms offer a unique inspiration for “biomimetic” crystal growth experiments and provide the basis for the design and synthesis of novel materials by synthetic methods.

*Biominerals*, whose composition, shape and properties range enormously depending on the organism and the location of the mineral within the living system have intrigued the materials engineer for years.<sup>[4]</sup> These biological systems are extremely wide-ranging, from micrometer-sized bacteria, plants and invertebrates to vertebrates, including humans. Many people are probably not even aware of the diversity of biologically formed minerals, so the diversity of biominerals and examples of their sophisticated structures is presented in the following sections in detail. Table 1.1 are examples of biominerals and functions. In these biominerals,

CaCO<sub>3</sub> and CaP with an endless variety of morphologies are relatively easy model systems to work with.

Biominerals are also usually organic-inorganic composites and often show very controlled hierarchical structures. It has been suggested that these form due to specific molecular recognition between for example, the organic macromolecules or proteins and inorganic crystals. These natural composite materials can also provide exceptional properties and a wide range of morphologies which can minimize the weaknesses or combine the best of the properties of the separate components.[4] Surprisingly, biominerals can even appear as single crystals even with high levels of organic occlusions.[6]

**Table 1.1** Examples of the diversity of biominerals

<b>Biogenic minerals</b>	<b>formula</b>	<b>organism</b>	<b>Biological location</b>	<b>Biological function</b>
Calcium carbonates (calcite, vaterite, aragonite, Mg-calcite amorphous)	CaCO <sub>3</sub> , (Mg,Ca) CO <sub>3</sub> , CaCO·nH <sub>2</sub> O	Many marine organisms, plants, mammals	Shell, test, eye lens, crab cuticle, eggshells, leaves, inner ear	Exoskeleton, optical, mechanical strength, protection, gravity receptor, buoyancy device, Ca ions store
Calcium phosphates (hydroxylapatite, dahllite, octacalcium phosphate)	Ca <sub>10</sub> (PO <sub>4</sub> ) <sub>6</sub> (OH) <sub>2</sub> , Ca <sub>5</sub> (PO <sub>4</sub> ,CO <sub>3</sub> ) <sub>3</sub> (OH), Ca <sub>8</sub> H <sub>2</sub> (PO <sub>4</sub> ) <sub>6</sub> ,	vertebrates, mammals, fish, bivalves	bone, teeth, scales, gizzard plates, gills, mitochondria	endoskeleton, ion store, cutting/ grinding, protection, precursor
sulfates (gypsum, celestite, barite)	CaSO <sub>4</sub> •2H <sub>2</sub> O, SrSO <sub>4</sub> , BaSO <sub>4</sub>	jellyfish, acantharia, loxodes, chara	statoconia, cellular, intracellular statoliths	gravity receptor, skeleton gravity device/receptor or

The aim of this thesis is to understand the formation of biominerals, and to apply of this knowledge to the manufacture of new hybrid materials and the development of new fabrication techniques. Inspired by biominerals, a quest was started to unravel the mechanisms of biomineral formation, not only to understand but also to mimic the crystallization pathway and to produce extraordinary materials with a high amount of control over the phase, size, orientation and morphology under atmospheric conditions.[6, 7]

## **1.2 Crystallization Concepts**

### **1.2.1 Amorphous Phase and Crystals**

In general, amorphous materials can be defined as substances lacking long-range order. Amorphous materials thus are less stable and more soluble than crystalline ones. With isotropic properties and no preferred form, amorphous phases can be readily molded to give the desired product shape for structural purposes, and they are found widely in biominerals, such as the siliceous diatoms and radiolaria.[8] More generally, amorphous phase materials include some metals, polymers, glass, silica and ice.[9-12] Considering inorganic materials, some carbonate minerals[13-16] and iron oxide[17] have been reported to form amorphous phases, as precursors to form crystalline phases.[14, 15, 17, 18] More details about amorphous phases will be discussed in Chapter 4, 6 and 7. In contrast to amorphous materials, there are two different kinds of crystalline material can be formed, namely single crystals and polycrystalline materials, where these can be used for a wide variety of functions in organisms.[19] An ideal single crystal can be defined as “a solid body with a large coherence length, which shows diffraction behaviour characteristic of a perfect three-dimensional alignment of its building units” unbroken to the edges.[20] Notable examples are individual calcite single crystal elements of disc-like coccoliths [21] and some with complex three-dimensional structures such as sea urchin skeletal elements.[22] With these single crystals or grains aggregating together in random crystallographic orientations, a polycrystalline particle with complex structure is formed.[23] Mollusk nacre provides an example of a polycrystalline calcium carbonate material with excellent mechanical properties.

This polycrystalline nacre high stiffness, strength and toughness and is 3000 times more resistant to fracture than a single crystal of pure aragonite.[24-26]

### 1.2.2 Classical Crystallization

The dissolved atoms, molecules or ions in solution induce the starting point of crystallization. The supersaturation,  $S$ , is a measure of the degree by which the concentration of the solution exceeds the solubility of the species and is considered to be the thermodynamic driving force of crystallization. More specifically,  $S$  is defined as the following dimensionless ratio.

$$S = C / k_{sp} \quad (\text{Equation 1.1})$$

where  $C$  is the concentration of species and  $k_{sp}$  is the equilibrium molecular solubility product. In a case where there are multiple species involved,  $C$  is the product of the concentrations (or, more correctly, the activities) of the individual components. Equation 1.1 shows that the supersaturation is directly related to the solubility of the product to be formed. Therefore, it implies that at any given concentration there will be different driving forces to the formation of different polymorphs. Conversely, controlling the solution concentration plays an important role in dictating the polymorph formed.

It is well known that the pure thermodynamic equilibrium treatment of classical crystallization based on Ostwald's rule provides a good basis for understanding that the first occurring polymorph is the least stable and is closest in the free energy to the mother phase. It is then followed by phases in order of increasing stability.[27] However, this theory cannot predict crystal polymorphs in all cases because crystallization and the resulting polymorphs are kinetically driven.

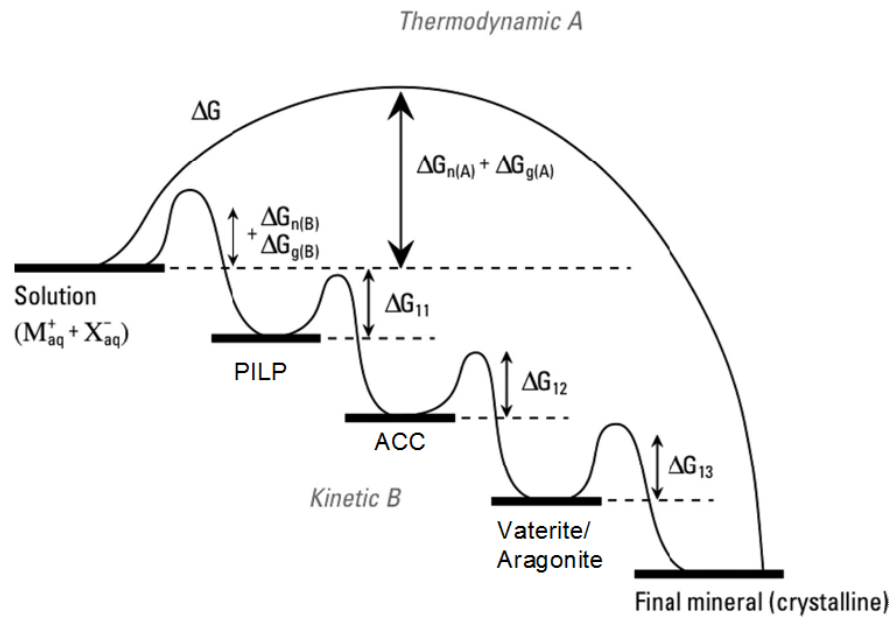


**Figure 1.1** Route A is the classical crystallisation pathway where  $\text{CaCO}_3$  is formed by the ion-by-ion route from solution without any intermediate phases. Route B is a lower energy pathway, occurring via the amorphous precursor phase and other metastable phases. Adapted from Ref [28]

### 1.2.2.1 Nucleation

The crystallization process consists of two major steps, nucleation and crystal growth. When the solute molecules disperse, the molecules tend to form clusters on the nanometer scale. At this stage, the atoms arrange in a defined and periodic manner that defines the crystal structure. If these clusters are stable they continue to form nuclei, while when the clusters are not stable, they redissolve. Depending on whether the nucleation occurs in solution or on a substrate, nucleation processes are classed as homogeneous or heterogeneous nucleation.

#### Homogenous Nucleation

In homogenous nucleation, the creation of a nucleus implies the formation of an interface at the boundaries of a new phase. Due to their large surface areas and small volumes, these clusters are very unstable. The Gibbs free energy of cluster formation can be expressed as the sum of volume and surface terms.

$$\Delta G_i = \Delta \mu_i + \gamma A(i) \quad (\text{Equation 1.2})$$

where  $\Delta G_i$  is the chemical potential,  $\Delta\mu_i$  is the chemical potential of the cluster (usually negative, related to the formation of the new bonds),  $A(i)$  the surface area of the cluster and  $\gamma$  the surface free energy (which is usually positive).[29] For a spherical cluster with radius  $r$ , the free energy of nucleation can be written as:

$$\Delta G = \left(\frac{4\pi r^3}{3\Omega}\right) k_B T \ln S + 4\pi r^2 \gamma \quad (\text{Equation 1.3})$$

Where  $\Omega$  is the volume of a molecule inside the crystal,  $k_B$  is the Boltzmann constant,  $T$  is the Temperature and  $S$  is the supersaturation level, which is the driving force (per molecule) of crystal formation and  $\gamma$  is the interfacial free energy between the forming nucleus and the solution. Thus the surface term is now proportional to  $4\pi r^2$  while the volume term is proportional to  $4\pi r^3$ .

When the cluster grows, the surface area is proportional to  $r^2$  and the volume to  $r^3$ . Therefore, when a small cluster grows at the beginning of the process, the surface contribution will be bigger than the volume factor which means that the free energy will be positive. As the cluster grows, the volume increases with  $r^3$ , such that the volume contribution grows faster than the surface, and eventually dominates. When it reaches a maximum free energy, the nucleus reaches a particular radius,  $r^*$ , that is called the critical nucleus (shown in Fig 1.2). At this point (the critical nucleus), nucleation ends and crystal growth begins.

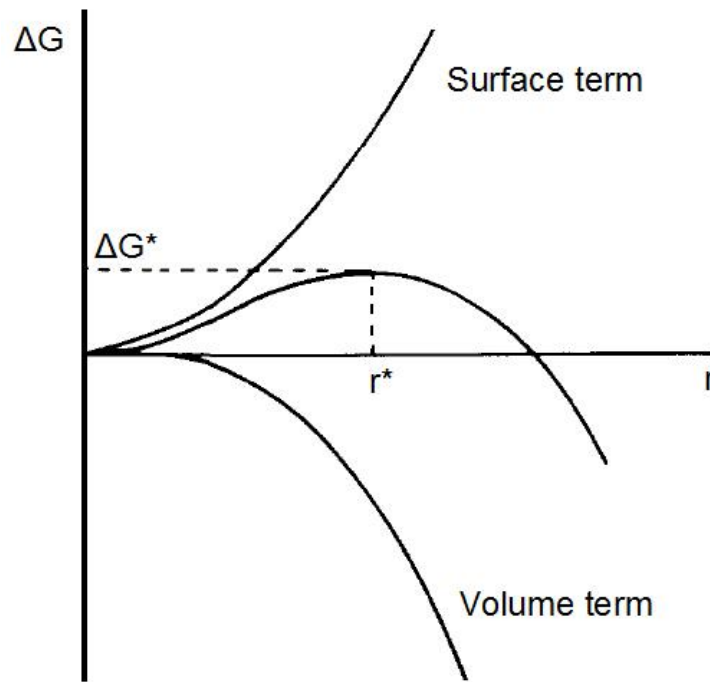


**Figure 1.2** Activation free energy for nucleation as a function of nucleus size,  $\Delta G^*$  represents the critical free energy at the critical radius  $r^*$  (Adapted from reference[30])

### **Heterogeneous nucleation**

In heterogeneous nucleation, surfaces or dispersed components already present in the solution, such as dust particles or crystal seeds, act as nuclei and provide the starting surface for crystallisation. Since a surface is already available in solution, the surface energy term will be reduced in heterogeneous nucleation, thus reducing the barrier to nucleation. This results in an increased rate of nucleation.[31] Heterogeneous nucleation will always dominate at low supersaturation, whereas at high supersaturation, homogeneous nucleation can also occur. This is because the nucleation sites for heterogeneous nucleation will be much more limited in comparison to those for homogenous nucleation.

#### **1.2.2.2 Crystal Growth**

Crystal growth occurs after a nucleus has reached a critical size, and solute molecules and atoms adsorb to an existing crystal face. Growth at the crystal surface occurs when the flux of atoms, ions or molecules attaching to the surface is greater

than that of the ones re-entering the solution. Then the rate at which a specific surface grows depends on the ability to catch ions, which in turn depends upon the strength and the number of interactions that can be made.[32]

Before being attached to a surface, an incoming ion can encounter three different environments on an existing crystal in 3-dimensions (shown in Fig1.3) as defined by the Hartman-Perdock system.[33] A kinked face offers three bonds for attachment (shown in Fig1.3a, denoted by K), a stepped face provides two bonds (shown in Fig1.3a, denoted by S), and a flat or smooth surface can make a maximum of one bond with the incoming unit (shown in Fig1.3a, denoted by F). Furthermore, the growth unit will have to overcome a number of energy barriers such as (partial) desolvation, diffusion across the surface to a step site, and further desolvation to enter a kink site to reach the binding site on the surface. This explains why the typical crystal has flat faces, straight edges and sharp corners – any kinked or stepped sites quickly vanish during crystal growth. So, the mechanisms by which mature crystals continue to grow are principally concerned with the propagation of flat faces. As shown in Figure 1.3b, faces that grow quickly vanish during crystal growth, while slow growing faces will stay, and are expressed in the final crystal morphology.

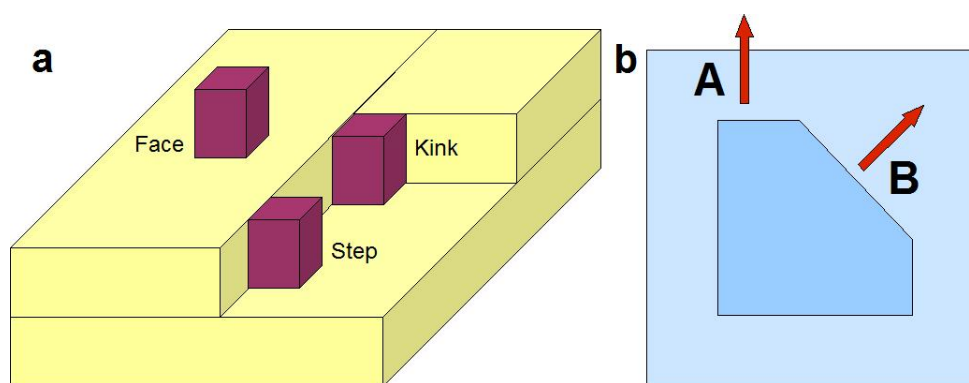


**Figure 1.3** a) Schematic representation of the growth of a crystal with the face, kink and step sites. The schematic in b) shows the growth of a crystal where surface B grows much faster than surface A and is finally almost lost in the crystal morphology.

As a result of predominance of either nucleation or crystal growth, crystals with different sizes are obtained. Depending on the supersaturation, the two steps can occur simultaneously, as this is the driving force behind the crystallization, which controls the rate of nucleation and growth. Once the supersaturation is exhausted, the solid–liquid system reaches equilibrium and crystallization is complete.

### **1.2.3 Non-Classical Crystallization**

#### **1.2.3.1 Oriented Attachment**

In contrast to classical crystallization processes, which under thermodynamic control are considered to operate under low supersaturation and additive concentrations, non-classical crystallization under kinetic control becomes increasingly important with increasing supersaturation and additive concentrations to produce the formation of many crystalline nuclei.[34] In a non-controlled way this leads to the formation of polycrystalline particles based on a non-oriented aggregation of nanoparticles. By the use of additives however, it is possible to stabilise the nanoparticles and control their aggregation process. In this case, a different pathway of non-classical crystallization can come into play which involves the oriented attachment and fusion of particles followed by the formation of a product with single crystal characteristics.

These pathways of classical and non-classical crystallization are outlined in Figure 1.4. In Fig 1.4, (a) represents the classical crystallization pathway where ions or molecules form unstable clusters which grow until they reach the size of the critical nucleus. They then grow to form a primary nanoparticle, which is amplified to a single crystal. The primary nanoparticles followed by the nucleation clusters can also assemble to form an iso-oriented crystal, where the nanocrystalline building units can crystallographically lock in and fuse to form a single crystal, as shown in path (b). Mesocrystals can be formed if the primary nanoparticles get covered by a polymer or another additive before they undergo a mesoscale assembly (path c). Path d shows that monocrystals can even form from pure nanoparticles.[35]

Pathway b mentioned the oriented attachment process which involves the arrangement of primary particles into an iso-oriented crystal. These primary nanoparticles spontaneously self-organise into a superstructure with a common

crystallographic orientation, and a single crystal can form after fusion of the nanoparticles.[34, 36] The driving force for this process is a reduction in the surface energy. When nanoparticles come close enough to each other, Van der Waals forces start to act between all particles in solution and therefore play a role in the aggregation of nanocrystallites in non-classical assembly. Due to the thermal energy of these nanoparticles, they are still able to rearrange themselves to find the low-energy configuration represented by a coherent particle-particle interface.[35] Nanocrystalline titania prepared under hydrothermal conditions was the first observation to reveal this oriented attachment phenomenon in crystallization.[20, 37]) This mechanism is particularly relevant in the nanocrystalline regime since in this case, particles with high specific surface areas preferably fuse together due to the gain of a substantial amount of energy by elimination of two high-energy surfaces.[38] Oriented attachment process can also be found in pathway c where an iso-oriented crystal forms through the oriented aggregation of stabilized units. Then a single crystal can be formed by the subsequent fusion of those units.

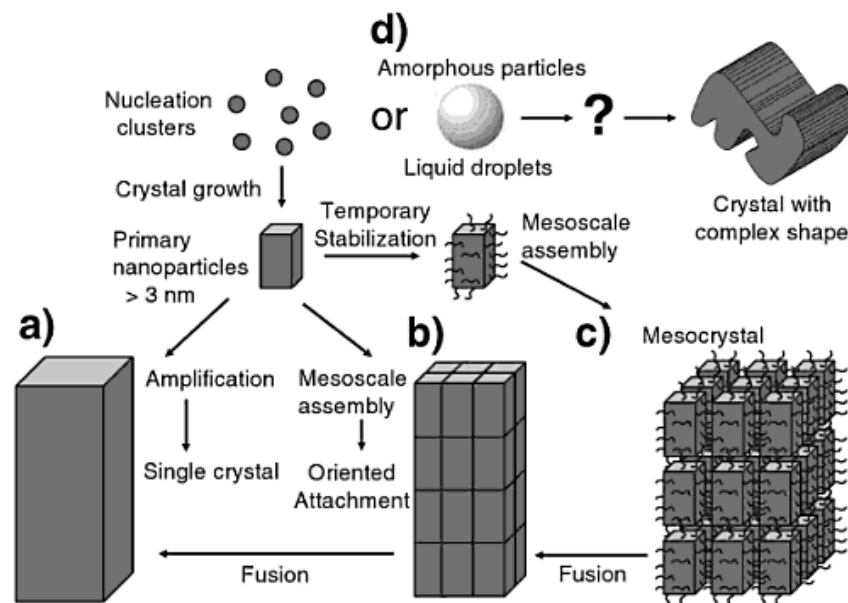


**Figure 1.4** Schematic representation of classical and non-classical crystallization. (a) Classical crystallization pathway, (b) oriented attachment of primary nanoparticles forming an iso-oriented crystal upon fusing, (c) mesocrystal formation via self-assembly of primary nanoparticles covered with organics. (d) Amorphous particles are formed, which can transform before or after their assembly to complicated morphologies. Image reproduced from ref [39]

### **1.2.3.2 Mesocrystal formation**

In the presence of inhibitor additives, the aggregation-based pathway may be hindered by additives such as polystyrene sulfonate (PSS), block copolymers and other kinds of additives[4, 40] that adsorb onto specific faces of nanocrystals, thus leading to a subsequent aggregation process (shown in Fig 1.4c). In this case, non-classical crystallization can come into play which involves the oriented attachment and fusion of particles followed by the formation of a product with single crystal characteristics.[28] These particle-mediated crystallization pathways further involve the mesoscopic transformation of self-assembled, metastable or amorphous precursor particles into nano-sized superstructures,[41] which later form an ordered nanoparticle superstructures.[2] Mesocrystals were recently redefined as “mesoscopically structured crystals” based on their structures rather than their formation mechanism. They have therefore been defined as “a crystal comprising a 3D array of iso-oriented single crystal particles of size 1–1000 nm (mesoscale dimensions).[42] This mesocrystal structure can therefore be distinguished from a randomly oriented polycrystal.[42]

## **1.3 Biological control of crystallization**

In biological crystallization, the most widespread control strategy employed is undoubtedly the use of soluble additives, where these can selectively affect nucleation and growth processes, leading to changes in particles numbers and sizes as well as morphology and polymorph, or even inhibition of crystal growth.[43] There is, however, strong evidence that the physical environment in which a crystal forms can also lead to control over many features such as morphology, size, orientation and polymorph.[44] Indeed, although experiments attempting to mimic biological crystallization are usually carried out in bulk solution, many biological and geological processes actually occur within small volumes,[45, 46] where the confining surfaces become increasingly important in defining the product material.

### **1.3.1 Magnesium and Proteins Control Crystal Formation**

For many years, various impurities in biological crystallization processes have been discovered, and it is known that these can sometimes modify the shapes of crystals and/or retard crystal growth rates. Much of the biomimetic experimental work directed at an understanding of these effects, however, has been qualitative in nature, and the emphasis has been on crystal habit modification.

#### **1.3.1.1 Magnesium ions**

Magnesium incorporation in some important biominerals, such as calcium carbonate, calcium phosphate and calcium oxalate, suggests it intimately involved in controlling crystallization processes. Magnesium incorporation in calcium carbonate biominerals is particularly interesting. Magnesium is typically incorporated within biogenic calcite present at levels of a few percent to around 20% [47-49] and values of up to 44% have been observed in sea urchin teeth.[4]. Magnesium concentrations ranging from 0.5% in outer tooth enamel layers to 2% in the innermost dentine have also been noted.[50]

Mg is a very effective crystal-growth inhibitor. Biology can generate magnesian calcites under conditions where aragonite would form rather than calcite in synthetic systems.[51, 52] The effect on polymorph is attributed to the higher hydration energy of  $Mg^{2+}$  than  $Ca^{2+}$  and to the fact that magnesium can be incorporated in the aragonite but not in the calcite lattice.[53-55] The morphology of calcite is also modified by  $Mg^{2+}$  ions, resulting in the generation of elongated, seed-like particles with roughened, faceted faces.[53, 56] It has also been suggested that calcite may be precipitated via an amorphous precursor phase rather than direct from solution in the presence of magnesium ions.[32, 57] Also, traces of magnesium ions have been shown to influence calcium phosphate formation by reducing the overall rate of seeded calcium phosphate crystallization[35] and they can markedly delay the transformation of amorphous calcium phosphates to more stable apatitic phases.[58] Magnesium ions were also induced to urine to investigate its reduction on calcium oxalate formation in humans.[47]

### **1.3.1.2 Proteins**

Proteins with complex sequences have also been used to control the nucleation and growth of biominerals. Detailed characterization of shell structures has revealed that macromolecules used to control the polymorph and morphology of crystals contains high percentages of acidic amino acid residues, including aspartic acid and glutamic acid residues.[50, 59] Proteins containing acidic residues were extracted from the aragonitic crossed-lamellar component of a gastropod shell, and were shown to play an important role in determining the mechanism by which ACC transforms to an aragonite phase via a vaterite intermediate.[60] Bones and teeth, which are made from calcium phosphates, also grow under the control of proteins.[61] Formation of the apatitic phase proceeds through a complex phase transformation[1, 51] and ACP (amorphous calcium phosphate) has been identified in the early stages as an important intermediate of bone and tooth mineralization.[58, 62, 63] Proteins that contain polyaspartic acid and glutamic acids found in urine are known to inhibit the formation of kidney stones, where these form due to the aggregation of calcium oxalate (CaOx) and/or calcium phosphate.[64] Calcium oxalate tends to favour COD (calcium oxalate dihydrate) formation in preference to COM (calcium oxalate monohydrate).[65] In addition, a change of COM morphology was also observed, resulting in dumbbell-shaped particles in the presence of urinary macromolecules.

### **1.3.2 Control of Biomineral growth in Confined volumes**

Many biological reactions occur under the control of specific boundary spaces to regulate the size and shape of biominerals. Like protein matrix frameworks, vesicles and cellular membrane, they can all provide structural and chemical environment that control crystal formation. These organic compartmentalization structure are always assembled before mineralization through covalent and non-covalent interactions between the molecules.[1] The spatial control is often related to both the physical dimensions such as passive enclosure and the mechanisms for active chemical control such as moving selective ions and molecules into the mineralization zone. Generally, confinement on biological processes can determine the morphology, orientation, and location of the biominerals through control of precursor ions and phases. There are three main types of organic structures that are

recognized in spatial boundary biomineralization, vesicle, including phospholipid and polypeptide vesicles, cellular assemblies and macromolecule frameworks. [1]

### **1.3.2.1 Intracellular Vesicles**

Biomineralization unicellular organisms often occurs within intracellular vesicles. Amorphous calcium carbonate as temporary storage deposits is formed in various vesicles[18] and silica deposition was controlled by small cytoplasmic vesicles of about 300 to 400 Å in diameter.[66] These specially formed biological compartments are fluid-filled sites that usually enclosed by a membrane containing a bilayer of lipid molecules with embedded proteins. [1] Through their ability to self-assemble and compartmentalize, lipid enable the formation of a large variety of biomaterials with controlled micro- or nano-vesicles.[66]

Self-organized of vesicles membrane is based on the balancing of hydrophobic and hydrophilic interactions that exist for amphiphilic nature biomolecules that dispersed in a polar solvent. Most lipid molecules are composed of a polar or charged headgroup, one or more (generally have two) hydrophobic tails, and a backbone structure that connects the two. The polar or charged headgroup can consist of any number of charged or uncharged polar moieties. And the tail regions can contain aromatic groups, saturated or unsaturated aliphatic chains. There are also variety of the connected backbone structures, from polyol-based structure such as glycerol, to the aromatic polycyclic structure of cholesterol and other isoprenoids.[66] Thus these lipids are often categorized according to the backbone structure such as phospholipids, isoprenoids, sphingolipids, ceramides and fatty acids etc. Here phospholipids are key membrane constituents of biological vesicles. In aqueous solution, the hydrophilic headgroup are solvated and extrovert in character whereas the hydrophobic chains introvert intent to shield themselves. When they exhibit a strong tendency to self-assemble, the hydrophobic residues become internalized within a supermolecular aggregate such as micelles, reverse micelles or bilayers (as shown in Fig 1.4).

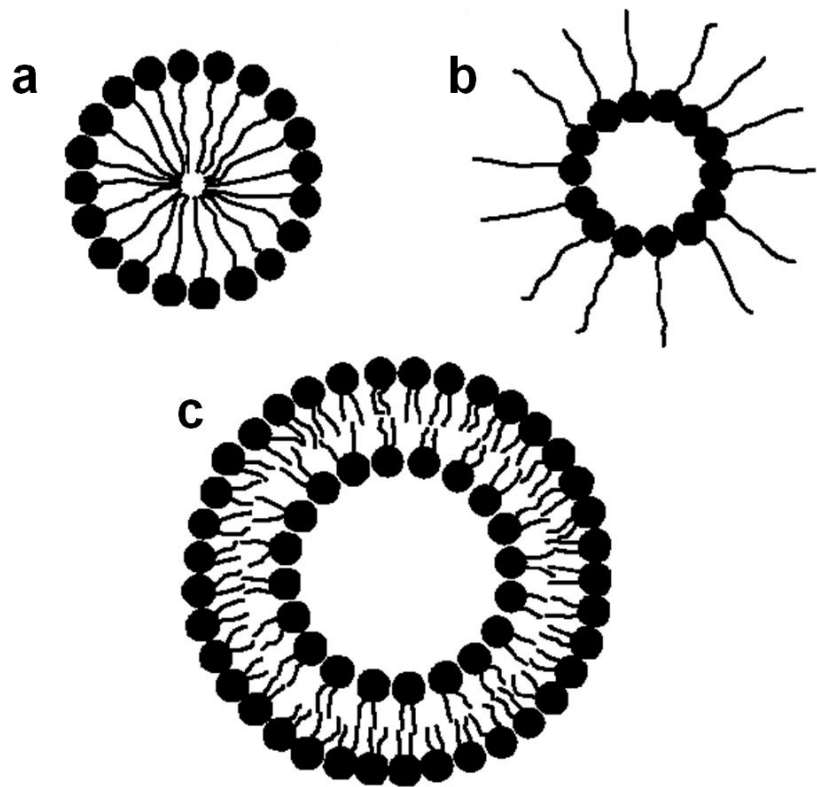


**Figure 1.5** Common self-assembled structures of lipids a) micelle, b) inverse micelle and c) bilayer vesicle.

### 1.3.2.2 Cellular assemblies

The formation of calcium phosphate which in teeth and bone also provide another method of sealing off biological space.[67] In the bone formation process, the bone-forming cells which are called osteoblasts assemble to produce a compartment that is separated from the blood and contains the mineralized tissue (as shown in Fig 1.6). Compact bone is covered and controlled by a layer of tightly packed osteoblasts. As shown in Fig 1.6, the osteoblasts are direct contact with the bone cells-osteocyte that forms an interconnection network inside the bone. And on the outer side of the membrane, they are exposed to the extracellular fluid which helps the equilibrium in the blood.[1] Thus, the osteoblasts are not only to provide the space of deposition the bone, but also provide a communication between the external and internal environments that enable the bone to grow.

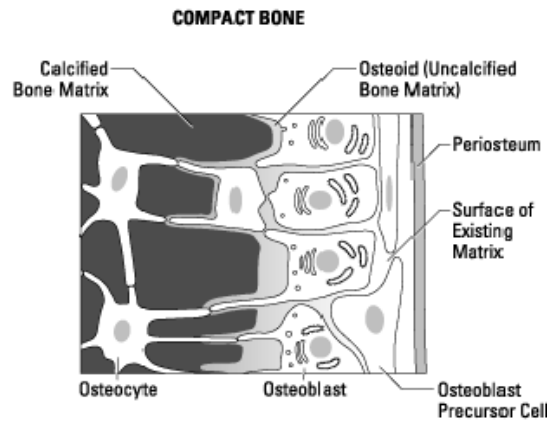


**Figure 1.6** Osteoblasts, cells that take up calcium compounds from the blood and secrete sturdy bone matrix, live on the surface of existing matrix. Cells gradually become embedded in their own matrix, forming uncalcified bone matrix (osteoid). The addition of calcium phosphate forms the calcified bone matrix, which surrounds the mature bone cells (osteocytes). Reproduce from Reference [68]

A similar model of cellular assemblies is the layer of closely-packed cells which group together in association with a solid substrate such as a polymerized layer of macromolecules or a pre-existing mineral surface (as shown in Fig 1.7) as occurs in the shell layers of molluscs.[69] The outer prismatic calcite layer develops in a space formed by a packed sheet of epithelial cells which are used to seal off the biomineralization sites and control the chemistry of the internalized fluid-filled environment.

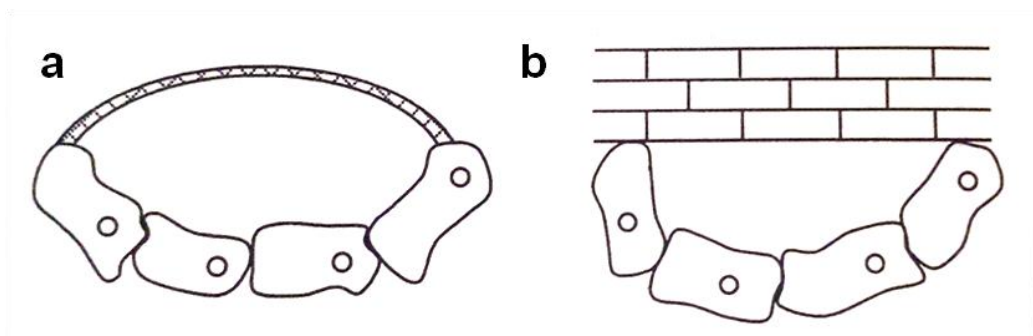


**Figure 1.7** Space delineation using groups of cells in associations with: (a) an impervious polymerized organic sheet and (b) an existing mineralized structure.[70]

### 1.3.2.3 Macromolecular frameworks

The small size of vesicles in the intercellular or intracellular systems as discussed above is not generally compatible with building large biomaterials such as bone, teeth or shells. Therefore, the processes occurring in the extracellular spaces are regulated through the use of semi-permeable organic matrices with open framework structures.[1] For example, the avian eggshell provides a micrometer-sized compartment in which calcite crystals can grow in a spongy organic matrix that is secreted between an epithelial cells layer and an insoluble fibrous membrane.[71, 72] Actually, it is possible to propose a four-step mechanism of biomineralization where the structure and growth of minerals is controlled in the compartment.[73] As shown in Fig 1.8, the crystals nucleate at well-ordered and specific sites on the organic sheet which is composed of  $\beta$  chitin or X collagen. Then, crystal growth occurs with a polyanionic gel and extends along their crystallographic  $c$  axes. With time, the formation and the thickness of the crystal is related to the fabrication axes of new inert scaffolding or the deposition of particular hydrophobic inhibitory proteins.

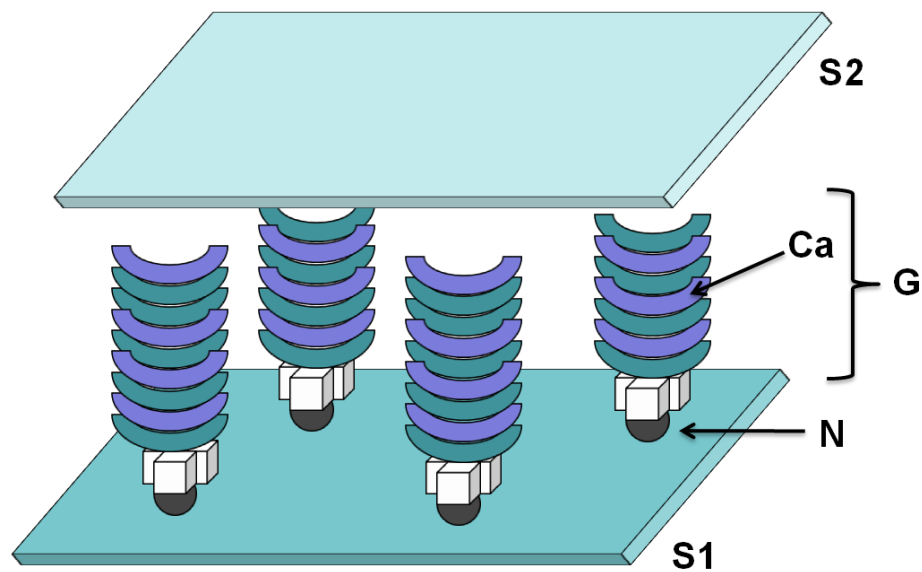


**Figure 1.8** A model of shell mineralization. Crystal nucleation occurs on an organic sheet (S1) coated with polyanionic nucleation sites (N). Crystal growth (Ca) occurs within a polyanionic gel (G). Mineralization arrest is associated with the deposition of another organic sheet or specific macromolecules (S2).

## **1.4. Synthetic Control of Crystal Growth**

Many important phenomena as varied as the generation of nanomaterials, pharmaceuticals and food stuffs, weathering and frost heave, ice formation in the atmosphere and the construction of biominerals such as seashells are based on crystallization. The ability to effectively control crystallization processes therefore promises, for example, to optimise products and synthetic methods, to minimise undesirable processes such as scale deposition or kidney stone formation and to achieve repair over structures such as bones and teeth.

### **1.4.1 Additives control of Crystal Growth**

In the synthesis of many industrially-important materials, the ability to control crystallization process is a critical requirement. Therefore the presence of additives can be used to control polymorph, the location of nucleation, crystal size and shape, crystallographic orientation, composition, stability, and hierarchical assembly of the crystals.[50] Some additives can suppress growth entirely; some may enhance growth, while others may exert a highly selective effect, acting only on certain crystallographic faces and thus modifying the crystal habit. Some additives can exert an influence at very low concentrations, less than 1 part per million, whereas others need to be present in fairly large amounts before having any effect. Any substance other than the material being crystallized can be considered an “impurity”, so even the solvent from which the crystals are grown is in a sense an impurity, and it is well known that a change of solvent frequently results in a change of crystal habit. In this way, these additives must selectively adsorb to certain faces and modify crystal morphologies by reducing the surface energies of this family of faces.[34] This behaviour will be expressed in a modification of the equilibrium crystal morphology, as expressed by Wulff’s rule. This rule is usually derived from a variational principle by minimizing the surface free energy of the crystal by keeping its volume constant. The additive which can cover the outer faces of the crystals can reduce the crystal growth rate. Fig 1.9 shows the effect of additives upon the crystal morphology when selectively adsorbed onto two crystal faces only. This causes the uncovered faces, with higher surface energies, to continue to grow. [34]

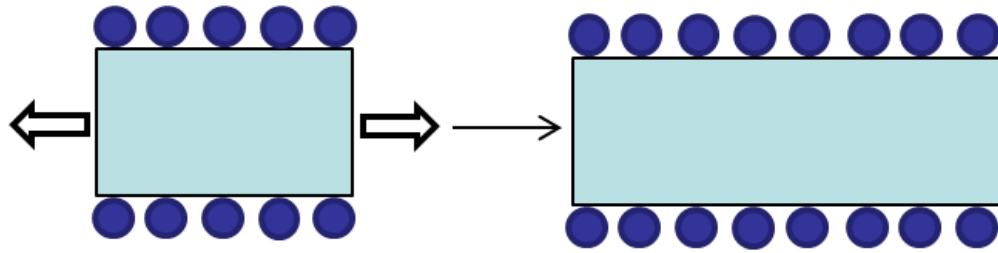


**Figure 1.9** Adsorption of an additive (filled circles) onto a crystal surface lowers its surface energy and, thus, its growth rate. The crystal predominantly grows at the uncovered faces.[58]

However, sometimes it is not necessary to cover the entire surface with additives to block its further growth. As seen in Fig 1.10, three sites may be considered at which impurity species may become absorbed and disrupt the flow of growth layers across the faces, at the kink and between steps. Briefly, if kink site absorption is possible, growth retardation may be affected at a low impurity concentration in the solution. More impurity would be needed if step site absorption is the preferred mode while much higher impurity concentration may be required if absorption only occurs on the crystal faces. Cabrera and Vermilyea (1958) introduced the *Cabrera – Vermilyea Model* which hypothesized that “immobile” impurities can absorb on terraces of crystal surface and “pin” steps. Thus, the process of step movement and the growth of layers on a crystal surface is blocked by individually-absorbed impurity species. They also proposed that complete stoppage of growth would occur when the distance between the absorbed impurities species was  $< 2r_c$ , where  $r_c$  represented the radius of a critical two-dimensional nucleus[74].

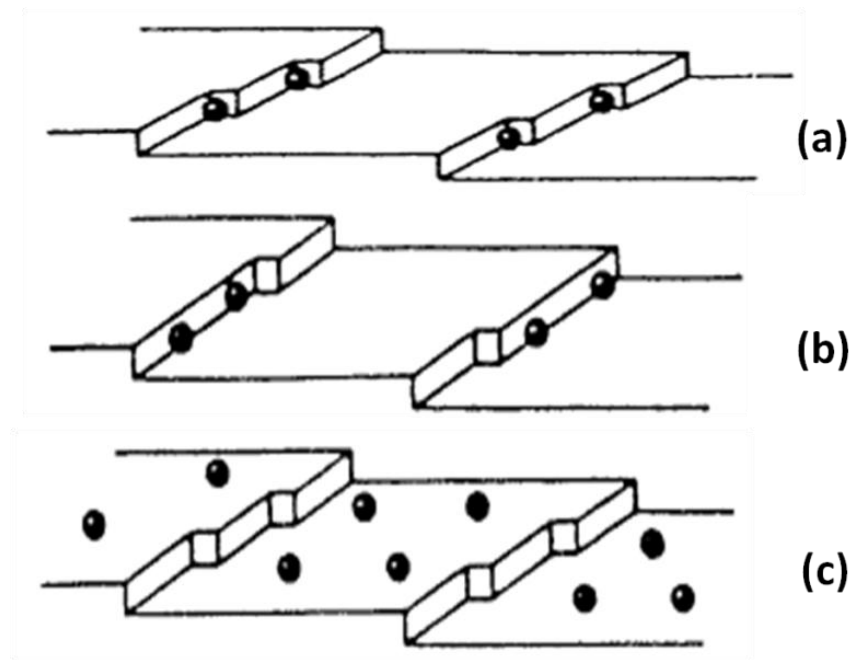


**Figure 1.10** Sites for impurity absorption on a growing crystal, based on Kossel model: (a) kink; (b) step and (c) face. [74]

For the years, different additives have been developed and are extensively used as precipitation inhibitors for various sparingly soluble salts i.e., calcium carbonate, calcium phosphate, calcium sulfate, calcium fluoride and barium sulfate. Studies have shown that inhibitor performance strongly depends on polyelectrolyte architecture, molecular weight and ionic charge. These additives are also believed to participate in both nucleation and growth processes[75] and can be incorporated into a crystal to generate a composite material where the specific placement of the additives introduces a characteristic texture and anisotropy into the crystal lattice[76] More recently, it has also recognized that many crystalline biominerals form via an amorphous precursor, which is stabilized by organic additives which lead to control over the crystal properties.[9] However, although this biogenic strategy was used extensively, the mechanisms by which these additives influence specific features such as their size and structure affect the crystal lattice, remain poorly understood.[77]

#### **1.4.1. 1 Simple Ionic Additives**

Ions such as  $Mg^{2+}$  or  $Li^+$  can have a marked effect on crystallization, particularly with regard to habit modification, as observed for  $CaCO_3$  precipitation.[78] Specific faces of calcite crystals were strongly suppressed and a polymorph change to aragonite was observed. During the formation of calcium phosphate, the inhibitory effect of  $Mg^{2+}$  is well known, and  $Zn^{2+}$ ,  $Mn^{2+}$ ,  $Ni^{2+}$ ,  $Co^{2+}$ , and  $Cr^{2+}$  have also been found to significantly inhibit the crystal growth.[49, 52, 56, 79] The influence of  $Mg^{2+}$ ,  $Zn^{2+}$ ,  $Mn^{2+}$ ,  $Cu^{2+}$ , on the growth of calcium oxalate has been studied. It was shown that zinc was the most active inhibitor of calcium oxalate growth among the ions tested.[80]

#### **1.4.1.2 Low Molecular Mass Organic Additives**

Given the importance of aspartic-rich proteins in biomineralization, some low-molecular-weight organic species were chosen to mimic the active proteins. During the crystallization of calcium carbonate, citric and maleic acid have been shown to strongly influence the crystal morphology, especially in the presence of magnesium ions.[81] Studies have also shown that aspartic acid can bind to specific step edges at the crystal surface, resulting in control over the morphology of calcite crystals.[82] Other amino acids, such as alanine, lysine, and glycine, have similar effects.[83] Recently, it has been shown to be possible to produce a material in vitro with a structure that is similar to the structure of bone. The synthesis of hydroxyapatite (HA)–aspartic acid and HA–glutamic acid nanocrystals was carried out in the presence of different amounts of the amino acids.[84] Citrate also has a significant effect on the solubility of calcium oxalate (especially calcium monohydrate), causing a reduction of crystal size (approximately 37% decrease), crystal number (approximately 53% decrease) and total crystal mass (approximately 72% decrease). Citrate also causes up to 85% of the adherent COM crystals to detach from renal tubular cell surfaces. [85]

#### **1.4.1.3 Polymer additives**

The importance of polymeric additives in the formation of biominerals is further supported by several studies. For example, the crystallization of calcite often occurs

in combination with aspartic-rich proteins,(Berman, Hanson et al. 1993; Archibald, Qadri et al. 1996) which can alter the chiral morphology of calcite crystals by binding to specific step edges at the crystal surfaces.(Addadi, Raz et al. 2003)

Simple anionic polymers, such as poly(acrylic acid), were used to inhibit crystallization and causing changes in the mean crystal size, morphology and polymorphs. (Zhang and Gonsalves 1998; Kato 2000; Ouhenia, Chateigner et al. 2008) A good example of a nonclassical crystallization pathway which leads to  $\text{CaCO}_3$  mesocrystal formation is the use polystyrene sulfonate. This inhibits the nucleation and growth in all directions which may result in the formation of unusual  $\text{CaCO}_3$  superstructures.[86] Polyaspartate has also been used to control the formation of calcium phosphate crystals by introducing clusters that are loosely bound to the surface of collagen fibrils.[61] Amorphous calcium phosphate was also more stable when precipitated in the presence of polyacrylate, poly-L-glutamate and poly-L-lysine.[87] Synthetic macromolecular inhibitors such as poly(aspartic acid), poly(glutamic acid)[88], or glycosaminoglycans (GAGs)[89] were studied to gain insight into the molecular mechanisms of calcium oxalate crystal interactions.

#### **1.4.2 Synthesis in confined reaction spaces**

Biological and chemical reactions can be dramatically affected by confinement, which has stimulated a rapidly growing interest in this effect [90]. Previous studies have shown that porous single crystals of calcite can be grown within templates such as colloidal crystals [9] and porous polymer membranes [4] while ice templates have been used to form porous hydroxyapatite/collagen composites [91]. The lifetime of amorphous phases, the interaction of a growing crystal with soluble macromolecules and the aggregation behaviour of precursor mineral particles can be greatly changed in small pores. In Section 1.3.2, we discussed the roles that compartments such as vesicles, cellular assemblies and macromolecular frameworks play in biological systems. Each of these has been mimicked in synthetic systems, such as synthetic vesicles, bacterial threads and polymer sponges. Some systems that offer restricted volumes and which have been used to produce crystals with controlled sizes and morphologies will now be discussed in more detail.

#### **1.4.2.1. Synthetic Vesicles**

Vesicles are central to many biomineralization processes, as discussed in Section 1.3.1.1. In the laboratory, synthetic vesicles can be readily prepared from amphiphilic molecules which self-assemble into vesicles.[92] Use of vesicles as reaction compartments to generate nanosized calcite enables us to control their microscopic structures and macroscopic properties, and reveals that the confinement affects the calcite lattice from the atomic to the micrometre length scale. For calcium phosphate, synthetic liposomes were used to investigate the possible roles of membrane lipids in calcification.[93, 94] In this method, phosphate encapsulated in the aqueous interiors of liposomes is allowed to come into contact with  $\text{Ca}^{2+}$  from the external suspending medium. After the apatite mineral precipitates first inside the liposome, the crystals then rupture the membrane and seed further precipitation in the surrounding solution.[95] The advantage of this method is that the liposomes permit precipitation to occur in two separate fluid compartments, where the second layer acts as a membrane barrier.[96] Reverse micelles are also being increasingly used to prepare nanowires and nanorods, where they behave as microreactors that can compartmentalize reactants at the nanometer level. Calcium sulfate nanowires with diameter less than 30 nm and lengths of over 2  $\mu\text{m}$  were obtained in reverse micelle together with some nanoparticles.[97] Therefore, these synthetic vesicles and micelles can have a great influence on the size, morphology and polymorph of particles.

#### **1.4.2.2. Polymer sponges**

Polymer sponges can be prepared from polyesters such as poly(lactic acid) (PLA), poly(glycolic acid) (PGA) and their copolymers (PLGA). These have been used to develop porous 3-D scaffolds using various fabrication techniques.[98-101] These scaffolds, which have specific biological factors and physical characters, can be utilized to induce the formation of new biominerals for specific applications. Some synthetic polymers, such as homopolymers and copolymers of lactic and glycolic acids are generally considered to be biocompatible and are attractive candidates for fabricating tissue engineering scaffolds.[101] In contact with aqueous solutions, these gel scaffold undergo reversible swelling to give an open-cell structure with pores several nanometres across. These can be infiltrated and mineralized with

organic components.[70] The hydrolytic degradation properties of these polymers [102] leads to the ultimate formation of a completely natural, engineered tissue with no permanent foreign material.[101] For hydroxyapatite, these macroporous scaffolds have controllable pore sizes and interconnected pores, where their microstructures can be controlled to enhance the mechanical properties.[103, 104]

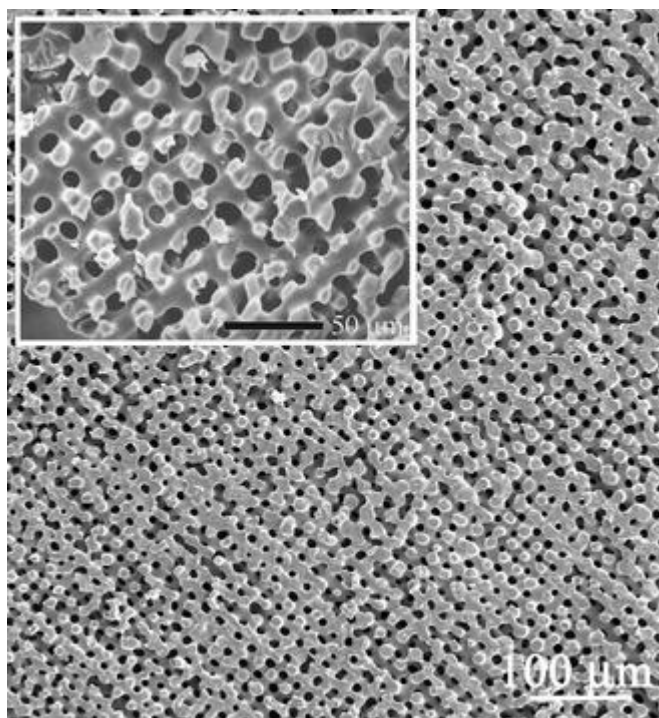


**Figure 1.11** Polymer membrane formed as a replica of a sea urchin plate. Inset shows the structure of the original urchin plate. Adopted from Ref [105]

#### **1.4.2.3. Droplet Arrays**

Another kind of confined system is arrays of metastable solution droplets of 20 μm diameter formed on self-assembled monolayers (SAMs). These have been used to study heterogeneous nucleation[106] and have most frequently been used to crystallize a variety of organic compounds including amino acids, proteins, and active pharmaceutical ingredients.[107-110] Amorphous calcium carbonate was formed in droplets and then transformed into calcite at the interface. This precipitation occurs under humid conditions to prevent evaporation.[111] This kind of system can also be used to study heterogeneous nucleation of crystals of the organic compounds glycine, sulfathiazole, and mefenamic acid.[112, 113] The mechanism of nucleation and growth can also be investigated in this reagent-limited

condition. Fig 1.10 shows a schematic of the organic assemblies used for templated crystallization of  $\text{CaCO}_3$ , where they have been shown to support highly efficient face-selective nucleation of calcite.

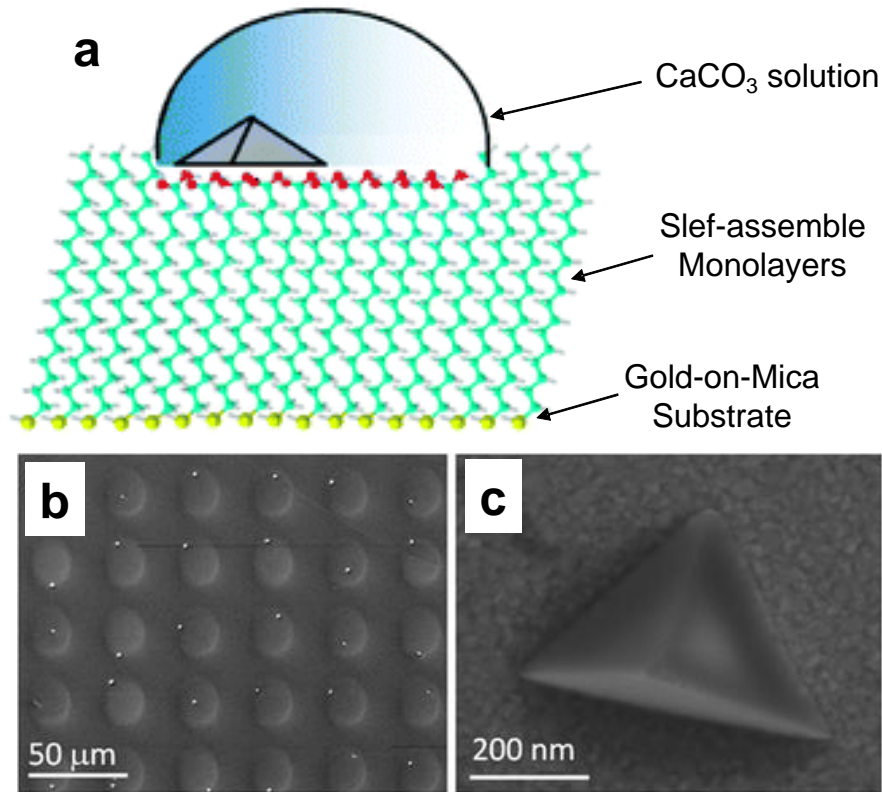


**Figure 1.12** Schematic diagram of the fabrication of the droplet arrays.(a) Deposition of droplets by passing a  $\text{Na}_2\text{CO}_3/\text{CaCl}_2$  solution across the patterned self-assemble monolayer at 100% humidity.(b) SEM images showing  $\text{CaCO}_3$  bulk solution onto surfaces patterned with 20 μm radius circles. And (c) Calcite crystal precipitated from single droplet. Adopted from Ref [114]

#### 1.4.2.4. Track-etch membranes

Another simple biomimetic system, a polycarbonate track-etch membrane of 10 μm thickness (pore diameter 3 μm) was used as a crystallization environment.[115] These pores provide regular cylindrical channels which are very similar to the dimensions of sea urchin embryo spicules. ACC was precipitated in the pores by placing the membrane between two identical, half U-tubes, with  $\text{CaCl}_2$  solution and  $\text{Na}_2\text{CO}_3$  solution. The experiment was carried out at 4-8°C to induce the

transformation from ACC precursor phase to rod-shaped calcite whose form has been dictated from the surrounding membrane pores.[116]

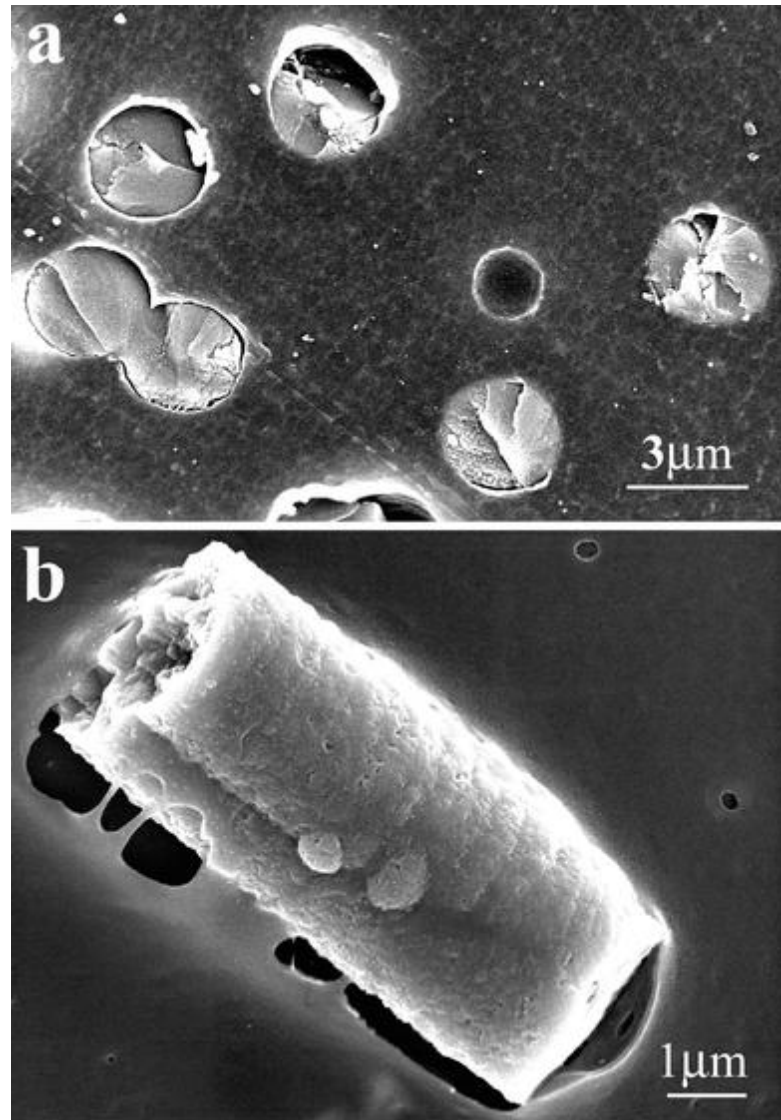


**Figure 1.13** (a) Calcium carbonate crystals grown within membrane pores. (b) Intra-membrane crystal isolated from the membrane, showing cylindrical morphology and dimensions identical to the membrane pores. Both images are of samples after 24 h.[117]

#### 1.5.2.5. Crossed-cylinders

Previous studies showed a new technique that SAMs can provide well orientated of crystals and using two half cylinder glasses to form confinement will be explored deeply.[118, 119] The volume between two crossed cylinders provides a well-defined annular wedge. The confined reaction environment varies continuously from

dimensions of angstroms to micrometers and therefore the investigation of the effect of confinement over a large range of dimensions in a single system. This kind of system is free access of reagent into the reaction space which overcomes problems of limited reagent which occurs in many confined systems. The surface separation  $h$  between crossed cylinders of equal radius of curvature  $R$  is equal to that between a sphere of radius  $R$  and a flat surface. It is related to the radial distance  $x$  from the contact point by:

$$h = R - \sqrt{R^2 - x^2} \approx x^2/2R \quad (1)$$

$h$  hence varies continuously from zero around the contact point to 2-3 mm at the vapour interface of the solution droplet, some 7-8 mm from the contact point. In this system, the surface of the glass half-cylinders are functionalise using SAMs, which using  $\omega$ -terminated alkanethiols ( $\text{HS}(\text{CH}_2)_n\text{X}$ ) supported on thin evaporated films of Au as a well-defined substrate to control the surface chemistry of the reaction environment. More details of this part will be shown in Chapter 5.

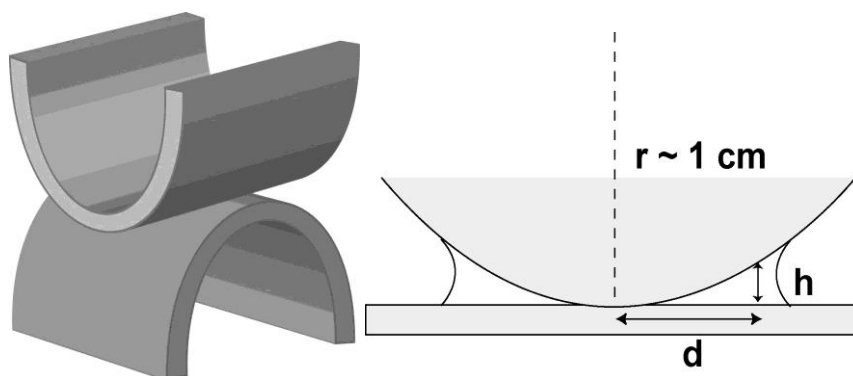


**Figure 1.14** The crossed-cylinder glasses provide a small volume to growth of crystal [118]

## Chapter 2 Experimental Methods



This section describes the general methods used for the preparation of apparatus and the precipitation of Ca-based minerals, together with the techniques used for the characterisation of precipitates.

## 2.1 Experimental Preparation

As discussed in Chapter 1, crystallisation is highly sensitive to the presence of impurities, and trace amounts of contaminants, such as surfactants, dust particles, organic molecules or metal ions are known to dramatically affect both nucleation rates and crystal morphologies. Therefore, rigorous cleaning procedures were undertaken before each experiment.

Basic experimental tools, such as tweezers, scissors or scalpels etc. were rinsed with ethanol and dried with nitrogen gas prior to use. Preparatory glassware, such as bottles, vials or slide substrates were cleaned by sonication. These glassware, which may contain organic contaminants, were soaked in a 10% wt/v solution of NaOH for 15 mins in an ultrasonic bath, resulting in a gradual etching of the glass surface and the removal of impurities. They were then sonicated in Milli-Q deionized water (resistivity  $18.2 \text{ M}\Omega\text{cm}^{-1}$ ) for 15 mins to remove any residue. Sonication provides additional mechanical cleaning and is useful in the removal of larger contaminants, such as organic molecules which always attached on the glass surface.

Glass substrates, such as slides or half cylinder glasses, which were used for crystallization were further cleaned by immersing in “Piranha solution” over night. The “Piranha solution” is defined as a solution of 3:1 sulfuric acid: hydrogen peroxide ( $\text{H}_2\text{SO}_4$ :  $\text{H}_2\text{O}_2$ ). The mixture became very hot (up to  $170^\circ\text{C}$ ) and can bubble and spit hot  $\text{H}_2\text{SO}_4$  after  $\text{H}_2\text{O}_2$  was added to  $\text{H}_2\text{SO}_4$ . Therefore it should be carried out in fume cabinet with great care. These glass pieces were then removed after one night and were carefully rinsed with Millipore water to remove all traces of Piranha solution. After that, the glassware was stored under Millipore water until it was used. The ability of Piranha solution to effectively clean is due to its high acidity and ability to dehydrate, and it can dissolve organic particles which can modify crystal growth. In addition, it can also dissolve mineral deposits which could act as seeds for crystallization.

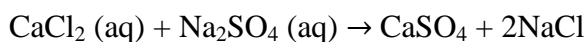
## **2.2 Crystallization**

### **2.2.1 General procedure**

These calcium-based minerals which will be mentioned in the next four chapters, were precipitated using double-decomposition methods that involve simply mixing two solutions to form a final solution which is supersaturated in a third product. Typically, equimolar solutions, such as  $\text{CaCl}_2$  (Sigma-Aldrich) are mixed with  $\text{Na}_2\text{CO}_3$  (Sigma-Aldrich),  $\text{Na}_2\text{SO}_4$  (Sigma-Aldrich) or  $\text{K}_2\text{HPO}_4$  (Sigma-Aldrich) in equal molar and equal volumes. Whereas the two components are highly soluble,  $\text{CaSO}_4$ , CaP or  $\text{CaCO}_3$  are sparingly soluble and therefore precipitate out when the initial solutions are combined. In some cases when the samples were investigated using SEM, crystal growth was terminated by removing the substrate from solution and rinsing with ethanol and drying under nitrogen gas. When samples were investigated using XRD, Raman or IR, filtration methods were used to collect precipitates; samples were filtered through track-etch membranes with 200 nm pores.

### **2.2.1 Crystallization of $\text{CaSO}_4$**

For  $\text{CaSO}_4$  crystallization, the experiments were carried out using double decomposition methods in which equal volumes and equal concentrations of calcium chloride (Sigma-Aldrich) and sodium sulfate (Sigma-Aldrich) solutions were mixed at the room temperature. Detailed descriptions are provided where they were used in Chapters 3, 4 and 5. The crystallization follows the pathway below:



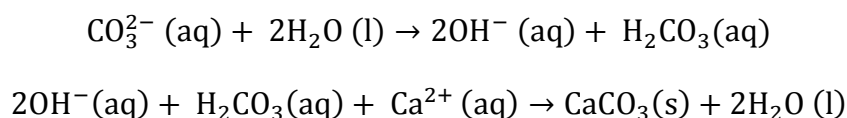
### **2.2.2 Crystallization of Calcium Phosphate (CaP)**

For the precipitation of calcium phosphate, experiments were carried out in Tris-Saline buffer solutions of composition 8.77g of NaCl, 6.61g of Tris-HCl and 0.96g of Tris-base which was corrected to pH 7.4.[120] This solution was then used to prepare a solution of composition 9 mM  $\text{CaCl}_2 \cdot 2\text{H}_2\text{O}$  and 4.2 mM  $\text{K}_2\text{HPO}_4 \cdot 3\text{H}_2\text{O}$ , and the pH was adjusted to 7.4 at 37 °C. Poly(aspartic acid), sodium salt solution

(poly-(alpha,beta)-DL-aspartic acid sodium salt Mw 2000 - 11000 Da) was added to the  $K_2HPO_4$  solution with a concentration from 10  $\mu\text{g/ml}$  to 100  $\mu\text{g/ml}$ . Calcium phosphate were precipitated in bulk solution and in the crossed-cylinder apparatus, as described in detail in Chapter 6.

### 2.2.3 Crystallization of $\text{CaCO}_3$

The double-decomposition method is a general approach to precipitate  $\text{CaCO}_3$ . Equimolar solutions of  $\text{CaCl}_2$  (Sigma-Aldrich) and  $\text{Na}_2\text{CO}_3$  (Sigma-Aldrich) in Milli-Q water were combined in equal volumes.[120] The experiments described in Chapter 7 were performed with concentrations ranging from 2 mM to 10 mM with growth periods from seconds to several hours. Crystallization follows the pathways below:



## 2.3 Characterization Technique

### 2.3.1 Scanning Electron Microscopy (SEM)

Scanning Electron microscopy is widely used in the work described in this thesis. It is a type of electron microscopy where a focused beam of electrons is scanned across the surface of an electrically conductive specimen. A deposited conductive layer on the surface of the specimen is therefore necessary to avoid charging.

A schematic diagram of a basic SEM instrument is shown in Fig 2.1. The electrons are produced and accelerated using a field emission gun (FEG) or thermionic source in a high vacuum column. The electrons are then focused on the sample by passing through two or three condenser lenses which demagnify the spot size down to 0.4 nm to 5 nm in diameter. The electron spot is then rastered by deflection coils. The electrons interact with the surface of the specimen with a resolution down to 1 nm, generating the electrons which form the image.[121] Different interactions between the electron beam and the surface of the specimen occur, with secondary electrons and back scattered electrons being most common. Used for image formation,

secondary electrons (<50 eV) were most commonly used in the work described here.[121] The secondary electrons emitted by the sample were collected by a Everhart-Thornley (E-T) detector and are represented on the screen by a brightness which corresponds to the measured intensity.

In this thesis all samples were examined using a Phillips XL-30 ESEM operating at 5-30 kV or a Leo 1530 Gemini FEGSEM microscope operating at 3.00 kV. The glass slides supporting calcium sulfate particles were mounted on SEM stubs using conducting carbon tape and were sputter-coated with 5-10 nm layer of Pt using an Agar High Resolution Sputter Coater.

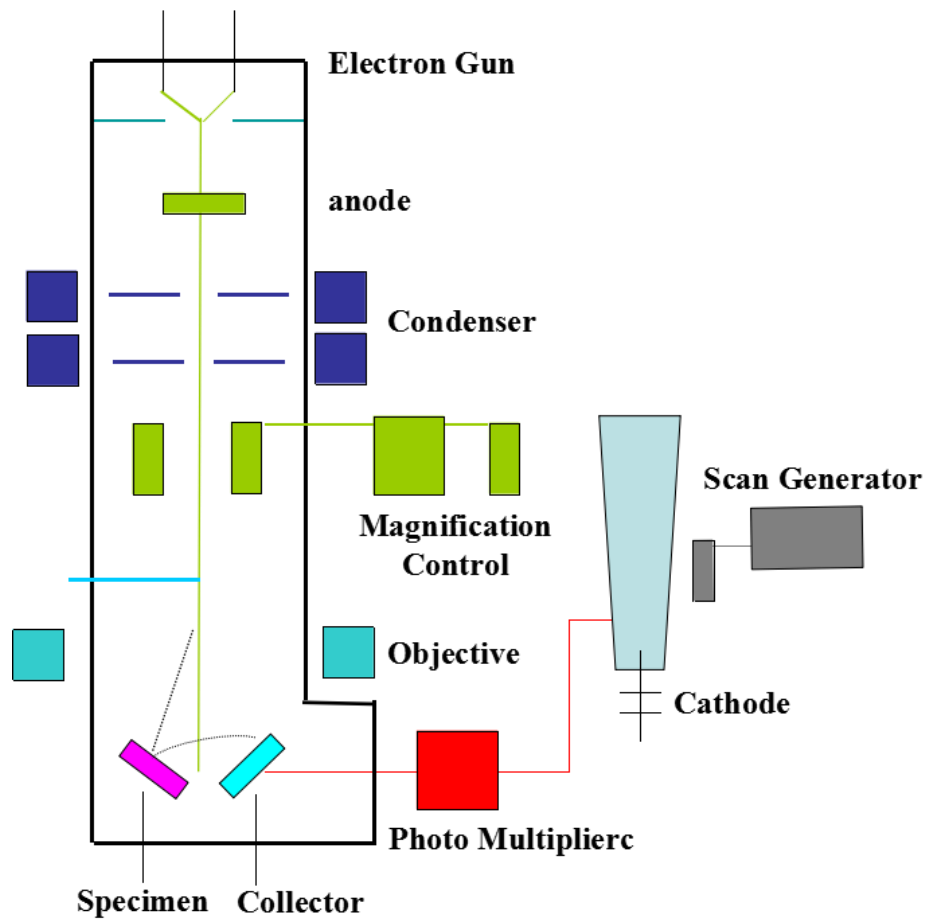


**Figure 2.1** Schematic diagram showing the components of an SEM column. A beam of electrons is produced at the top of the microscope by an electron gun. The electron beam follows a vertical path through the microscope, which is held within a vacuum. The beam travels through electromagnetic fields and lenses, which focus the beam down toward the sample. Once the beam hits the sample, electrons and X-rays are ejected from the sample.

## **2.3.2 Transmission Electron Microscopy (TEM)**

### **2.3.2.1 High-resolution transmission electron microscopy (HRTEM)**

Transmission electron microscopy (TEM) operates on the same basic principles as the light microscope but uses a beam of electrons that is transmitted through an ultra-thin sample less than 100 nm in thickness. The low wavelength of electrons used in TEM makes it possible to analyse materials down to a few angstrom ( $10^{-10}$  m)[122] The high magnifications made in TEM are valuable in medical, biological and materials research. The electron beam interacts with samples which were placed on a TEM grid as it passes through the sample. An image is formed from the interaction of the electrons and the sample and is magnified onto a viewing screen.

A TEM usually comprises several main parts[123], the vacuum system, the sample holder, the gun, the electromagnetic lens system, apertures and finally the detectors and screens (see Figure 2.2).

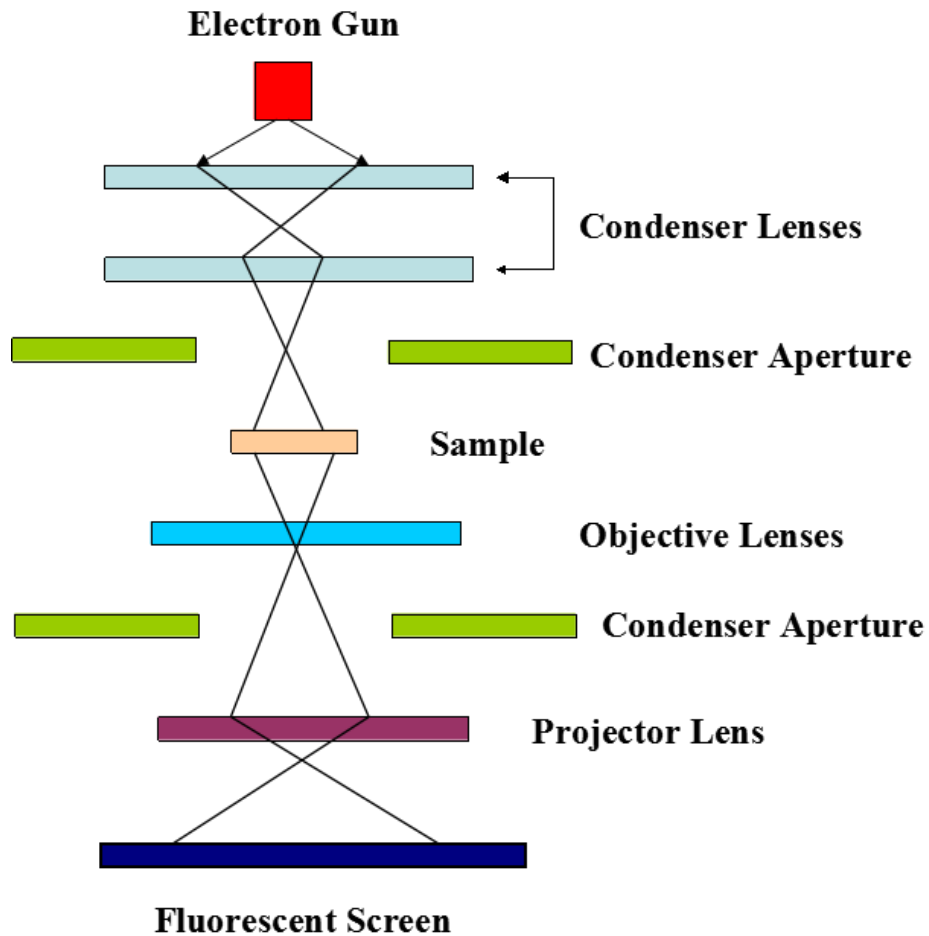


**Figure 2.2** Working principle of a Transmission electron microscope. The electrons emitted by the gun are focussed onto the sample by the condenser lenses. The electrons hit the sample and along with inelastically and elastically scattered electrons, characteristic X-rays are created. After transfer through the specimen a diffraction pattern is created in the back focal plane by the objective lens and the magnified image of the illuminated area is produced on the image plane.

A standard TEM is evacuated to low pressures to increase the mean free path of the electron-gas interaction. The vacuum system for evacuating a TEM typically operates at pressures in the order of  $10^{-4}$  Pa.[122] The sample holder design includes airlocks to minimise the increased pressure when inserted into the vacuum system. The TEM grids which support the samples are also designed as a standard size of 3.05 mm of diameter ring and 2.5 mm of inner meshed diameter. The grid materials are usually copper, platinum or gold. Once the holder has been inserted

into the TEM, the holder can be moved in the XY plane and Z direction. The electron gun is an electron emission source which is designed to generate and accelerate the electrons and also sends them to two or more condenser lenses.[124] These condenser lenses focus the electrons from the source and control the beam diameter and intensity when it hits the sample. When the electron beam passes through the objective lenses, it can be further controlled by objective and selected area electron diffraction (SAED) apertures which can be inserted or withdraw from the beam path or moved in the plane perpendicular to the beam path. These apertures are thick enough to decrease the beam intensity by filtering the electrons from the beam and also can remove electrons that are scattered to high angles, which may due to diffraction from interaction with the sample.[124]

When the electrons transfer through the sample and the objective lenses, the magnified images and diffraction patterns of the sample are created by control of the projector lenses. There is a series of projector lenses, where the first lens allows for placing the position of the electron wave distribution onto the viewing system. The viewing screen is often a fluorescent screen which is coupled to a detector such as a *charge-coupled device* (CCD) camera. The resolution of the image can be approximately proportional to the wavelength of its source or can be approximately equal as  $\lambda/2$ . [123] By the Louis de Broglie's equation, the relationship between the wavelength of electrons,  $\lambda$  and their energy, E, is given in equation.2.1.[125]

$$\lambda = \frac{1.22}{E^{1/2}} \quad \text{Equation 2.1}$$

Image formation in a TEM can happen in two different ways, bright field and dark field. The bright field imaging mode is the most common mode of operation for TEM, where the image is generated from electrons in the direct beam. If an image is formed from scattered electrons, this is known as dark field imaging.

These samples always exhibit contrast in the images which can be obtained in 3 ways: diffraction contrast, phase contrast and amplitude contrast. Diffraction contrast originates when the electron beam undergoes Bragg scattering, especially in the case of a crystalline sample. In this case, Bragg diffraction occurs when the electron beam passes through a crystalline region and is controlled by the orientation and the structure of the crystal. The corresponding diffraction pattern is a pattern of dots in the case of single crystals or a series of rings for polycrystalline samples. The apertures that are placed above the sample allow a specific area of the sample to be

selected for analysis, and the sample holder also allows tilting of the specimen to obtain specific diffraction conditions. Phase contrast occurs due to differences in the phase of electron waves which is caused by interaction of the incident beam of electrons with the atomic columns in the specimen. This allows us to image the atomic structure of crystalline materials.[125] Finally, when the electron beam interacts with different amounts of materials due to variation in mass and thickness, amplitude contrast is formed.[126] Incoherent, elastically-scattered electrons, the atomic number and even the thickness of the sample is related to the contrast. This kind of contrast is most important when looking at non-crystalline materials such as polymers..

### **2.3.2.2 Cryo-TEM Analysis**

Cryo-TEM is a kind of TEM technique where the sample is examined at cryogenic temperature. Samples can be examined frozen in an amorphous ice matrix, where vitrification was performed using an automated vitrification robot (FEI Vitrobot<sup>TM</sup> Mark III). The sample is preserved in a frozen-hydrated state, embedded in a thin film of vitrified amorphous ice. The sample is frozen in liquid ethane and maintained at low temperature in the sample holder using liquid nitrogen.[127]

Considering the fact that most biomaterials, which are surrounded by organic matrix in aqueous environment, are radiation sensitive, low-dose techniques are used to cause less damage to the sample. Furthermore, the sample in Cryo-TEM is always in solution and never in contact with an adhering surface. Therefore, the sample can be observed in its native environment to keep the true shape and structure of the hydrated molecules. It is not distorted by attachment/flattening against the supporting film which is usually the case in normal TEM. During sample preparation, freezing must be rapid such that cubic or hexagonal ice do not form. These can absorb electrons very easily and the frozen sample is basically worthless. Samples must also be thin enough to give good images of biomaterials which are rich in carbon, hydrogen and oxygen, and whose electron adsorption is low.

In this technique, copper grids covered with a carbon support film, type R2/2 Quantifoil Jena, were purchased from Quantifoil Micro Tools GmbH. Before use the grids were treated with a Cressington 208 carbon coater. A liquid sample of 3  $\mu\text{L}$  was administered to the grid inside the Vitrobot<sup>TM</sup> chamber at a 100% relative humidity, after which it was blotted to remove excess of solution (blotting time 2s, blot offset -2) and subsequently plunged into liquid ethane for vitrification.

Three different Cryo-TEM microscopes were used in this project. An FEI Tecnai 20 (type Sphera) was used to image large aggregate structures as well as selected area electron diffraction (SEAD). In this case, the electron microscope was operated at 200 kV and equipped with a LaB<sub>6</sub> filament. The Gatan Cryo-holder operated at approximately -170 °C and images were recorded with a 1 k by 1 k pixel CCD camera. Second, a TU/e CryoTitan equipped with a post column Gatan Energy Filter (GIF) and a field emission gun (FEG) operating at 300 kV was used for higher resolution imaging. The image were then recorded with the use of a post-GIF 2 k by 2 k pixel MutiScan<sup>TM</sup> Gatan CCD camera. Third, a Titan Krios<sup>TM</sup> by FEI company equipped with a emission gun and operating at 300 kV was also used for high resolution imaging and SEAD. In this case, the image was recorded using a 4 k by 4 k Eagle CCD camera. Software to visualize and edit the electron microscope image was Gatan Digital Micrograph<sup>TM</sup> (Sphera, TU/e CryoTitan) and TIA ES Vision.

TEM measurements for this thesis were performed using Phillips Tecnai FEG-TEM operating at 200 kV, with associated Energy-Dispersive X-ray analysis (EDX) and and Philips CM200 operating at 200 kV. Samples were taken from the reaction solutions for TEM analysis and were prepared by dipping a carbon-coated Cu TEM grid into the reaction solution for 10 s, rinsing with a 4:1 ethanol to water mixture, and then blotted with filter paper to remove excess solution. Cryo-TEM was performed by Dr. Paul H.H Bomans and Mr. Vladimir Dmitrović in Eindhoven using a TU/e CryoTitan (FEI) Cryo-TEM equipped with a field emission gun of 300 kV and with a post-column Gatan energy filter to enhance the quality of the image. The images were recorded using a 2k x 2k Gatan charge-coupled device CCD camera.

### 2.3.4 Raman spectroscopy

Raman is a spectroscopic technique and powerful tool used for structural and chemical analysis, where the light from a laser source is focused on the sample through a microscope objective (typically 50× or 20×) and the scattered light is collected through the same lens. It was carried out using a Renishaw 2000 Raman microscope operating with a 785 nm diode laser as the excitation source. The collected light can pass through various gratings and notch filters leaving only the Raman, or inelastically scattered light. The interaction of vibrational or rotational motions of molecules with electromagnetic radiation induce the Raman scattering.[8] Therefore, the intensity of the Raman scattered light as a function of incident wavelength is dependent on the various vibrational and rotational modes which are present within each unique substance. Then the structure and identity of individual particles can be determined through comparison with reference databases.

### 2.3.5 X-ray Diffraction

X-ray diffraction (XRD) is a non-destructive elastic X-ray scattering technique employed to investigate the crystal phase and to determine the additive-content samples. Powder X-ray Diffraction (PXRD) measures the scattering of X-rays from atoms in the crystal lattice. The crystal lattice provides an array of regular scattering centres, and constructive interference can occur at specific incident angles, as defined by Bragg's law, as shown in equation 2.2.[23]

$$2d \sin \theta = n \lambda \quad (\text{Equation 2.2})$$

where  $d$  defines the spacings between each of the diffracted planes,  $\theta$  is the incident angle,  $\lambda$  is the wavelength of the incident beam and  $n$  is an integer. From the Bragg's reflection, part of the incident beam is deflected by an angle  $2\theta$ , producing a reflection spot in the diffraction pattern. Here a Bruker D8 Advanced diffractometer with an X-ray source emitting  $\text{CuK}\alpha_1$  radiation (1.5418 Å) was used. Samples were typically collected by filtration and resuspended in ethanol. The suspension was then gently pipetted onto a silicon wafer XRD holder and allowed to dry. XRD data were collected between  $10^\circ$  and  $60^\circ$  in intervals of  $0.02^\circ$  and a scan rate of  $0.05^\circ/\text{minute}$ .

### **2.3.6 Atomic absorption (AA)**

Atomic absorption spectrometry (AA) is an analytical technique that measures the concentrations of elements. According to the Beer-Lambert law, it can establish a relation between the sample absorbance and the reference concentration with known content. Normally, the electrons of the atoms can be promoted from one energy level to an higher excited state in nanoseconds by absorbing a defined quantity of energy. Generally, the wavelength which corresponds to an electron transition is specific to each element. Therefore, the technique is elemental sensitive and can measure down to parts per billion of a gram ( $\mu\text{g dm}^{-3}$ ) in a sample. The Mg: Ca ratios of Mg-calcium sulfate precipitates were determined using AA to support the XRD analyses. AA measurements were carried out using a Perkin-Elmer A Analyst 400 spectrometer that had previously been calibrated using calcium and magnesium AA standard solution (Aldrich).

### **2.3.7 Infrared spectroscopy (FTIR)**

Further structural analysis was carried out using Perkin Elmer Spectrum100 FTIR (Fourier Transform Infrared) with diamond ATR. It is an analytical techniques based on the absorption (IR) of light from a certain source and will be absorbed by a vibrating molecule at certain frequencies. The characteristic frequencies are related to the structure of the molecule. After the crystal area has been cleaned and the background collected, the solid material is placed onto the small crystal area. Force is applied to the pressure arm to push the sample onto the diamond surface. The samples were scanned for 7 times with resolution  $4.00\text{ cm}^{-1}$ .

### **2.3.8 UV-Vis**

Ultraviolet and visible (UV-Vis) absorption spectroscopy is the measurement of the attenuation of a beam of light after it passes through a sample or after reflection from a sample surface. Ultraviolet and visible light are energetic enough to promote outer electrons to higher energy levels, and UV-Vis spectroscopy is usually applied to molecules or inorganic complexes in solution. The light source is usually a deuterium discharge lamp for UV measurements and a tungsten-halogen lamp for

visible and NIR measurements. The instruments automatically swap lamps when scanning between the UV and visible regions. The wavelengths of these continuous light sources are typically dispersed by a holographic grating in a single or double monochromator or spectrograph. The spectral band pass is then determined by the monochromator slit width or by the array-element width in array-detector spectrometers. Spectrometer designs and optical components are optimized to reject stray light, which is one of the limiting factors in quantitative absorbance measurements. The detector in single-detector instruments is a photodiode, phototube, or photomultiplier tube (PMT). UV-Vis-NIR spectrometers utilize a combination of a PMT and a Peltier-cooled PbS IR detector. The light beam is redirected automatically to the appropriate detector when scanning between the visible and NIR regions. The diffraction grating and instrument parameters such as slit width can also change.

Most commercial UV-Vis absorption spectrometers use one of three overall optical designs: a fixed or scanning spectrometer with a single light beam and sample holder, a scanning spectrometer with dual light beams and dual sample holders for simultaneous measurement of  $P$  and  $P_0$ , or a non-scanning spectrometer with an array detector for simultaneous measurement of multiple wavelengths. In single-beam and dual-beam spectrometers, the light from a lamp is dispersed before reaching the sample cell. In an array-detector instrument, all wavelengths pass through the sample and the dispersing element is between the sample and the array detector. Time-driven dual-beam spectrophotometry measurements were obtained using a Perker-Elkin UV-Vis spectroscopy at a 500 nm wavelength in transmission mode, for a time period of 3600 s. All measurements were taken for 1 ml of solution by using disposable plastic cuvettes (Fisherbrand). Various experimental parameters were investigated and are described in detail in section 7.1.4 and 7.2.4.

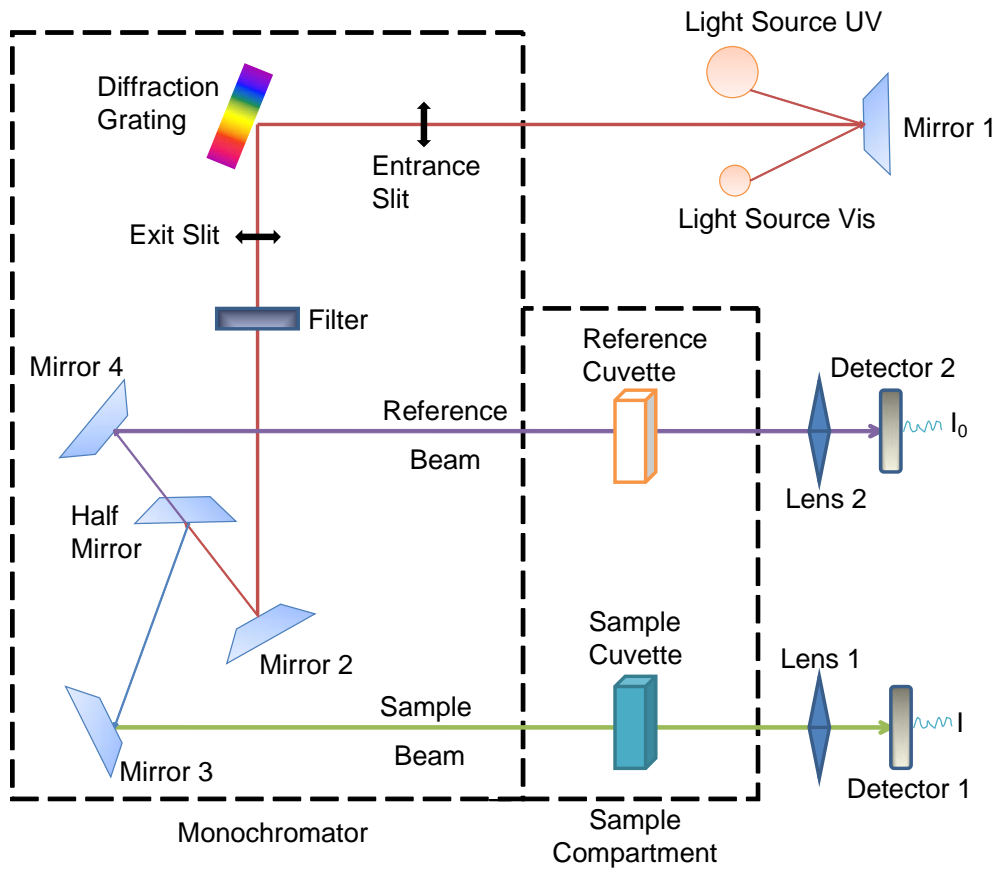
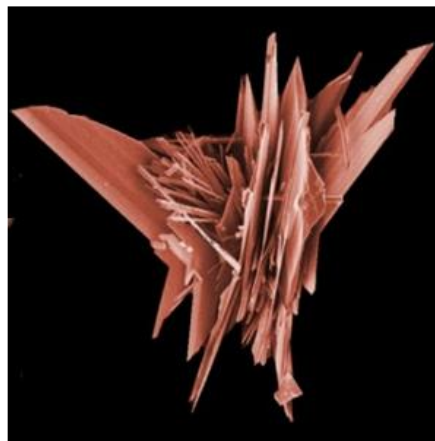
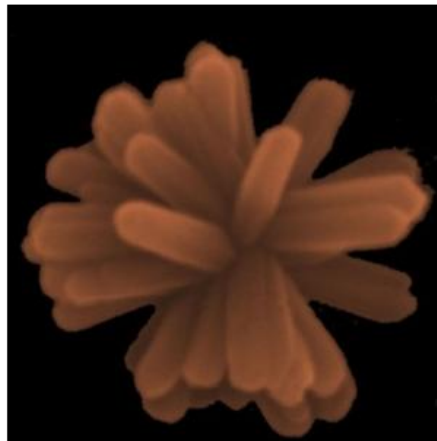
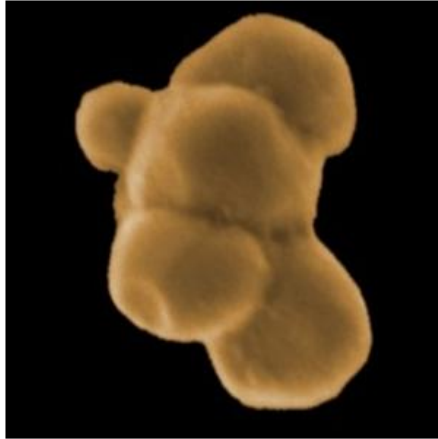


**Figure 2.3** Schematic diagram showing the components of time-driven dual-beam spectrophotometry.

**Chapter 3: A New Precipitation Pathway for Calcium Sulfate Dihydrate (Gypsum) via Amorphous and Hemihydrate Intermediates**



This work investigates the precipitation of calcium sulfate in aqueous solution at room temperature. The focus is on the stability and transformation of hemihydrate and gypsum (calcium sulfate dihydrate) and a new precipitation mechanism is revealed. It is widely known that gypsum is the most stable phase at low temperatures, and hemihydrate is metastable at all temperatures [128]. The reported typical transition temperature for gypsum/hemihydrate is approximately 97 °C.[37] To investigate this further, the early stages of calcium sulfate precipitation in bulk solution were studied by isolating precipitates and characterising them with a range of techniques including TEM, XRD and Raman microscopy. Interestingly, the existence of an amorphous calcium sulfate (ACS) phase was demonstrated, where this rapidly transforms to calcium sulfate hemihydrate before converting to the thermodynamically-stable phase calcium sulfate dihydrate (gypsum). This work therefore also provides the first report of the formation of calcium sulfate hemihydrate in solution at room temperature and the existence of amorphous calcium sulfate.

Another set of experiments were also performed at calcium sulfate concentrations between 5 mM and 50 mM. This was inspired by previous findings that calcium sulfate hemihydrate (bassanite) forms below its solubility limit and acts as a stable precursor for the crystallization of gypsum.[129] The observed bassanite formation in this “forbidden region” was attributed to a size-dependent surface enthalpy of bassanite which makes this mineral phase more stable than gypsum at small particle sizes. This size-dependent stabilization of metastable phases is a well-known phenomenon and has been described for various minerals.[130, 131] To understand the mechanism that stable nanocrystalline precursor phase can form below its bulk solubility, a range of techniques were used including constant-composition titrations, CryoTEM and normal TEM. It was therefore suggested that the amorphous nanoparticles and bassanite form prior to gypsum below its bulk solubility level.

### 3.1 Introduction to Calcium Sulfate

Calcium sulfate is a common laboratory and industrial chemical. It is widely found in nature as a translucent, crystalline white rock. Calcium sulfate dihydrate and anhydrite are the stable phases which are normally found in sedimentary environments. It is usually precipitated in lakes and highly saline waters that are recognized to be of marine origin,[125] as well as in hot springs, from volcanic vapours, and sulfate solutions in vein rocks.[18, 120] Calcium sulfate has great importance in a wide range of applications, e.g. as an additive for the production of cements, where slow hydration of calcium sulfate hemihydrate offers the benefit of rapid hardening to form calcium sulfate dihydrate.[121] Calcium sulfate has also enjoyed a long history of clinical use to fill bone defects and as an adjunct to dental implant placement with its well-tolerated, rapid resorption and non-inflammatory response.[128] In addition to its medical use, calcium sulfate can be used as a carrier material to deliver antibiotics and pharmacologic agents as it exhibits excellent properties regarding biocompatibility and antibiotic release.[124]

While calcium sulfate and its hydrates are rare in biomineralization, especially when we compare this to the huge number of organisms that use carbonates or phosphates[4, 120] it has been reported as statoliths (gravity receptors) in medusae and in green algae of the family Desmidiaceae.[128] This may be due to the comparably high solubility of calcium sulfate which will be discussed in the next parts.

#### 3.1.1 General Overview of Calcium Sulfate

It has long been believed that calcium sulfate has three major formations as defined by their water contents:  $\text{CaSO}_4 \cdot 2\text{H}_2\text{O}$  (gypsum),  $\text{CaSO}_4 \cdot 0.5\text{H}_2\text{O}$  (bassanite) and  $\text{CaSO}_4$  (anhydrite). All three have long been used in the construction industry. Recently, an amorphous precursor phase has also been reported, but it has never been confirmed as a biomineral.[128] Table 3.1 lists the crystallographic data available for the various polymorphs of calcium sulfate.

**Table 3.1** Crystallographic and physical data of the different calcium sulfate phases.[18, 120, 132-137]

Property	Gypsum	Bassanite $\alpha$ -form $\beta$ -form	Anhydrite -I	Anhydrite -II	Anhydrite - III
formula	CaSO <sub>4</sub> ·2 H <sub>2</sub> O	CaSO <sub>4</sub> ·0.5 H <sub>2</sub> O	$\alpha$ -CaSO <sub>4</sub>	$\beta$ -CaSO <sub>4</sub>	$\gamma$ -CaSO <sub>4</sub>
Molecular Mass	172.17	145.15	136.14	136.14	136.14
space group	<i>I</i> 2/ <i>c</i>	<i>I</i> 121	<i>P</i> 31 <i>c</i>	<i>A</i> <i>mma</i>	<i>C</i> 222
crystal system	monoclinic	monoclinic	cubic	orthorhombic	orthorhombic
lattice constants / Å	a=5.679 b=15.202 c=6.522 $\beta$ =118.4°	a=12.028 b=6.931 c=12.692 $\beta$ =90.2°	a=b=5.064 c=7.978 $\gamma$ =120°	a=7.006 b=6.998 c=6.245 $\alpha$ = $\beta$ = $\gamma$ =90°	a=12.078 b=6.972 c=6.304 $\alpha$ = $\beta$ = $\gamma$ =90°
density /g·cm <sup>3</sup>	2.31	2.757 2.621	undetermined	2.95	2.56
Solubility in water at 20°C, g / 100g	0.21	0.67 0.88	-	(0.27)	Hydrates to hemihydrate
Thermodynamic Stable, °C	<100	metastable	170-1180	>1180	metastable
abundance	very common	rare	artificial	artificial	rare

Gypsum is the most stable calcium sulfate phase at room temperature and pressure and is one of the most common minerals in the environment where it is found either in discrete deposits or together with other minerals. It is thermodynamically stable precipitated from aqueous solution under ambient conditions, or at temperatures up to 100 °C. Both industrial and mineralized gypsum can undergo dehydration by heating to form hemihydrate and anhydrous phase which are then widely used in the

material industry as, for example, plaster, wall board, cement, fertilizer, paint filler and ornamental stone.[135] The crystal structure of gypsum has been determined from X-ray Diffraction measurements, and it belongs to the monoclinic system.[14] The positions of atoms in this unit cell are shown in Fig 3.1 which was made according to Boeyens model.[138] The structure is composed of double layers of  $\text{CaO}_8$  polyhedra with the terminal oxygen atoms belonging either to tetrahedral  $\text{SO}_4$  species or to water molecules.[18] Between the  $\text{CaO}_8$ -polyhedra is a layer of water molecules. The oxygen atoms of the water molecules do not lie on any symmetry element and the hydrogen atoms have been assumed to form hydrogen bonds between the sulfate ions and the water molecules.[139] The hydrogen bonds lie on planes parallel to the (010) plane which allow easy cleavage of gypsum crystals along 010 faces. Gypsum is thermally stable at temperatures below  $100\text{ }^\circ\text{C}$ . Above this temperature, bassanite or anhydrite will form when water begins to leave the crystal lattice. Details about the interconversion with  $\text{CaSO}_4 - \text{H}_2\text{O}$  are discussed in Section 3.1.2.

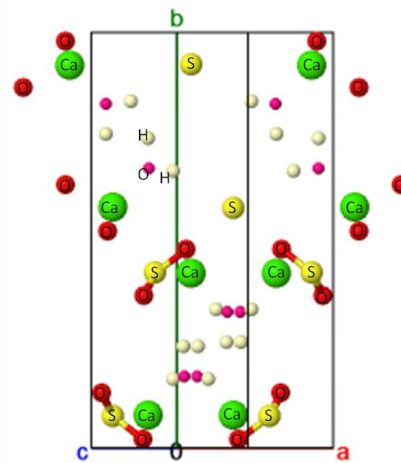


**Fig 3.1** The crystallographic unit cell of gypsum contains four ‘molecules’ of  $\text{CaSO}_4 \cdot 2\text{H}_2\text{O}$ . Reproduced from reference.[138]

Bassanite ( $\text{CaSO}_4 \cdot 0.5\text{H}_2\text{O}$ ) is a natural mineral found in dry regions of the earth and occurs in two different forms,  $\alpha$ -hemihydrate and  $\beta$ -hemihydrate. They differ from each other in their applications and methods of preparation. For example,  $\alpha$ -hemihydrate is made from autoclaving and  $\beta$ -hemihydrate by calcining[140]. However, the two forms exhibit the same crystallographic characters; both have monoclinic structures but different particle morphologies. Fig 3.2 shows the unit

cell structure of bassanite, as determined from Ballirano and Maras.[141] The water molecules in the bassanite crystal lattice are not arranged in layers like in gypsum, but fill in the channels formed by  $\text{CaO}_8$  polyhedra and  $\text{SO}_4$  tetrahedra, which reduces the symmetry.[120] These channels form the base structure for both  $\alpha$  and  $\beta$  bassanite. While the  $\alpha$ -form shows large, rectangular primary crystals with sharp edges and compact forms, the  $\beta$ -form shows flaky, rugged secondary particles made up of extremely small crystals (submicron in size). The solubility in water also differs for the two forms,  $\alpha$ - having a solubility of 0.67% and  $\beta$ -form of 0.88% at 20 °C. The differences in other characteristic properties are shown in Table 3.1.

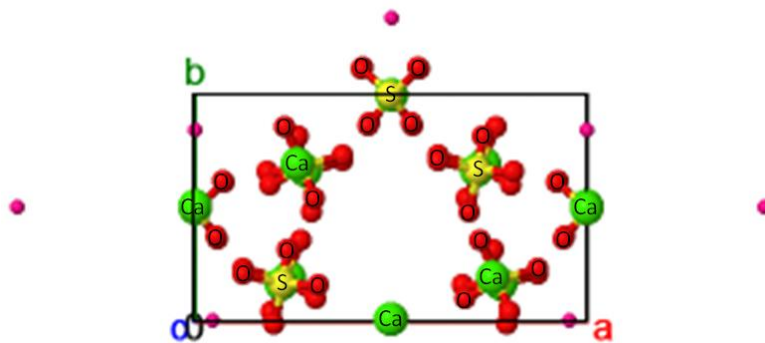
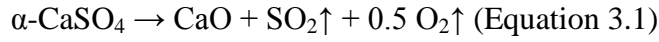


**Fig 3.2** The crystallographic unit cell of bassanite,  $\text{CaSO}_4 \cdot 0.5\text{H}_2\text{O}$ . Reproduced from reference.[141]

In its anhydrous form, calcium sulfate is used as a desiccant or as a coagulant in the construction industry. There are three kinds of anhydrous calcium sulfate, where these are formed depending on the processing method used. Anhydrite III is metastable in dry air at room temperature and is difficult to prepare pure in the presence of water or water vapour. It is normally found in mineral deposits along with gypsum..[142] Dehydration of bassanite under heating can also give anhydrite III with slight mechanical change in the crystal but leaves the crystal lattice unaltered. The crystal structures of bassanite and anhydrite-III are very similar, and only differ in some low intensity peaks under XRD. [143, 144] Anhydrite II begins to form with continuous heating of anhydrite-III in an irreversible reaction. This corresponds to a real phase transition because no water is left in the structure. It is a purely artificial product with connected  $\text{CaO}_8$  polyhedrons that form within a tight net. Anhydrite-I is the high-temperature modification of calcium sulfate and only

exists above 1180 °C. [135] Above 1260 °C, calcium sulfate decomposes into calcium oxide, sulphur dioxide, and molecular oxygen[145] according to:



Anhydrite I only exists above 1180 °C, while anhydrite II begins to form above 100 °C and is stable between 100 °C to 1180 °C.

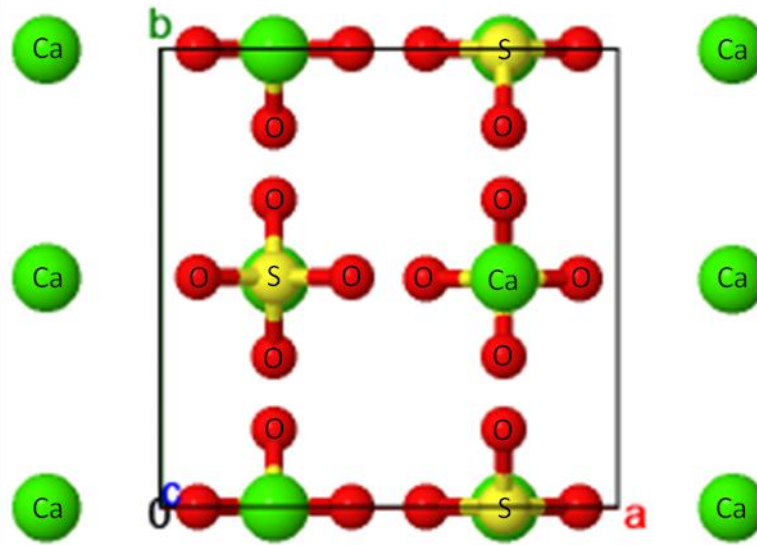
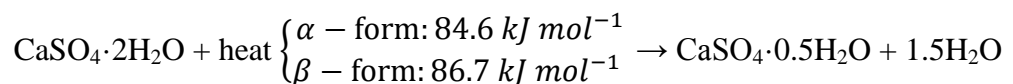


**Fig 3.3** The crystallographic unit cell of anhydrite III, CaSO<sub>4</sub>. Reproduced from reference.[132]

### 3.1.2 Interconversion between the CaSO<sub>4</sub>·xH<sub>2</sub>O Polymorphs

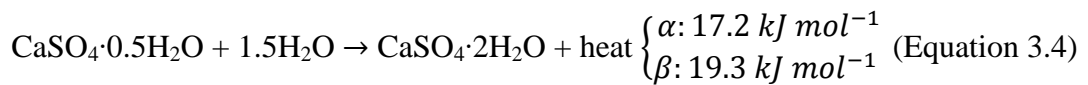
Calcium sulfate dihydrate, gypsum, is both the starting material before dehydration and the final product after rehydration. Gypsum dehydration kinetics have been investigated by several authors including Freyer[146] and Oetzel[147]. When heated, both industrial and geological gypsum readily loses water and undergoes a progressively dehydration in the order: dihydrate → hemihydrate → anhydrite I → anhydrite II. Above 1180 °C, anhydrite I forms; below 1180 °C, it reverts to anhydrite II.[135]



(Equation 3.2)



When subjected to heat, gypsum loses approximately 75% of its water to form hemihydrate crystals. Products were characterized by XRD and indicated that  $\text{CaSO}_4 \cdot 2\text{H}_2\text{O}$ ,  $\text{CaSO}_4 \cdot 0.5\text{H}_2\text{O}$  and  $\text{CaSO}_4$  were formed at  $\leq 100$  °C, 130-160 °C and  $\geq 170$  °C, respectively[136] In contrast, calcium sulfate hemihydrate and anhydrite III are metastable in dry air at room temperature. Thus, gypsum crystallization always takes place during hydration under ambient conditions. Hydration of hemihydrate is a highly exothermic reaction in which water is incorporated to produce gypsum, which occurs as:



When hydration occurs in solution with enough water, then a homogeneous, fluid, stable, non-sedimenting slurry forms. This reaction is known, for example, in the setting of plaster. According to calcium sulfate crystallization theory, calcium sulfate hemihydrate in water first forms a saturated solution, about 8 g/L at 20 °C. However, this solution is actually supersaturated, because at 20 °C, calcium sulfate dihydrate has a solubility of only 2 g/L, thus this mixture sets and hardens because calcium sulfate dihydrate needles form. Through this physico-mechanical process, the hardened mass is not a compact solid, but a highly porous material with a relatively large internal surface consisting of interlocking crystals in the form of plates and needles[135]. The elongated and interlocked crystals give the material good stiffness. Variation in the hydration conditions can alter the degree of interlocking, the texture, and the size distribution of the component crystals. Hardened gypsum pastes with this particular microstructure and rigidity are widely used in buildings, ceramics and even medical applications.

Formation of gypsum from hemihydrate conforms to the general laws of nuclei formation and crystal growth. In aqueous conditions, hemihydrate powder is more soluble than the dihydrate, and thus dissociates into  $\text{Ca}^{2+}$  and  $\text{SO}_4^{2-}$  ions as it comes into contact with water. These ions form an impermeable layer of dihydrate, which hinders the approach of water molecules to the surface of hemihydrate and thus results in the well-known induction period[148]. Followed by a short induction period, nuclei begin to form from the supersaturated solution. Subsequently, after

this nucleation, crystal growth begins. The crystallization pathway of calcium sulfate will be discussed in detail in the next section.

### 3.1.3 Crystallization Pathway of Calcium Sulfate

The precipitation and transformation of calcium sulfate has been a topic of considerable interest recently because of its application in dental and construction industries, and because it also has implications for the understanding of biological mineralization. A significant amount of work has been done to improve the understanding of the nucleation and growth mechanisms of calcium sulfate dihydrate crystals. Practically, induction periods,  $t_{ind}$  are easier to measure than nucleation rates, since a lot of previous work has been done to measure the induction time by mixing equal volume and molar  $Ca^{2+}$  and  $SO_4^{2-}$  solutions.

The time which elapses between the onset of supersaturation and the formation of critical nuclei or embryos is defined as the true induction period. However, as highlighted by Söhnel and Mullin,[149] it is not possible to experimentally measure the real induction period because no method has yet been devised for the detection of a critical nucleus. It is therefore accepted that the time elapsing between the moment when liquid movement ceases and the first change in turbidity is recorded as the induction period,  $t_{ind}$ . Recently, the induction time has also been defined as the time elapsing between the attainment of supersaturation and the appearance of the first crystals.[150] Several studies have shown that the induction time depends primarily on solution supersaturation and temperature. In 1974, A. Packter[151] measured the induction period of calcium sulfate dihydrate solutions of supersaturation 1.5 to 16 by optical microscopy and chemical analysis. He found that the induction periods decreased from 12,000 to 3 seconds when the calcium sulfate concentration was increased from 20 mM to 240 mM. He also proposed the relationship at medium supersaturation (25-200 mM)

$$t_{ind} \propto (c - c_{eq})^{-4} \text{ (Equation 3.5)}$$

where  $c$  is the calcium sulfate concentration ( $mol/m^3$ ) and  $c_{eq}$  is the calcium sulfate solubility ( $mol/m^3$ ). The induction periods were found to decrease very rapidly from high values on increasing the concentration from 23 to 45 mM but less rapidly with increasing concentration from 50 mM to 240 mM. Amathieu and Boistelle in

1988[152] studied the crystallization kinetics of calcium sulfate dihydrate both in homogeneous and in heterogeneous conditions. A conductimetric method was used to form gypsum from a dense suspension of calcium sulfate hemihydrate. The dissolution rate of hemihydrate is very fast so crystals of gypsum form immediately, due to heterogeneous nucleation onto the hemihydrate particles.

While the induction time of calcium sulfate can be measured, little is known about the polymorphs existing at the early stages of this process. It is well known that nucleation of crystals from aqueous solution is a highly complex process involving ion dehydration, approach of like charges and the arrangement of the constituent ions or molecules into an ordered 3-dimensional lattice. It has also been suggested that in classical nucleation theory, the earliest particles that form in aqueous solution have the crystal structure of the end product.[128] However, non-classical crystallization mechanisms suggest that a combination of the electrostatic ion-ion interactions and water interactions might be sufficient to stabilize these early clusters in solution[153]. Initially, the cluster is highly disordered, and then depending on the substrate, the water in the system would be removed to form the crystalline structure. Therefore, we perhaps should not be surprised that some crystals precipitate from solution via amorphous phases.

Amorphous precursors are intrinsically unstable with respect to the crystal, so the chances of observing such an intermediate depends on its lifetime and a short-lived species may well be overlooked. Two such materials have been discussed a lot recently: calcium carbonate and calcium phosphate according to their industrial relevance, and their importance as biominerals and biomaterials.[128] Further, both amorphous calcium carbonate (ACC) and amorphous calcium phosphate (ACP) can be very stable in solution, making their observation, isolation and characterisation relatively straightforward (These two amorphous phases will be discussed in Chapter 5 and Chapter 6).[128] Indeed, a recent investigation of the precipitation of metal carbonates in levitated droplets suggested that many crystalline metal carbonates may precipitate via amorphous phases.[128] Here, we investigate the early stages of precipitation of calcium sulfate from aqueous solution in order to characterise the crystallisation mechanism and in particular to search for any amorphous precursor phase.

## **3.2 Aims of this Project**

All the experiments discussed in the literature provided evidence that gypsum is the most stable phase and that bassanite can be formed at high temperatures. Yet, due to their low solubilities in water, it is often difficult to clarify the precipitation pathway in aqueous conditions, and in particular, to characterise the early stages of crystal growth. Experiments were therefore carried out here to gain further understanding of the crystallization pathway of calcium sulphate in aqueous solution. This was achieved by investigating the crystal species present in reaction solutions of different concentrations at different times. Various techniques including Raman microscopy, TEM, SEM, IR, and XRD were used to investigate the possibility that amorphous calcium sulfate exists as a precursor phase at early reaction times, and how this transforms to gypsum under ambient conditions.

Experiments were also carried out using a titration method combining immersed ion-selective electrodes, conductivity sensors and turbidity probes to detect and characterize the different stages of calcium sulfate precipitation in solution. High resolution techniques like cryo-TEM were also used to trace and observe the nucleation pathway, and to investigate the growth of early phases and their transformations.

## **3.3 Experimental**

### **3.3.1 Materials**

Calcium chloride and sodium sulfate solutions were prepared by dissolving  $\text{CaCl}_2 \cdot 2\text{H}_2\text{O}$  and  $\text{Na}_2\text{SO}_4$  (Sigma-Aldrich) in 18 M $\Omega$ /cm ultra-pure Millipore water.

### **3.3.2 Early Stages of Precipitation of Calcium Sulfate**

Calcium sulfate was precipitated by combining equal volumes of equimolar solutions of calcium chloride dihydrate ( $\text{CaCl}_2 \cdot 2\text{H}_2\text{O}$ , Sigma-Aldrich) and sodium sulfate anhydrite ( $\text{Na}_2\text{SO}_4$ , Sigma-Aldrich) in Milli-Q water, to give final  $\text{Ca}^{2+}$  and  $\text{SO}_4^{2-}$  concentrations of 5 mM – 100 mM. Samples were taken from the reaction solutions for TEM analysis at times between 10 s and nearly 1 year and were

prepared by dipping a carbon-coated Cu TEM grid into the reaction solution for 2 s, rinsing with a 4:1 ethanol to water mixture, and finally drying at room temperature. Samples were also isolated by filtration of passing through 200 nm or 450 nm pore-sized membranes for further characterization and drying in the air.

### 3.3.3 Titration Experiments

A Metrohm® commercial titration setup was used. The setup contains a computer which runs software Tiamo 2.1 that controls two 809 Titrande titrating units, three 2 ml Dosino dosing units and a magnetic stirrer plate. The setup is shown in Fig 3.4. A double junction micro pH glass electrode (6.0234.100) and a polymer membrane (PVC) calcium ion selective electrode (Ca-ISE, 6.0508.110) were utilized to measure the pH and concentration of free  $\text{Ca}^{2+}$  ions in solution, respectively; each was connected to one of the Titrande 809 stations. The pH electrode was calibrated daily using Metrohm buffer standards at pH=4.0 (No. 6.2307.100), pH=7.0 (No. 6.2307.110) and pH=9.0 (No. 6.2307.120), while the Ca-ISE was calibrated before each experiment.

All solutions were freshly prepared for each experiment utilizing fresh Milli-Q water (resistivity  $18\text{M}\Omega\cdot\text{cm}$  at  $20^\circ\text{C}$ ). A sodium hydroxide solution of 10mM was prepared by dissolving NaOH pellets in water; 10mM hydrochloric acid was prepared by the dilution of HCl 25%. Calcium chloride 250 mM solutions used for titrations and calibrations were obtained by dissolving calcium chloride dihydrate in water, while 250 mM solution of sodium sulfate was obtained by dissolving sodium sulfate anhydrite in water. The first experiment was performed by adding 250 mM calcium chloride solution into 25 ml of 250 mM sodium sulfate solution with additional rate of 0.1 mL/min. The second experiment was performed by adding 250 mM solutions of calcium chloride and sodium sulfate into 25 ml of fresh Milli-Q water (resistivity  $18\text{M}\Omega\cdot\text{cm}$  at  $20^\circ\text{C}$ ) in same additional rate of 0.1 mL/min. The stirring rate in all performed experiments was 900RPM. All beakers, electrodes and burette tips were cleaned with 10% acetic acid and rinsed with distilled water after every experiment. To convert measured  $\text{Ca}^{2+}$ -activities into concentrations, for the calculation of the activity coefficients, the (Davies-extended) Debye-Huckel Equation was applied.

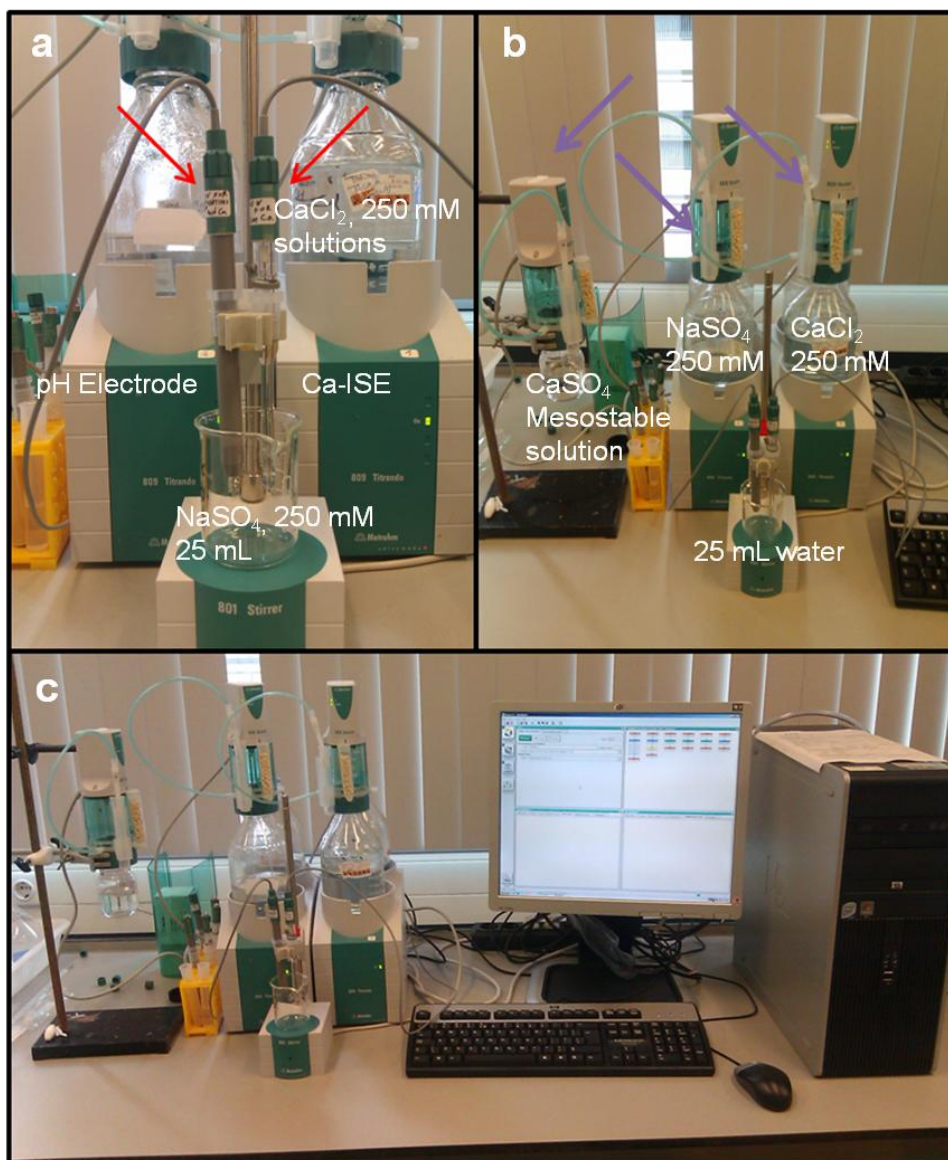


**Fig 3.4** Metrohm® commercial titration setup. a) two 809 Titrando titrating units that containing micro pH glass electrode and a polymer membrane (PVC) calcium ion selective electrode. b) CaSO<sub>4</sub> solution of different concentration was prepared by adding 250 mM solutions of calcium chloride and sodium sulfate into 25 ml of fresh Milli-Q water (resistivity 18MΩ•cm at 20°C). c) The Metrohm® commercial titration setup contains a computer which runs software Tiamo 2.1.

### 3.3.4 Characterization Methods

The precipitates were imaged with a Phillips Tecnai Electron Microscopy (TEM) operating at 200 kV, and elemental composition and polymorph were determined using Energy-Dispersive X-ray Analysis (EDX) and electron diffraction

respectively. TEM studies were performed of calcium sulfate precipitates formed at room temperature from 5 mM calcium sulfate solution (equal-molar and equal-volume) after reaction times of between seconds and 8 months. Further confirmation of polymorph was obtained using Raman microscopy, powder XRD and Thermogravimetric Analysis (TGA). Samples were isolated by filtration, and the Raman analysis was performed using a Renishaw 2000 inVia-Raman microscope, operating with a 785 nm laser. PXRD was performed using a Bruker D8 Advanced diffractometer with X-ray source emitting Cu K $\alpha$ 1 radiation. Samples were gently ground and placed on a piece of silicon wafer, and XRD data were collected between 10° and 60° in intervals of 0.02° and a scan rate of 1°/ minute. The composition of the precipitates was determined using a TA-Instruments Q600 Simultaneous TGA/DSC, with analysis being performed under air in the temperature range ambient to 850 °C with a heating rate of 5 °C/min.

Accurate induction times were determined by measuring the intensity of transmitted light as a function of time. Turbidity measurement were obtained using a Perkin-Elmer Lambda UV-Vis system, operating in a time-drive mode ( $\lambda = 500$  nm, exposure time = 1 s). Supersaturated solutions of calcium sulfate were prepared by mixing two clear equimolar solutions which were calcium chloride and sodium sulfate solutions in a cuvette. A magnetic stirrer was also used to stir the mixed solutions for different times. (Characterization of precipitation using turbidity measurements is described in detail in Chapter 7)

Cu grids, R2/2 Quantifoil Jena grids (Quantifoil Micro Tools GmbH) were surface-plasma treated for 40 s using a Cressington 208 carbon coater before use. Then, vitrification was carried out using an automated robot (FEI Vitrobot Mark III) by plunging the sample grid into liquid ethane. The chamber from the vitrobot was kept at 100% humidity to prevent drying. Vitrified samples were studied using the TU/e CryoTitan (FEI, [www.cryotem.nl](http://www.cryotem.nl)), equipped with a field-emission gun operating at 300 kV and a post-column Gatanenergy filter. Images were recorded using a post-GIF (Gatan imaging filter) 2.2 kGatan CCD (charge-coupled device) camera. Diffraction patterns were recorded on a pre-GIF Gatan CCD camera.

### 3.4 Results

#### 3.4.1 CaSO<sub>4</sub> Precipitation in Bulk Solution

Calcium sulfate was produced by mixing equal volumes of equi-molar solutions with concentrations from 15-200 mM. The morphologies of the precipitates of calcium sulfate in solution varied with the solution concentration (Fig 3.5). The rate of precipitation depended strongly on the CaSO<sub>4</sub> solution compositions, and increased significantly with increasing Ca<sup>2+</sup> and SO<sub>4</sub><sup>2-</sup> concentrations. The morphologies of crystals were plate or needle-like after 1 hour depending on the concentration of the reaction solution. Plate or needle-like morphologies implied that the crystals precipitated were gypsum, where this was confirmed by Raman microscopy. With increasing concentrations, crystallization resulted in crystal structures that transformed from submicron needles to plate-like structures, and also from single needles to clusters of needles or plates crystals. Clusters of needles appeared to result from multiple needles growing from a single nucleation point.

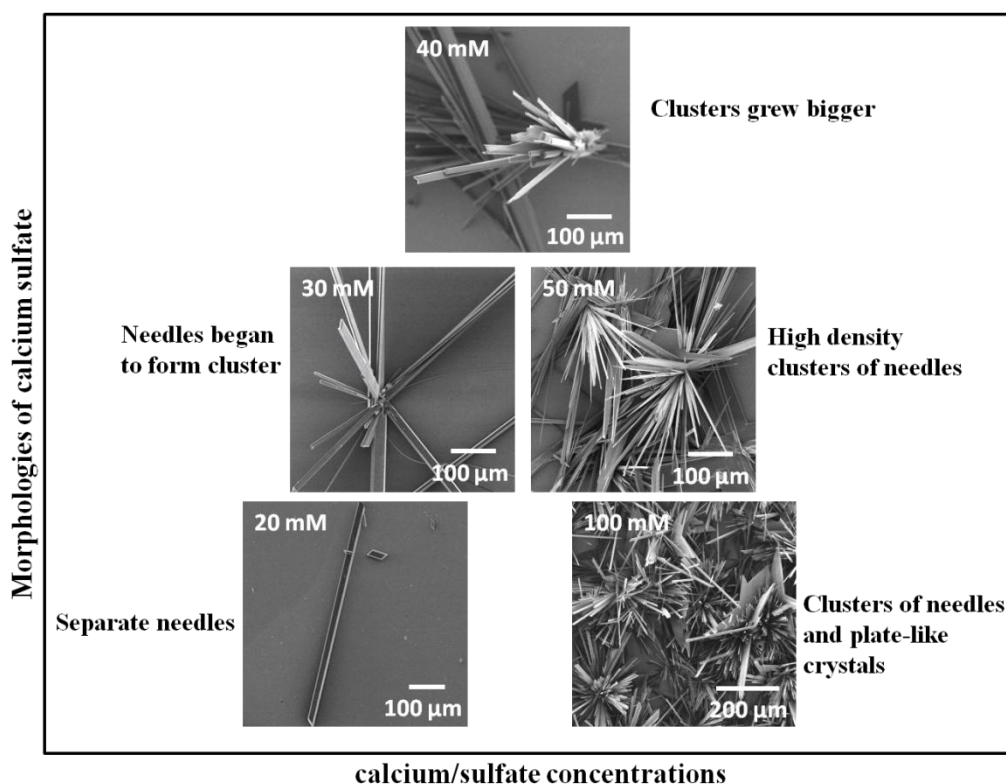


**Fig 3.5** SEM images of calcium sulfate precipitates produced at different solution concentrations after 1 hour reaction time.

The induction time is defined as the time which elapses between achievement of supersaturation and appearance of nuclei. Generally, the value of  $t_{ind}$  can be determined by monitoring the transmission of light through calcium sulfate supersaturation solutions. The transmission is plotted against the reaction time. Figure 3.6 shows an example of plots obtained for calcium sulfate at 100 mM, 80 mM and 50 mM. It can be seen that the turbidity increased very quickly at higher solution concentrations, while the lower the concentration, the longer the induction time (Table 3-2). Precursor phases are thus more likely to be observed in solutions of lower concentrations.

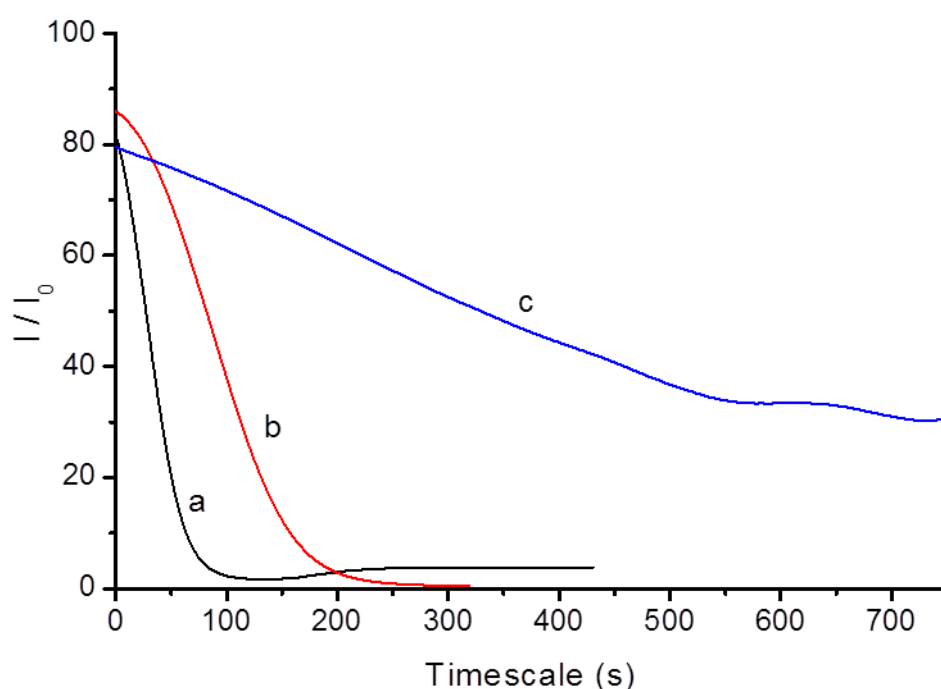


**Figure 3.6** Intensities of transmitted light vs. time for calcium sulfate precipitation at 25 °C from solutions of concentrations, a) 100 mM, b) 80 mM and c) 50 mM

**Table 3.2** Induction periods at various concentrations as a function of time

Final concentration of CaSO <sub>4</sub>	stirring time (s)	induction time (s)
100 mM	30	100
80 mM	110	200
50 mM	900	900

### 3.4.2 Early Stages of CaSO<sub>4</sub> Precipitation in Bulk Solution

The early stage of calcium sulfate precipitation was first investigated by examination of the 50 mM calcium sulfate solution after 2 h. Micron-size needles (Figure 3.7a), which were shown to be CaSO<sub>4</sub>·2H<sub>2</sub>O (gypsum) with electron diffraction (Table 3-3) were observed at this time. Gypsum is the most stable polymorph of CaSO<sub>4</sub> at room temperature, and this is in keeping with expectation[154]. Further confirmation of polymorph was obtained by filtering out the precipitates after 2 hours from solution and characterising them with Raman microscopy (Figure 3.8a). Comparison with reference samples (Figures 3.9a) showed that the Raman spectra of the hemihydrate and dihydrate are reasonably similar but the lowest wave number peak at 435 cm<sup>-1</sup> for the hemihydrate and at 417 cm<sup>-1</sup> for the dihydrate, and the well-defined peak at 1139 cm<sup>-1</sup> for the dihydrate provides clear fingerprints for these two polymorphs. There was excellent correspondence between the Raman spectra of the precipitates in the 50 mM solution and the gypsum reference sample.[155]

The 50 mM solution was also characterised at early reaction times, and interestingly, the products after 1 min showed the presence of blocky, rod-like particles, which were morphologically quite distinct from the high aspect-ratio gypsum needles found at longer times (Figure 3.7b). These rods were typically 0.2 – 1.0 μm long and electron diffraction conclusively showed that they were hemihydrate rather than gypsum (Table 3-3). Raman microscopy (Figure 3.8b) further confirmed that they were hemihydrate (Figure 3.9a). This was the first report of the precipitation of hemihydrate at room temperature from salt-free CaSO<sub>4</sub> solutions.

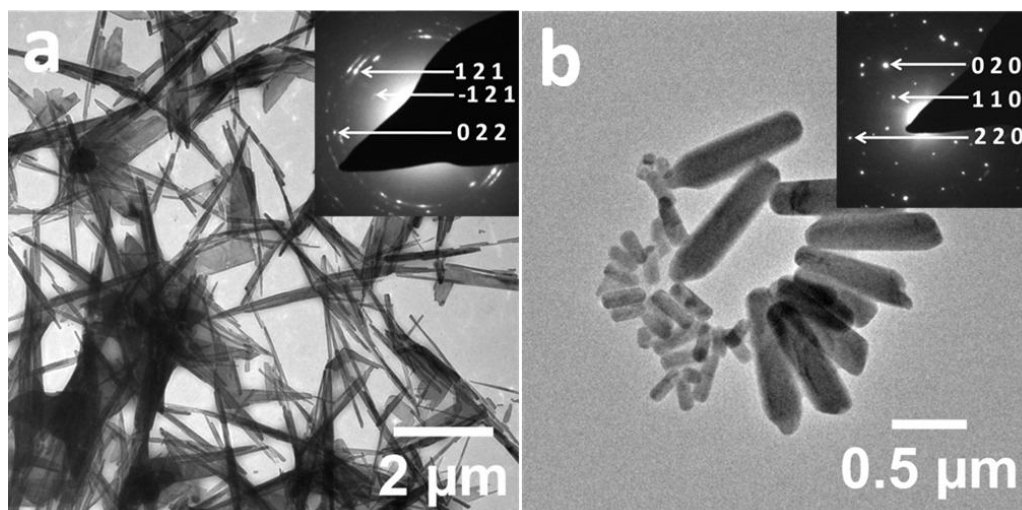


**Figure 3.7** TEM images, selected area electron diffraction patterns a) 2 h, as calcium sulfate dihydrate (gypsum) and b) 1 min, as hemihydrate.

**Table 3.3** Measured  $d$ -spacings of electron diffraction patterns obtained from calcium sulfate particles (a) precipitated from a 50 mM solution after 2 hours, showing calcium sulfate dihydrate and (b) 1 min, corresponding to calcium sulfate hemihydrate. (c) Gypsum particles produced by heating nanosized calcium sulfate particles precipitated from 15 mM reaction solutions after 30 secs, after heating in TEM electron beam for 1 min. Powder XRD data of calcium sulfate hemihydrate, calcium sulfate dihydrate and anhydrite are shown for the sake of comparison. The numbers in brackets represent the expected relative intensities of randomly oriented powder samples.

(a) $d$ (Å) 50 mM after 2 hs	(b) $d$ (Å) 50 mM after 1min	(c) $d$ (Å) ACS after heating in TEM	$d$ (Å) CaSO <sub>4</sub> (Intensity)	$d$ (Å) CaSO <sub>4</sub> ·0.5H <sub>2</sub> O (Intensity)	$d$ (Å) CaSO <sub>4</sub> ·2H <sub>2</sub> O (Intensity)
	5.9898		6.0384 (99.90)	6.0051 (99.74)	
4.2614			4.3607 (1.70)	4.285 (2.35)	4.2669 (100.00)
	3.4560		3.4850 (15.10)	3.4647 (30.80)	3.5427 (4.09)
		3.0157	3.0192 (40.3)	3.0394 (7.36)	3.0497 (73.30)

	2.9833			3.0026 (100.00)	
2.8692	2.8043	2.8555		2.8044 (83.69)	2.8621 (52.99)
		2.7226	2.7230 (50.0)	2.7157 (8.31)	2.7168 (1.57)
2.6631		2.6734		2.6942 (1.05)	2.6679 (36.27)
2.4826		2.5006			2.4929 (12.46)

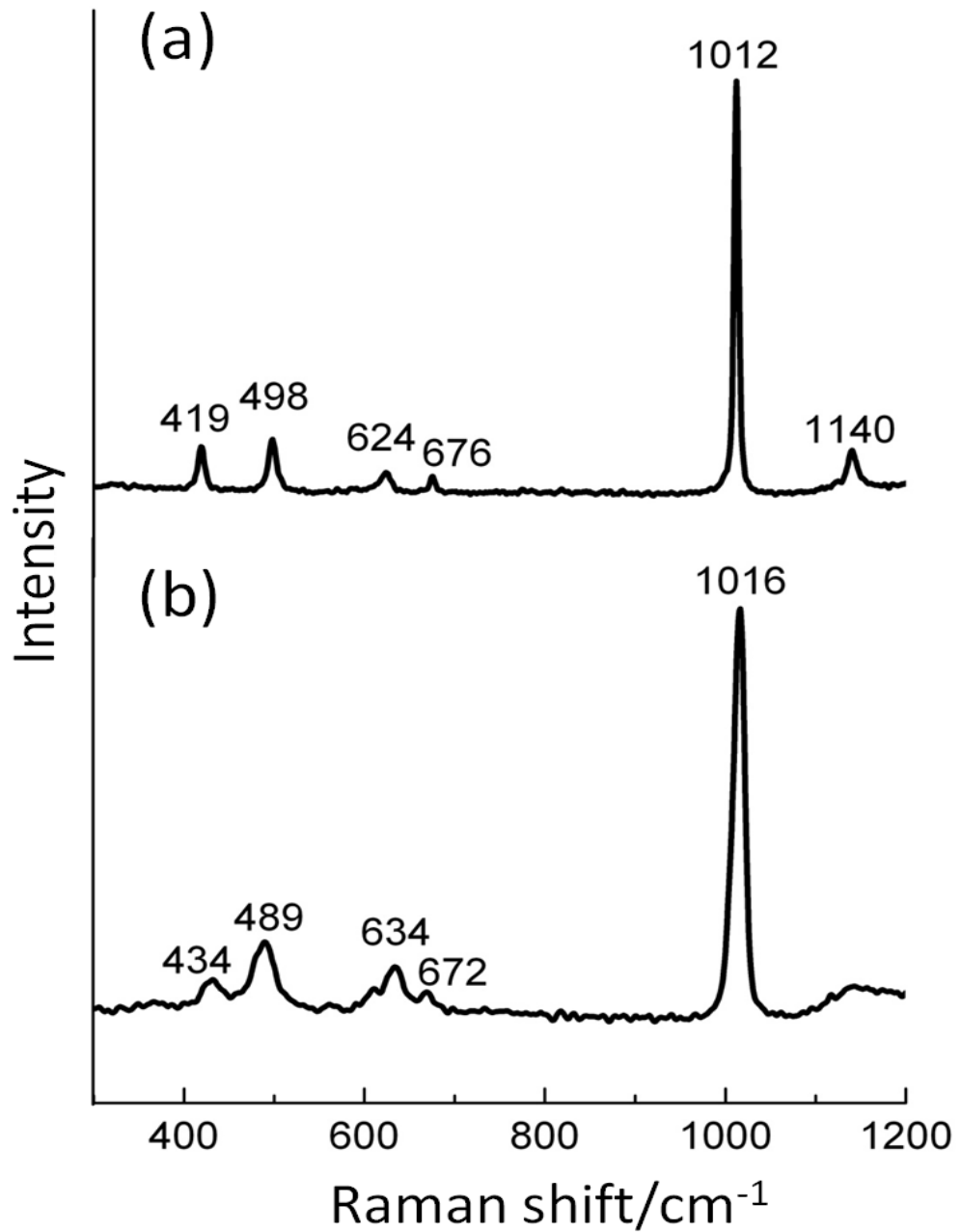


**Figure 3.8** Raman spectra of  $\text{CaSO}_4$  particles precipitated from a 50 mM solution after a) 2 h, as dihydrate (gypsum) and b) 1 min, as hemihydrate.

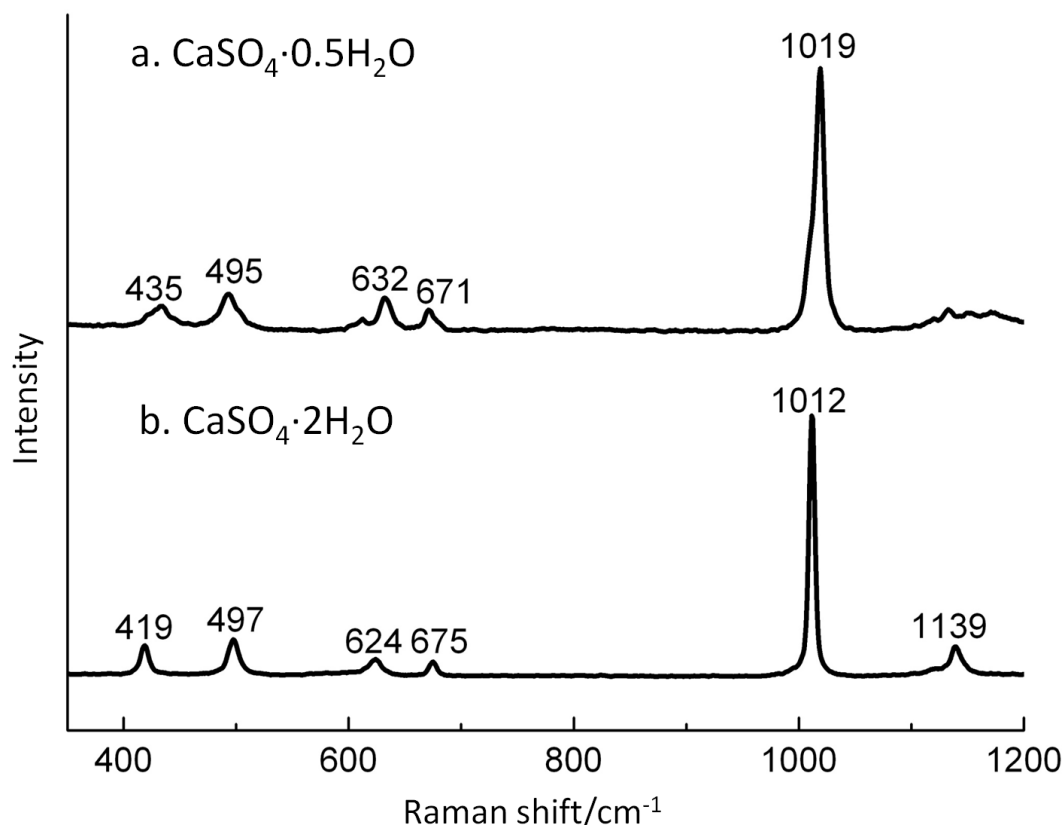


**Figure 3.9** Raman spectra of reference samples (a) calcium sulfate hemihydrate (from heating up gypsum to 120 °C) and (b) calcium sulfate dihydrate. The peaks correspond to the  $\nu_1$  symmetric stretch of sulfate (1019  $\text{cm}^{-1}$  in hemihydrate and 1012  $\text{cm}^{-1}$  in gypsum), the  $\nu_2$  symmetric bending of sulfate (435  $\text{cm}^{-1}$  and 495  $\text{cm}^{-1}$  in hemihydrate, and 419  $\text{cm}^{-1}$  and 497  $\text{cm}^{-1}$  in gypsum), the  $\nu_3$  antisymmetric stretching of sulfate (1139  $\text{cm}^{-1}$  in gypsum and less well-defined in hemihydrate) and the  $\nu_4$  anti-symmetric bending of sulfate (632 and 671  $\text{cm}^{-1}$  in hemihydrate, and 624  $\text{cm}^{-1}$  and 675  $\text{cm}^{-1}$  in gypsum)[155].

Other techniques were also used to confirm the polymorph of calcium sulfate present at the early stages of the reaction. Fig 3.10 shows the reference XRD spectra of calcium sulfate precipitates, where hemihydrate was prepared by heating gypsum at 120 °C. Figure 3.11 shows XRD spectra of precipitates isolated from 50 mM

solutions after approximately 1 minute, where these show the presence of both hemihydrate and gypsum (peaks labelled \*). A mixture of hemihydrate and gypsum polymorphs was obtained due to the time taken to filter the volumes of solution required to give sufficient material for analysis. With time, hemihydrate starts to transform to gypsum, as shown by an increase in the intensity of the peaks at  $2\theta = 11.575$  and  $47.88$ . This is because calcium sulfate hemihydrate is not stable in air and it hydrates to form gypsum as shown in previous research.[135]

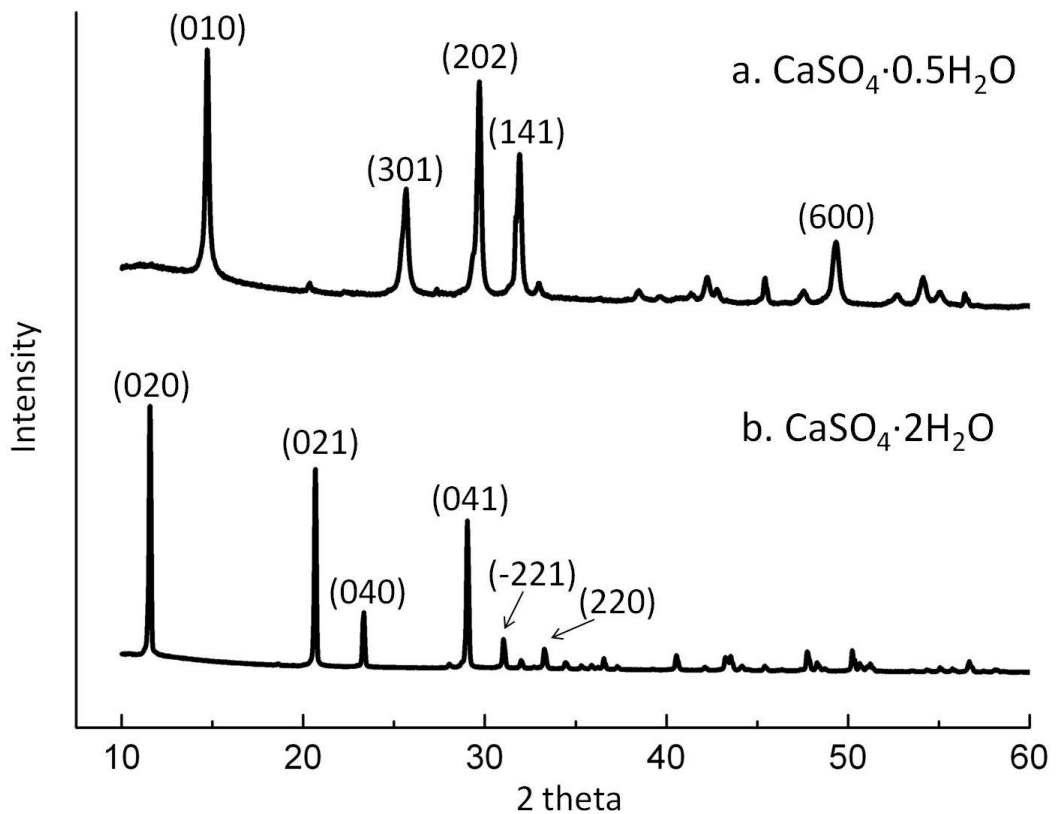


**Figure 3.10** An XRD patterns of the reference samples, where a) is calcium sulfate hemihydrate (prepared by heating gypsum at  $120^\circ\text{C}$ ) and b) is calcium sulfate dihydrate.

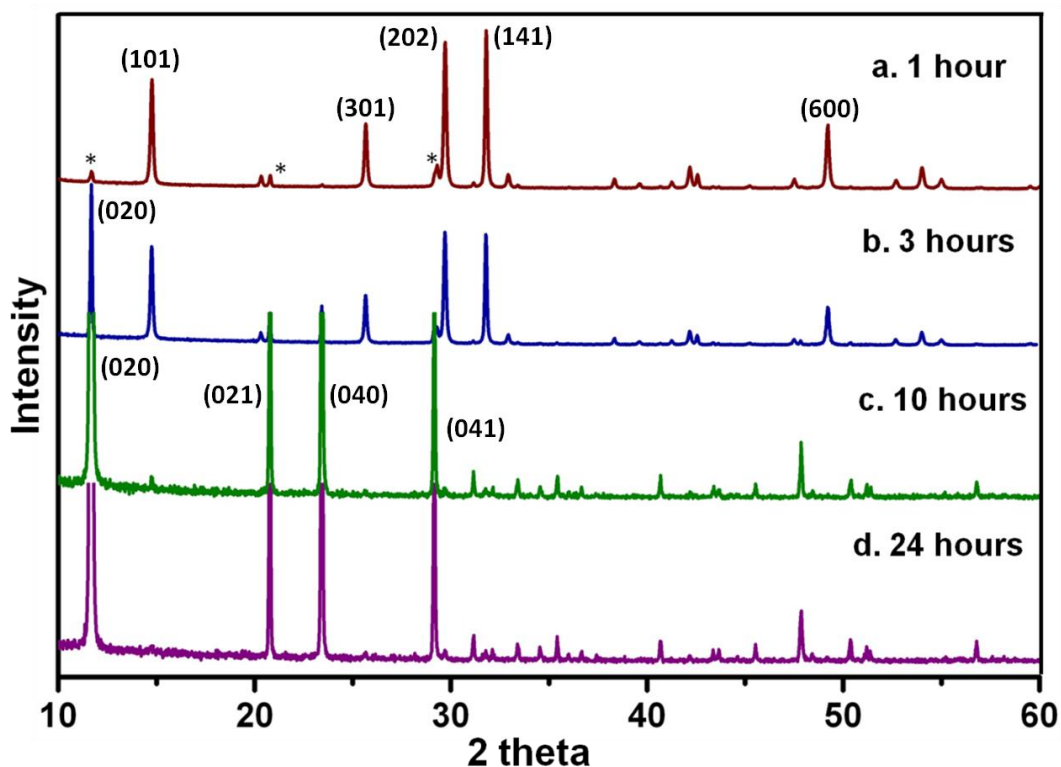


**Figure 3.11** XRD patterns of calcium sulfate precipitated at 50 mM, isolated from solution after 1 minute and then left in air for (a) 1 hour, showing that the sample is primarily hemihydrate, (b) 3 hours, showing peaks at  $2\theta = 11.575$  and  $47.88$ , demonstrating the presence of gypsum, (c) after 10 hours, where only traces of hemihydrate remain (as shown by the principal hemihydrate peak at  $2\theta = 14.746$ ) and (d) 24 hours, showing that all hemihydrate has transformed to gypsum.

TGA was also used to analyze the differences in the amount of water in the calcium sulphate precipitates, and therefore to identify the ration of gypsum to hemihydrate. The gypsum sample loses 21.6 wt% on heating, which is consistent with the loss of  $2\text{H}_2\text{O}$  per  $\text{CaSO}_4$  unit, while the precipitate isolated from 50 mM solution after 1 minute loses 8.6 wt% on heating. In this case, the sample comprised 84 mol% hemihydrate ( $\text{CaSO}_4 \cdot 0.5\text{H}_2\text{O}$ ) and 16 mol% gypsum (as shown in Fig 3.12)

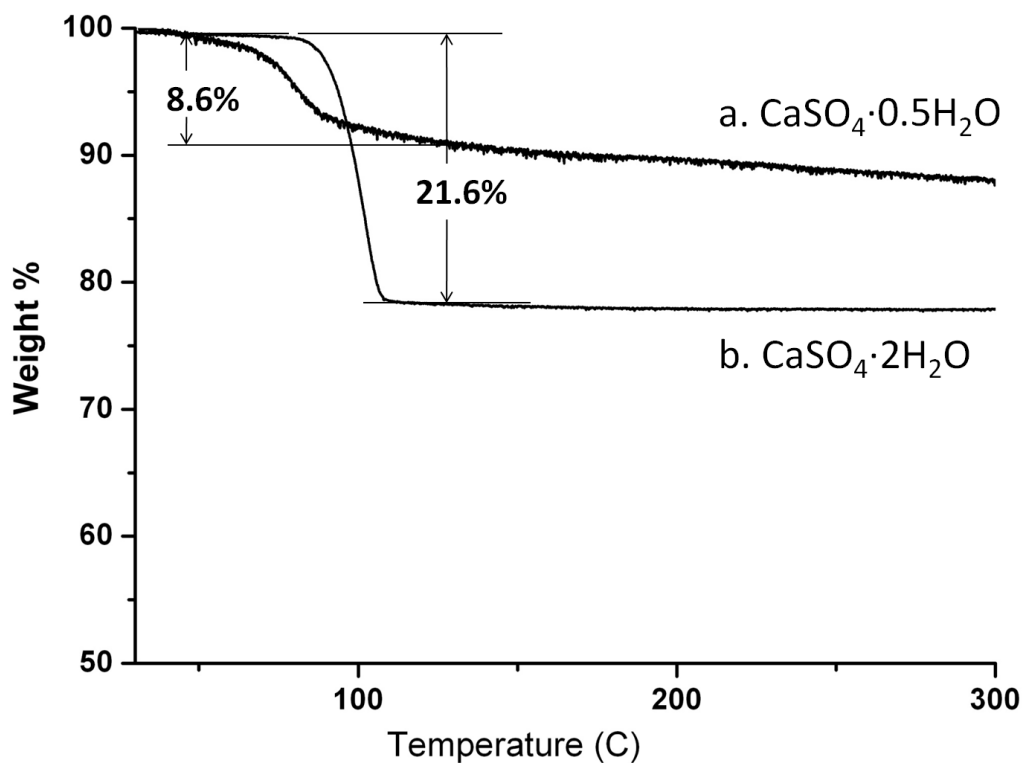


**Figure 3.12** TGA spectra of (a) the precipitate isolated from the 50 mM solution after approximately 1 minute and (b) a sample of gypsum. The gypsum sample loses 21.6 wt% on heating, which is consistent with the loss of 2H<sub>2</sub>O per CaSO<sub>4</sub> unit, while the precipitate loses 8.6 wt% on heating which is consistent with the sample comprising 84 mol% hemihydrate (CaSO<sub>4</sub>·0.5H<sub>2</sub>O) and 16 mol% gypsum.

The solution was also sampled at intermediate times between 1 minute and 2 hours, and after 1 hour revealed the presence of both gypsum needles (Figure 3.13a) and hemihydrate nano-rods (Figure 3.13b). The data therefore demonstrate that CaSO<sub>4</sub> hemihydrate is stable for at least 1 hour on precipitation from a pure 50 mM CaSO<sub>4</sub> solution.

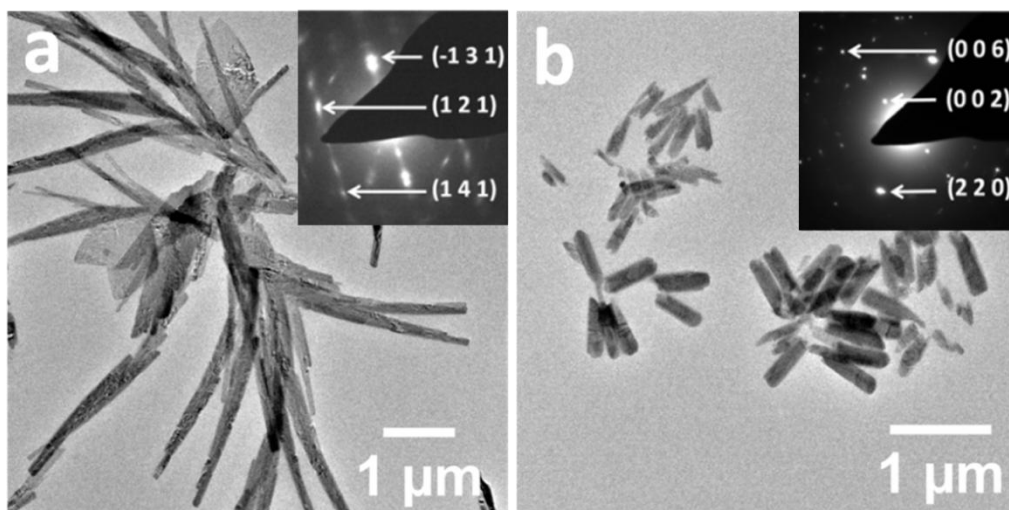


**Figure 3.13** (a) Calcium sulfate dihydrate and (b) calcium sulfate hemihydrate crystals precipitated from the 50 mM solution after 1 hour, and the corresponding selected-area electron diffraction pattern.

Given that the reaction proceeded rapidly even in the 50 mM solution, a more dilute solution (15 mM) was also studied. While the precipitates produced after 7 days were gypsum, analysis of the solution after just 1 min demonstrated the presence of needles of both gypsum and hemihydrate (Figures 3.14a and b). Most of the precipitates were nano-rods of hemihydrate which were less than  $1\ \mu\text{m}$  in length. The gypsum was usually in the form of long needles, and plate-like gypsum was seldom observed. The inserted images shown in Fig 3.14 are the corresponding selected-area electron diffraction patterns of gypsum and hemihydrate.

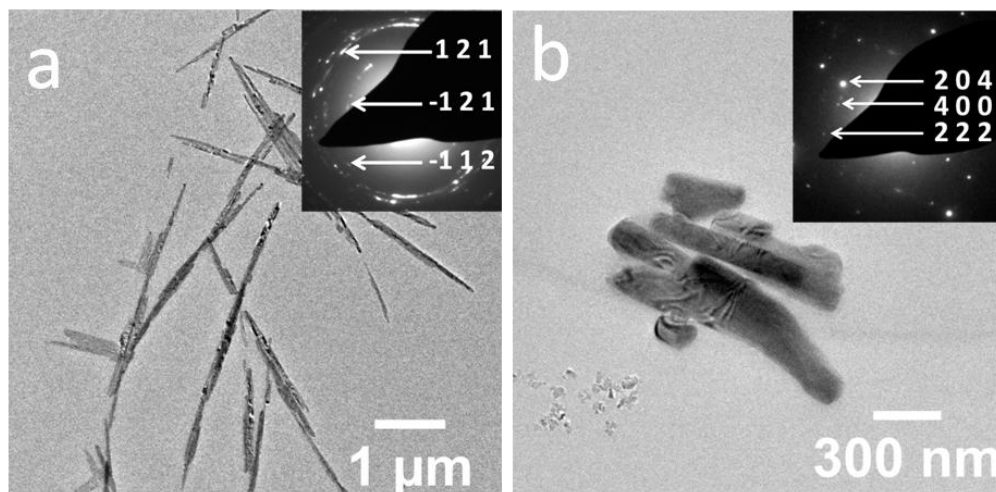


**Figure 3.14** (a) Calcium sulfate dihydrate and (b) calcium sulfate hemihydrate crystals precipitated from the 15 mM solution after 1 minute, and the corresponding selected-area electron diffraction pattern.

Interestingly, individual nanoparticles which were 20-30 nm in diameter were also observed (Figure 3.15a). Elemental dispersive X-ray (EDX) analysis of aggregates of these particles confirmed the presence of Ca and S (Figure 3.15b, inset). The weak Na peak in EDX shows no salt contamination left in the nanoparticles. Fig 3.16a also shows there was no evidence for crystallinity by selected area electron diffraction, which suggests that these particles were hydrated amorphous  $\text{CaSO}_4$  (ACS). By continued exposure to the electron beam after 1 minute, partial crystallisation was apparent, and electron diffraction demonstrated that the nanoparticles had crystallised to gypsum. This shows that the particles were amorphous and that the absence of diffraction patterns was not due to a lack of sufficient material to give recordable diffraction patterns in this area (Figure 3.16b and Table 3-3). Finally, a more concentrated solution was also studied for comparison, and gypsum needles were the sole product after 1 min in a 100 mM solution.

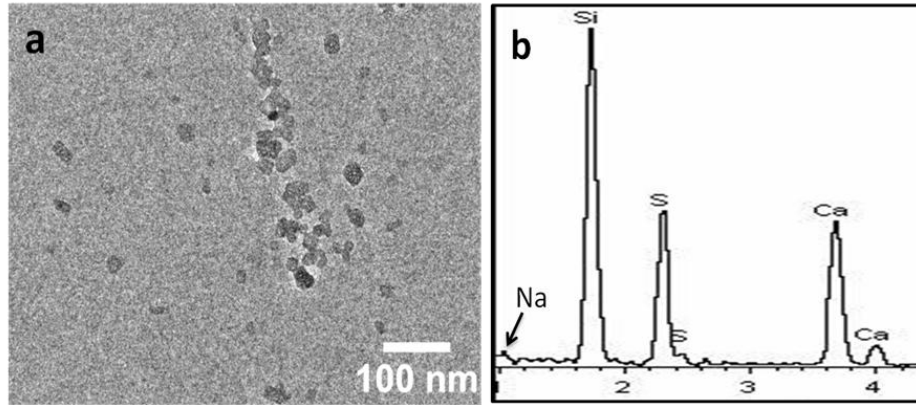


**Figure 3.15** a) TEM image of amorphous  $\text{CaSO}_4$  particles precipitated from a 15 mM solution after 1 min. b) The corresponding EDX spectrum demonstrates significant Ca and S, and negligible Na (position arrowed) (Si peak may be from the glass which is used as the substrate).

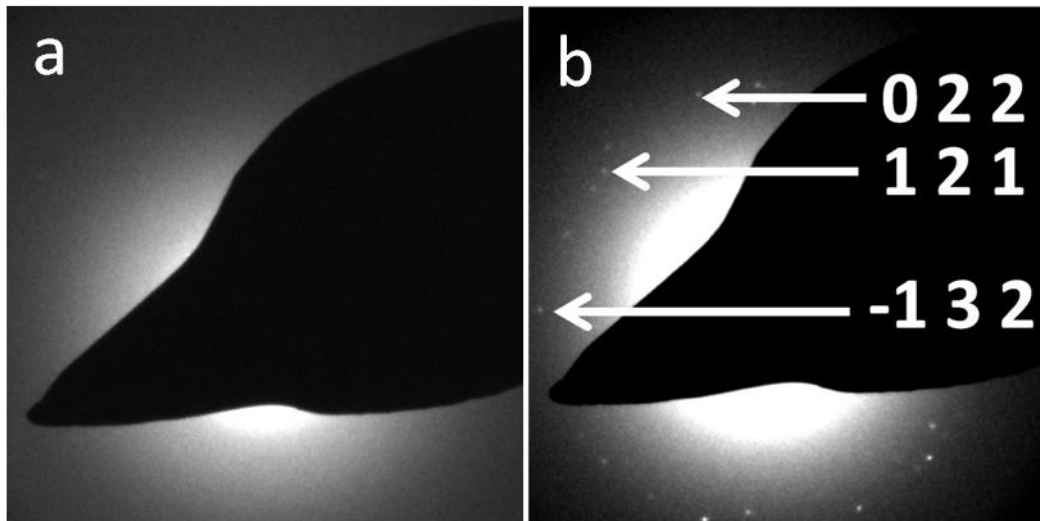


**Figure 3.16** a) The selected area electron diffraction pattern of this sample, showing that it is amorphous. b) After 1 min irradiation with the electron beam, crystallisation to  $\text{CaSO}_4$  dihydrate (gypsum) occurs.

## 3.4.2 Precipitation from Undersaturated Solutions

### 3.4.2.1 TEM and Raman analysis

These experiments demonstrated that calcium sulfate can precipitate from solutions of concentration 5 mM, which is significantly below the bulk solubility limits of both bassanite (80 mM) and gypsum (15 mM). As also described by Van Drieschen

et al,[129] the 5 mM CaSO<sub>4</sub> solution was obtained by mixing equal volumes of 10 mM CaCl<sub>2</sub> and 10 mM NaSO<sub>4</sub> solutions. As counter ions affect the solubility of the mineral, the salinity of the solution must be taken into account. At the given salinity (20 mM NaCl) the bulk solubility of bassanite and gypsum are 82 mM and 17mM, respectively,[128] which are well above the 5 mM concentration of the reaction solution investigated here.

Surprisingly, when this 5 mM solution was left for periods exceeding several months, we visually observed the formation of small amounts of precipitate. This prompted us to prepare fresh solutions, from which samples were taken for TEM and electron diffraction analysis over the course of 8 months (shown in Fig 3.17). Already after a week, as shown in Fig 3.17a, precipitates were observed, where these consisted of aggregates of amorphous calcium sulfate nanoparticles that transformed into bassanite upon prolonged irradiation with the electron beam. After 2 weeks, amorphous calcium sulfate was still the majority product although some bassanite crystallites were now also present (Fig 3.17b). TEM and electron diffraction showed that these consisted of 5-10 nm nanocrystals that had formed a crystallographically aligned assembly, suggesting an oriented attachment-like growth process, similar to that reported by Van Driessche *et al.*[129] In the next period (3 - 6 months after sample preparation) these developed further, as was evidenced by the finding of rod-like crystals 100-300 nm in length and ~ 50 nm in width. These were identified as bassanite by electron diffraction and Raman spectroscopy (Fig 3.17c,d). Further aging of the sample up to 8 months resulted in the TEM observation of crystals with lengths 200-500 nm. These were gypsum, as was demonstrated by electron diffraction and Raman spectroscopy (Fig 3.17e, f).

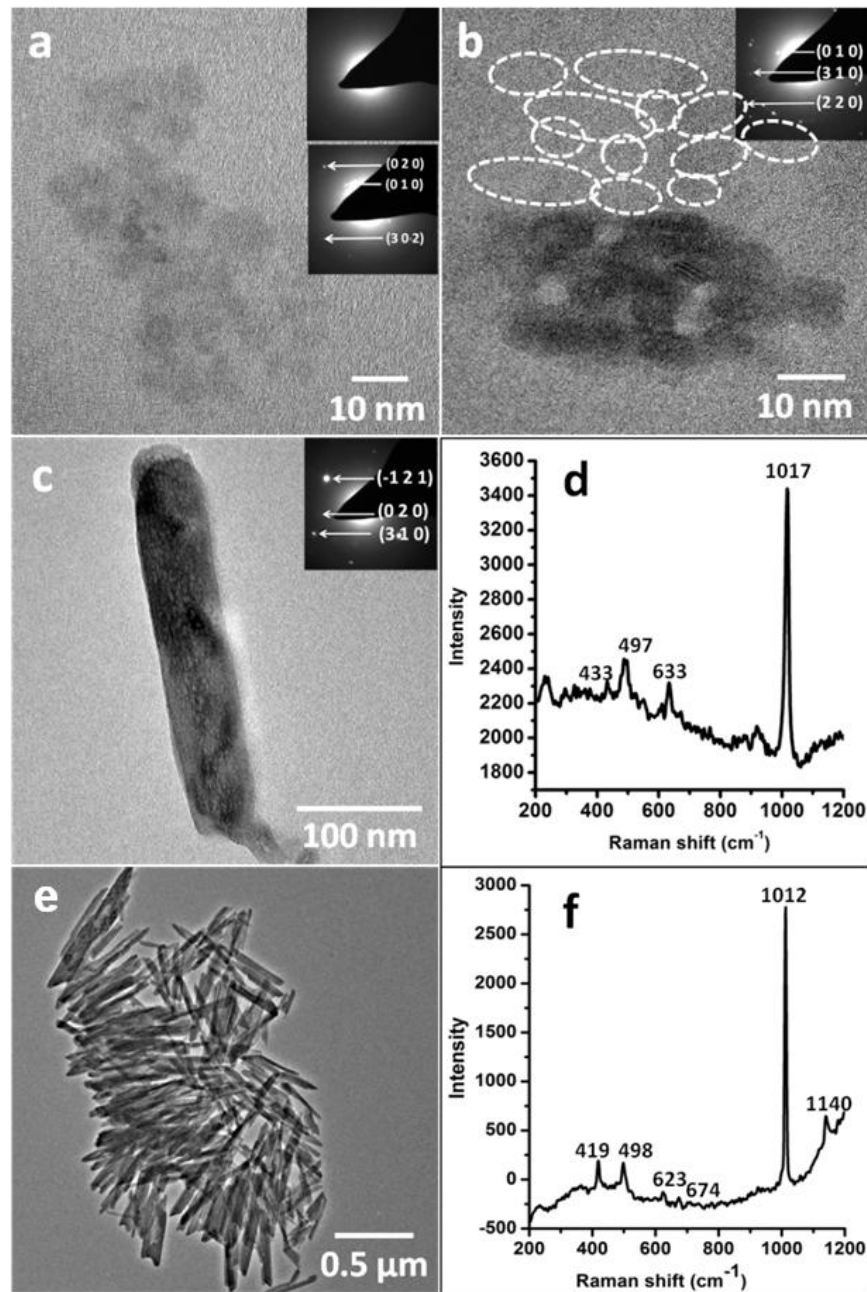


**Fig 3.17** Precipitates present in a 5 mM calcium sulphate solution, as characterised by TEM and Raman. (a) After 1 week, all the precipitates were amorphous, where these crystallized to hemihydrate after irradiation with the beam; (b) After 2 weeks, some hemihydrate crystals, less than 10 nm in length, were observed; (c) After 4 months, all these hemihydrates nanorods were 100-200 nm in length and d) exhibited Raman spectra consistent with hemihydrate, with shifts at 433, 497, 633 and 1027 cm<sup>-1</sup>; (e) After 8 months, gypsum started to form, (f) as identified by Raman microscopy.

The above observations are remarkable as currently no mechanism exists to explain the formation of solid precipitate at concentrations significantly below the solubility of the most stable and insoluble form of a mineral, which for  $\text{CaSO}_4 \cdot 2\text{H}_2\text{O}$  is gypsum. However, the solubility of calcium sulfate has been a subject of many discussions, as calcium sulfate solutions are known to contain a large fraction (up to 50-60 mol%) of undissociated ions, which have been attributed to the presence of ion pairs. This soluble but undissociated fraction of the mineral complicates the relation between the solubility of the mineral and the solubility product ( $K_{\text{sp}}$ ) as determined from measuring the concentration of (free) ions. Furthermore, it has been stressed that the strong binding of calcium and sulfate in solution, as well as the presence of counter ions, requires the use of ion activity products rather than the ion products to characterize the solubility of the mineral.

To obtain further insight into the observed phenomenon, we determined the free calcium ion concentration ( $[\text{Ca}]_{\text{free}}$ ) in the solution using a calcium ion selective electrode (Ca-ISE). Interestingly, after aging for 6 months the same free calcium concentration was measured (84 mol% of the total) as directly after preparation (4.8 mM, which is 86 mol% of the total). This implies that the precipitate is formed from bound calcium ions, leaving the concentration of free calcium ions, and hence the equilibrium between the solid and the dissociated ions untouched. Such a mechanism in which both  $[\text{Ca}]_{\text{free}}$  and pH are unchanged can only exist if the mineral is formed from calcium and sulfate ions bound in ion pairs or clusters, both of which have the same 1:1 Ca:SO<sub>4</sub> stoichiometry as the resulting solid. Moreover, these then would have to associate, forming a solid according to



without changing their solution activity, which otherwise would shift the equilibrium.

### 3.4.2.2 Titration Experiments

To further investigate the ratios of free and bound ions in the presence and absence of a solid mineral phase, we performed an experiment in which the supersaturation is gradually increased by titrating equal amounts of  $\text{CaCl}_2$  (250 mM) and  $\text{Na}_2\text{SO}_4$  (250 mM) solutions into water while monitoring  $[\text{Ca}^{2+}]_{\text{free}}$  (shown in Fig 3.18). In

this way, a typical LaMere curve was obtained in which the nucleation event is indicated as the top of the curve, after which a rapid drop in the measured calcium concentration is observed, which indicates the formation of a solid phase. As during the reaction the pH was found to be nearly constant at 6.8, the Ca-ISE data could be used without corrections. However, to compensate for deviations in nucleation kinetics of the different experiments, the time scale was normalized by setting the nucleation point (NP) as 1NP with  $t = \text{time(s)} / \text{time of NP (s)}$  (shown in Fig 3.19). We define the reaction period of 0-1NP as the pre-nucleation stage, period from 1-1.4NP as the nucleation event and 1.4-2NP as the post-nucleation stage.

The total calcium concentration is shown as a dashed line, and corresponds to the amount of calcium ions added during the titration (Fig 3.18a). The concentrations of free calcium ions ( $[\text{Ca}]_{\text{free}}$ ) at all times lie significantly below the total calcium concentration. The difference in the curves reflects the binding of calcium to the sulfate ions, and the concentrations of bound calcium ( $[\text{Ca}]_{\text{bound}}$ ) were calculated from the free calcium levels ( $[\text{Ca}]_{\text{free}}$ ) measured by Ca-ISE. As the pH is nearly constant at  $\text{pH} = 6.87$  during the reaction, we can assume that nearly all soluble sulfate is present as  $\text{SO}_4^{2-}$ , and hence that no deprotonation is required for binding to  $\text{Ca}^{2+}$  and that calcium and sulfate bind in a 1:1 ratio. Hence, the change in the free sulfate concentration ( $[\text{SO}_4]_{\text{free}}$ ) due to calcium binding was estimated from  $[\text{Ca}]_{\text{bound}}$  and this was used to determine the ion activity product (IAP) in the different stages of the reaction (Fig 3.18b).

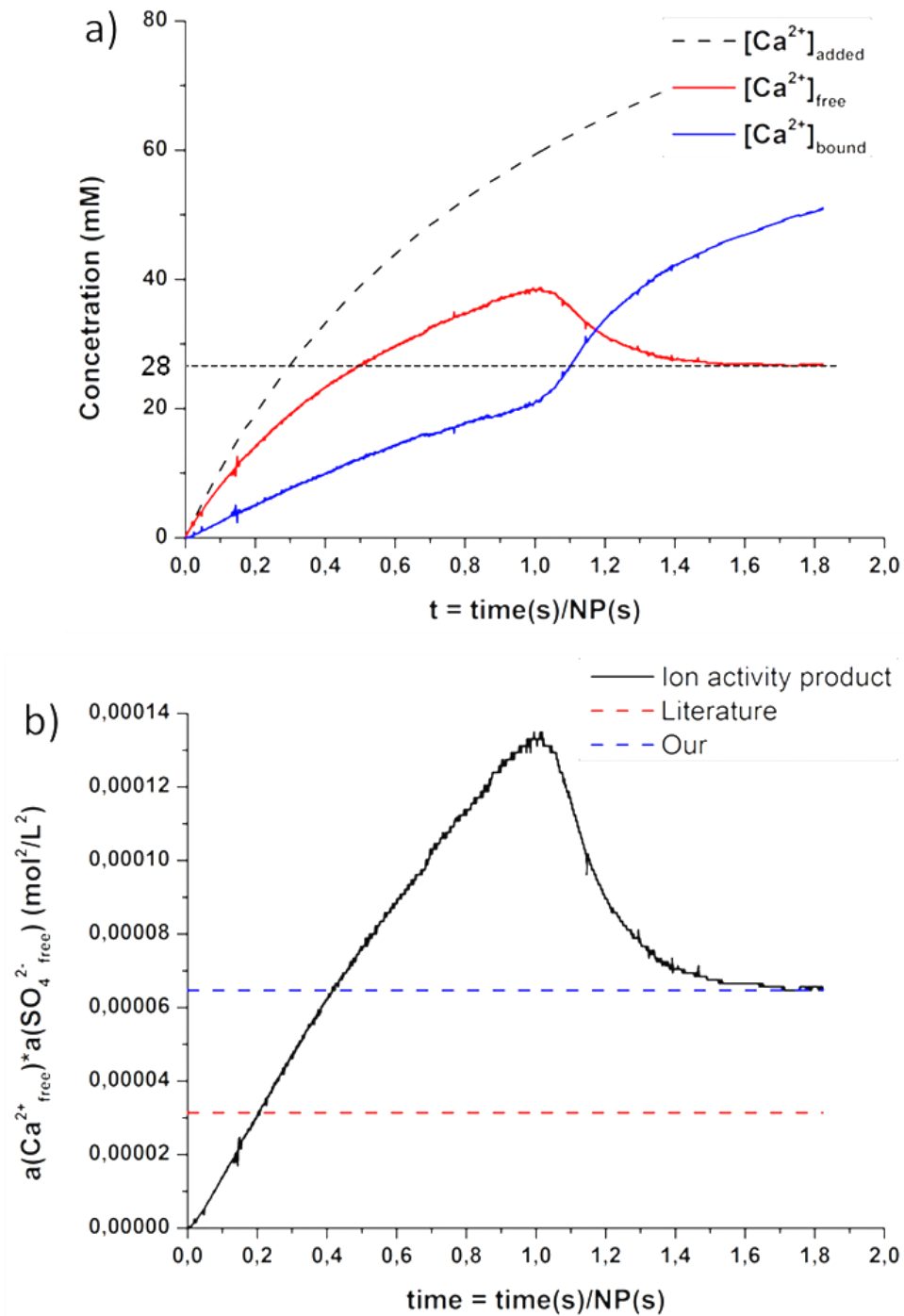


**Figure 3.18** a) Titration curve showing the development of  $[\text{Ca}^{2+}]_{\text{free}}$  ions (red line) compared to the total amount of  $[\text{Ca}^{2+}]_{\text{added}}$  (dashed black line) as a function of time normalized with respect to the NP, with  $t = \text{time (s)} / \text{time of the nucleation point (NP) (s)}$ . The amount of  $[\text{Ca}^{2+}]_{\text{bound}}$  is given by the blue line and was calculated as difference between  $[\text{Ca}^{2+}]_{\text{added}}$  and  $[\text{Ca}^{2+}]_{\text{free}}$ . b) Development of Ion Activity Product (IAP) as a function of time normalized with respect to the NP, with  $t = \text{time (s)} / \text{time of NP}$ .

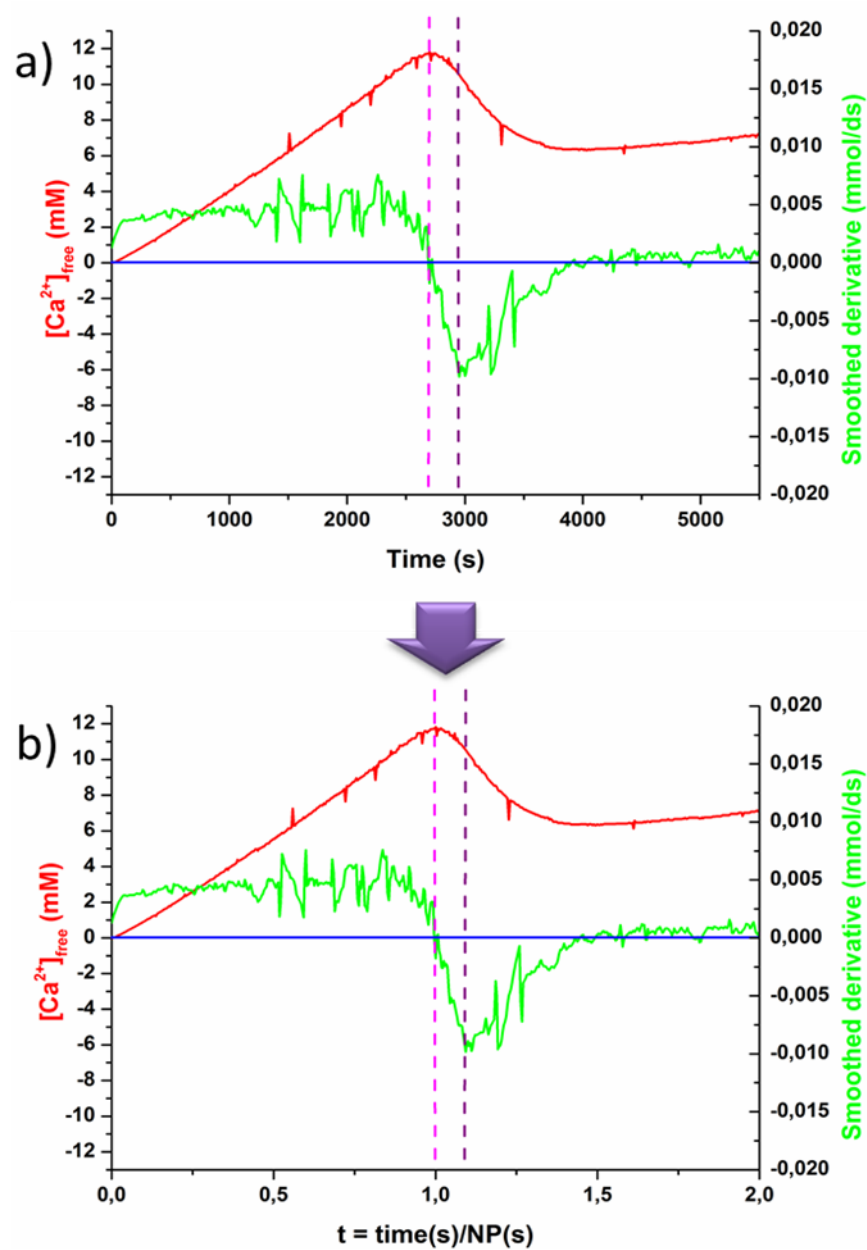


**Figure 3.19** An example of the normalization procedure applied to convert the time scale (in seconds) to the time scale where the nucleation point (NP) is normalized to 1. The derivative is calculated from the red free calcium concentration curve, resulting in the derivative which is subsequently smoothed 20 points (green line). Where this derivative equals zero, the nucleation point can be found. Doing so, in (a) the NP is found to be at 2700s (pink dotted line), which is normalized in (b) and thus defined as  $t=1$ . The bending point (BP) is defined as the minimum value of the derivative of the curve of free calcium concentration, here being at 2950s (purple dotted line).

The measurements indicated that in the pre-nucleation stage, the distribution of the calcium between its free and bound form changes dramatically. Table 3-4 shows the concentrations and percentages of added, bound and free calcium at different time points as calculated from the titration experiments. Starting with a bound calcium fraction of <5% in the first 2.5 minutes (< 0.02 NP), after 5 mins (0.04 NP), when  $[\text{CaSO}_4]_{\text{added}}$  had reached 5 mM, this had already increased to 14%. A further increase to ~ 30% occurred just before the nucleation point (0.9 NP). The data further showed that at  $[\text{CaSO}_4]_{\text{added}} = 5\text{mM}$ , the free calcium concentration (4.10 mM) and IPA ( $4.74 \times 10^{-6} \text{ M}^{-2}$ ) was the same as for the solution precipitation experiments, but significantly lower as after nucleation where the solution is thought to be in equilibrium with the solid phase  $[\text{Ca}]_{\text{free}}$  approximately stable at 28 mM (Fig 3.18a) and IAP =  $6.5 * 10^{-5} \text{ M}^{-2}$  (Fig 3.18b). The measured value of  $[\text{Ca}]_{\text{free}} = 28 \text{ mM}$  is in good agreement with the literature, as it is well below the reported solubility of calcium sulfate at high salinity (30-32mM for 200-300 mM NaCl). This confirms the dramatic difference between the crystallization conditions above and below the solubility limit.

Samples were also taken from the titration experiments in the undersaturated stages for cryo-TEM analysis with the aim of investigating the very early stages of mineral formation. Unfortunately, the very low concentrations of mineral made it impossible to reliably visualize mineral formation at concentrations below added calcium concentrations at 0-5 mM. However, at  $[\text{CaSO}_4]_{\text{added}} = 13\text{mM}$  (15 min, 0.13 NP), cryo-TEM in combination with low dose electron diffraction revealed the formation of bassanite (shown in Fig 3.20). At this point the solubility of bassanite and gypsum are estimated to be ~85 mM and ~20 mM respectively (salinity 50 mM NaCl)[156], when 18 % of the calcium is in its bound form with an IAP of only  $1.89 \times 10^{-5} \text{ M}^{-2}$ .

**Table 3.4** Concentrations and percentages of added, bound and free calcium at different time points, as calculated from the titration experiments.

	Time (min)	NP	[Ca] <sub>added</sub> (mM)	[Ca] <sub>free</sub> (mM)	[Ca] <sub>bound</sub> (mM)	% Ca <sub>free</sub>	% Ca <sub>bound</sub>	IAP (M <sup>2</sup> )
<b>Experiment 1</b>	2.5	0.02	2.44	2.20	0.23	90	10	1.78x10 <sup>-6</sup>
	5	0.04	4.80	4.10	0.70	86	14	4.74x10 <sup>-6</sup>
	11	0.09	10.10	8.40	1.70	83	17	1.31x10 <sup>-5</sup>
	15	0.13	13.38	10.93	2.45	82	18	1.89x10 <sup>-5</sup>
	209	1.82	78	28	50	36	64	6.50x10 <sup>-5</sup>
<b>Experiment 2</b>	6	0.13	5.7	1.3	4.4	22	78	3.24x10 <sup>-5</sup>
	25	0.55	22.3	6.2	16.1	28	72	1.31x10 <sup>-4</sup>
	34	0.75	29.5	8.9	20.6	30	70	1.77x10 <sup>-4</sup>
	45	1	37.5	11.8	25.7	32	68	2.13x10 <sup>-4</sup>
	63	1.4	49.5	6.4	43.1	13	87	9.12x10 <sup>-5</sup>
	98	2.17	69.6	7.6	62	11	89	7.60x10 <sup>-5</sup>

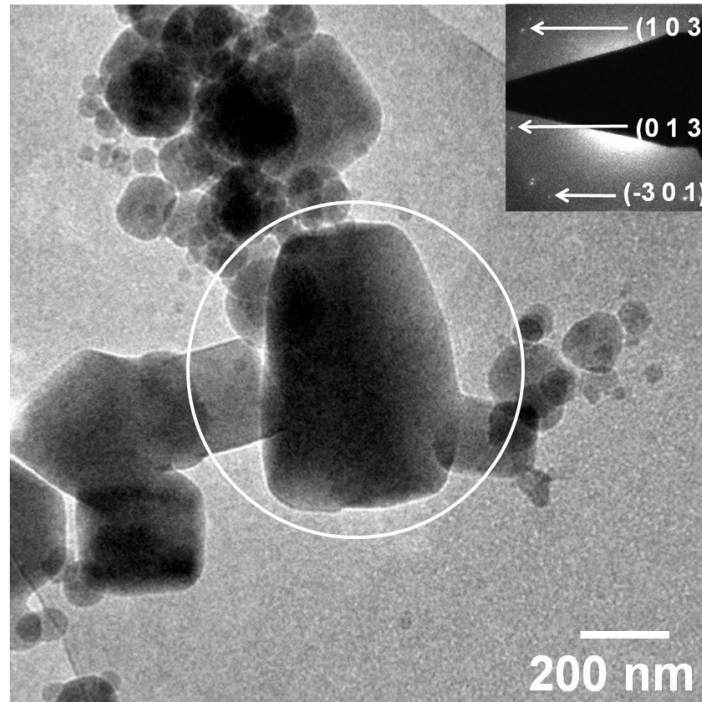


**Fig 3.20** Equal amounts of  $\text{CaCl}_2$  (250mM) and  $\text{Na}_2\text{SO}_4$  (250mM) solutions were titrated into water. The CryoTEM sample was taken at  $\text{CaSO}_4$  concentrations of approximately 13 mM. The diffraction pattern was from the particle in the white circle, which showed that it was hemihydrate.

### 3.4.3 $\text{CaSO}_4$ Precipitation from bound calcium in undersaturated solution

To further explore the precipitation of  $\text{CaSO}_4$  from bound calcium below the solubility limit of gypsum, the experimental set up was changed such that the supersaturation of  $\text{CaSO}_4$  was increased gradually using the titration of a 250 mM  $\text{CaCl}_2$  solution into 25 mL of a 250 mM solution of  $\text{Na}_2\text{SO}_4$ . [154] In this situation, the calcium ions are added to an excess of sulfate ions which should lead to a higher degree of ion pair formation (or cluster) formation. Indeed, before the nucleation point,  $[\text{Ca}]_{\text{free}}$  (Fig3.21a, red line) forms a straight line with a slope much lower as  $[\text{Ca}]_{\text{added}}$ . Hence, as compared to the previous experiment, a high fraction of the  $\text{Ca}^{2+}$  ions is present as bound calcium. [7]

The Ca-ISE measurements indicated that initially nearly all added calcium ions are bound, but that during the course of the reaction  $[\text{Ca}]_{\text{bound}}$  relaxes to an approximately steady level of ~ 70% free calcium at 0.75-1.0 NP (shown in Table 3-

4). As also in this case no changes in the pH are observed, and the  $\text{Cl}^-$  ions are accounted for in the calibration (see experimental section), already before the nucleation point the bound calcium must be present as  $\text{CaSO}_4$ , likely in the form of ion pairs or (prenucleation) clusters. Already at 0.75NP the solution became cloudy and developed a milky appearance at 0.9NP. At this point also dynamic light scattering (DLS) showed a dramatic increase in count rate (Fig 3.22). Nucleation occurred at  $[\text{Ca}]_{\text{added}} = 37.5 \text{ mM}$  (1.0 NP, Table 1) after which time  $[\text{Ca}]_{\text{free}}$  dropped to a value of 6.4 mM (1.4 NP,  $\text{IAP} = 9.12 \times 10^{-5}$ ) which reflects the low solubility limit of gypsum under the conditions used, i.e. in the presence of an excess of sulfate ions. Upon continued titration the  $[\text{Ca}]_{\text{free}}$  slowly increased again while the IAP further decreased due to the continuing addition of  $\text{CaCl}_2$  to balance the  $\text{Ca}/\text{SO}_4$  ratio.

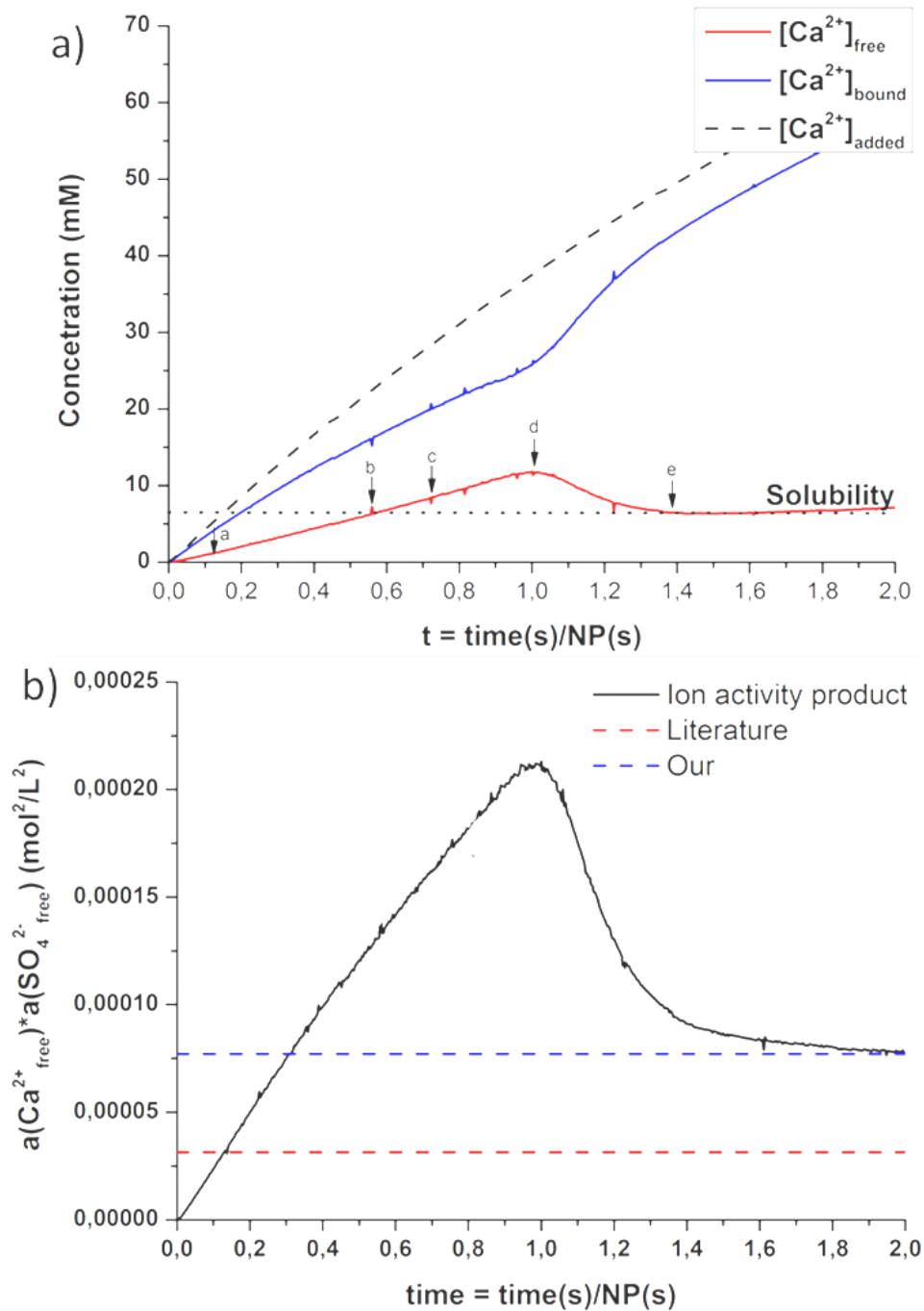


**Figure 3.21** a) Titration curve showing the development of  $[\text{Ca}^{2+}]_{\text{free}}$  ions (red line) compared to the total amount of  $[\text{Ca}^{2+}]_{\text{added}}$  (dashed black line) as a function of time normalized with respect to the NP, with  $t = \text{time (s)} / \text{time of NP (s)}$ . The amount of  $[\text{Ca}^{2+}]_{\text{bound}}$  is given by the blue line and was calculated as the difference between  $[\text{Ca}^{2+}]_{\text{added}}$  and  $[\text{Ca}^{2+}]_{\text{free}}$ . b) Development of Ion Activity Product (IAP) as a function of time normalized with respect to the NP, with  $t = \text{time (s)} / \text{time of NP}$ .

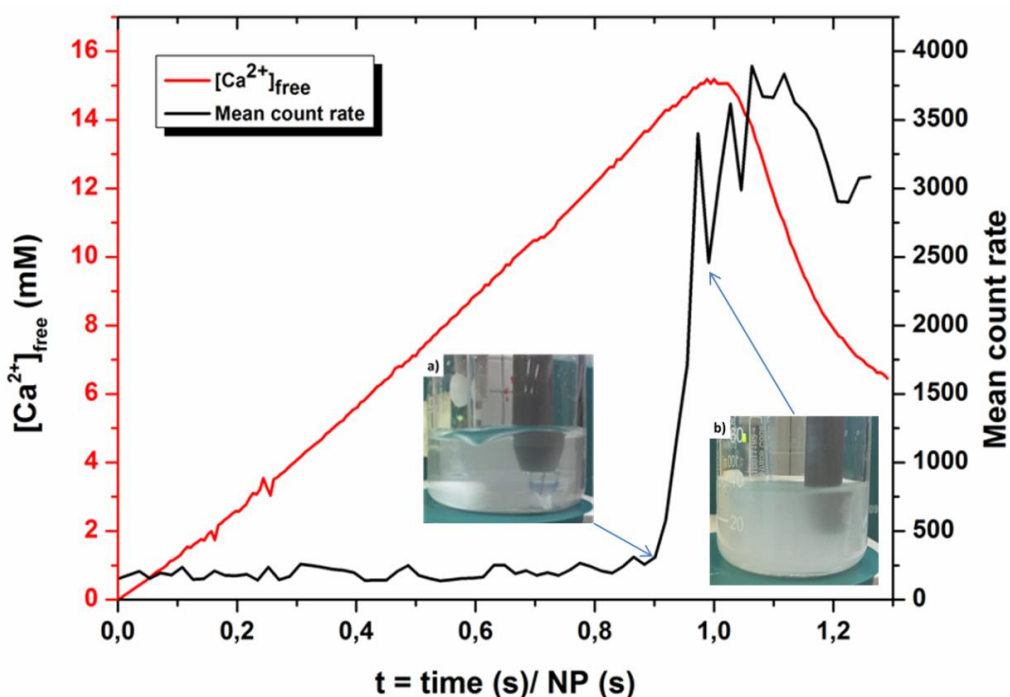


**Figure 3.22:** Dynamic light scattering (DLS) was performed of by adding 250 mM  $\text{CaCl}_2$  solution to 25 ml of 250 mM  $\text{Na}_2\text{SO}_4$ . The count rate increases somewhat prior to the nucleation point (0.9NP), where this corresponds to an increase in turbidity of the reaction solution (picture a). Picture (b) shows the solution at the NP.

In contrast to the first titration protocol, now the solution contained high amounts of bound calcium, and cryo-TEM could be successfully applied to visualize the early stages of mineral formation. At 0.13NP ( $[\text{Ca}]_{\text{free}} = 1.3 \text{ mM}$ ,  $\text{IAP} = 3.24 \times 10^{-5} \text{ M}^{-2}$ ) cryo-TEM demonstrated the formation of small clusters with diameters of  $\sim 2 \text{ nm}$  (Fig 3.23a). Samples taken at 0.55NP, where  $[\text{Ca}]_{\text{free}}$  was raised to 6.2 mM ( $\text{IAP} = 1.31 \times 10^{-4} \text{ M}^{-2}$ ) showed that the size of the nanoparticles had now increased to 5-10 nm (Fig 3.23b). By further increasing  $[\text{Ca}]_{\text{free}}$  to 8.9 mM, (0.75NP,  $\text{IAP} = 1.77 \times 10^{-4} \text{ M}^{-2}$ ) the nanoparticles aggregated to form larger assemblies which were still amorphous according to ED (Fig 3.23c). It is important to emphasize that these assemblies were observed at 0.75NP, hence before the point at 0.9NP where the solution turns turbid and DLS showed a dramatic increase in count rate (Fig 3.22). At 1.0 NP ( $[\text{Ca}]_{\text{free}} =$

11.8mM,  $IAP=2.13 \times 10^{-4} M^{-2}$ ), just before the calcium concentration dropped, cryo-TEM showed the formation of crystals with dimensions of 100 – 500 nm. These were identified as a mixture of bassanite and gypsum by ED (Fig 3.23d). After 1.4NP, when the free calcium concentration had dropped to a plateau at  $[Ca]_{free} = 6.4mM$ , only gypsum was found in the solution. Hence, under the conditions used, the first solid phase to appear is bassanite, which seems to form from the solution by the assembly of clusters. As described previously, the bassanite is transient and transforms to the thermodynamically more stable gypsum.

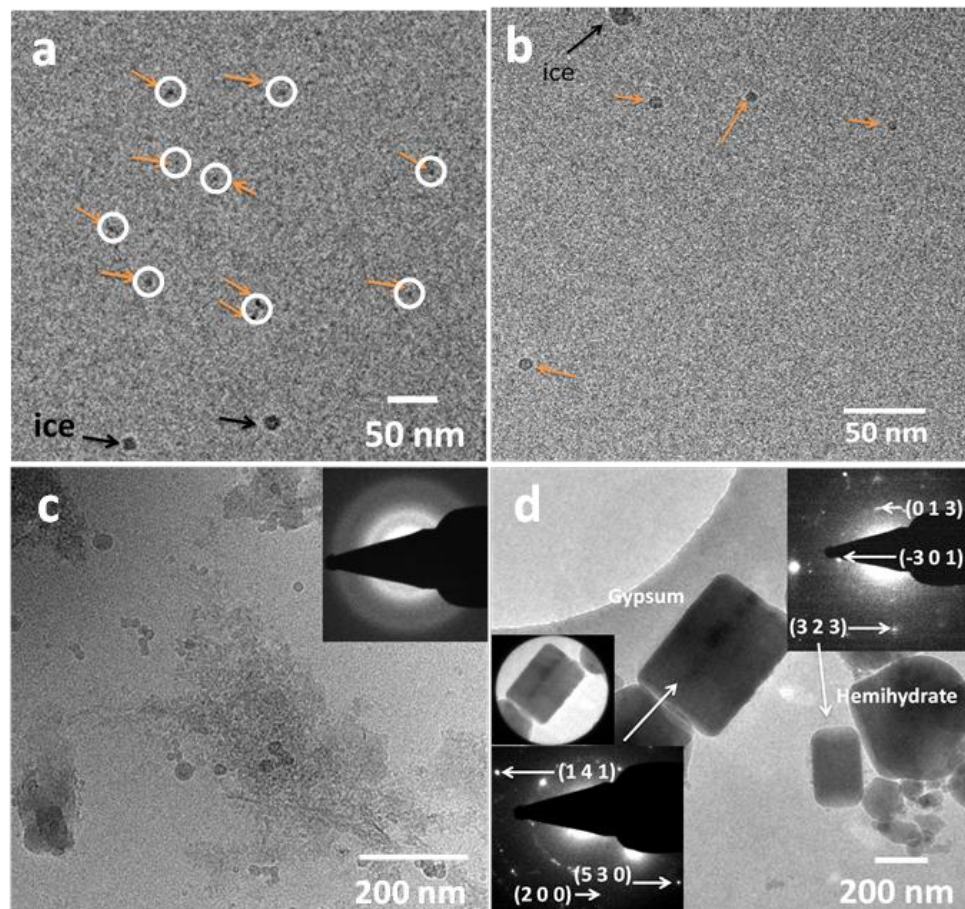


**Figure 3.23.** Cryo-TEM images of particles isolated from an experiment in which 250 mM  $CaCl_2$  solution was titrated into 250 mM  $Na_2SO_4$  solution with an addition rate of 0.1 mL/min, at a) 0.13NP; b) 0.55NP; c) 0.75NP; d) 1NP; e) 1.4NP. The images indicate that  $CaSO_4$  formation starts from nano assemblies, via amorphous flocks and hemihydrates, to ultimately form large gypsum crystals.

### 3.5 Discussion

These results provide a significant new understanding of the mechanism of precipitation of  $\text{CaSO}_4$ . Indeed, we are not aware of any previous reports of either an amorphous calcium sulfate phase or that gypsum can precipitate from aqueous solution via a hemihydrate precursor phase in ambient conditions. This may be partly attributed to the short lifetime and small size of the ACS, such that it will be overlooked in experiments designed to investigate, for example, the kinetics of nucleation and growth in bulk solution,[128] or the stability/transformation of polymorphs under different solution conditions.[128] Further, the solution concentrations employed here are lower than many of those previously used.[31] ACS and hemihydrate only show any appreciable stability in pure  $\text{CaSO}_4$  solutions at room temperature at concentrations just above saturation, and even in the 50 mM solution were we unable to take samples soon enough to observe a possible amorphous phase even in 1 minute.

As described in section 3.1, gypsum is the most stable phase at room temperature, anhydrite at high temperatures and hemihydrate is metastable at all temperatures [128]. Interestingly, metastable hemihydrate is an important intermediate phase during the transformation from gypsum to anhydrite and is co-precipitated with anhydrite from salt-free solutions above  $\approx 97^\circ\text{C}$  when its solubility product is exceeded.[128] According to the hydration properties, the precipitation of  $\text{CaSO}_4$  is also strongly affected by the water activity, such that the transition temperature of gypsum to anhydrite in seawater or saturated NaCl solution can approach room temperature.[37] Hence, it is possible that very high concentrations of salt may also support hemihydrate formation near ambient conditions.[157]

Our observation of pure hemihydrate at room temperature in a salt-free solution of  $\text{CaSO}_4$  therefore contradicts previous studies. Interestingly, however, there is one record of the formation of hemihydrate from solution at ambient conditions – courtesy of the humble jellyfish. Statoliths are the gravity-sensors that can be found in deep-sea medusa, and can be formed from both gypsum[142] and hemihydrate.[157] Although  $\text{CaSO}_4$  biominerals are rare, it is clear that the formation of these structures is under biological control, and that they are likely to be co-precipitated with organic additives and covered with lamellar membranes. The observation of a hemihydrate biomineral, however, provides conclusive support

for our results which show that it is possible to precipitate hemihydrate from solution at room temperature.

Precipitation at low solution concentrations but above the solubility level, where this provides a relatively long reaction time, allowed us to identify a previously unreported mechanism of  $\text{CaSO}_4$  precipitation, where transformation from amorphous calcium sulfate to hemihydrate, and then to gypsum occurs at room temperature. This new transformation pathway also follows Ostwald's Rule of Stages, where kinetic factors dictate the precipitation of progressively more stable polymorphs. Because of the very short lifetime and small quantities of amorphous calcium sulfate, it was unfortunately not possible to isolate this material to study its composition under XRD, Raman or IR. However, our data provides strong evidence that it is hydrated as  $\text{CaSO}_4 \cdot 2\text{H}_2\text{O}$  can be formed by heating ACS nanoparticles in the dry atmosphere of the TEM. The mechanism of transformation of ACS to hemihydrate cannot be elucidated from these experiments, but would make the subject of an interesting cryo-TEM study. It is well known that in solution, hemihydrate converts to gypsum (the setting of plaster) via a highly exothermic dissolution-reprecipitation reaction.[128] Indeed, it is possible that amorphous calcium sulfate nanoparticles can transform to hemihydrate nanorods via an aggregation-based mechanism. [128]

Following the experiments described above, cryo-TEM and titration experiments were used to analyse calcium sulfate precipitation from amorphous calcium sulfate to hemihydrate. The finding of an amorphous phase and hemihydrate as precursors for gypsum from 5 mM calcium sulfate solutions is in good agreement with the recent literature.[128] That such a reaction happens in undersaturated solutions suggests that at ambient conditions, the pathway for the precipitation from amorphous calcium sulfate to gypsum via hemihydrate transformation may be important. However, our results revealed that the solubility of bassanite nanorods that precipitated from solution must be lower than those obtained from dehydrated gypsum.

The titration experiment by adding equal amounts of  $\text{CaCl}_2$  (250 mM) and  $\text{Na}_2\text{SO}_4$  (250 mM) solutions into water while monitoring  $[\text{Ca}^{2+}]_{\text{free}}$  provide the results that before the nucleation point (before 50 mins) >80% of the calcium was present as free, unbound calcium. Furthermore, the IAP in the final state amounted to only 6.5

$\times 10^{-5} \text{ mol}^2\text{L}^{-2}$ , which is closer to the solubility product of gypsum ( $3.14 \times 10^{-5} \text{ mol}^2\text{L}^{-2}$ ). This implies that, as compared with the titration of a 250 mM  $\text{CaCl}_2$  solution into 25 mL of a 250 mM solution of  $\text{Na}_2\text{SO}_4$ , equal amounts of titration a far lower fraction of the calcium in the solution is present as bound calcium. This suggests a possible pathway of formation calcium sulfate avoid nucleation undersaturated level in the early stage.

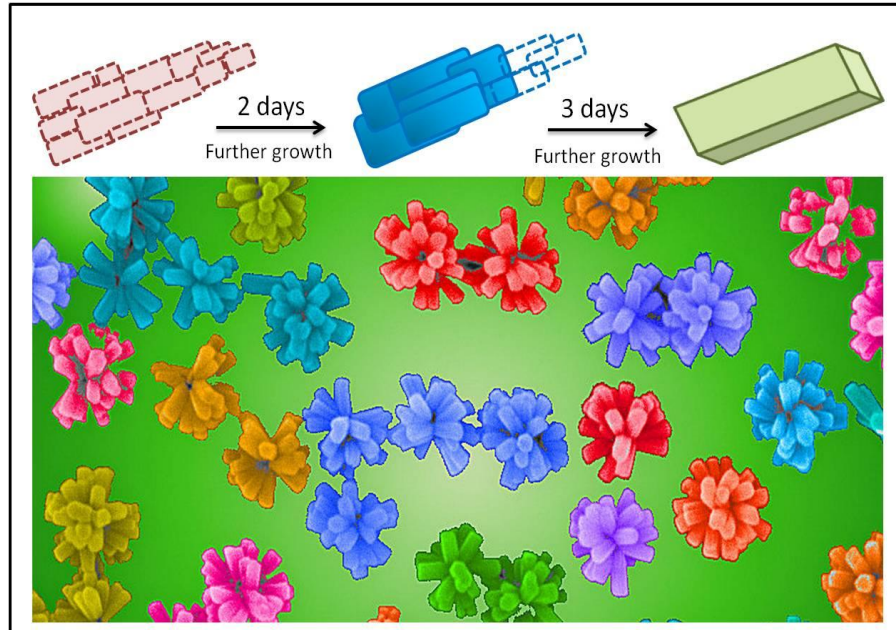
In contrast, the observation of nanoparticles prior to nucleation has not been previously described for calcium sulfate. However, the presence of pre-nucleation clusters has recently been reported for calcium carbonate and calcium phosphate[9]. Nevertheless, the remarkable observation that in the early stages (before the nucleation point) ~ 80% of the calcium ions triggered the notion that the presence of these pre-nucleation species may be due to the large excess of sulfate ions in the solution in the initial stages of the titration.

### **3.6 Summary**

In summary, investigation of the early stages of  $\text{CaSO}_4$  precipitation from salt-free solutions at room temperatures demonstrates for the first time the existence of an amorphous calcium sulfate (ACS) phase, and its subsequent step-wise transformation to gypsum via  $\text{CaSO}_4$  hemihydrate. There are also no previous reports of the synthesis of hemihydrate from salt-free  $\text{CaSO}_4$  solutions at room temperature. However, while it is tempting to suggest that gypsum always precipitates from solution by this mechanism, we cannot at this stage generalise, and it is certainly possible that gypsum can also precipitate directly from highly supersaturated solutions. That we have successfully identified these transient phases, which become progressively more short-lived with increasing supersaturation, is due to the use of relatively dilute solutions. This highlights the importance of employing conditions which enable investigation of the earliest stages of nucleation and growth. Complete characterisation of these processes will inevitably facilitate the development of novel control strategies over the precipitation of industrially important materials such as  $\text{CaSO}_4$ . Finally, in  $\text{CaSO}_4$  we have found a new system in which precipitation occurs via an amorphous precursor phase. This truly suggests

that this may be a widespread crystallisation mechanism, which is simply often overlooked due to the short lifetime of these soluble metastable phases. We can also conclude that the association of ion pairs (or clusters) to first form amorphous calcium sulfate and later crystalline particles does not change the activity of the solution (otherwise the calcium levels would change). The ion pairs therefore have an activity coefficient of  $\sim 1$ .

## Chapter 4: Additives Stabilize Calcium Sulfate Hemihydrate (Bassanite) in Solution



This work investigates the precipitation of calcium sulfate in aqueous solution at room temperature in the presence of poly(acrylic acid), poly(styrene-4-sulfonate), sodium triphosphate and magnesium ions. The focus is on the stability of hemihydrate and amorphous calcium sulfate. It is already known that amorphous calcium sulfate transformed to gypsum via hemihydrate.[16] Again, the early stages of calcium sulfate precipitates in bulk solution were studied with a range of techniques proved this new crystal growth pathway. Interestingly, in this chapter, these additives are also active in controlling the morphologies of the hemihydrate crystals, which can play a key role in defining properties such as porosity and mechanical strength. The results confirm the stepwise-precipitation of gypsum via amorphous and hemihydrate intermediates and suggest an alternative to the energy-intensive calcination processes which are currently widely used to prepare hemihydrate.

## 4.1 Introduction

For many years, it has been known that development of effective routes for controlling the crystallization of a substance is most effectively made based on an understanding of its nucleation and growth mechanisms. Inhibitors in crystallization processes that sometimes modify the morphologies or polymorphs of crystals and/or retard crystal growth rates works as an effective and simple way to investigate the crystal growth pathway. Much of the experimental work directed at understanding of this effect, and the emphasis has been on crystal habit modification.

In Chapter 3, we demonstrated a new mechanism of precipitation of calcium sulfate from solution, where calcium sulfate hemihydrate was precipitated as a precursor phase to gypsum[16]. This represented the first report of hemihydrate from a salt-free solution of calcium sulfate at room temperature. While this observation runs counter to previous studies which describe hemihydrate as an important metastable intermediary that is co-precipitated with anhydrite from salt-free solutions at temperatures above  $\approx 97$  °C, when its solubility product is exceeded[7, 36]. Further, we also observed precipitation of an amorphous calcium sulfate (ACS) phase prior to the hemihydrate in dilute solutions. This precipitation of gypsum *via* hemihydrate was subsequently confirmed by Van Driessche *et al.* who additionally observed that

this occurred by oriented aggregation of hemihydrate nanorods, and their subsequent transformation to gypsum[129].

To investigate this new precipitation mechanism of calcium sulfate further in salt-free bulk solution, we use soluble additives to control the precipitation of calcium sulfate, with the goal of stabilizing of the metastable polymorphs. While various additives have been widely used to inhibit the precipitation of calcium sulfate, and also to some extent to modify the morphology of gypsum, it is remarkable to note that no report has described of their ability to stabilize intermediate phases.

#### **4.1.1 Accelerators**

As calcium sulfate hemihydrate slurry is hydrated to form gypsum, the material gains strength and the strength of the plaster is dependent on the water-to-hemihydrate. Increasing density by reducing the water content provides a means to enhance the strength of gypsum. Therefore, high strength is achieved by adding to the gypsum only the amount of water needed for setting and crystallization (17 wt %) [158]. However, the challenge of many engineered materials is to optimize the strength and this involves controlling the rate of hydration or set time. Otherwise, the final gypsum composition material may lose a desired form before they harden sufficiently to hold a shape if the hydration rate is too slow. The most common accelerator is calcium sulfate dihydrate that has been finely ground, where the hydration rate increasing with a decrease in average particle size or increase in the specific surface area[159]. Many inorganic acids and their salts are also useful as accelerators, especially sulphuric acid and its salts. For example, potassium sulfate, increased the rate of the hydration reaction by increasing seeding and the rate of dissolution of calcium sulfate hemihydrate[160]. The effects of calcium hydroxide on the hydration of calcium sulfate hemihydrate in accelerated system was also investigated to generate microcrystalline dihydrate nuclei, resulted in a rapidly setting plaster with high strength[160, 161].The accelerating effect of these additives is due to an increase in solubility and the rate of dissolution of the calcined gypsum and to an increase in the rate of nuclei formation[135].

#### **4.1.2 Inhibitor**

In some industrial processes, gypsum deposition may have several disadvantages: gypsum may offer a resistance to the heat flow when it crystallized on heat transfer surfaces and they can accumulate in pipelines and other flow passages seriously impeding the process flow. Another technique to hinder or delay gypsum scale formation is the addition of inhibitor to the solution, which retards calcium sulfate formation. These additives can modify the shapes of the crystals, retard nucleation, growth rates, shape of the crystals and to control polymorphism.[42] The additives adsorbed onto the crystal growth sites thus altering the morphology of the growing crystals. This process prevents crystal growth or delays it for prolonged periods. Therefore, scale inhibition using additives is based on kinetic and not thermodynamic effects[162]. Over the years, different inhibitors have been developed and are extensively used as precipitation inhibitors for various sparingly soluble salts i.e., calcium carbonate, calcium phosphate, calcium sulfate, calcium fluoride and barium sulfate. Studies have shown that inhibitor performance strongly depends on polyelectrolyte architecture, molecular weight and ionic charge.

##### **4.1.2.1 Carboxyl groups(-COOH)**

A number of investigations have reported that the precipitation of calcium sulfate is significantly reduced in the presence of water soluble additives like organic acid and their salts, including polymers/copolymers with carboxyl groups(-COOH). Such as alginic acid, carboxy-methylcellulose, polyacrylic acid (PAA) and poly-methacrylic acid (PMA) were particular effective.[163, 164] It was also suggested that the additive acted as immobile impurities on the crystal surface, thus the crystal growth rate was inhibited by reducing the rate of step movement across the crystal surface. The additives can also prevent the coalescence of the small crystals during the crystallization process to increase the number of produced crystals. It was also noted that polymethacrylic acid showed much less activity than polyacrylic acid at the same concentration, because polyacrylic acid is a more flexible polymer molecule than polymethacrylic acid. And polymers with carboxyl groups on neighbouring atoms of the backbone chain may be more effective as inhibitors.[120] This prompted a study of a series of polyacrylic acid with different molecular weights [23]. The efficiency of the PAAs tested with respect to the threshold inhibition of

gypsum growth, decreased with increasing MW. It is possible that the low MW chains adsorb flat on the surface blocking the active sites of the critical nuclei which cannot grow further. With higher the MW polymers, the mode of adsorption may be such that the presence of loops and trains on the solid substrate do allow for a larger number of unblocked active sites.[132] In the presence of PAA, due to its retarded effect on the growth of [111] faces of gypsum crystals, more plate-like crystals were obtained compared with the precipitates from the same conditions but without additive. [23]

#### **4.1.2.2 Phosphonate**

Phosphonate, which are thought to achieve scale inhibition by absorbing onto specific crystallographic planes of a growing crystal nucleus after a nucleation event, are also a popular and effective inhibitor [29, 165, 166]. Some phosphorus compounds which contain ionisable phosphate group, such as phytic acid[167] and sodium hexametaphosphate[138] in aqueous solutions are shown to inhibit crystal growth and the spontaneous precipitation of gypsum. However, these compounds are not stable to hydrolysis at elevated temperatures which in turn may lead to the formation of hard calcium phosphate scale. In this case, organophosphorus additives which can increase thermal stability were also investigated with effectively inhibition of calcium carbonate formation.[14, 139] Normally, 1-hydroxyethylidene-1,1-diphosphonic acid (EHDP), nitrilotrimethylene phosphonic acid (NTMP) and N,N,N',N'-ethylene diaminetetramethylene phosphonic acid (ENTMP) were used as efficient inhibitors of calcium sulfate crystal growth.[137, 142, 143, 145] The morphology of calcium sulfate also changed with the adsorption of the organophosphorus compounds onto different gypsum crystal faces. Agglomeration of shorter and broader gypsum were formed in the presence of ENTMP, [N, N, N', N'-ethylene-diaminetetra (methylene phosphonic acid)] and TENTMP [N, N, N', N'-triethylenediamine -tetra (methylene phosphonic acid), while elongated prismatic crystals were obtained with addition of EHDP.[29, 168]

#### **4.1.2.3 Sulfonic acid (-SO<sub>3</sub>H)**

Sulfonic acid (-SO<sub>3</sub>H) and its salts are also used to prolong the induction period because they are nuclei poisons. Sulfonic anions may replace the sulfate ion in the

calcium sulfate lattice, thus enhancing the inhibiting capacity of the additive. It should be noted, however, additives such as poly(acrylic acid/sulfonic acid/sulfonated styrene) (PSA)[23] and poly(sodium 4-styrenesulfonate)(PSS)[169] contained hydrophobic sulfonate groups attached to the polymer chains. In general, the presence of the relatively lower affinity sulfonate groups have been reported to yield the poorer inhibition efficiency in comparison with the PAA.[152, 170] The morphology of gypsum appeared to be partial rosette and plate-like structures with PSS while all the crystals were observed to be rectangular in the presence of PAA in the same condition.[169]

#### **4.1.2.4 Surfactants**

Many studies have also been performed using low molecular weight species such as surface-active reagents. These always consist of two parts, the hydrophobic tail which is typically a long hydrocarbon chain and the hydrophilic head which is soluble in water or another polar solvent. The combined hydrophobic and hydrophilic moieties form aggregation such as micelles, where the hydrophobic tails form the core of the aggregate and the hydrophilic tails are in contact with the surrounding liquid. The compound is surface-active and is thus able to concentrate at the interface between a surfactant solution and a hydrophobic solvent. Sodium dodecyl sulfate (SDS) is an anionic surfactant which increased the induction time and decreased the growth efficiency of gypsum. The surface energy also decreased with compared with non-additive solution [42].

#### **4.1.2.5 Metal Ions**

Another effective method to modify the shapes of crystals, retard nucleation, and growth rates and to control polymorphism is the use of metal ions [171, 172]. For the processes in which gypsum was obtained as a by-product, crystallization solution carries a wide variety of impurities such as e.g.  $\text{Ca}^{2+}$ ,  $\text{Mg}^{2+}$ ,  $\text{Cr}^{3+}$ ,  $\text{Fe}^{2+}$ , and  $\text{Al}^{3+}$ . Addition of  $\text{Al}^{3+}$  ions up to 2% decreased the induction time and increased the growth efficiency while addition of  $\text{Mg}^{2+}$  increased the induction time and decreased the growth efficiency compared with additive-free solutions.  $\text{Mg}^{2+}$  can also decrease the crystal size.[173] In this case, magnesium ions decreased the amount of nuclei of

calcium sulfate by reducing the availability of sulfate ions for nucleus formation to form  $\text{MgSO}_4$  complexation.[174]

## **4.2 Aims**

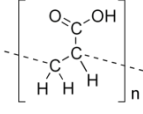
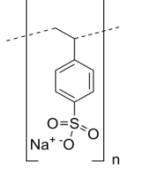
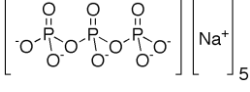
These studies of the effect of additives on gypsum nucleation can be carried out by evaluating the induction period. Our experiments here mentioned four additives, poly(acrylic acid) (PAA), poly(sodium-4-styrene sulfonate) (PSS), sodium triphosphate and magnesium chloride. The inhibition effect on gypsum precipitation and morphology described previously showed that all of these additives have significantly effects on the crystal size, morphology and polymorph. In this way we are also able to achieve both long-term (about 8 months) stabilization of calcium sulfate hemihydrate in solution in room temperature, and control over its size and morphology. With addition of both PAA and magnesium ions, morphological control over hemihydrate crystals, as achieved here, can also play a key role in definition of the properties of calcium-sulfate-based materials prepared from hemihydrate, such as porosity and mechanical strength[175].

## **4.3 Experimental**

### **4.3.1 Materials**

Calcium chloride and sodium sulfate solutions were prepared by dissolving  $\text{CaCl}_2 \cdot 2\text{H}_2\text{O}$  and  $\text{Na}_2\text{SO}_4$  (Sigma-Aldrich) in 18 M $\Omega$ /cm ultra-pure Millipore water. The additives poly(acrylic acid) (PAA, MW 8000), poly(sodium 4-styrene sulfonate) (PSS, MW 70,000), sodium triphosphate and  $\text{MgCl}_2 \cdot 6\text{H}_2\text{O}$  were also obtained from Sigma-Aldrich, and their chemical formulae, molecular weights and structures are shown in Table 1.

**Table 4.1** The additives used in the experiments

Acronym	Polymer	M.W.	Formula
<b>PAA</b>	Poly(acrylic acid)	8,000	
<b>PSS</b>	Poly(sodium-4-styrene sulfonate)	70,000	
<b>Phosphate</b>	Sodium triphosphate	367.86	
<b>MgCl<sub>2</sub> 6H<sub>2</sub>O</b>	Magnesium chloride Hexahydrate	203.3	MgCl <sub>2</sub> · 6H <sub>2</sub> O

#### 4.3.2 Precipitation of Calcium Sulfate

CaSO<sub>4</sub> was precipitated from aqueous solutions by the double decomposition method solutions by combination of equal volumes of 200 mM solutions of CaCl<sub>2</sub>·2H<sub>2</sub>O (pH ~6.64) and Na<sub>2</sub>SO<sub>4</sub> (pH ~6.68) in a crystallization dish under stirring to give a final concentration of 100 mM CaSO<sub>4</sub>. In the experiment done in the presence of polymeric inhibitors, PAA, PSS and sodium triphosphate, the additives were introduced into the sodium sulfate solution to avoid complexation[176], conformational changes[177], and even precipitation of calcium-polymer salts[178]. To avoid binding with SO<sub>4</sub><sup>2-</sup> ions, MgCl<sub>2</sub> 6H<sub>2</sub>O was added to the calcium chloride solution to prevent MgSO<sub>4</sub> precipitation. Calcium sulfate crystals were grown on cleaned glass slides (which were cleaned by Piranha solution over night, dried by nitrogen gas before rinsed by ethanol) or TEM grids.

The glass slides used to examine crystals with SEM were rinsed with ethanol to remove the residue solution and dried with nitrogen gas. These glass slides were left in a dried desiccator over night. TEM grids were dipped into calcium sulfate solution to collect precipitates and were analyzed under TEM. Precipitated crystals isolated by filtration (filter membrane with 200 nm pore size) were analyzed using XRD AA and Raman microscopy.

Recrystallization experiments were carried out by adding a droplet of water to dried precipitates and then placing them in humid atmosphere. The precipitates from early stages of calcium sulfate precipitation in the presence of PAA (amorphous phase of calcium sulfate) were heated up to 200 °C for about 4 hours. In this case, water was removed from amorphous phase to form crystals.

### **4.3.3 Characterization Methods**

The calcium sulfate precipitates were characterized using a range of techniques. Scanning Electron Microscopy (SEM) and Transmission Electron Microscopy (TEM) were used to determine the shapes and sizes of calcium sulfate precipitates. For SEM, the glass slides supporting calcium sulfate particles were mounted on SEM stubs using conducting carbon tape, and were then sputter-coated with 5 nm of Pt. Samples were examined using a Phillips XL-30 ESEM operating at 3 kV. TEM samples were prepared by dipping a carbon-coated Cu TEM grid into the reaction solution, rinsing with a 4:1 ethanol to water mixture, and then blotting with filter paper. Imaging and electron diffraction studies were performed using a Phillips Tecnai FEG-TEM operating at 200 kV, with associated Energy-Dispersive X-ray analysis (EDX). EDX was performed to determine the elemental composition and confirm the presence of sulfur and calcium. In addition to electron diffraction, polymorph characterization was carried out using Raman microscopy, Infra-red spectroscopy and powder X-ray diffraction (XRD), for which the precipitates were isolated by filtration through a 0.2 µm filter membrane, washing with ethanol and air-drying. Raman microscopy was carried out using a Renishaw 2000 Raman microscope operating with a 785 nm diode laser, while infra-red spectroscopy was carried out using a Perkin Elmer Spectrum 100 FTIR fitted with a diamond ATR. XRD was used to further confirm polymorph, and to determine the Mg-content of samples, and XRD data were collected between 10° and 60° in intervals of 0.02° and a scan rate of 0.05°/ minute. Finally, the Mg: Ca ratio in the calcium sulfate precipitated in the presence of magnesium, was also determined using atomic absorption spectroscopy (AA), with a Perkin-Elmer AA Analyst 400 spectrometer that had previously been calibrated using standard solutions (Aldrich).

## 4.4 Results

### 4.4.1 Precipitation of Calcium Sulfate in additive-free solution

The inhibition influence of a range of additives – poly (acrylic acid) (PAA), poly (sodium 4-styrene sulfonate) (PSS), sodium triphosphate and magnesium ions was explored, with the goal of gaining control over the precipitation of calcium sulfate crystal polymorphs and morphologies. Initial control experiments were performed in which calcium sulfate was precipitated from a 100 mM calcium sulfate solution, as used throughout, and results consistent with our previous studies were obtained[16]. The precipitates isolated after 30s were a combination of nanospheres 100-200 nm in diameter (Figure 4.1a) and 100-200 nm nanorods in length. After 1 minute, all the calcium sulfate precipitates were 200-300 nm nanorods (Figure 4.1b) Raman microscopy identified these nanorods after 1 min as calcium sulfate hemihydrate, where the lowest wavenumber peak at  $435\text{ cm}^{-1}$  ( $\nu_2$ ) provides a clear fingerprint for this polymorph (Figure 4.2a)[155]. The precipitates obtained after 1 hour, in contrast, were gypsum and exhibited characteristic morphologies of bundles of needles or plates 200-400  $\mu\text{m}$  in size (Figure 4.1c). The polymorph was characterized using Raman microscopy (Figure 4.2b) where the peaks at  $419\text{ cm}^{-1}$  ( $\nu_2$ ) and  $1139\text{ cm}^{-1}$  ( $\nu_3$ ) identified the dihydrate phase in the Raman measurements[155].

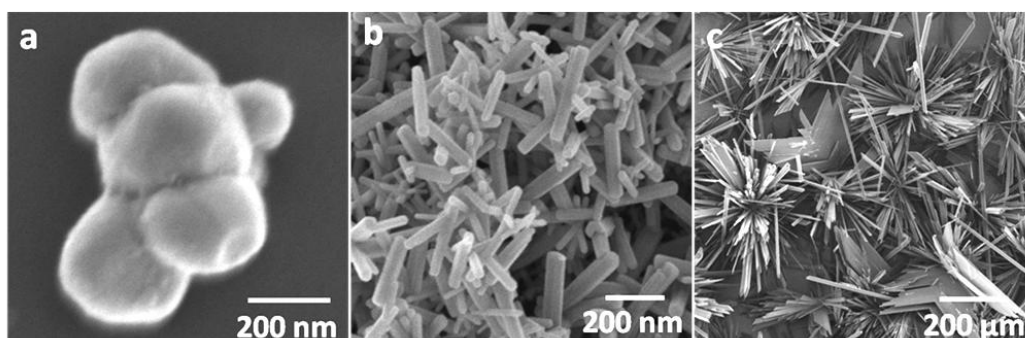


**Figure 4.1.** SEM images of calcium sulfate crystals precipitated from 10 mM solutions in the absence of additives after a) 30s, shown as a mixture of nanospheres and nanorods. b) 1min, shown as hemihydrate nanorods and c) 1 hour, where all crystals are gypsum in hundreds of micrometer size at the concentration of 100 mM without any additives

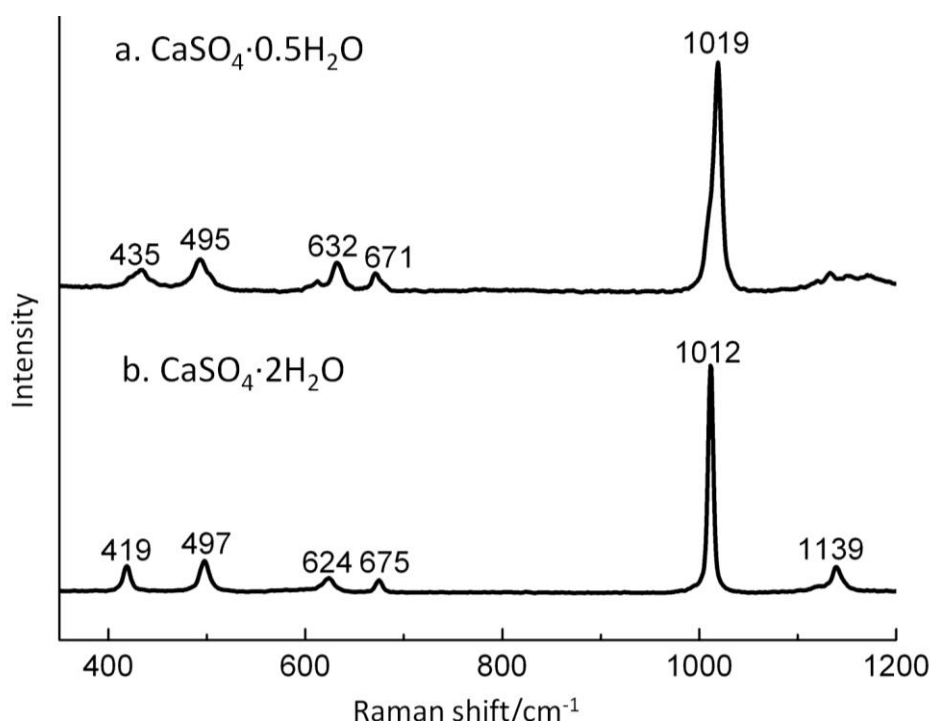


**Figure 4.2** Raman spectra of reference samples (a) calcium sulfate hemihydrate produced after 1 minute and (b) calcium sulfate dihydrate (gypsum) precipitated from a 100 mM solution and isolated after 1 hour.

#### 4.4.2 Precipitation of Calcium Sulfate in the Presence of PAA

Our previous work demonstrated that it is possible to extend the lifetime of hemihydrate in solution by reducing the supersaturation of the solution from which it precipitates[179], although this obviously comes at the price of the generation of less precipitate for a given volume of solution. We therefore explored the possibility of using additives to extend the lifetime of the hemihydrate phase, as well as to control the crystal size and morphology. Here, inhibition efficiency of PAA was investigated in the concentration range 50-3000  $\mu\text{g/ml}$ , and the precipitates were isolated after 1 hour.

Even at a polymer concentration of 50  $\mu\text{g/ml}$ , the strong interaction between the –COOH groups on PAA and the crystallizing CaSO<sub>4</sub> resulted in significant change in the crystal size, morphology and polymorph. After a reaction time of 1 hour, two distinct crystal morphological forms were observed. These comprised small rods (~200 nm in length) with rough surfaces, together with short gypsum particles(1-2  $\mu\text{m}$  in length).

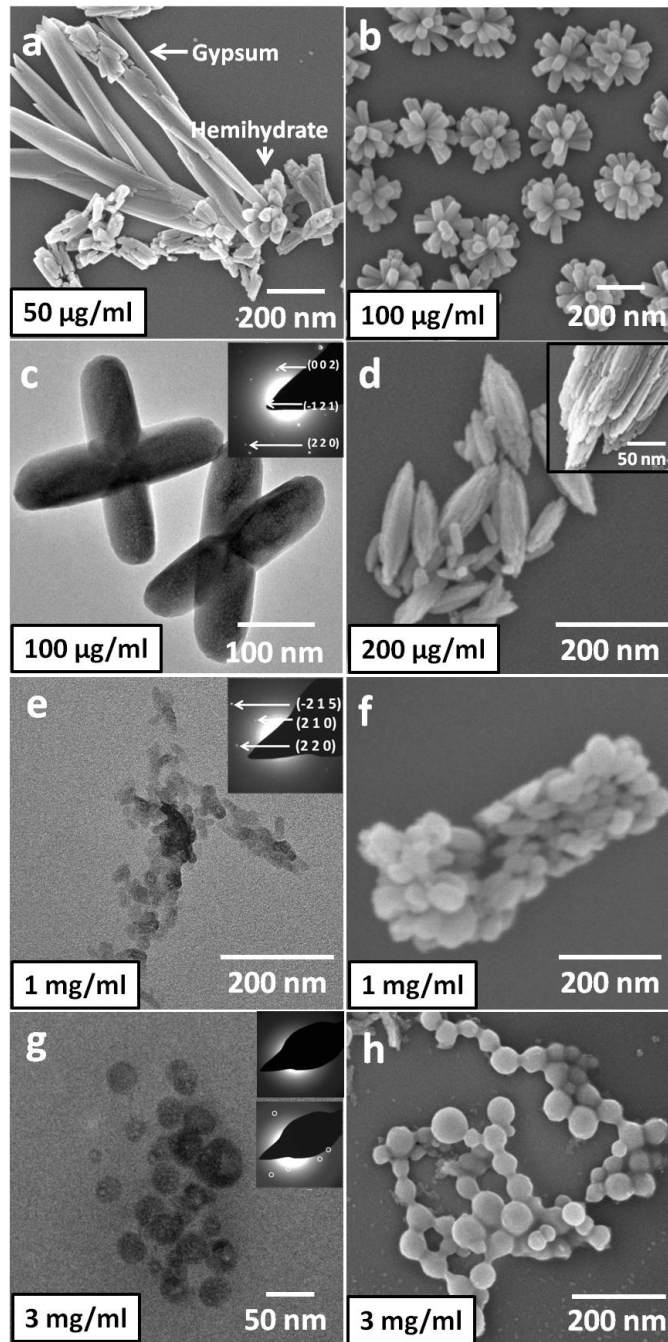


**Figure 4.3** SEM and TEM images, and electron diffraction patterns of calcium sulfate particles precipitated after 1 hour, in the presence of PAA of concentration (a) 50  $\mu\text{g/ml}$ , where both gypsum and hemihydrate are formed (inset shows the hemihydrate at higher magnification), (b) and (c) 100  $\mu\text{g/ml}$ , where pure hemihydrate forms, as shown by electron diffraction (inset), (d) 200  $\mu\text{g/ml}$ , where hemihydrate forms, (e) and (f) 1000  $\mu\text{g/ml}$ , where the hemihydrate consists of nanospheres and (g) and (h) 3000  $\mu\text{g/ml}$ , where amorphous spheres form. The inset in (g) shows that crystallization occurs on irradiation with the electron beam.

In the presence of additive, gypsum also loses the prismatic structure and transforms to rod-like crystals (Figure 4.3a). Characterization of these crystals using electron diffraction patterns showed the long rod crystals were still gypsum, while nanorods were hemihydrate (shown in Figure 4.4).

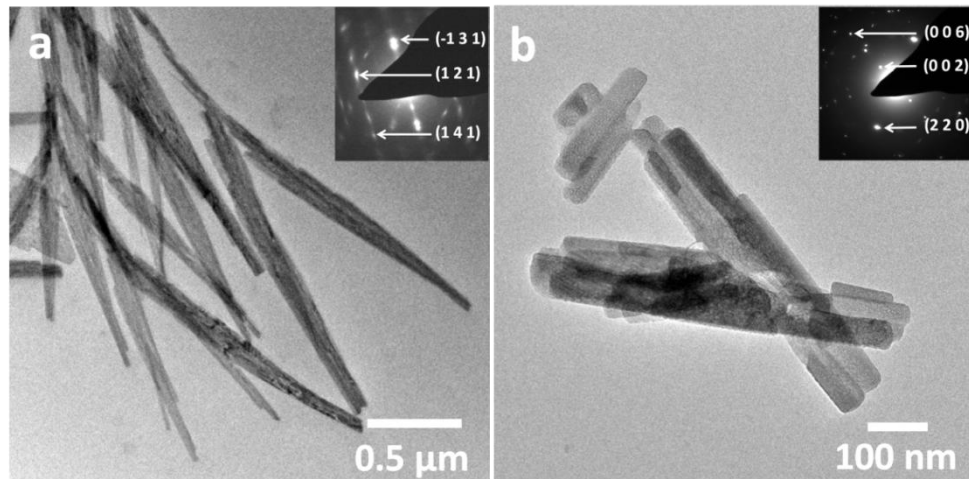


**Figure 4.4** TEM images of calcium sulfate crystals precipitated in the presence of 50  $\mu\text{g/ml}$  PAA after 1 hour. The precipitates were a combination of (a) gypsum and (b) hemihydrate.

With an increase in the PAA concentration to 100  $\mu\text{g/ml}$ , a large change in the crystals was observed with the unique production of 200-300 nm star-shaped aggregates of nanorods (Figures 4.3b). Analysis using electron diffraction (Figure 4.3c, inset) and Raman microscopy (Figure 4.5a) showed that these precipitates were calcium sulfate hemihydrate. These particles therefore present very different morphologies from the hemihydrate precipitated in the absence of additives, where the PAA clearly promotes aggregation of the hemihydrate nanorods.

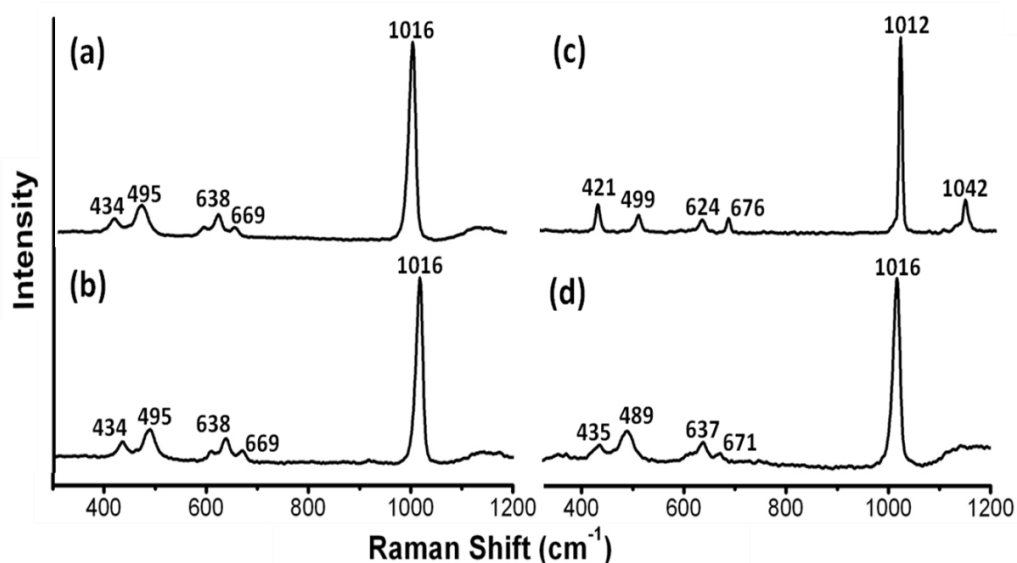


**Figure 4.5** Raman spectra of  $\text{CaSO}_4$  particles precipitated after 1 hour with addition of (a)  $100\mu\text{g/ml}$  PAA, as hemihydrate, (b)  $100\mu\text{g/ml}$  PSS, as gypsum, (c)  $200\text{ mM}$   $\text{MgCl}_2$ , as hemihydrate, and (d)  $100\mu\text{g/ml}$  phosphate, as hemihydrate.

The presence of water in gypsum can also be detected by its two characteristic absorption bands under infrared spectroscopy. It is clear from the absorption spectra of gypsum that the presence of two bands at  $1680$  and  $1620\text{ cm}^{-1}$  (bending vibration) are due to the presence of two types of water molecules in gypsum, loosely and strong held. The band  $1680\text{ cm}^{-1}$  is for loosely held water molecule, and the  $1620\text{ cm}^{-1}$  band arises from strongly held water molecules[180]. The two bands at  $3400$  and  $3540\text{ cm}^{-1}$  in gypsum are assigned as O-H stretching. When heating up to  $120\text{ }^\circ\text{C}$  for hours, the loosely bonded water was removed from gypsum. The strongly held water possesses the only bending vibration at  $1620\text{ cm}^{-1}$ , shown as hemihydrate (Fig 4.6b). In hemihydrate, there are less water molecules than in gypsum. In this case, the hydrogen bonding lowers the frequency and broadens the band in  $3600\text{ cm}^{-1}$  region.[181] Thus, the band  $3540\text{ cm}^{-1}$  in gypsum increased to  $3600\text{ cm}^{-1}$  in hemihydrate and the band  $3547\text{ cm}^{-1}$  in hemihydrate from  $3400\text{ cm}^{-1}$  in gypsum indicated the hydrogen bonding. Fig 4.6c showed the precipitates with addition of PAA  $100\mu\text{g/ml}$  after 1 hour. The single band  $3540\text{ cm}^{-1}$  indicated there was only strong held water in the system and the broadening band in  $3600\text{ cm}^{-1}$  region also shown as hemihydrate.

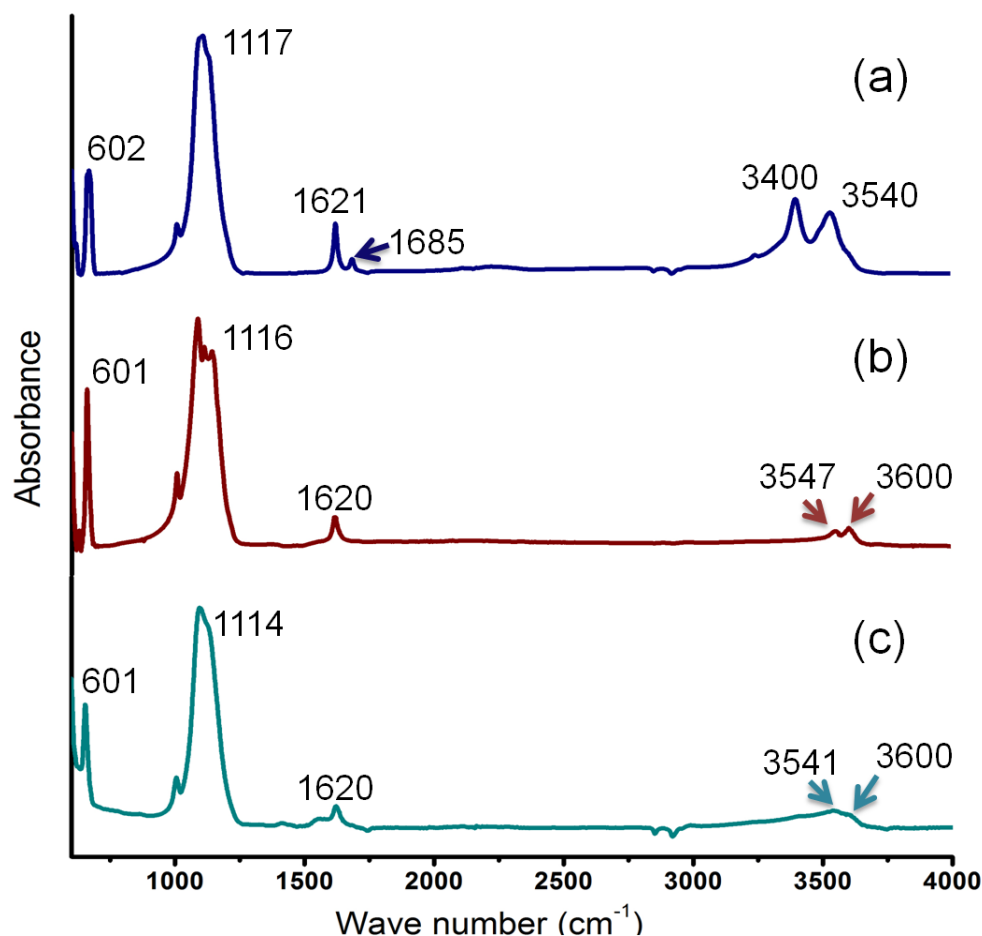


**Figure 4.6** IR spectra of CaSO<sub>4</sub> particles precipitated from 100 mM calcium sulfate solution (a) in the absence of additive after 1 hour, shown as gypsum, (b) sample from heating up gypsum at 120 °C for 8 hours, shown as hemihydrate and (c) in the presence of PAA 100µg/ml after 1 hour, shown as hemihydrate.

TGA analysis confirmed these precipitates from 100 mM additive-free calcium sulfate solution loses 21wt% on heating, which can match with the weight percent of water lose in gypsum. And the precipitates from 100 mM calcium sulfate with presence of PAA losing approximately 8.6 wt% on heating revealed the sample is consistent with hemihydrate (Fig 4.7b).

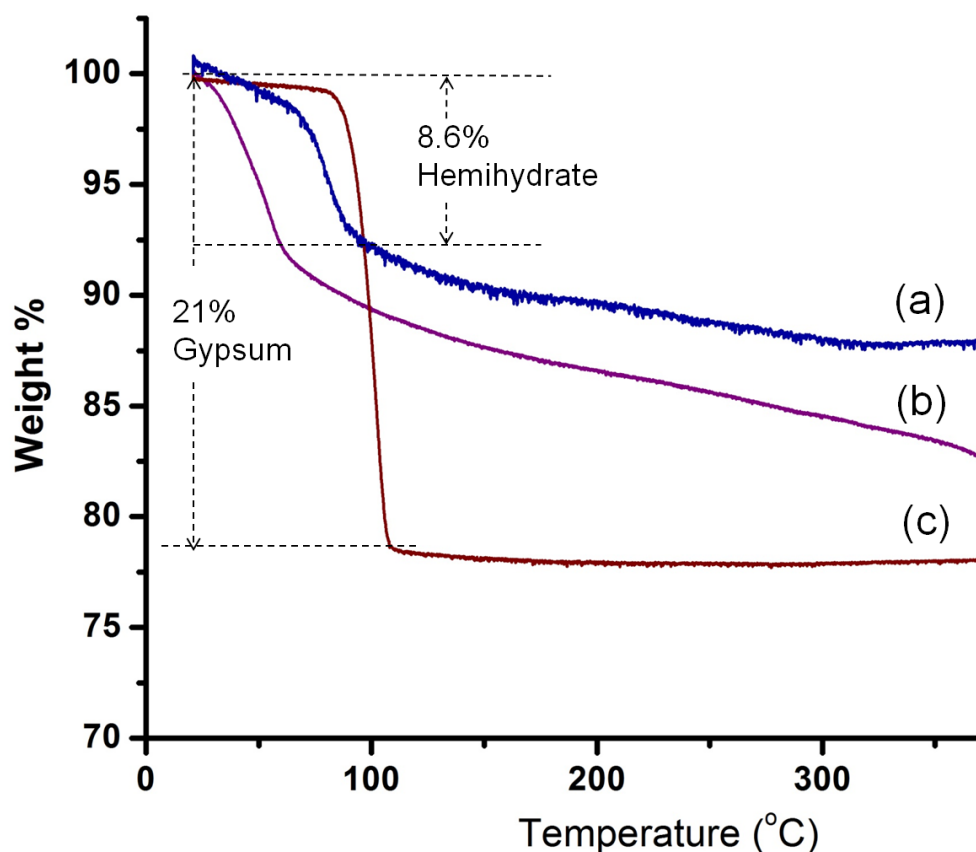


**Figure 4.7** TGA spectra of the precipitate isolated calcium sulfate 100mM solution after (a) approximately 1 minute, (b) 1 hour with presence of PAA 100  $\mu\text{g/ml}$  with losing 8.6 wt% on heating which is consistent with the sample comprising 84 mol% hemihydrate ( $\text{CaSO}_4 \cdot 0.5\text{H}_2\text{O}$ ). And (c) after 1 hour in the absence of PAA which shown as gypsum with losing 21wt% on heating.

In order to further explore the growth mechanism of calcium sulfate, typical powder X-ray diffraction spectra of the sample precipitated from 100 mM calcium sulfate solution with addition of PAA 100  $\mu\text{g/ml}$  after 1 hour. Fig4.8a-e are the references spectras and Fig 4.8f demonstrated that the main peaks with  $d$ -values around 14.724, 25.643, 29.695, 31.912 and 45.432 are hemihydrate which are comparable to the correspondly values of the relative intensity of (101), (301), (202), (141) and (600) in the reference hemihydrate (Fig 4.8b) and sample hemihydrate (Fig 4.8d and e).

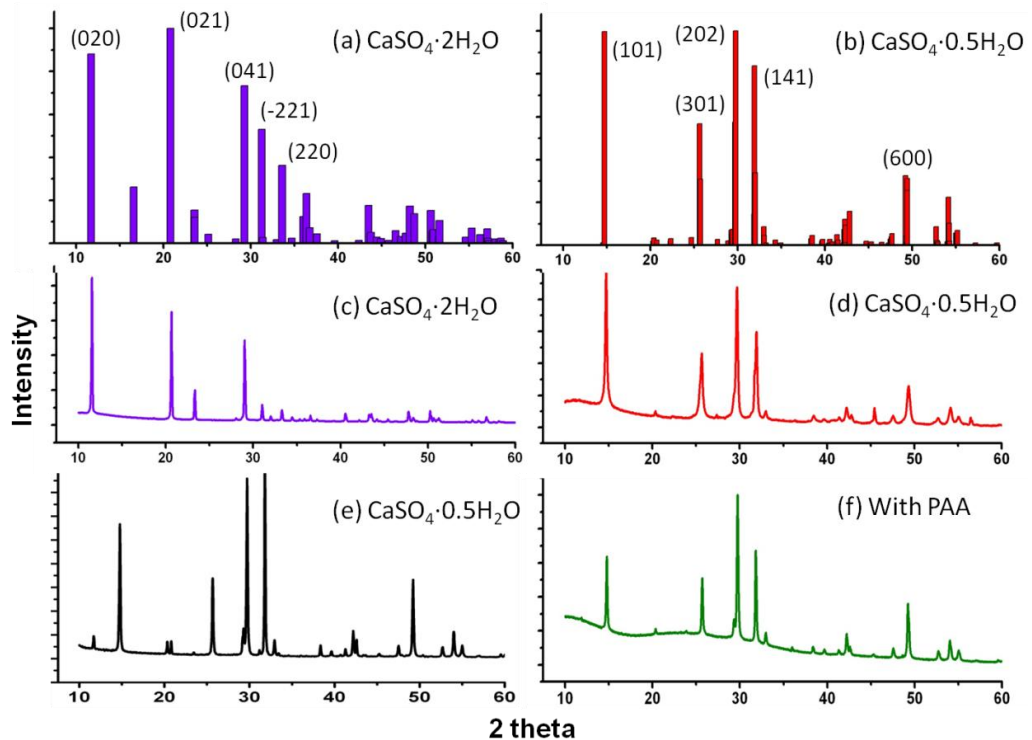


**Figure 4.8** XRD patterns of (a) a natural gypsum sample [182] and (b) Hemihydrate as reported in reference[154] (c) gypsum precipitated from a 100 mM solution after 1 hour, (d) calcium sulfate hemihydrate, produced by annealing gypsum at 120 °C for 10 hours, (e) hemihydrate precipitated from a supersaturated solution after 1 min in the absence of additives, and analysed after 1 hour, (f) hemihydrate precipitated in the presence of 100 µg/ml PAA, isolated after 1 hour, and analysed after 1 hour.

Calcium sulfate hemihydrate crystals was also observed at a PAA concentration of 200 µg/ml, although the morphology of these hemihydrate changed to spindle-shaped with rough surface (Figure 4.3d). Interestingly, many of the larger crystals appeared to comprise an oriented aggregate of smaller nanorods, giving the appearance of rough surfaces (Figure 4.3d, inset). A further change in crystal polymorph occurred with an increase in the additive concentration to 1000 µg/ml. Here, 40 nm hemihydrate nanorods which were aggregated of nanoparticles were produced (Figure 4.3e and f). These nanoparticles phase was finally confirmed at the highest additive concentration which employed of 3000 µg/ml. Amorphous spheres with diameters of 20-50 nm were produced after 1 hour (Figures 4.3g and 4.3h). Again, the corresponding TEM image (Figure 4.3g) showed the amorphous

character with no electron diffraction pattern (Figure 4.3g, insert, top) then confirmed by the development of crystallinity on heating under the electron beam (Figure 4.3g, inset, bottom).

#### **4.4.3 Effect of the reaction time in the presence of PAA**

In order to gain additional evidence for the formation mechanism of the complicated calcium sulfate morphologies obtained here, further insight into the mechanism of calcium sulfate precipitation from amorphous calcium sulfate to calcium sulfate hemihydrate and ultimately gypsum in the presence of PAA was obtained by isolating samples at different times during the reaction. Figure 4.9 shows SEM images of the precipitates present in a solution of composition 100 mM CaSO<sub>4</sub> with 200 µg/ml PAA, at times between 1 minute and 10 days. After 1 minute reaction time, when the solution was slightly opaque, but not obviously turbid, 10-30 nm nanospheres were observed (Figure 4.9a). These nanospheres were amorphous under electron diffractions (shown in Figure 4.9b) and the PAA stabilized them, such that these remained amorphous after irradiation by the electron beam for over 2 minutes. The amorphous calcium sulfate was therefore confirmed using EDX analysis, which showed Ca and S peaks (Figure 4.9b, inset), and by annealing the particles at 200 °C for 4 hours, after which time they crystallized to hemihydrate (Figure 4.9b, inset). After 30 mins, the longer reaction time resulted in the formation of hemihydrate nanorods approximately 100 nm in length (Figure 4.9c), as confirmed by electron diffraction (Figure 4.9d). Bundles of hemihydrate rods, where the rods were now almost half a micron in length (Figure 4.9e) were still observed in solution after 24 hours, consistent with remarkable stability in the presence of PAA. The transformation of hemihydrate to gypsum was observed after 2 days, when both hemihydrate and gypsum were identified in the solution (Figure 4.9f). As noted at 3 days (Figure 4.9g), the surface of the micron-rods sized becomes smoother when the nanorods appear to fuse. Transformation of these oriented aggregates to gypsum became apparent with incubation time. After 10 days, most of the crystals were gypsum particles which were covered by sponge-like mass of tiny crystals (Figure 4.9h). Here effect of the PAA could be seen in the morphology of the gypsum particles. These had round edges and rough surfaces which are not seen in additive-

free sample. These effects can be attributed to selective binding of the additives on crystal faces[183].

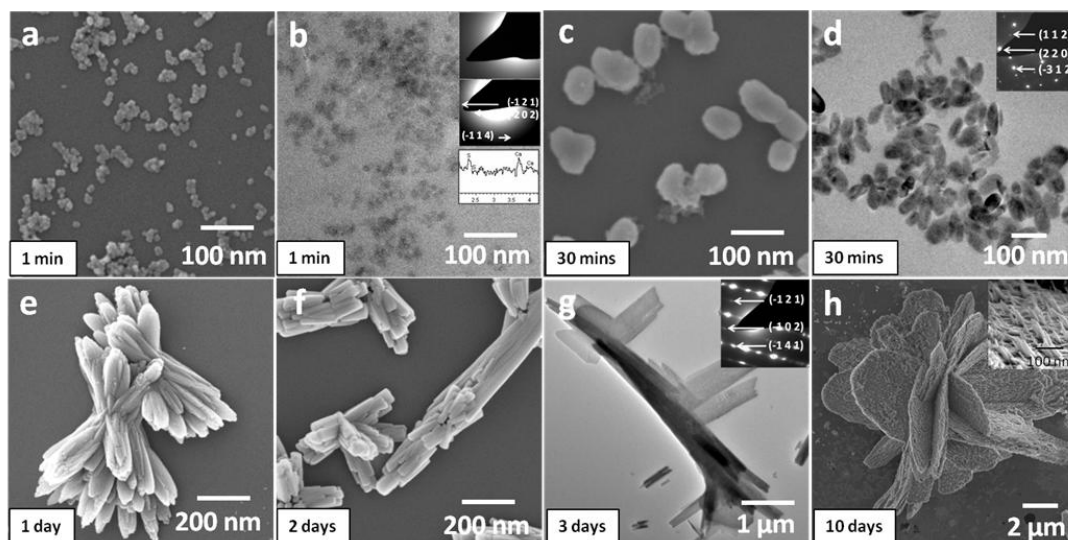


**Figure 4.9** SEM and TEM images and electron diffraction patterns of calcium sulfate crystals precipitated in the presence of 200  $\mu\text{g/ml}$  PAA after (a) and (b) 1 minute, where the insets in (b) show an EDX spectrum and electron diffraction patterns of the particles before and after heating. (c) and (d) show hemihydrate crystals after 30 mins reaction time, and their corresponding electron diffraction pattern, (e) 1 day, showing bundles of hemihydrate, (f) 2 days, showing a mixture of hemihydrate and gypsum, (g) 3 days, showing plate-like gypsum, and (h) 10 days, showing gypsum.

#### 4.4.4. Transformation of amorphous to crystalline phases

The transformation of amorphous calcium sulfate to calcium sulfate hemihydrate and ultimately gypsum was significantly retarded with addition of PAA which enables us to gain insight into the mechanisms by which these transformations occur. An aggregation of hemihydrate nanorods was formed in the presence of 200  $\mu\text{g/ml}$  PAA after 1 day. The aggregated calcium sulfate nanorods gave a rod-shaped particles, a few micrometers in length (Figure 4.10a). Despite their aggregated morphology, TEM and electron diffraction analysis showed that these micrometer sized particles were still hemihydrate (Figure 4.10b). More extensive aggregated particles were formed after 2 days, which appear as bundles of needles characteristic of gypsum. TEM showed, however, that these long needles were still hemihydrate

nanorods (Figure 4.10d). When the surface of these aggregated particles becomes smoother and the nanorods appear to fuse (Figure 4.10e), the transformation of these oriented hemihydrate nanorods to gypsum became apparent after 3 days. Some part of these orientated nanorods were still hemihydrate (Figure 4.10f).

It is also well known that calcium sulfate hemihydrate is the thermodynamically unstable form of the three crystal polymorphs of  $\text{CaSO}_4$ . Without any additives, the hemihydrate phase transforms into stable gypsum as an intermediate phase readily and irreversibly in solution, as mentioned in Chapter 3. Finally, the ability of PAA to stabilize hemihydrate was also investigated for dry samples left in air at room temperature. The hemihydrate precipitates with PAA 200  $\mu\text{g}/\text{ml}$  incubated in aqueous solution for 1 hour were filtered and washed with ethanol and then isolated precipitates were placed at room temperature. The precipitates of hemihydrate in the presence of PAA was stable in the air for at least 1 week; no evidence for the presence of gypsum was obtained from powder XRD or Raman spectroscopy. This can be contrast with hemihydrate precipitates in the absence of additives which started to transform to gypsum after just 1 hour. These results therefore provided evidence that the precipitation of calcium sulfate hemihydrate with PAA offers a highly efficient mechanism for retarding the crystallization of gypsum both in solution and in air.

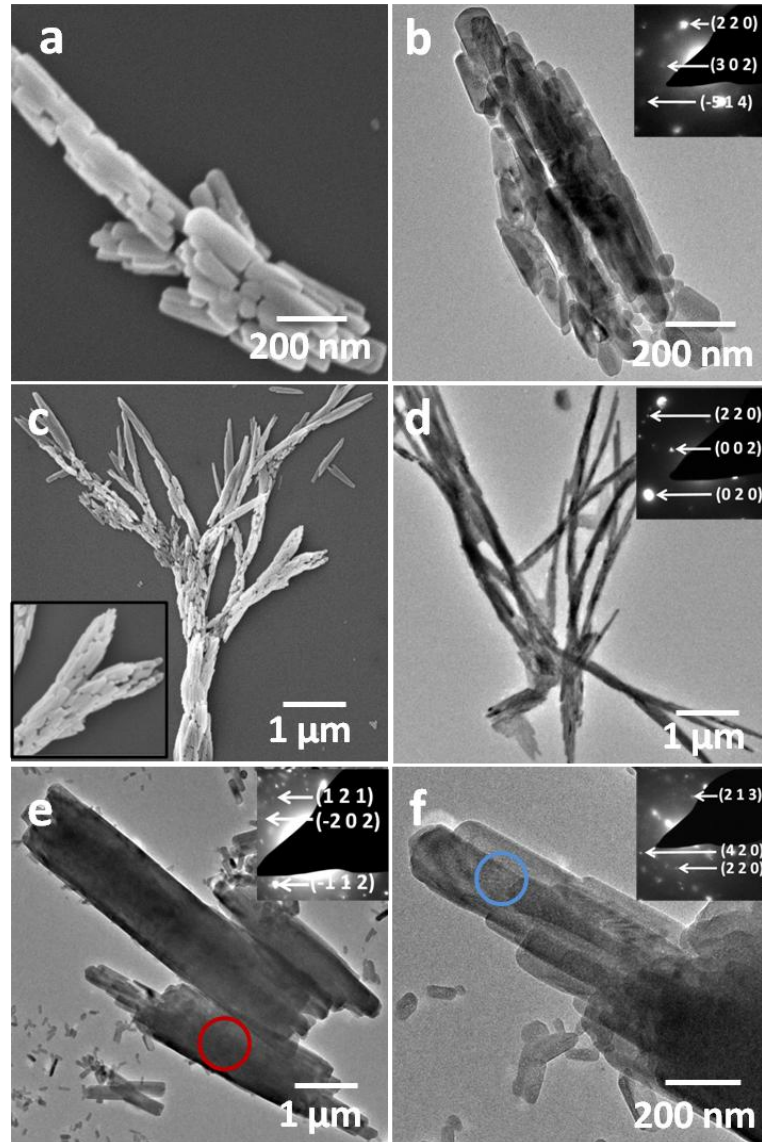


**Figure 4.10** SEM and TEM images, and electron diffraction patterns of calcium sulfate particles precipitated in the presence of 200 µg/ml PAA, and isolated after (a) and (b) 1 day, where the precipitates are hemihydrate, (c) and (d) 2 days, shown as hemihydrate and (e) and (f) 3 days, where the areas circled are gypsum (e) and hemihydrate in (f).

#### 4.4.5 Inhibition Efficiency of other Additives

The inhibitory effect of the additives, poly (styrene sulphonate) (PSS),  $\text{MgCl}_2 \cdot 6\text{H}_2\text{O}$  and sodium triphosphate were also investigated. SEM images presented in Fig 4.11 shows calcium sulfate precipitates obtained 100 mM calcium sulfate solution in the presence of water-soluble polymer PSS from a concentration of 100 µg/ml to 1

mg/ml and isolated after 1 hour. Similar to the case in which no additives were present, 30-50  $\mu\text{m}$  long monoclinic needle-like crystals of gypsum were principally produced. Addition of 100  $\mu\text{g/ml}$  PSS had relatively minor effects on the calcium sulfate precipitates, that only a small number of hemihydrate nanorods were obtained (Fig 4.11a, inserted). Polymorph confirmation was achieved using XRD (Figure 4.12b). Addition of 100  $\mu\text{g/ml}$  PSS indeed reduces the rate of crystal growth somewhat, but offers little stabilization of hemihydrate and has no effect on the morphology of the gypsum crystals. More stabilized hemihydrate was obtained with increase to 200  $\mu\text{g/ml}$  PSS. The precipitation was significantly suppressed in the presence of 500  $\mu\text{g/ml}$  of PSS and the hemihydrate was stable after 1 hour (Fig 4.11c). TEM showed all the precipitates were hemihydrate with addition of 1 mg/ml PSS (Fig 4.11d).

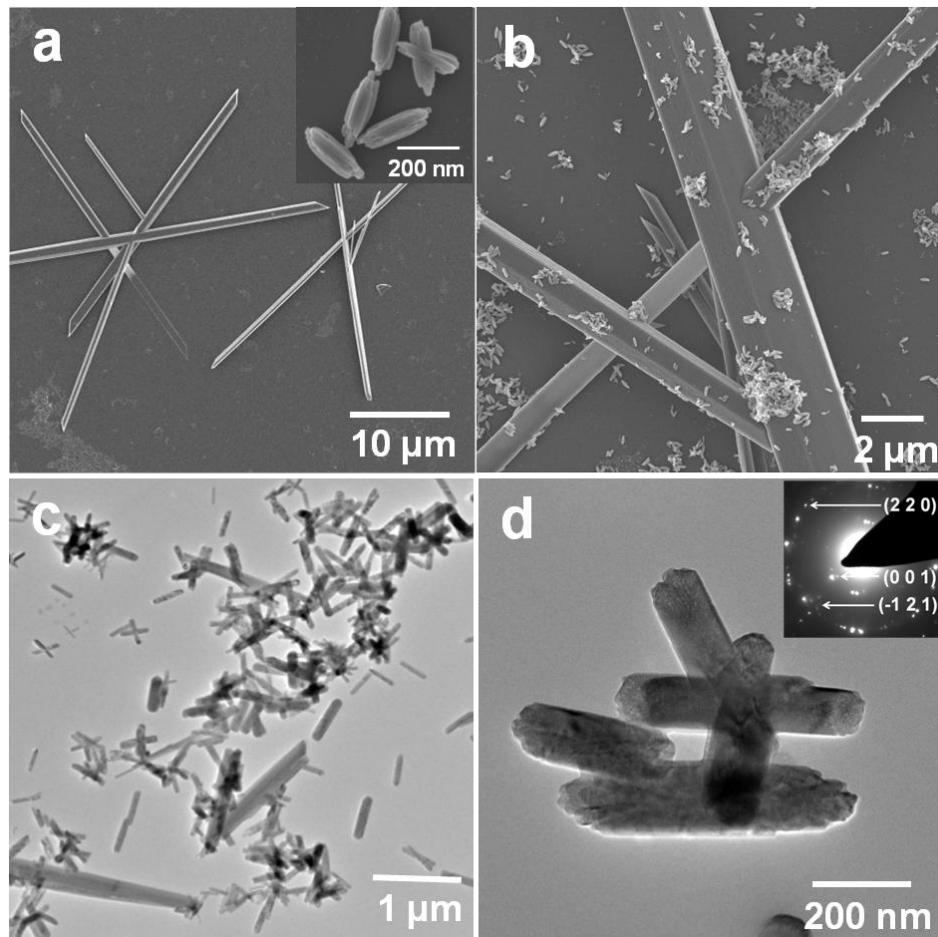


**Figure. 4.11** Scanning electron micrographs of calcium sulfate crystals precipitated spontaneously at the final concentration of 100 mM after 1 hour, 25 °C; (a) with addition of PSS 100 µg/ml, most crystals are gypsum (b) 200 µg/ml, hemihydrate can be observed with micro-sized gypsum (c) 500 µg/ml, mixture of hemihydrate and gypsum (d) 1 mg/ml, all crystals are hemihydrate.

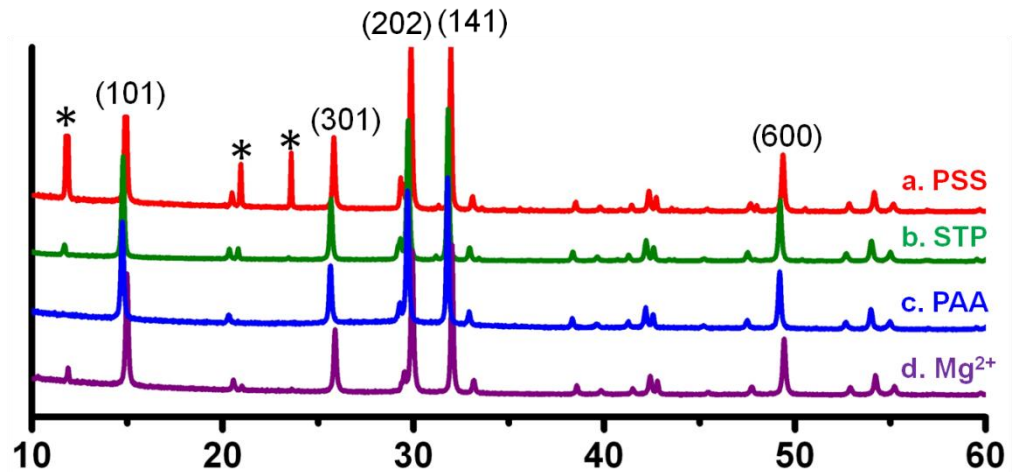


**Figure 4.12** The XRD patterns of calcium sulfate particles precipitated in the presence of (a) PSS 100µg/ml, shown as mixture of hemihydrate and gypsum, \* showed the peaks from gypsum (b) 100µg/ml sodium triphosphonate, (c) PAA 100µg/ml, and (d) 200 mM MgCl<sub>2</sub> 6H<sub>2</sub>O, shown as hemihydrate.

Varies concentrations of sodium triphosphonate were tested from 10-100 µg/ml as phosphate-based compounds are widely used industrially as effective inhibitors of gypsum precipitation. At 10 µg/ml phosphonate, most of the crystals were still gypsum, but with shorter crystal length than the sample without inhibitions. When the concentration increased to 20 µg/ml, all crystals were hemihydrate, 200-500 nm in length (Fig 4.13a). 100-200 nm hemihydrate nanorods were obtained with addition of phosphonate 50 µg/ml (Fig 4.13b). Amorphous calcium sulfate can be observed very clearly with addition of 100 gm/ml sodium triphosphonate after 1 hour. Loose aggregates of uniform nano-spheres around 20 nm were obtained (Fig 4.13d), together with short nanorods 50-80 nm in length, with flat, smooth surfaces (Fig 4.13c). The calcium sulfate precipitates of nano-spheres and nanorods were investigated with Raman microscopy (Fig 4.5d) and XRD (Fig 4.13b) showed that

they were hemihydrate. As shown using electron diffraction, these nanospheres were amorphous phase, while EXD patterns confirmed the presence of Ca and S (Fig 4.14, insert). These amorphous nanoparticles were extremely stable and remained the amorphous phase after 2 mins irradiated under the electron beam. Crystallization to hemihydrate occurs after heating the amorphous phase to 200 °C for 4 hours (Figure 4.14c).

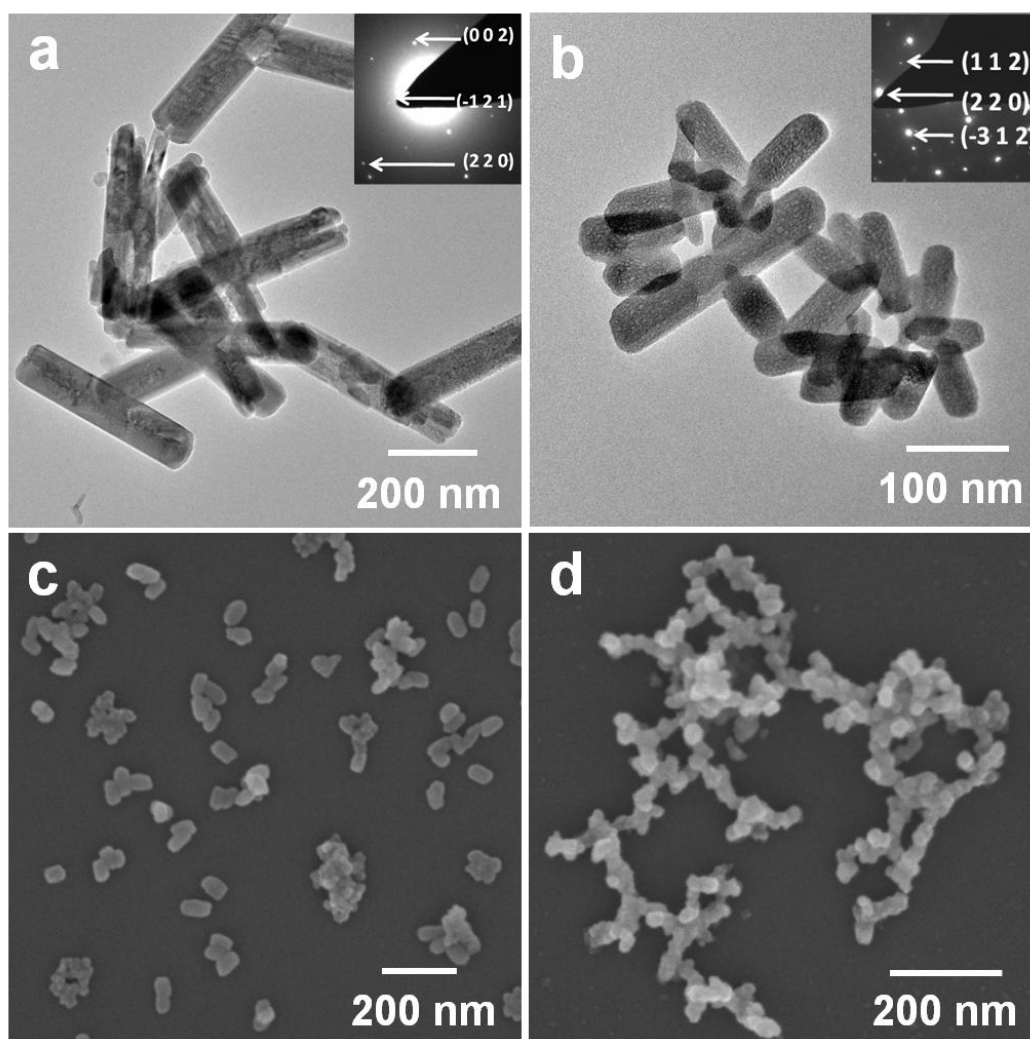


**Fig. 4.13** Scanning electron micrographs and TEM of calcium sulfate crystals precipitated spontaneously at the final concentration of 100 mM after 1 hour, 25 °C; with addition of phosphonate (a) 20 µg/ml, all crystals were hemihydrate, 200-500 nm in length, (b) 50 µg/ml, small size of hemihydrate, 100-200 nm in length; (c) and (d) 100 µg/ml, shows a mixture of hemihydrate (c) and amorphous phase (d).

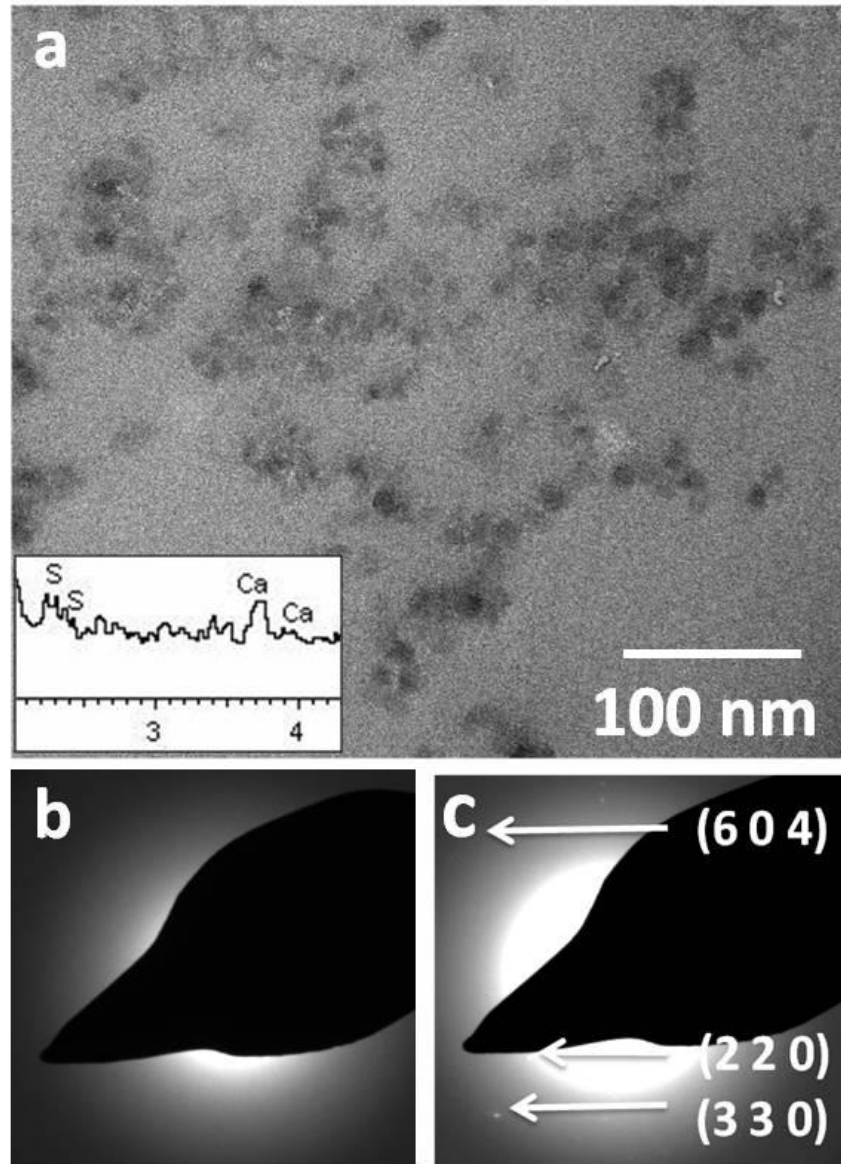


**Figure 4.14**  $\text{CaSO}_4$  particles precipitated in the presence of 100  $\mu\text{g}/\text{ml}$  sodium triphosphonate, and isolated after 1 hour (a) TEM image of amorphous particles, where the inset shows the corresponding EDX spectrum with Ca and S peaks. (b) A selected area electron diffraction pattern of this sample, showing that it is amorphous. (c) After heating the sample to 200 °C for 4 hour, the sample crystallises to  $\text{CaSO}_4$  hemihydrate.

To understand the effect of  $\text{Mg}^{2+}$  ions on the crystallization of calcium sulfate precipitates, different concentrations of  $\text{MgCl}_2 \cdot 6\text{H}_2\text{O}$  were used to investigate its inhibition efficiency. At ratio of  $\text{Mg}^{2+}/\text{Ca}^{2+} = 1:1$ , after 1 hour reaction time, the mixed solution is still clear, in comparison to cloudy solution without additive.

Under SEM, all crystals were about 200 nm in length (Fig 4.15a) and most formed rosettes of nanorods. This method provides an economical way to decrease the crystal growth rate to form fine, nanorods in industry. Interestingly, the crystal mean size was found to decrease with increased  $Mg^{2+}$  concentration. At the ratio of  $Mg^{2+}/Ca^{2+} = 2:1$ , shown in Fig 4.15b, the size of the clusters of nanorods decreased nearly to 100 nm in length. Both Raman spectroscopy (Figure 4.5c) and XRD (Figure 4.12d) confirmed that these rosettes were hemihydrate, stabilized in the presence of  $Mg^{2+}$ . The stability of these hemihydrate nanorods in solution was investigated after 1 day (Fig 4.16a) that the transformation to gypsum started and was completed after 3 days (Fig 4.16b). The amount of Mg substituted in the lattice of calcium sulfate precipitates was also determined by atomic absorption spectroscopy (AA). Samples for analysis were isolated after 1 hour from mixed solution. The molar percentage of Mg in the calcium sulfate hemihydrate lattice was 1.2 mol%, which is much higher than gypsum precipitates collected under the same conditions after 24 hours, the 0.40 mol%. Interestingly, the  $d$ -spacings in the XRD spectrum of the hemihydrate decreased with addition of  $Mg^{2+}$  (Fig 4.17d), while no change was observed for the corresponding gypsum sample with addition of  $Mg^{2+}$ . In the presence of PAA, PSS or triphosphate, in either hemihydrate or gypsum precipitated, no change in  $d$ -spacings were observed (Fig 4.17). According to the literature the foreign ion may either occupy interstitial positions among the structural water molecules, or form a normal solid solution[184]. The results are therefore consistent with the previous research that shows that only limited incorporation of  $Mg^{2+}$  ions occurs into hemihydrate.

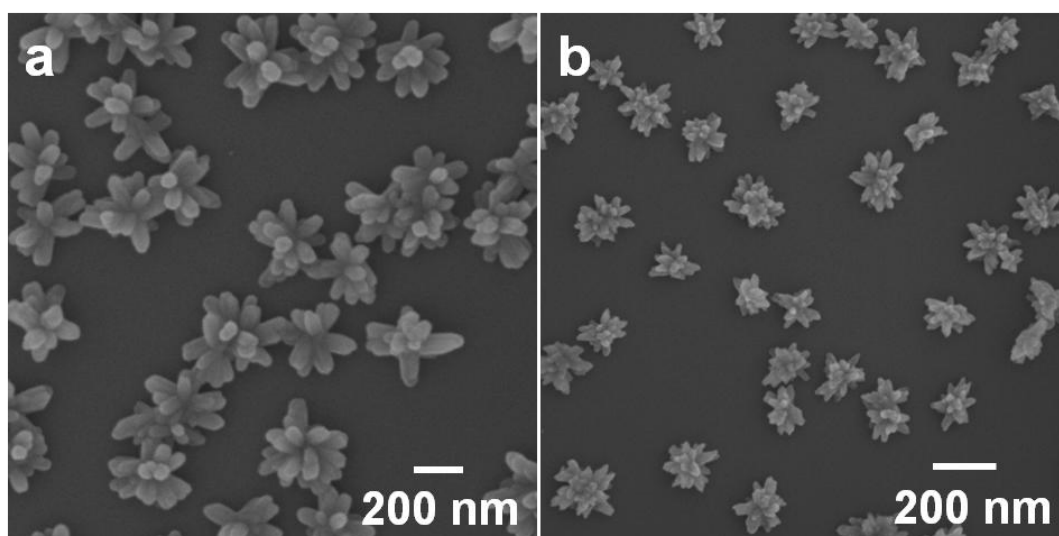


**Fig. 4.15** Scanning electron micrographs of 100 mM calcium sulfate crystals precipitated spontaneously after 1 hour, 25 °C; (a) with addition of MgCl<sub>2</sub> 100 mM, all crystals were hemihydrate, ~200nm in length, (b) with addition of MgCl<sub>2</sub> 200 mM, small size of hemihydrate, ~100 nm in length.

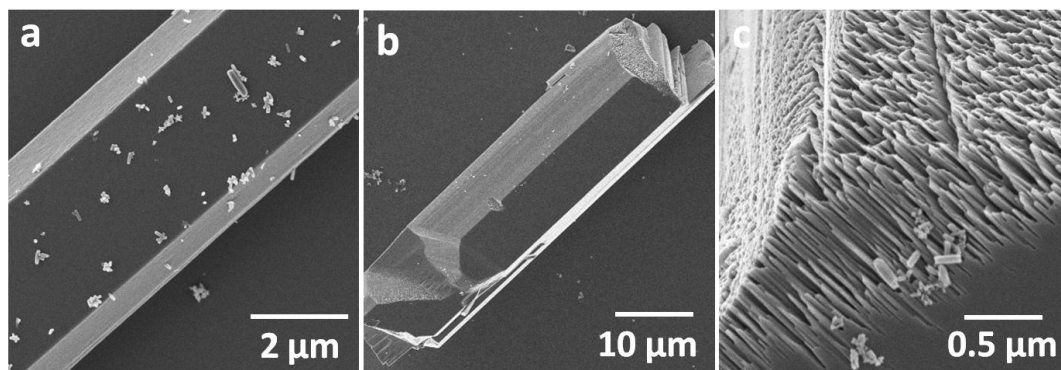


**Figure 4.16:** Scanning electron micrographs of calcium sulfate crystals precipitated spontaneously at the final concentration of 100 mM with addition of Mg<sup>2+</sup> 200 mM, 25 °C, after (a) 1 day, some areas start to transform to gypsum. (b) 3 days, typical gypsum with smooth surface, 50μm in length (c) higher magnification of Fig b.

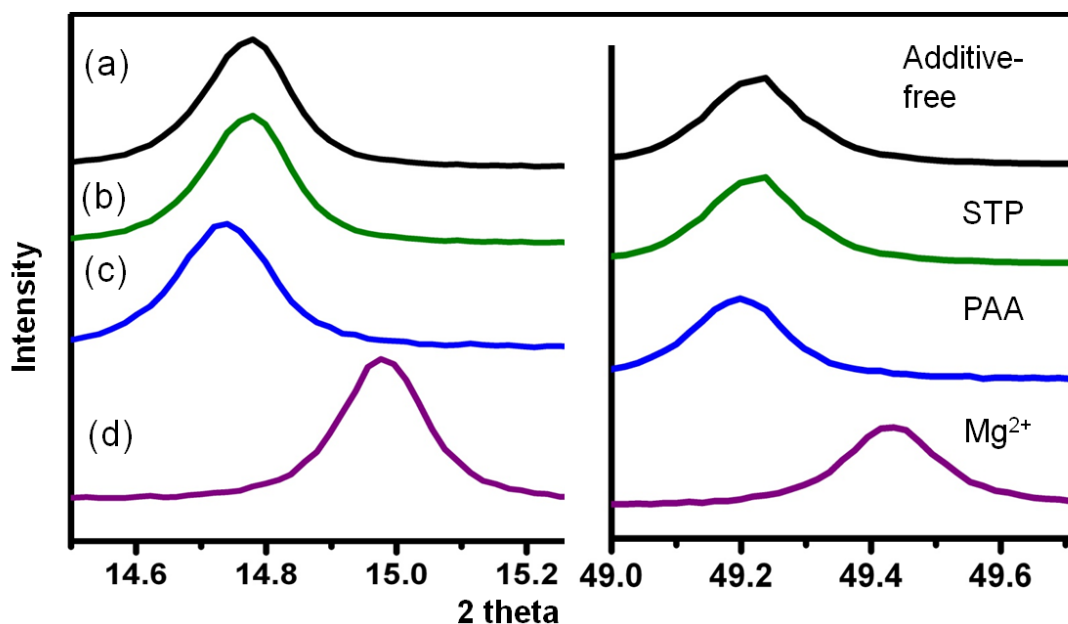


**Figure 4.17** X-ray diffraction patterns of calcium sulfate hemihydrate precipitates (a) from additive-free solution, (b) with 100 μg/ml of sodium triphosphate (STP), (c) 100 μg/ml PAA and (d) 200 mM Mg<sup>2+</sup>.

Finally, addition of both PAA and  $\text{Mg}^{2+}$  was explored as a route to control over the crystal polymorph and morphology. Fig 4.18 shows SEM images of calcium sulfate hemihydrate precipitates in the presence of 100  $\mu\text{g/ml}$  PAA and 200  $\text{mM}$   $\text{Mg}^{2+}$  after 1 hour, where the particles display characteristic morphologies from both additives. The shapes of all the precipitates in this case are based on bundles of hemihydrate nanorods. These nanoparticles are stable as was observed with PAA and also become rounded with rough surface, as reflects the influence of the  $\text{Mg}^{2+}$  ions.

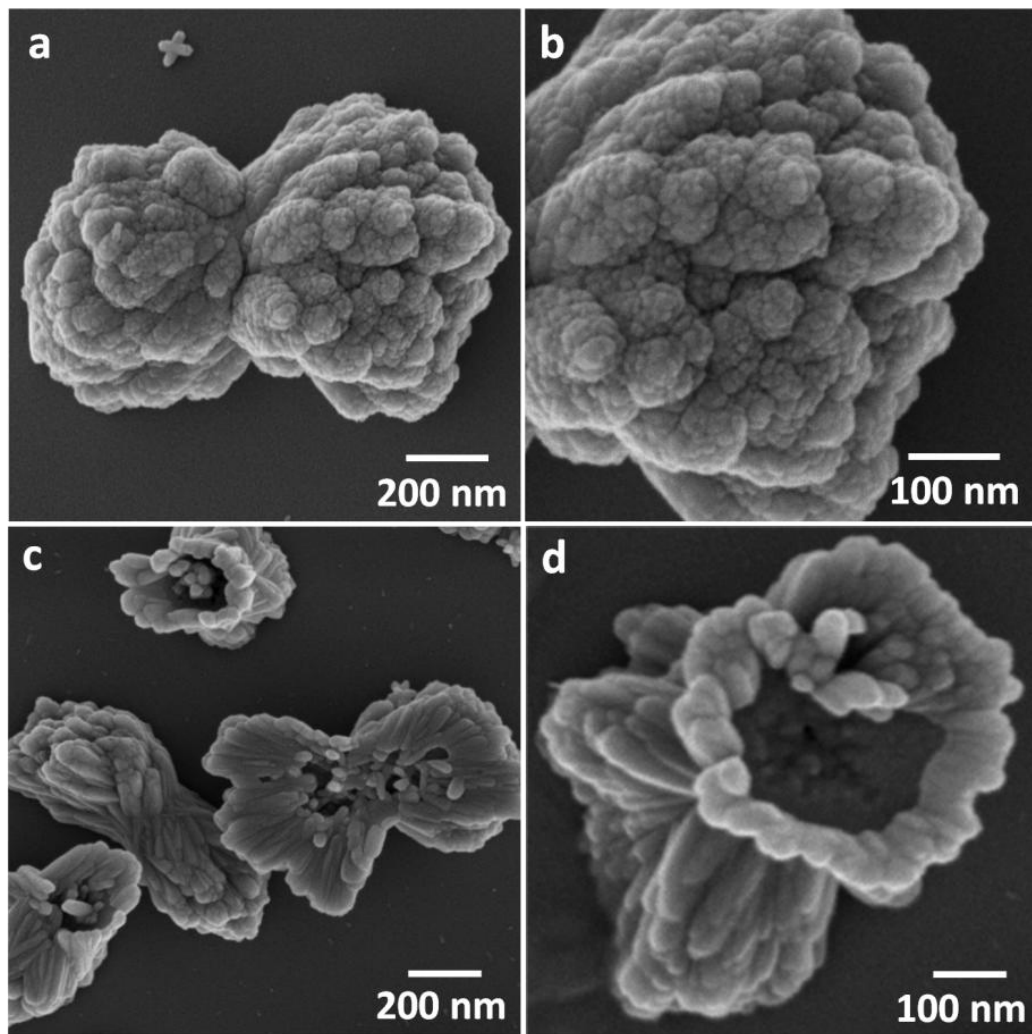


**Figure 4.18** SEM images of calcium sulfate hemihydrate formed in the presence of 100 $\mu\text{g/ml}$  PAA and 200  $\text{mM}$   $\text{Mg}^{2+}$  after 1h.

## 4.5 Discussion

The inhibitory effect of additives on  $\text{CaSO}_4$  nucleation and growth can be attributed to adsorption of the additives on developing nuclei and the crystal surfaces. The early stages, such as amorphous calcium sulfate (ACS) and hemihydrate, were successfully produced and stabilized in the presence of PAA and triphosphate at the room temperature, and the formation of gypsum inhibited. With addition of 100  $\mu\text{g/ml}$  PAA or 20  $\mu\text{g/ml}$  triphosphate, hemihydrate was still stable in solution after 1 hour, as compared with full conversion to gypsum at this time in the absence of additives. Magnesium at a 2:1 Mg:Ca ratio also stabilized hemihydrate and inhibited gypsum formation while PSS was notably less effective at comparable concentrations. To enable direct comparison of the effect of these additives, 100  $\mu\text{g/ml}$  is equivalent to a concentration of 1.4 mM carboxylate groups in PAA, 0.8 mM phosphate groups in triphosphate and 0.5 mM sulphonate groups in PSS. Significantly higher concentrations of magnesium ions are therefore required to stabilize hemihydrate as compared with the soluble organic additives, of which triphosphate is by far the most effective.

The inhibition of calcium sulfate crystal growth with addition of PAA can be explained by the Cabrera and Vermilyea model [185]. In this model, impurities can strongly adsorb onto terraces on crystal surfaces and “pin” steps. During the induction period, most of the active growth sites can be poisoned by the additive molecules/ions. Thus, the step movement and hence growth rate, would be very low or halted. The induction time and early stages of precipitation of calcium sulfate were investigated in the presence of different amount of polymers, and as expected, the inhibition efficiency improved with increased PAA concentrations. With the addition of PAA at a concentration of 200 $\mu\text{g/ml}$ , in the supersaturated solution, after 1 hour, there were still amorphous phase and hemihydrate was stable for at least 1 day. Here the PAA inhibition efficiency provides further evidence that hemihydrate is the precursor phase of gypsum. Without any additives, the hemihydrate phase rapidly transforms into stable gypsum.[16] The results presented here show that PAA exhibited a strong stabilizing effect and retarded this phase transformation. The XRD spectra showed that the intensity of the (101) peak in hemihydrate became

weaker than normal. It is thus possible that carboxylic groups were preferentially adsorbed on the (101) face, driving the formation of rod-shaped crystals (Fig 4.8f).

In comparison with PAA ( $M_w = 8,000$ ), PSS is less effective at the same concentration. Part of the difference in the effectiveness may be due to the higher molecular weight of PSS ( $M_w = 70,000$ ). The higher molecular weight polymer may adsorb as loops on crystal surfaces, which may not bind efficiently to active sites. A further point of difference is that PSS contains hydrophobic phenyl groups attached to the polymer chain. In general, the polymers which contain hydrophilic groups, like carboxyl groups on neighbouring atoms of the backbone, are more efficient inhibitors. The presence of the phenyl group may, therefore, explain the weaker inhibitory effect as compared with PAA. It should be noted, however, that sulfonic anions are present in PSS molecules. These sulfonic anions may replace the sulfate groups in the calcium sulfate lattice, and thus inhibit the formation of calcium sulfate crystals. However, it was found that PSS did not perform better than the PAA polymers, which contain carboxylate groups. It may therefore be suggested that the presence of hydrophobic groups in PSS affects the conformation of the polymeric chains[23].

An alternative model for inhibition is based on preferential adsorption of inhibitor ions on the surface of nuclei. The nuclei remain subcritical and disappear if the inhibitor ions are rapidly adsorbed. The inhibitor ions are then available for repeated adsorption at the edges of newly developing nuclei.[186] Phosphonate inhibitors are relatively small, molecular compounds. It is generally accepted that small inhibitors are preferentially adsorbed to active growth sites which are provided by steps, originating from two dimensional surface nucleation and by kink sites in the steps. For large macromolecular additives, the occupied surface area is largely dependent on their effective number of bonding possibilities. To make optimum use of, e.g. PAA bonding possibilities, relatively few inhibitor ions will be required for growth blockage in comparison with the required number of phosphonate inhibitor ions. It is inevitable that the polyacrylic ions partly extend in loops and tails into the surrounding solution, even in the case of a flat configuration upon the surface. However, it seems unlikely that PAA inhibitor ions can preferentially be absorbed

along the steps because of the entropy loss involved in such an arrangement. Even if the PAA were randomly adsorbed, the final results of PAA and Phosphonate would be the same, and the step propagation will be blocked as soon as the advancing steps are covered by adsorbed inhibitor molecules[187].

The influence of  $Mg^{2+}$  ions on the precipitation of gypsum has also been studied in this chapter. The precipitation of calcium sulfate nanoparticles (probably as hemihydrate, although this was not confirmed in the paper) at 90 °C in the presence of  $Mg^{2+}$  ions was inhibited,[188] where this was dependent on the concentration of  $Mg^{2+}$ . At low to moderate concentrations of magnesium, the  $Mg^{2+}$  ions adsorb to and poison active growth sites. As the concentration of  $Mg^{2+}$  was increased, crystallization could be promoted at sufficiently high magnesium concentrations, as indicated by a reduced induction period. It is noted that the acceleration effect at high concentration of  $Mg^{2+}$  ions is attributed to the higher hydration energy of  $Mg^{2+}$  than  $Ca^{2+}$ . [189] As  $Mg^{2+}$  ions have significantly higher hydration energies than  $Ca^{2+}$  ions, and at sufficient concentrations they may be able to compete with water on incoming  $Ca^{2+}$  ions and on the mineral surface, favouring attachment of lattice ions.

The results discussed above show that the induction time increased and the crystal growth rate of calcium sulfate decreased with addition of inhibitors. In the calcium sulfate solution, all these adsorbed impurities would lower the rate of transport from the solution to some extent. In the limit of complete surface coverage, diffusion through the adsorbed film could become the rate-controlling process.[163] Similarly, in our experiment, the surface diffusion would be retarded by the presence of inhibitors in the adsorbed layer, especially by inhibitor molecules strongly adsorbed on the nuclei or the crystal surface.

Notably, the effect of additives on the crystallization of gypsum from hemihydrate has been studied for years. However, there has been no report of the fact that these additives can stabilize the intermediate calcium sulfate hemihydrate phase on precipitation from solution at room temperature. One report mentioned that precipitation of both hemihydrate and gypsum in calcium sulfate solution occurs with addition of poly(acrylate) at 100 °C, where the higher temperature stabilizes

hemihydrate [190]. In order to find effective inhibitors, it is also noted that the vast majority of experiments aimed to explain the influence of the selected additives on induction times and growth rates.[166, 189, 191, 192] Measurement of the crystallization progress was typically achieved by measuring, for example, changes in conductivity during precipitation, and the precipitates at each of stages were then characterized. The whole precipitation process was monitored within a time frame from several minutes to hours. Lower concentration of additives were also used to decrease the reaction time.

It was investigated by monitoring the changes in conductivity accompanying calcium sulfate precipitation, in a 100 mM  $\text{CaSO}_4$  solution containing 5  $\mu\text{g/ml}$  PAA, and extracting samples for analysis at key points along the reaction (Fig 4.19). In the absence of PAA, the reaction proceeded rapidly with the conductivity decreasing rapidly after approximately 2 mins and reaching completion after about 16 mins (Fig 4.19, solid line). By comparison with the reaction with PAA, the conductivity decreased very slow during the first 25 mins. Then there was a rapidly decrease of the conductivity, at the similar rate to that in the additive-free solution at a comparable stage of the reaction. In the first 15 mins, TEM and electron diffraction analysis showed that the precipitates in this stage were uniquely hemihydrate nanorods, 200-300 nm in length (Fig 4.19a). During the rapid drop in conductivity, the precipitates extracted after 26 mins were a mixture of hemihydrate nanorods and gypsum needles a few microns in length (Fig 4.19b). After the full completion of the reaction, when the conductivity was approaching its minimum value, the vast majority of the precipitates extracted after 50 minutes were gypsum (Fig 4.19c).

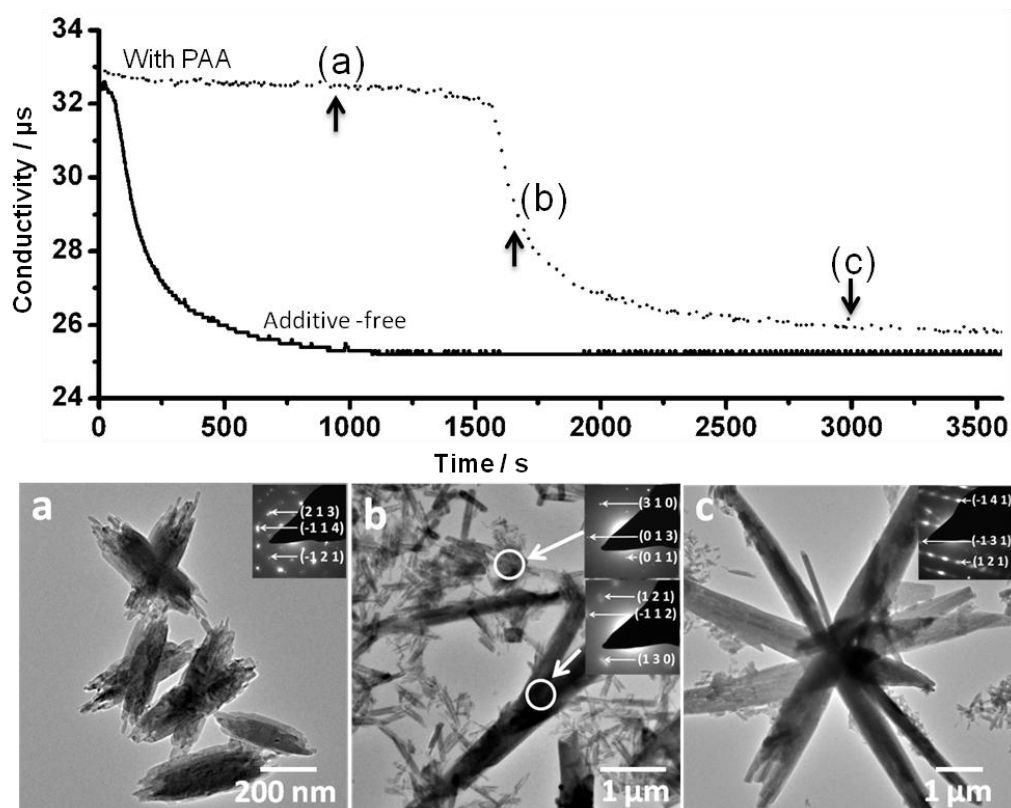


**Figure 4.19** Conductivity-time profiles for the spontaneous precipitation of a 100 mM calcium sulfate solution in the absence (solid line) and in the presence of 5  $\mu\text{g}/\text{ml}$  PAA (dotted line). The TEM images show precipitates extracted from the reaction solution containing PAA after (a) 15 mins, where most of precipitates were hemihydrate, (b) 26 mins, showing a mixture of hemihydrate (nanorods) and gypsum (needles) and (c) 50 mins, where the vast majority of crystals were gypsum.

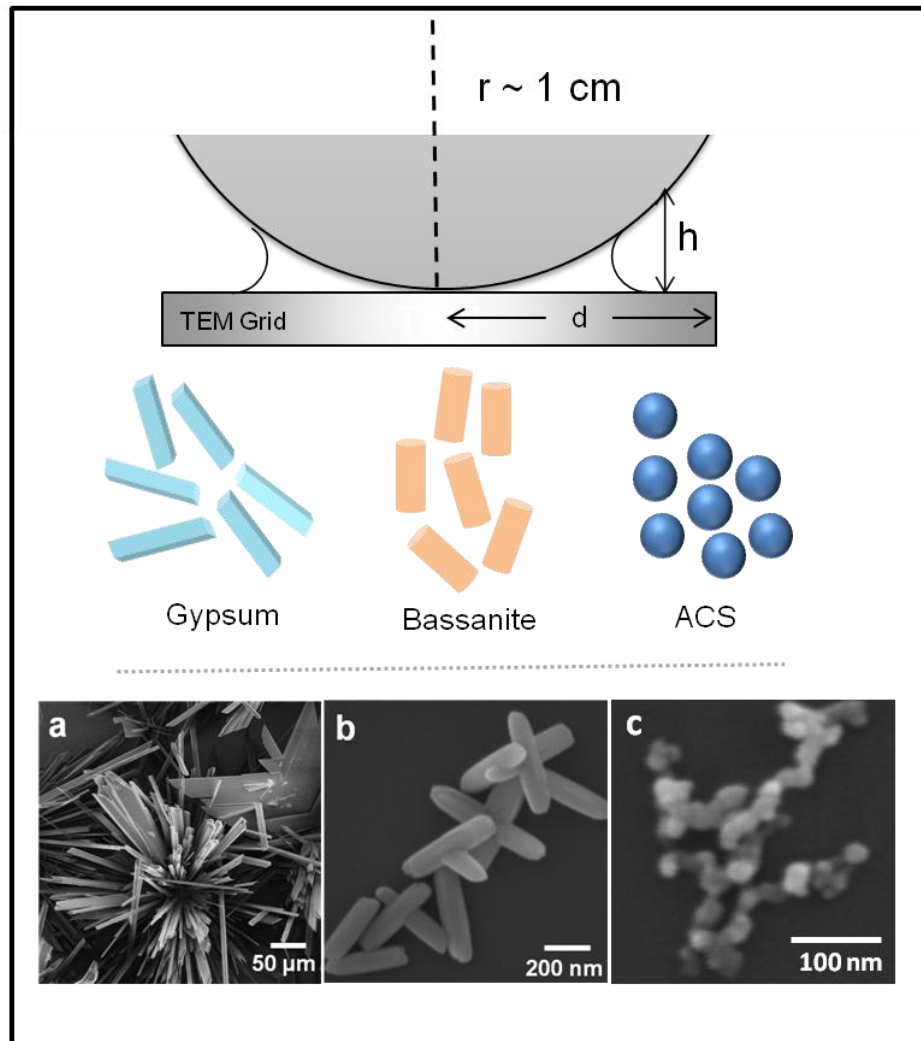
Although there were some records of changes in the calcium ion concentration or conductivity, it is also interesting that no signature of hemihydrate intermediate phases were observed. This indicates that transformation of hemihydrate to stable gypsum is a continuous process and that the hemihydrate is not generated in a single nucleation burst. According to the literature, it is commonly reported that the transformation of hemihydrate to gypsum in solution occurs via dissolution-reprecipitation, where nucleation of gypsum is the rate-determining step [193-195]. In contrast, a recent report also mentioned that hemihydrate nanorods aggregate to form rod-like structures which subsequently recrystallize to gypsum, where the transformation of hemihydrate to gypsum occurs via an aggregation-based

mechanism [196]. The new mechanism of calcium sulfate transformation was also proved in our results (Fig 4.10). Actually, this aggregation process contrasts with goethite ( $\alpha$ -FeO(OH)) crystallization. There, spherical ferrihydrite ( $\text{Fe}_{10}\text{O}_{14}(\text{OH})_2$ ) particles transformed to needle-like goethite through aggregation-based crystallization, but it is believed that the ferrihydrite particles crystallize to goethite prior to aggregation [197]. However, the star-shaped shaped assemblies of hemihydrate nanorods observed here at certain concentrations of magnesium ions and PAA certainly cannot further aggregate due to steric hindrance, suggesting that gypsum can also nucleate either *de novo* in solution or (more likely) on existing, hemihydrate particles[194]. Aggregation of hemihydrate nanorods therefore cannot be an essential precursor to this process. It is therefore clear that this cannot be the only mechanism by which hemihydrate transforms to gypsum in solution.

## 4.6 Summary

The results presented here demonstrate that the additives poly(acrylic acid) (PAA), poly(styrene sulfonate) (PSS), sodium triphosphate and  $\text{Mg}^{2+}$  can be used to inhibit calcium sulfate precipitation, and in doing so, generate amorphous calcium sulfate (ACS) and calcium sulfate hemihydrate with high levels of stability in solution at room temperature. In retarding the precipitation, and producing both ACS and hemihydrate with considerably longevity, additives can therefore be used as an effective means for synthesizing these metastable phases. Indeed, it is quite possible that Nature also uses this strategy to stabilize calcium hemihydrate at room temperature, resulting in its occurrence as a biomineral within deep-sea medusae [141, 198]. Stabilizing the metastable phases using additives also facilitates investigation of the crystallization mechanism, and our results support the suggestion that the oriented aggregation of hemihydrate nanorods into rod-like monoliths can precede their transformation to gypsum under suitable reaction conditions. Finally, face-specific interaction of the additives with the growing crystals, and promotion of aggregation also provided a simple route to controlling the crystal morphologies, which can be integral to defining key properties of calcium-sulfate-based materials such as porosity and mechanical strength.

## Chapter 5: Confinement Leads to Control over Calcium Sulfate Polymorph



The work described in this chapter describes an investigation into the effects of confinement on the precipitation of calcium sulfate. While it is widely known that nanoscale confinement can control the polymorphs of organic crystals, [44], there have been few systematic studies of the precipitation of inorganic crystals in constrained volumes. To investigate this further, the precipitation of calcium sulfate in confinement were studied in this chapter, focusing on the stability and transformation of amorphous calcium sulfate and hemihydrate at different surface separations. Two half-crossed cylinders were used to create an annular wedge which provided a separation that varies continuously from zero to tens of microns. The crystal polymorph changed from calcium sulfate dihydrate to amorphous calcium sulfate via calcium sulfate hemihydrate with enhanced confinement. Interestingly, as described in Chapter 4, the growth of calcium sulfate is also inhibited by the presence of additives. In this chapter, the combined effects of confinement and additives are also investigated. With the addition of inhibitors like poly(acrylic acid) or sodium triphosphate, the lifetimes of the amorphous phase and hemihydrate were extended with increased concentration of additives. It was therefore suggested that these results not only have immediate relevance to salt weathering and biomineralization processes, but are also important to the many crystallization and aggregation-driven processes occurring in small volumes.

## **5.1 Introduction**

Control of crystallization is essential for many reasons, including, for example, to minimise undesirable crystal deposition such as the precipitation of calcium oxalate to form kidney stones or to optimise repair of structures such as bones and teeth. In biological systems, the most widespread control strategy employed is believed to be the use of soluble additives, which can affect the nucleation and growth pathway, and can inhibit or accelerate crystal growth. The sizes and numbers of crystals, as well as their morphologies and polymorphs may also change in the presence of additives. [43] However, in these biological systems, crystallization does not occur in bulk solution, but in constrained volumes, where the physical environment can also control many features. For example, the crystal morphology, size, orientation and polymorph [44] can be controlled in confined volumes. [45, 46] As the degree

of confinement increases, it becomes increasingly important in defining the crystal characteristics.

### **5.1.1 Effect of Confined Volumes**

### **5.1.2 Calcium Sulfate Precipitation in Confinement**

With its polymorphic character and widespread use, calcium sulfate provides an excellent candidate for our investigation. Recently, various methods have been used to synthesise calcium sulfate in compartments. Rees and Evans-Gowing in 1999 formed nanoparticles and nanowires in water-in-oil microemulsions by mixing  $\text{Ca}(\text{NO}_3)_2$  and  $\text{Na}_2\text{SO}_4$  solutions[15]. The two reactant-containing micro-emulsions are mixed in equal volumes at concentrations of 100 mM. Short rods which were 17-50 nm in size were observed by TEM after 1 h. Fractal networks of 8-12 nm diameter spheres were also apparent at higher concentrations of surfactant. The polymorph of these nano sized particles of calcium sulfate was not determined. Reverse micelles, like the Triton X-100/ cyclohexane /water system[97] were also used to prepare  $\text{CaSO}_4$  nanowires, nanorods and nanospheres, where these provide nano-scale reactors that can compartmentalize reactants in discrete water droplets. Reverse osmosis (RO) membrane surfaces was also used to support the growth of calcium sulfate[199]. Decreasing the axial distance from the entry, the structures of calcium sulfate transformed from plate-like crystals which were mm in length to needle like crystals, in the submicron size range. Synthesis of submicron  $\alpha$ -calcium sulfate hemihydrate submicron-rods in water/n-hexanol/CTAB reverse microemulsions was successfully synthesized metastable or hydrated hemihydrate at the temperature that lower than the temperature needed for  $\alpha$ -HH precipitation[200].

## **5.2 Aims of this Project**

All the confined systems that have been discussed in the literature provided evidence that confinement can affect the crystallization pathway of substances.[44] Yet, due to the technical limitations, it is often difficult to investigate the effects of confinement over multiple length scales in one system. In order to gain further understanding of the crystallization pathway of calcium sulfate, and in particular the

effects of confinement on crystallisation, in this chapter we employed a simple crossed cylinder apparatus which generates an annular wedge. The crossed-cylinder configuration enables the effects of confinement to be easily assessed, by offering separations ranging continuously from angstroms to macroscale in a single system. A TEM grid was placed between the crossed-cylinders to enable characterization of the particles formed using TEM. The experiments also investigated the combined effects of both confinement and soluble additives on crystallization – both of which are present in many natural/ synthetic systems. The results provide further evidence for the existence of earlier stages of precipitates and the stability of amorphous phase and hemihydrate.

## **5.3 Experimental**

### **5.3.1 Materials**

Calcium chloride and sodium sulfate solutions were prepared by dissolving  $\text{CaCl}_2 \cdot 2\text{H}_2\text{O}$  and  $\text{Na}_2\text{SO}_4$  (Sigma-Aldrich), respectively, in 18 M $\Omega$ /cm ultra-pure Millipore water to the concentrations of 200 mM.

### **5.3.2 Precipitation of Calcium Sulfate**

Calcium sulfate was precipitated by combining equal volumes of equimolar solutions of calcium chloride dihydrate ( $\text{CaCl}_2 \cdot 2\text{H}_2\text{O}$ , Sigma-Aldrich) and sodium sulfate anhydrite ( $\text{Na}_2\text{SO}_4$ , Sigma-Aldrich) in Milli-Q water, to give final  $\text{Ca}^{2+}$  and  $\text{SO}_4^{2-}$  concentration of 100 mM.

### **5.3.3 Crossed-Cylinder Experiment**

Glass tubes with diameters of 25 mm were cut to produce 25 mm long half-cylinders. The half-cylinders were cleaned by immersing them in Piranha solution (sulfate acid: hydrogen acid= 3:1) over night, followed by rinsed with Millipore (18.2 M $\Omega$ ) water and ethanol and then drying with nitrogen gas. The cylinder glasses were mounted on Teflon holders to hold them in place. A TEM grid was placed between two glass cylinders before they were brought into contact with the

curved surfaces facing each other. A spring and the metal screws on the top of the holder provide a slowly increasing force to make the glass surfaces contact gently.

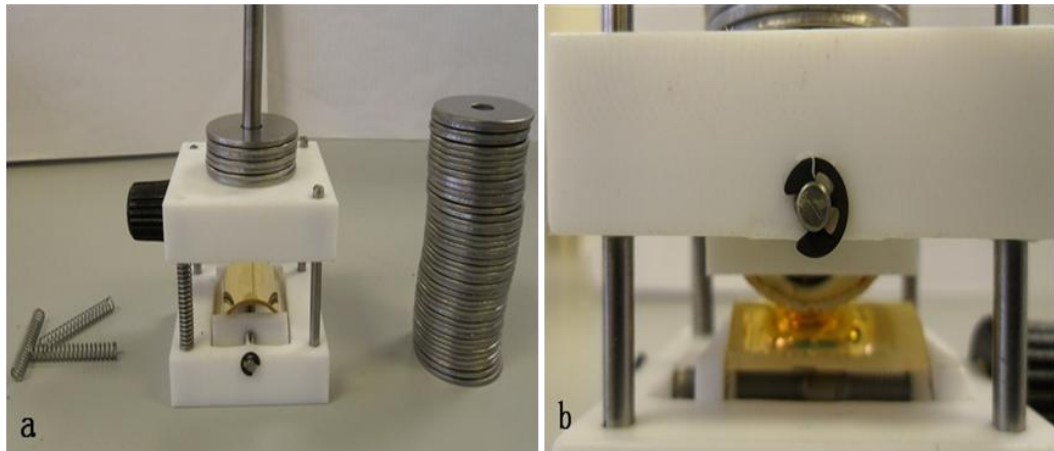


**Fig 5.1** a) Metal pieces are gradually placed on the top of the holder surface. b) Pieces are added until the surface contact. It is essential. Note: Make sure the surfaces come in contact smoothly and gradually increase the weight so as to not damage the surfaces.

CaSO<sub>4</sub> precipitation was initiated around the contact point of the two half cylinders with 20µL of the metastable crystal growth solution, which was prepared by combining 10 µL volumes of CaCl<sub>2</sub> and Na<sub>2</sub>SO<sub>4</sub> solutions of concentrations 200 mM). For experiments carried out in the presence of the additives poly (acrylic acid) (PAA, MW 8000) and sodium triphosphate (Sigma-Aldrich), these were introduced into the sulfate solution prior to mixing with the calcium.

The surface separation  $h$  between crossed cylinders of equal radius of curvature  $R$  is equal to that between a sphere of radius  $R$  and a flat surface. It is related to the radial distance  $x$  from the contact point by:

$$h = R - \sqrt{R^2 - x^2} \approx x^2/2R$$

$h$  hence varies continuously from zero around the contact point to 2-3 mm at the vapour interface of the solution droplet[201].

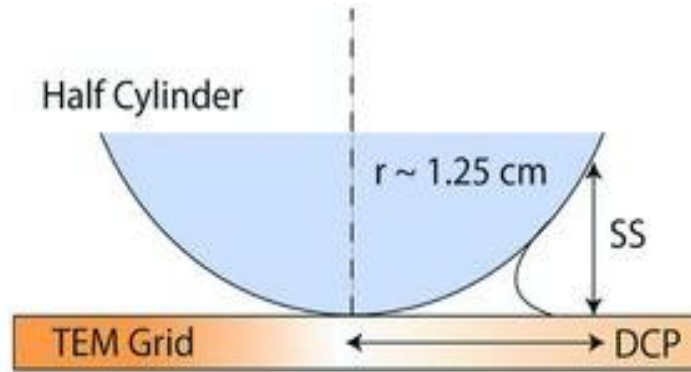


**Fig 5.2** The crossed-cylinder glasses, where  $r$  is the radius of cylinder, DCP is the distance from the contact point and SS is the surface separation.

The holders were kept in a humid atmosphere to reduce the evaporation which otherwise occurs over time. Precipitation was then terminated between 1 hour and 30 hours by flushing the system with ethanol while the surfaces were still in contact. The TEM grid was rinsed with ethanol and dried with filter paper and the half cylinders were then slowly separated. Where necessary, TEM grids supporting calcium sulfate precipitates were also heated to 200 °C for 10 hours.

### 5.3.4 Characterization Methods

The precipitates were imaged with Scanning Electron Microscopy (SEM) and Transmission Electron Microscopy (TEM) with associated Energy-Dispersive X-ray Analysis (EDX). For SEM, glass cylinders supporting calcium sulfate particles were mounted on SEM stubs using conducting carbon tape, which were then sputter-coated with a 5 nm layer of Pt. All samples were examined using a Phillips XL-30 ESEM or a Leo 5000-SEM operating at 3 kV. The region on the TEM grid around the contact point of the half-cylinders was found by identifying a region with scratches and devoid of precipitates using a Phillips Tecnai FEG-TEM operating at 200 kV. EDX was performed to determine the elemental composition and confirm the presence of sulfur and calcium.

## 5.4 Results

### 5.4.1 CaSO<sub>4</sub> Precipitation in Confinement

The effects of confinement on the growth of calcium sulfate were investigated using a crossed-cylinders apparatus, which is based on the surface forces apparatus. [202] This crossed-cylinders apparatus generates an annular wedge between two crossed half cylinders, in which the calcium sulfate is precipitated, and the surface separations of the cylinders range continuously from zero to the macroscale.[203, 204] The experiments demonstrated that the morphologies, sizes and polymorphs of the CaSO<sub>4</sub> particles were influenced by confinement, according to their radial distance from the contact point (*DCP*) of the half-cylinders. SEM and TEM were used to analyze the precipitates formed. A TEM grid was placed between the half-cylinders at the contact point to enable characterization of small particles, providing vital information about polymorph from electron diffraction. Fig. 5.3 shows an overview of a typical bottom cylinder after 1 hour precipitation from 100 mM calcium sulfate solution. The morphologies of calcium sulfate obviously change according to the confinement. When the surface separation is about 15  $\mu\text{m}$  (shown in Fig 5.3d), the particle density of gypsum was lower than in the sample grown in aqueous solution, and the precipitates were a mixture of needle and plate-like gypsum (Fig 5.3, inset I). On increasing the confinement to 5  $\mu\text{m}$ , most of the gypsum crystals were needle-like and were much shorter than those formed in bulk solution (Fig 5.3, inset II). Moving towards the contact point, a higher-magnification SEM image is shown in Fig 5.4, where the contact point is identified by a region devoid of precipitates and where the surface is damaged.

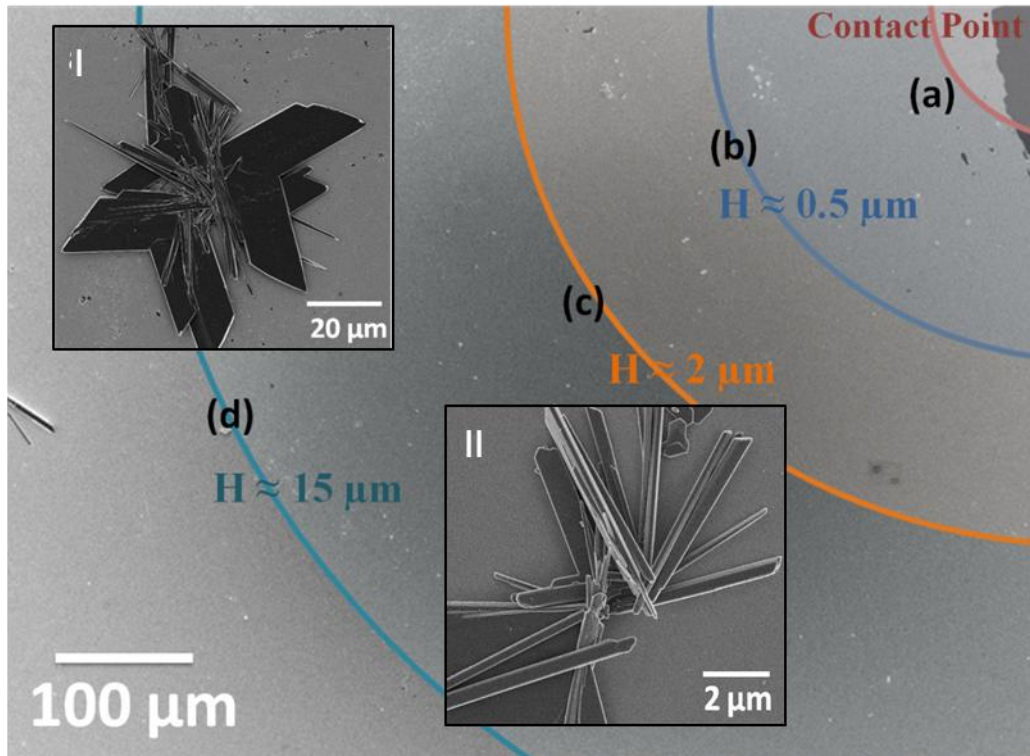


**Figure 5.3** SEM image of a) the contact point with scratches and different surface separations of b) 0.5, c) 2 and d) 15 μm. The inset SEM images show calcium sulfate precipitates formed at separations around 15 μm (I) and around 5 μm (II).

The experiment was also carried out by placing a TEM grid between the cylinders (shown in Figure 5.5). The confined volume obviously alters when a TEM grid is placed between the cylinders, such that the surface separation ( $SS$ ) corresponding to a given  $DCP$  is now half that when the grid is absent. It should also be noted that it is impossible to guarantee that the plane of the TEM grid is perfectly parallel to the cylinder axes, such that there may be some error in the precise surface separations (although not the trends) quoted. However, at the given surface separations, the particles that precipitated on the surface of half glass cylinders or on the TEM grid give similar results.

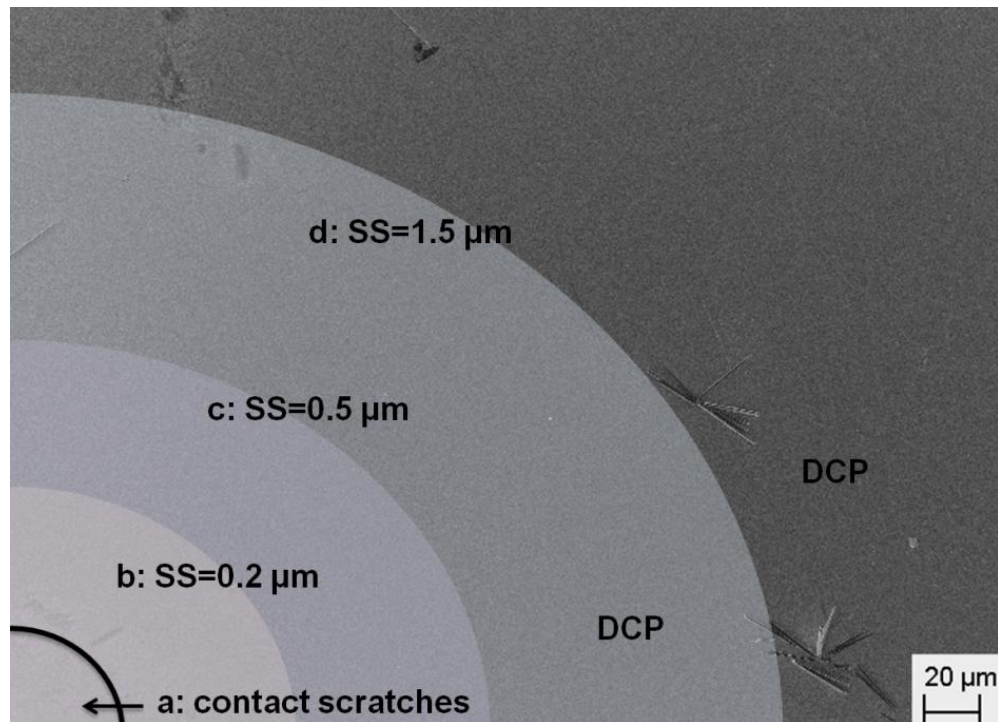


**Figure 5.4** SEM image of calcium sulfate particles precipitated in confinement on glass cylinders, showing (a) the contact point, and (b – d) different distances from the contact points (*DCP*), corresponding to surface separations (*SS*) of approx. (b) 0.2 μm, (c) 0.5 μm and (d) 1.5 μm.

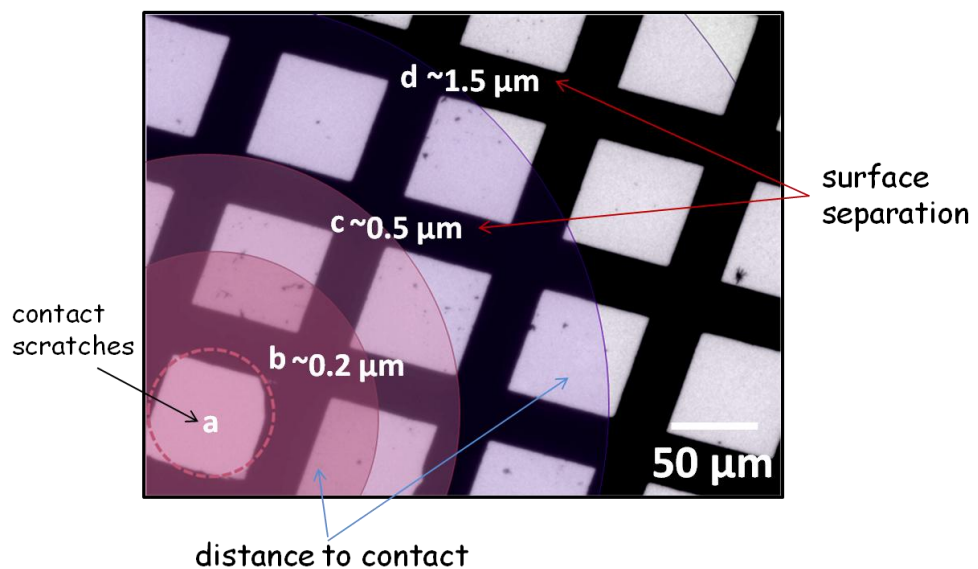


**Figure 5.5** TEM image of the grid surface in the region of a) contact point with starches and different surface separations of b) 0.2, c) 0.5 and d) 1.5 μm.

When the *DCP* (distance from particle position to contact point) was greater than 350  $\mu\text{m}$ , which corresponds to an *SS* (surface separation)  $> 5 \mu\text{m}$ , the crystals grew as bunches of micron-size, intergrown needles, together with some plate-like particles (Figure 5.6a) which were confirmed as gypsum using electron diffraction (Figure 5.7a, inset). These crystals are thus identical to those precipitates in bulk solution, but appear at lower particle densities. Closer to the contact point, at *DCP* = 200  $\mu\text{m}$  and *SS* = 1.5  $\mu\text{m}$ , marked changes in the  $\text{CaSO}_4$  precipitates were observed and the crystals now appeared as 300-600 nm blocky nanorods together with micron-size, well-defined plates, (Figure 5.6b, the arrows shown two different precipitates) in roughly equal amounts. Electron diffraction (Fig 5.7b) confirmed that the nanorods are hemihydrate while the micron-sized plates are gypsum, an analysis which is consistent with the crystal morphologies. Unlike gypsum crystals precipitated in bulk, the gypsum particles formed at *SS* = 1.5  $\mu\text{m}$  are invariably non-aggregated and show very well-defined plate-like morphologies. Further changes in the calcium sulfate precipitates were observed at smaller surface separations. In the region where *DCP* = 160  $\mu\text{m}$  *SS* = 1  $\mu\text{m}$ , only aggregates of hemihydrate nanorods were observed (Fig 5.6c), as confirmed by electron diffraction (Figure 5.7c). These were principally about 200 nm in length, although some larger rods and aggregates of micro-sized rods were also present. Individual nanorods of hemihydrate formed at surface separations below 0.5  $\mu\text{m}$ , as shown in Figure 5.6d and 5.7d with lengths of 100-200 nm.

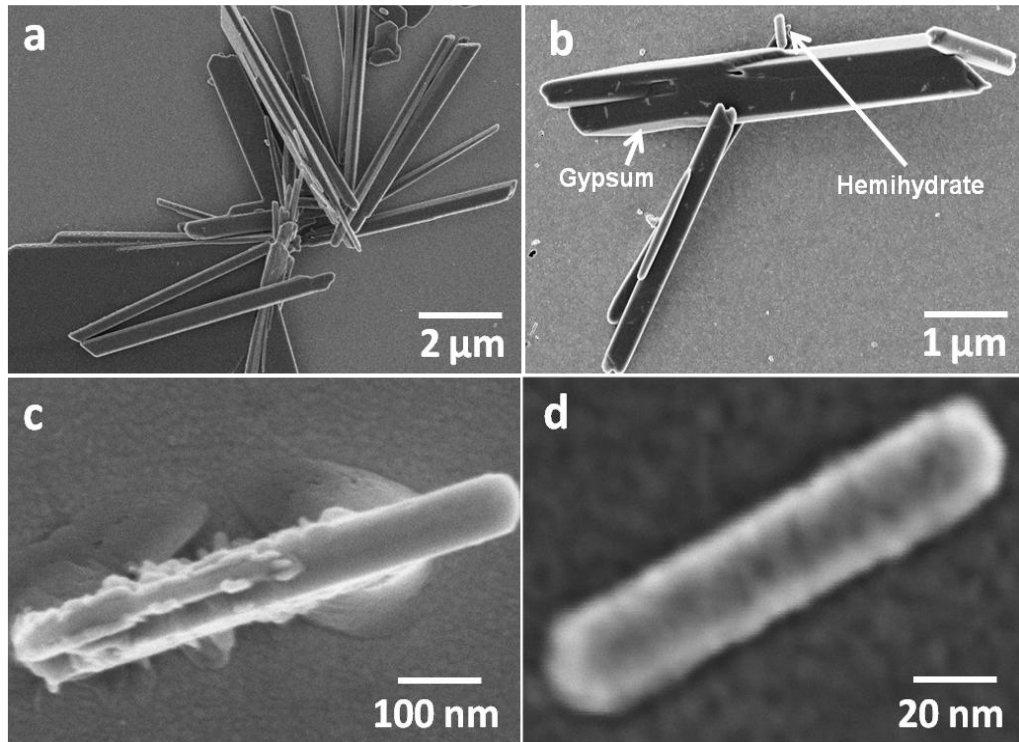


**Fig 5.6** SEM images of calcium sulfate crystals precipitated after 1 hour on glass crossed-cylinders. The surface separation is approximately (a) 5 μm (particles shown are gypsum), (b) 1.5 μm (particles shown are a mixture of gypsum and hemihydrate), (c) 1 μm (particles shown are hemihydrate with larger hemihydrate rods, more than 500 nm in length), and (d) 0.5 μm (particle shown is hemihydrate).

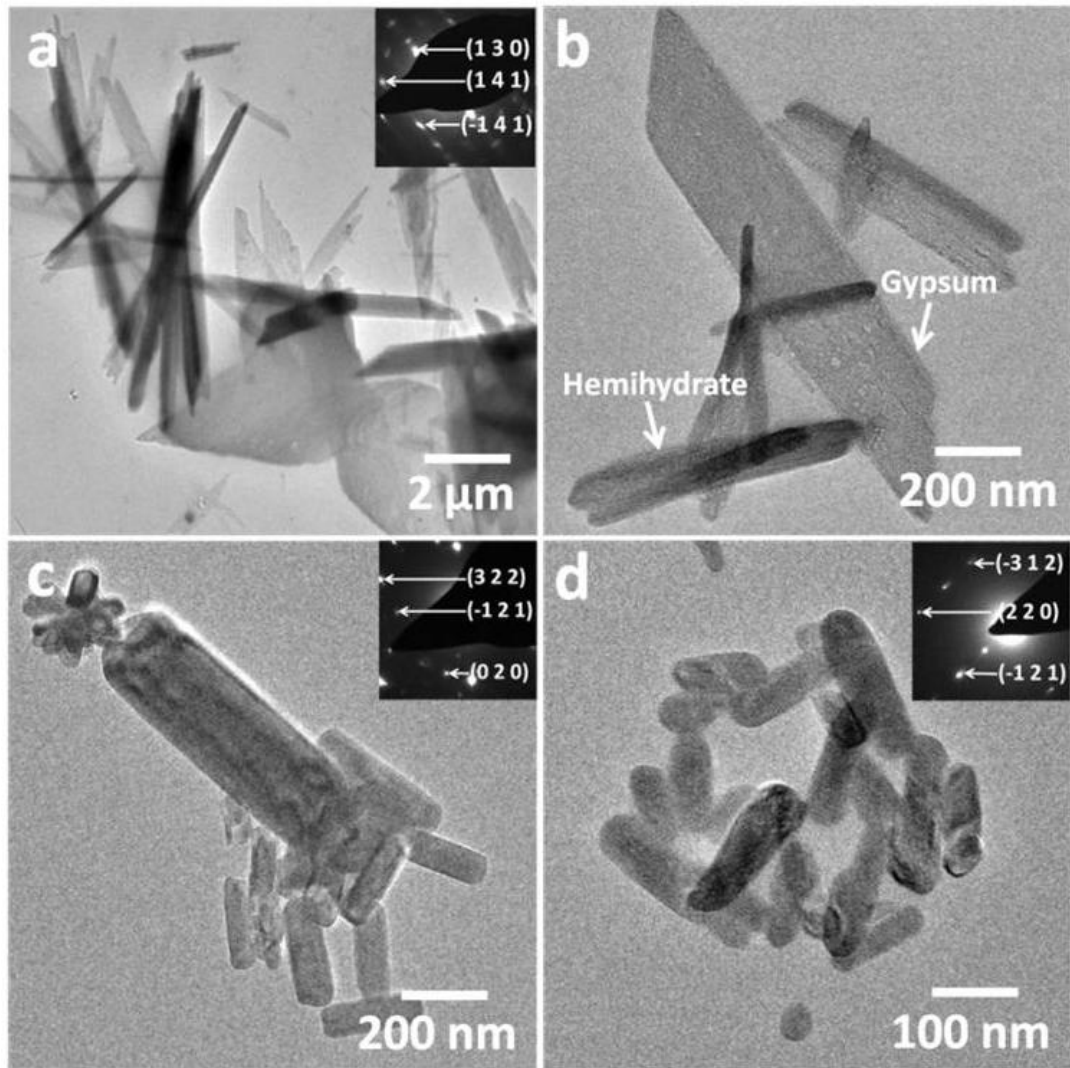


**Fig 5.7** TEM images of calcium sulfate crystals grown at a final concentration of 100 mM on a TEM grid in the crossed-cylinders system after 1 hour. The surface separation is approximately a) 5 (shown as gypsum), b) 1.5 (shown as a mixture of gypsum and hemihydrate), and c) 1 (shown as aggregation of hemihydrate), and d) 0.5 $\mu\text{m}$  (shown as hemihydrate) in this location.

The edges and faces of the precipitated crystals also became progressively more irregular with increased confinement, as shown in Figures 5.8a and b, for  $SS = 0.2 \mu\text{m}$ . In this nano-sized separation regime, the hemihydrate nanorods were only around 50 nm in length, and 50-30 nm nanoparticles (Figure 5.9) were observed in some areas.

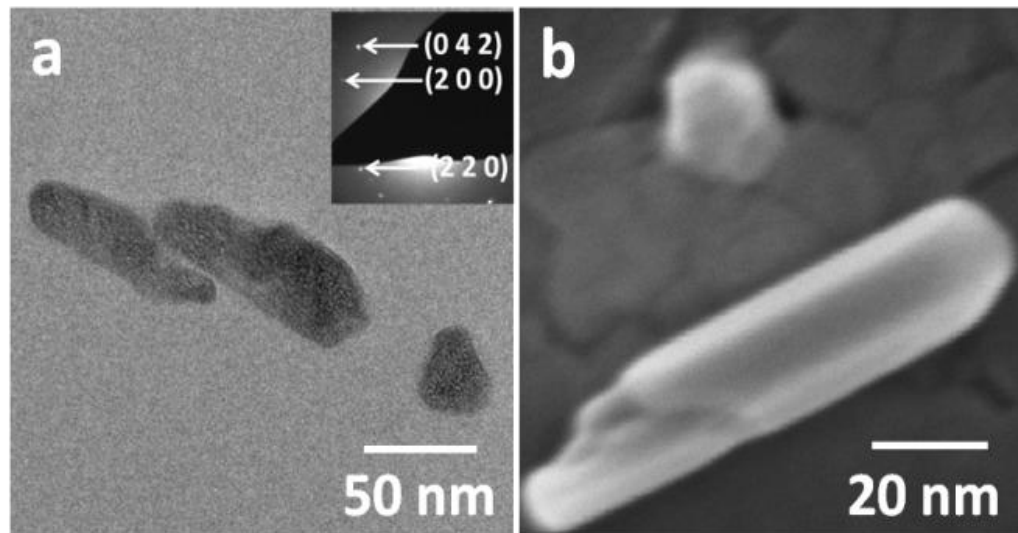


**Fig 5.8** TEM and SEM images of calcium sulfate particle grown at a final concentration of 100 mM of the crossed-cylinders system after 1 hour at a surface separation of 0.2  $\mu\text{m}$ .

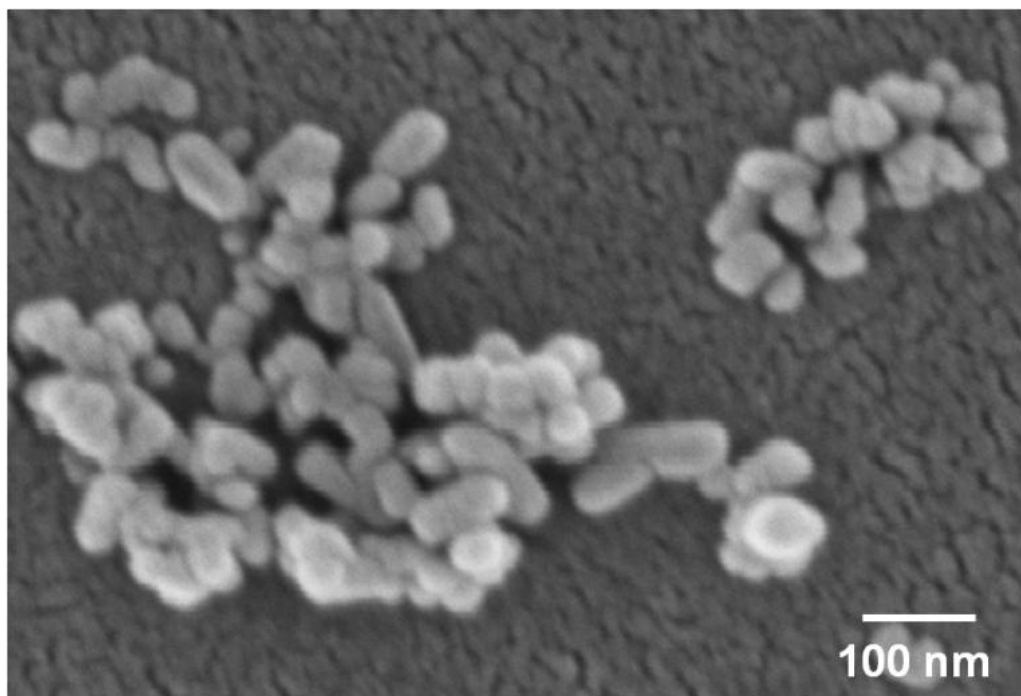


**Figure 5.9** SEM images of calcium sulfate particles grown at a final concentration of 100 mM in the crossed-cylinders system after 1 hour. Surface separation = 0.2  $\mu\text{m}$ . It shows a mixture of nanoparticles, approximately 30 nm in the diameter and hemihydrate nanorods.

In some areas, the sizes of these nano particles were 10-30 nm in diameter. Elemental dispersive X-ray (EDX) analysis of aggregates of these particles confirmed the presence of Ca and S (Figure 5.10a, inset), while no evidence for crystallinity was found by selected area electron diffraction (Figure 5.10b). Conclusive evidence that these particles were hydrated amorphous CaSO<sub>4</sub> (ACS) (rather than lack of sufficient material to give recordable diffraction patterns) was obtained by continued exposure to the electron beam. Partial crystallisation was apparent after 2 mins of exposure, and subsequent electron diffraction demonstrated that the nanoparticles had crystallised to gypsum (Figure 5.10c). These non-faceted and round particles as appear to be amorphous, just as found at early stages of reaction in bulk solution from 15 mM CaSO<sub>4</sub> solutions after 1 minute, as ACS is stable for longer periods at lower supersaturations.[179] Insufficient material was present to enable characterization using Raman, so the particles were analysed using TEM.

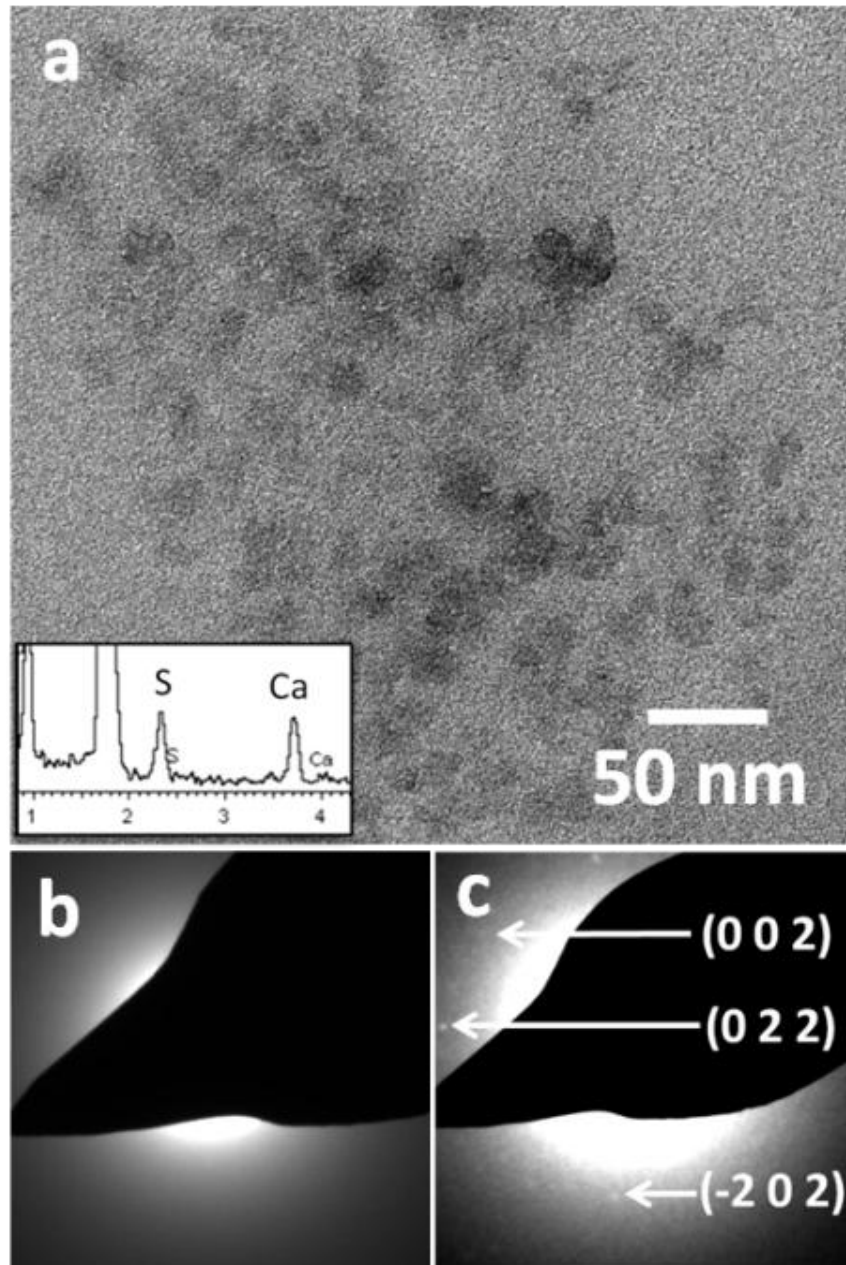


**Fig 5.10** TEM images of amorphous  $\text{CaSO}_4$  particles precipitated after 1 hour from a 100 mM solution at a surface separation of  $0.2 \mu\text{m}$ . The inset in (a) shows the corresponding EDX spectrum which demonstrates significant Ca and S (b) The selected area electron diffraction pattern of this sample, showing that it is amorphous. (c) After 2 min irradiation with the electron beam, crystallisation to  $\text{CaSO}_4$  dihydrate occurs.

#### 5.4.2 CaSO<sub>4</sub> Precipitation in Confinement in the Presence of Additives

In nature, and indeed many practical systems, it is commonly observed that crystallization occurs under the effects of both confinement *and* soluble additives. Experiments were therefore performed in which calcium sulfate was precipitated in the presence of poly(acrylic acid) (PAA) or sodium triphosphate, under systematic control of the degree of confinement. As essential control experiments, calcium sulfate was also precipitated from a 100 mM bulk solution containing 100 µg/ml PAA or 10 µg/ml sodium triphosphate. These experiments gave results consistent with those shown in Chapter 4 [205] which show that both additives can retard the crystallization of gypsum from hemihydrate. It was shown that star-like aggregates of calcium sulfate hemihydrate nanorods were obtained after 1 h, where these were somewhat smaller with sodium triphosphate (diameter approx 250 nm) than with PAA (diameter approx 350 nm) (Figure 5.11). The recrystallization of hemihydrate to gypsum was therefore effectively inhibited such that the full transformation to gypsum was only achieved after 7 days in the presence of 100 µg/ml PAA and 5 days in the presence of 10 µg/ml sodium triphosphate. It was also demonstrated in Chapter 4 that with higher concentrations of these additives, the transformation of amorphous calcium sulfate to hemihydrate was retarded and that ACS was present for much longer times than in their absence.[205]

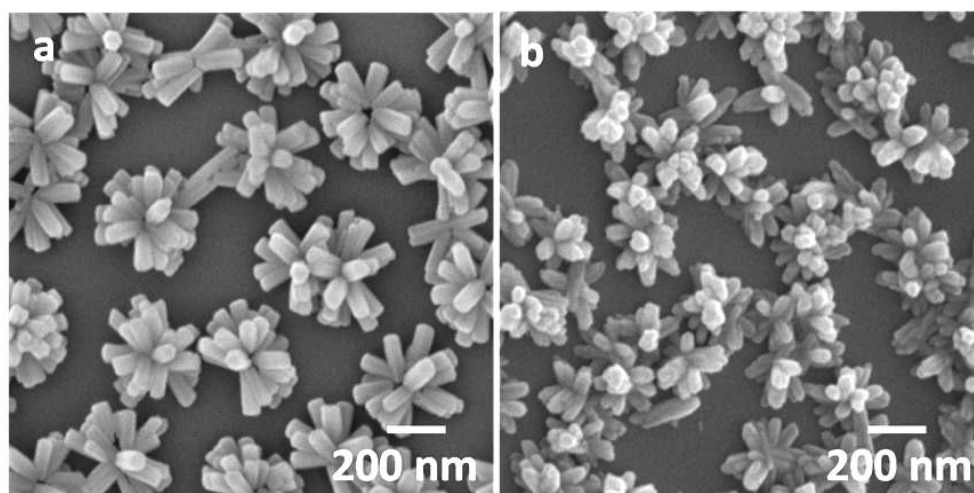


**Figure 5.11** SEM images of CaSO<sub>4</sub> particles precipitated from 100 mM solution in bulk after 1 h in the presence of (a) 100 µg/ml PAA and (b) 10 µg/ml sodium triphosphate.

Precipitation of calcium sulfate in the presence of PAA in confinement resulted in a marked stabilisation of the metastable phases and a marked increase in the yield of nanoparticles. Fig 5.12a shows that after 1 hour and at a 0.5  $\mu\text{m}$  surface separation, all the nanospheres of diameter  $\sim 10$  nm were amorphous, and did not give electron diffraction patterns. In comparison, only individual hemihydrate nanorods were found in confinement at  $SS = 0.5$   $\mu\text{m}$  after 1 h in the additive-free system. These particles showed considerable stability, crystallizing only slowly in the apparatus. They also failed to crystallize even after 5 minutes irradiation in the electron beam in the TEM. After heating up the sample to 200  $^{\circ}\text{C}$  for 10 hours, this amorphous phase crystallized to gypsum. Fig 5.12b shows that at the same area, after 5 hours, some amorphous nanoparticles started to crystallize to hemihydrate generating irregular particles around 20 – 50 nm in length. In contrast, the additive-free calcium sulfate precipitates formed in confinement showed significant crystallinity at  $SS = 0.5$   $\mu\text{m}$  after the same time period. Also in the bulk solution, with the same concentration of PAA, after 5 hours, the precipitation is a mixture of hemihydrate and gypsum. After 15 hrs, all these hemihydrate nanocrystals grew to nanorods, which were less than 50 nm in length (Figure 5.12c). Most of these hemihydrate nanocrystals continued to grow to 100 nm nanorods after 24 hours (Figure 5.12d). In contrast, both gypsum and hemihydrate are found at  $SS = 0.5$   $\mu\text{m}$  after 24 hrs in the absence of PAA for 10 mM calcium sulfate solutions (Figure 5.13a and b), with gypsum only being micron-sized in length. Figure 5.13c and d shows a hemihydrate and gypsum mixture formed in the presence of 100  $\mu\text{g/ml}$  PAA after 24 hrs from a 100 mM calcium sulfate solution.

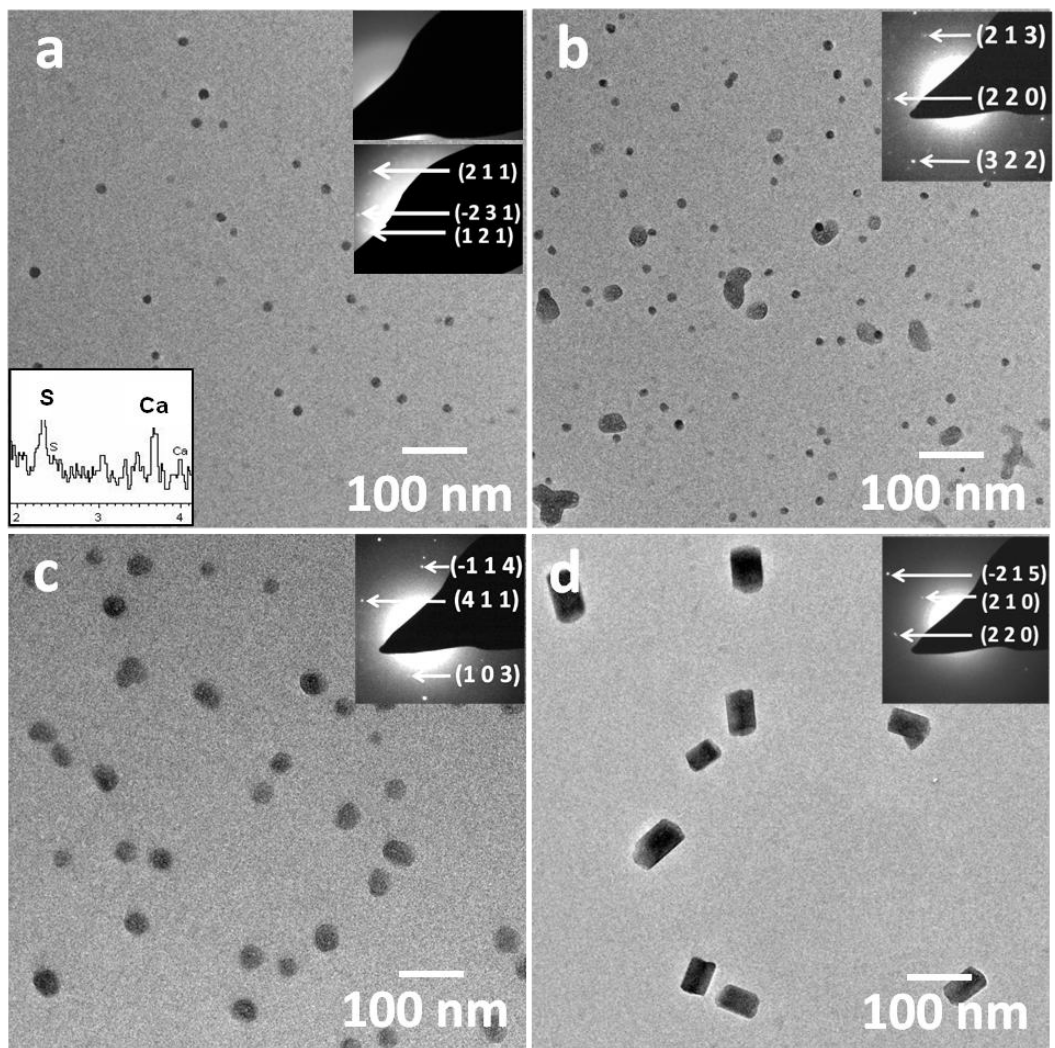


**Fig 5.12** TEM images and corresponding electron diffraction (EDX) patterns of calcium sulfate particles precipitated in confinement in the presence of 100 µg/ml PAA at a surface separation of  $\approx 0.5$  µm after different incubation times. (a) 1 h, showing 20 nm amorphous spheres, together with the corresponding EDX spectrum (inset) showing the presence of Ca and S. The lower inset ED pattern shows crystallization of the amorphous particles to gypsum after heating, (b) 5 h, where some amorphous particles have started to transform to hemihydrate, (c) 15 h, when hemihydrate nanoparticles are present and (d) after 24 h, showing hemihydrate nanorods.

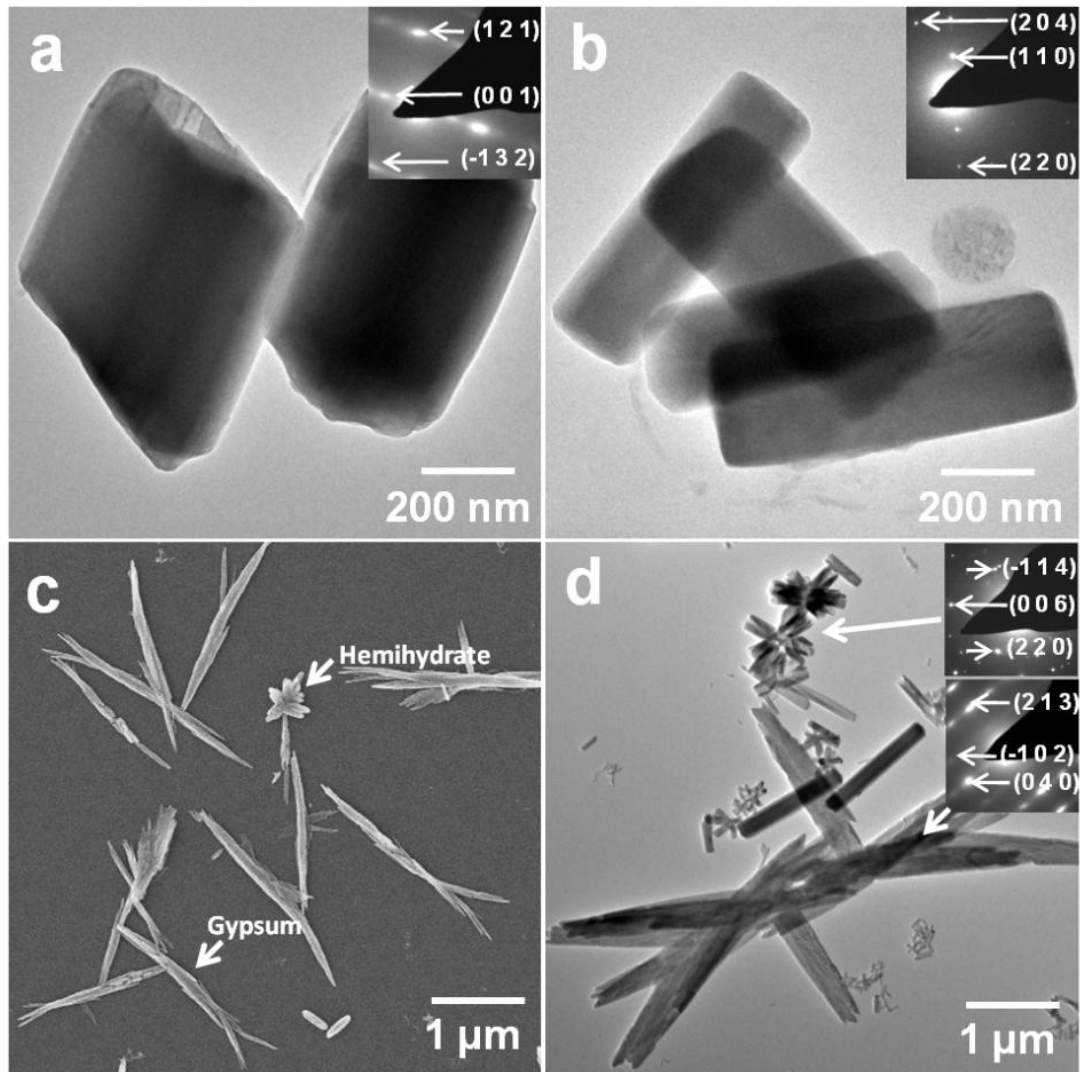


**Figure 5.13.** TEM images of calcium sulfate crystals precipitated after 24 hours on glass crossed-cylinders. The surface separation is approximately 0.5  $\mu\text{m}$ . Particles shown are a mixture of (a) gypsum and (c) hemihydrate. It is also shown mixture of both gypsum and hemihydrate (c) and (d) with PAA 100  $\mu\text{g}/\text{ml}$  after 24 hours in bulk solution.

The effect of sodium triphosphate (10 $\mu\text{g}/\text{ml}$ ) on the precipitation of  $\text{CaSO}_4$  in confinement was also used investigated, where this demonstrated significant stabilisation of the metastable phases. In the absence of additives, ACS shows limited stability on confinement. Examination of  $\text{SS} = 0.5 \mu\text{m}$  with addition of 10 $\mu\text{g}/\text{ml}$  sodium triphosphate showed that the precipitates were still 10 nm amorphous nanoparticles after 1 hour (Fig 5.14a), while the particles had a

significant degree of crystallinity, and were principally 50 nm irregular hemihydrate particles after 24 hours (Fig 5.10b). That confinement plays a key role in offering stabilisation was demonstrated by studying larger surface separations of  $SS = 1 \mu\text{m}$ . This level of confinement was insufficient to stabilise ACS after 1 h reaction time in the additive-free system, when well-defined 50 – 100 nm hemihydrate nanorods were observed (Figure 5.14c). These continued to grow in size with longer reaction times, but hemihydrate remained the sole phase present after 24 h (Figure 5.14d). The experiments therefore demonstrate that in combination, confinement and additives can provide considerable stabilization of the metastable polymorphs of calcium sulfate.

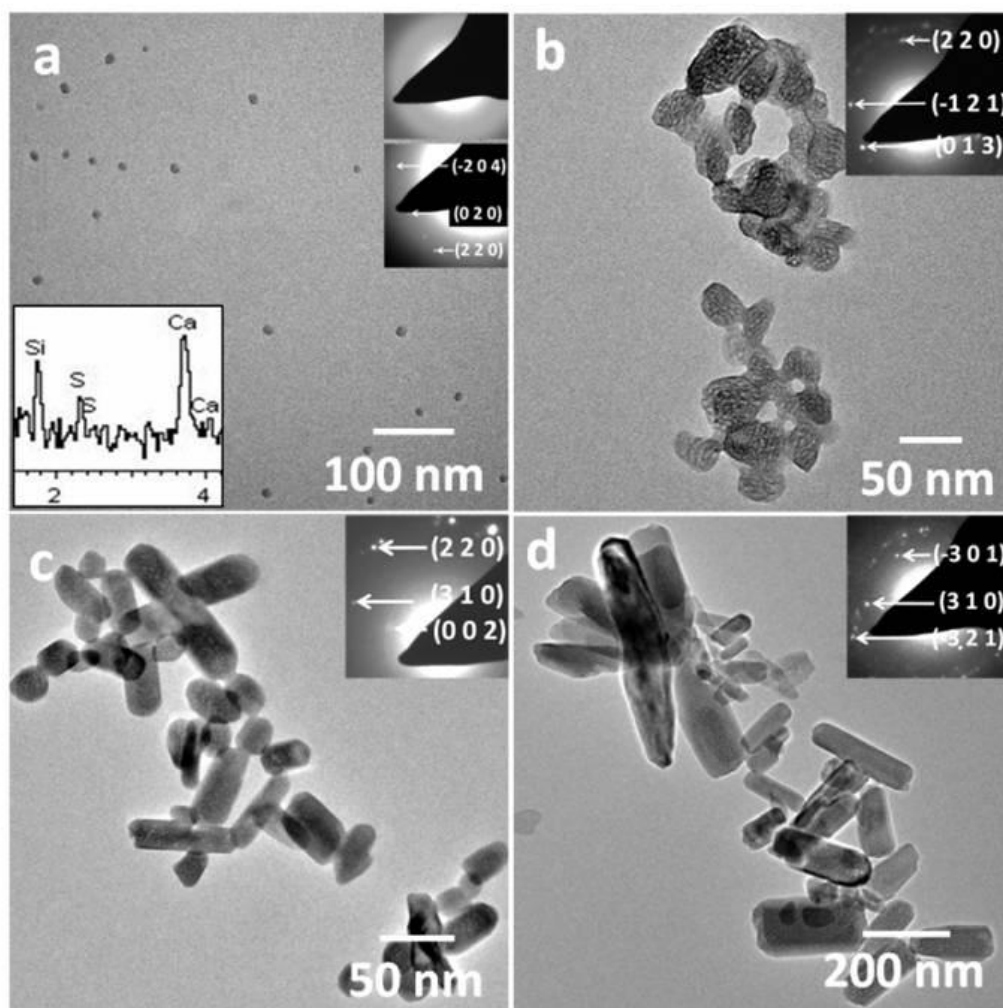


**Fig 5.14** TEM images and corresponding electron diffraction patterns of calcium sulfate particles precipitated in confinement in the presence of 10  $\mu\text{g}/\text{ml}$  sodium triphosphate at different surface separations ( $SS$ ) and incubation times. (a)  $SS = 0.5 \mu\text{m}$ ,  $t = 1 \text{ hr}$ , showing amorphous nanoparticles, together with EDX spectrum (inset) showing the presence of Ca and S. The lower inset ED pattern shows crystallization of the amorphous particles to gypsum after heating. (b)  $SS = 0.5 \mu\text{m}$ ,  $t = 24 \text{ hrs}$ , showing hemihydrate nanoparticles, (c)  $SS = 1 \mu\text{m}$ ,  $t = 1 \text{ hr}$ , showing hemihydrate nanorods, and (d)  $SS = 1 \mu\text{m}$ ,  $t = 24 \text{ hrs}$ , showing hemihydrate nanorods.

## 5.5 Discussion

Our previous investigation of the early stages of  $\text{CaSO}_4$  precipitation from salt-free solutions at room temperature demonstrates that calcium sulfate exhibits a complex precipitation behaviour, as shown in Chapter 3 and 4. It was long considered that gypsum is the most stable phase at room temperature and hemihydrate was only precipitated together with anhydrite from supersaturated, salt-free calcium sulfate solutions at temperatures over  $97^\circ\text{C}$ . [37] These results were called into question by our observation which demonstrated the existence of an amorphous calcium sulfate (ACS) phase, and showed that it underwent a step-wise transformation to gypsum via  $\text{CaSO}_4$  hemihydrate. [179, 196, 206] All these results demonstrated that the transformation from hemihydrate to gypsum is slower at low calcium sulfate concentrations, and hemihydrate nanorods can be stable in solution for extended periods. Interestingly, it was shown that hemihydrate can also be observed below its reported thermodynamic (long-term) solubility. [196] This was attributed to the slow conversion from hemihydrate to gypsum. Our new precipitation pathway of ACS-hemihydrate-gypsum is entirely in accord with Ostwalds rule of stages in that the metastable phases precipitate first. [207, 208] We do not believe this suggests any long-term stability of hemihydrate, [196] and it is unnecessary to invoke negative surface energies, which are not possible in a rigorous, thermodynamic interpretation. [209]

The experiments performed here demonstrated that confined volumes have a significantly influence over calcium sulfate precipitation, which leads to an extended lifetime of the metastable phases ACS and hemihydrate. In our system, gypsum was the major product on precipitation from 100 mM bulk solution after just 10 mins while particles identical in morphology to those produced in bulk were only observed after 1 h at surface separations (*SS*) of  $\sim 5 \mu\text{m}$ . Changes in the shapes, sizes and polymorphs of the  $\text{CaSO}_4$  precipitates were also observed with a reduction in the surface separation. For example, when the surface separation is around  $1.5 \mu\text{m}$ , a mixture of gypsum and hemihydrate was observed after 1 hour, while the gypsum formed in confinement appeared as isolated particles rather than the bundles of needles and plates seen in bulk. When the surface separation is between  $1 \mu\text{m}$  to  $0.5 \mu\text{m}$ , hemihydrate was the only phase to be observed after 1 hour and the particles became smaller as the confinement increased. In contrast, hemihydrate is unstable at room temperature at this concentration in bulk solution, such that pure hemihydrate only occurs at times less than 1 minute in 100 mM bulk calcium sulfate solutions, as shown in Chapter 3.[179] Perfect placing the grid between cylinders achieves  $0.1\sim 0.2 \mu\text{m}$  separation precipitated ACS nanoparticles. The diffraction patterns also provided evidence that, at sub-micrometer separations, the confined particles appear to consist primarily of amorphous and hemihydrate, which cannot be seen in the bulk solution.

The most striking feature of our results is that the amorphous precursor and hemihydrate were stabilised in confined volumes at room temperature, and a marked increase in stability was observed at surface separations from hundreds of nanometers up to as much as micrometers. ACS together with hemihydrate and gypsum was only detected after 1 min from a dilute 15 mM solution formed by direct mixing of solutions of  $\text{CaCl}_2$  and  $\text{Na}_2\text{SO}_4$ , [179] while no ACS was detected at reaction times as early as 10 sec in 25 mM solutions. [196] Recently, the existence of ACS was also proved as a brief appearance (within 15-30s) from the direct dissolution of hemihydrate to yield solution concentration of 55 mM then rapidly crystallized to gypsum. [206] The transformation from amorphous phase to gypsum is in the absence of intermediate hemihydrate. In this case, the higher net  $\text{CaSO}_4$

concentration and the lack of background electrolyte would increase the effective concentration, or activity of  $\text{CaSO}_4$ .

A further striking result from our experiments is that the polymorphic control that is achieved at surface separations that are relatively large compared to those detectable effects of confinement.[44, 210, 211] In our crossed cylinder apparatus, the stabilization of hemihydrate was observed at separations of up to 1  $\mu\text{m}$ , and ACS were noted at separations less than 200 nm. As the previous research which use the same crossed cylinder apparatus to analyse the precipitation of calcium carbonate, amorphous calcium carbonate (ACC) was observed and stabilized with respect to the thermodynamically most stable polymorph calcite at separations in the order of 0.5–1  $\mu\text{m}$ . [212] In this calcium carbonate precipitates, the common polymorph, vaterite was not observed. It was considered that the stabilization of ACC in confinement was thermodynamic stable while with respect to calcite would only be expected at surface separation of a few nanometers and below. Thus it also demonstrated that the stability of ACC is also kinetic in origin. It can be also assumed that the difference in free energy between calcite and ACC is of the same order as that between gypsum and hemihydrate which is also clearly shown that stabilization of hemihydrate at the length scales observed here is not a thermodynamic effect either. Although there is no quantitative data from the literatures on the free energy of ACS, this should also be true for amorphous calcium sulfate.

In bulk solution, the transformation of hemihydrate to gypsum appears to occur via an aggregation-based process.[196] The results presented in Chapters 3 and 4 also suggested that hemihydrate may form via an analogous assembly-based process and subsequent crystallization of ACS nanoparticles in the presence of additives.[205] From the growing number of mechanistic studies of the precipitation of insoluble inorganic compounds, it is now suggested that aggregation-based processes may be widespread.[12, 13] This Chapter also shows that this occurs in confinement, and a large number of precipitates comprising aggregates of nanoparticle units were observed (shown in Fig 5.15). Both Raman microscopy and electron diffraction (Fig 5.15a, inserted) identified that these aggregated precipitates were hemihydrate, formed from ACS precursor particles. Fig 5.15b shows particles undergoing an aggregation-based transition from hemihydrate to gypsum.

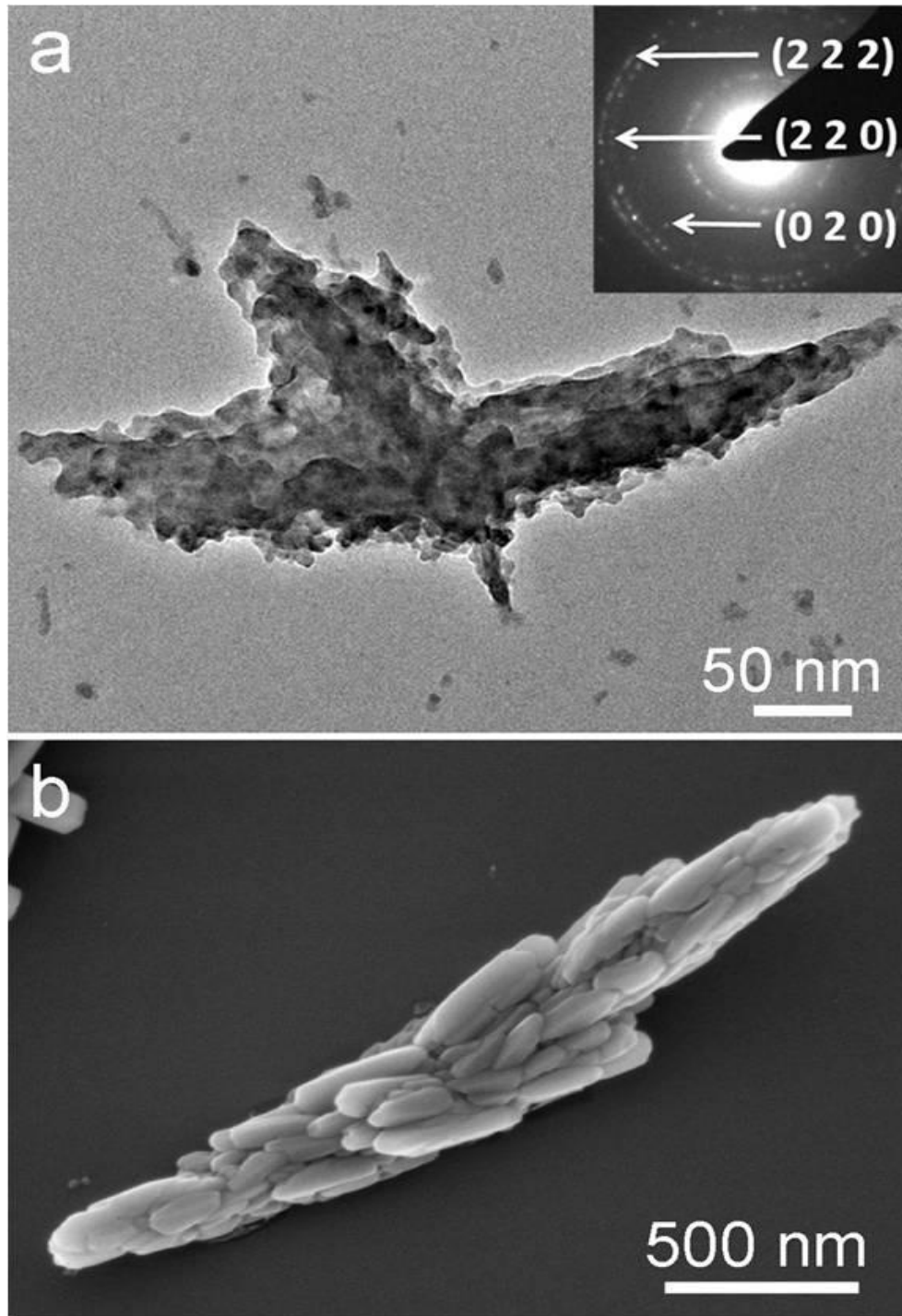


**Figure 5.15** Calcium sulfate particles precipitated in the crossed-cylinder system from a solution of concentration 100 mM after 24 h. a) TEM image and corresponding diffraction pattern of hemihydrate particle precipitated at  $SS = 0.2 \mu\text{m}$  and b) SEM image of rod precipitated at  $SS = 1 \mu\text{m}$ , comprising an aggregate of hemihydrate nanorods.

If hemihydrate transforms to gypsum via an aggregation-based pathway, then this should be significantly limited in confined volumes. Diffusion coefficients ( $D$ ) are increasingly reduced as confinement increases and according to the literature, the diffusion coefficient of a 200 nm spherical particle is only 25% of its bulk value at a separation of 0.5  $\mu\text{m}$  (which approximates to our hemihydrate rods at 0.5  $\mu\text{m}$  surface separation).[17] Furthermore, the diffusion coefficients ( $D$ ) of 190 nm particles in bulk solution (similar to the particles seen in our experiments) are typically at least two orders of magnitude smaller than the diffusion coefficients of divalent ions.[29] It is also shown that the hindered diffusion of ions would only begin to become noticeable for surface separations of 20 nm and below.[17] The surface separations in our system are as low as 100 nm which is much larger than the noticeable surface separations. Thus, while the confinement levels used here will significantly affect the aggregation of 200 nm particles, the diffusion of ions is totally unaffected.

It is obvious that aggregation-based processes are diffusion-controlled, and the extreme restrictions near the contact zone in the crossed-cylinder device can be conveniently illustrated as follows. Indeed, for  $SS = 200$  nm, this surface separation is comparable to the lengths of the hemihydrate! It is easy to imagine that any process that requires the aggregation of 100 nm particles will be impeded out to  $SS$  values of at least a micron. Even diffusion of nm-size molecules in vapour, which is normally much more rapid than diffusion of particles in a liquid, has been shown to prevent accumulation of material from vapour in the crossed-cylinder geometry for all but the highest vapour concentrations.[203] Substances with vapour pressures below ca. 1 mm Hg were unable to diffuse sufficiently rapidly into the contact region to give any detectable crystal growth from vapour.

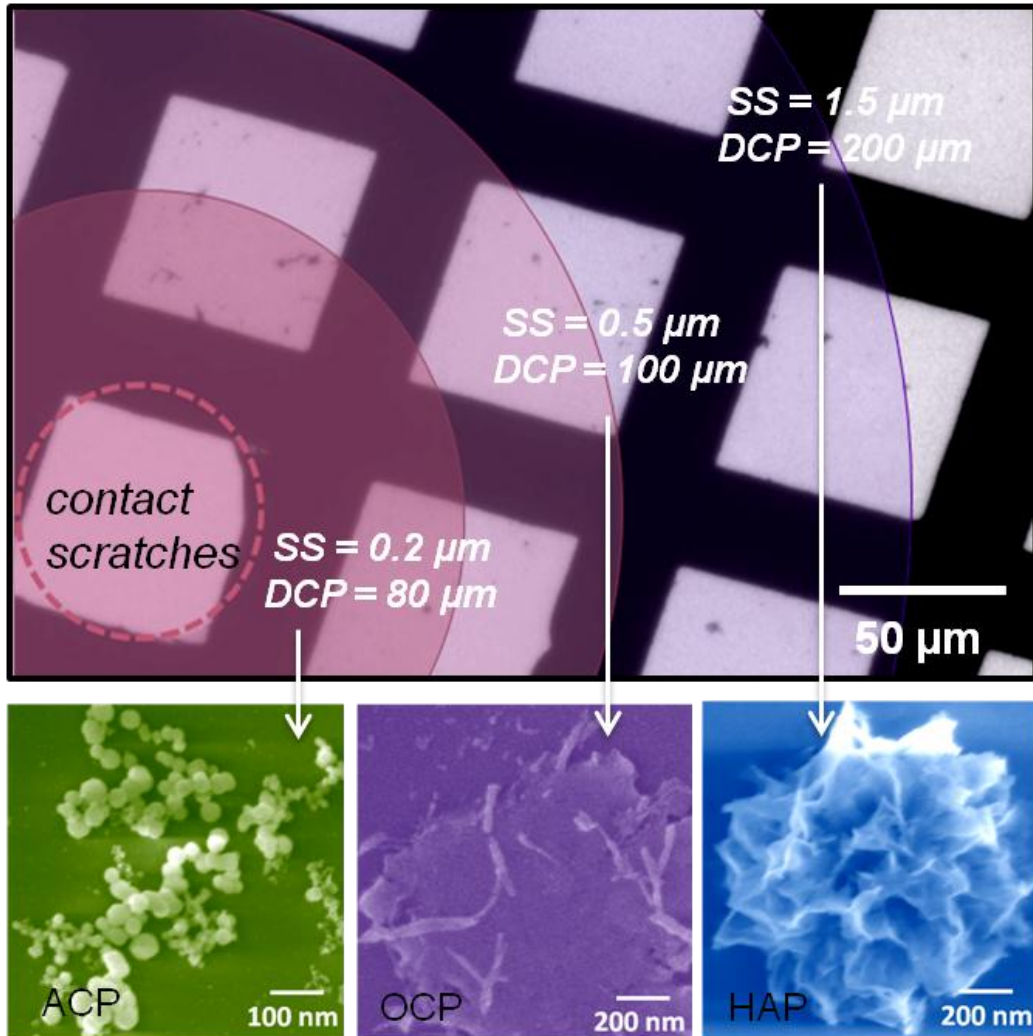
In common with the calcium carbonate system, transformation of ACS to gypsum ( $\text{CaCO}_3 \cdot 2\text{H}_2\text{O}$ ) via hemihydrate ( $\text{CaCO}_3 \cdot 0.5\text{H}_2\text{O}$ ) involves changes in the degree of hydration. While the small quantities of ACS precipitated preclude full characterisation of this phase, it is clear that ACS must be hydrated as irradiation by the electron beam in the TEM can generate either hemihydrate or gypsum. Nevertheless, the very different morphologies of the isolated hemihydrate crystals as compared with the flat, micron-scale masses of ACC shows that restricted contact

with the solution cannot be a factor hindering the conversion. We therefore conclude that our experiments have revealed two very different mechanisms which can confer stability in confinement, one due to restricted contact with the solution (ACC), and the other due to hindered diffusion and aggregation (ACS).

## **5.6 Summary**

This chapter described investigations into the effects of confinement on the precipitation of calcium sulfate and demonstrates a remarkable stabilization of both amorphous calcium sulfate (ACS) and calcium sulfate hemihydrate with respect to gypsum in small volumes. Due to the aggregation-based mechanism of formation of calcium sulfate, the diffusion of the precursor particles is retarded in confinement, which slows down the transformation from hemihydrate to gypsum. The stabilization of ACS in confinement also demonstrates that confinement provides an effective route for identifying new polymorphs which may be too short-lived to detect during precipitation from bulk solution. This effect can be also enhanced with additives which can confer considerable additional stability on the metastable intermediate phases. Thus, these results provide evidence that the observation of hemihydrate statoliths (gravity-sensors) in deep-sea medusa,[198, 213] is likely to be due to the combined effects of both soluble additives and confinement.

### Chapter 6: ACP and OCP is Stable in Confinement



This work investigates the effect of confinement on the crystallization of calcium phosphate (CaP) crystals in the presence and absence of PAsp, extensively focus on the stability and transformation of amorphous phase and octacalcium phosphate different surface separations with the aim of better understanding the biological control which lead to the formation of bones and teeth. It is widely known that the precipitation of calcium phosphate in bone occurs in confine volumes and previous research also showed that that polyaspartic acid (PAsp) can influence the mineralisation of CaP in a similar way to the acidic non-collagenous proteins (NCPs) present in bone, leading to the effective infiltration of CaP particles into the gaps in collagen.[4, 32, 33] To investigate this further, calcium phosphate was precipitated in the presence and absence of polyaspartic acid (PAsp), in crossed-cylinder apparatus as mention in Chapter 5, to mimic the effect of confinement. Some thin plate-like octacalcium phosphate (OCP) crystals were formed, at the surface separation of 1  $\mu\text{m}$ , in the absence of PAsp. Interestingly, with addition of PAsp, agglomerations of nanoparticles were nanospheres also observed, shown as OCP. Both amorphous thin films and amorphous of calcium phosphate were observed in both confinement and additive. Thus the addition of PAsp seems to have a major effect to induce and stabilize metastable and amorphous phases in confinement. Although the method and reaction system employed was rather simple so it cannot be considered as a direct mimic of calcium phosphate precipitation in collagen, we do believe the experiments can provide insight into the control mechanisms which may operate *in vivo*.

## 6.1 Introduction to Calcium Phosphate

In contrast to many  $\text{CaCO}_3$  biominerals, the calcium phosphate (CaP) crystals found in biology are less interesting from a morphological perspective and usually take the form of nanometer scale platelets with irregular and ill-defined morphologies.[214] Calcium phosphate (CaP) biominerals are the main mineral constituents of the vertebrates, where they form bones and teeth. They have also been extensively investigated to understand the remarkable structure and physical properties of these biominerals, and from a mineral perspective their growth, dissolution, and phase stability.[65] The structural arrangement of bones is hierarchical such that small platelets are embedded within the fibrils of collagen. For example, osteonal bone is formed by calcium phosphate that is arranged concentrically around the vasculature, and the platelets are aligned roughly parallel within lamellae.[214] The high degree of mineral loading with collagen provides skeletal support with high strength and rigidity. The study of calcium phosphate formation is complicated by the possibility of forming several calcium phosphate phases at various conditions.

### 6.1.1 Transformation of the Polymorphs of Calcium Phosphate

Calcium phosphate exists in a range of phases with different molar ratios (Ca/P). In general, the lower the Ca/P ratio, the more acidic and soluble the calcium phosphate phase.[215] Most calcium phosphates are sparingly soluble in water, but all of them can dissolve in acids. The least soluble and most stable phase is hydroxyapatite (HAP). It has the formula  $\text{Ca}_{10}(\text{PO}_4)_6(\text{OH})_2$ , a molar ratio Ca/P of 1.67, and is preferentially formed under neutral or basic conditions. HAP may have either monoclinic or hexagonal unit cells in which rows of phosphate ions are located along the *a* axis, with calcium and hydroxide ions localized between the phosphate groups.[216] While in more acidic solutions, phases such as brushite (DCPD), which has the formula  $\text{CaHPO}_4 \cdot 2\text{H}_2\text{O}$  and molar ratio Ca/P of 1.00 and octacalcium phosphate (OCP), which has the formula  $\text{Ca}_8(\text{HPO}_4)_2(\text{PO}_4)_4 \cdot 5\text{H}_2\text{O}$  and molar ratio Ca/P of 1.33 are often encountered. [217, 218] The chains of  $\text{CaPO}_4$  are arranged parallel to each other in the DCPD crystal lattice with water molecules interlayered between the calcium phosphate chains.[15] The interesting aspect of this structure is that the two water bilayers have different ordering properties. The first is considered as the lattice water which is highly ordered while the second water layer exhibits

low ordering, which is correlated with the low solubility of DCPD in water.[15] The triclinic structure of octacalcium phosphate has a remarkable structural similarity to the hexagonal structure of HAP due to its layered structure involving apatitic and hydrated layers. This similar property makes OCP a possible precursor during the formation of HAP in the hard tissues of vertebrates.[219] Even under ideal HAP precipitation conditions, both DCPD and OCP have been implicated as possible precursors to the formation of apatite, suggesting nonstoichiometric precipitates. *In vivo*, this may occur during pathological calcification, and these acidic calcium phosphate phases, DCPD and OCP are usually detected where the pH is lower than normal. In the normal case, these phases are rarely observed, suggesting the involvement of other precursors or the formation of an initial amorphous calcium phosphate phase (ACP) followed by transformation to stable apatite. This precipitation pathway in biology is complicated by the presence of small peptides, proteins, and inorganic additives which have a considerable influence on crystallization, making it difficult to predict the possible phases that may form.[220]

### **6.1.2 Amorphous Calcium Phosphate**

Generally, it is believed that ACP was firstly described by Aaron S. Posner in the mid 1960s.[97] It is now agreed that, both *in vitro* and *in vivo*, amorphous calcium phosphate can act as a precursor phase that is structurally and chemically distinct from HAP.[97] This noncrystalline and hydrated calcium phosphate ( $\text{Ca}_3(\text{PO}_4)_2 \cdot x\text{H}_2\text{O}$ ) has Ca/P molar ratios from 1.18-2.50. The value of the pH is an important parameter in controlling of the Ca/P ratio of ACP phases. At pH 6.6, the Ca/P ratio is 1.18, at pH 11.7 the Ca/P ratio is 1.53, and values up to 2.50 can be reached.[219] The structure of ACP normally consists of roughly spherical, close-packed  $\text{Ca}_9(\text{PO}_4)_6$  clusters, with water in the interstices.[97] The amorphous calcium phosphate precursors at lower or higher pH values have the same  $\text{Ca}_9(\text{PO}_4)_6$  clusters (Ca/P ration is 1.35) with water composition, but differ in morphology and solubility.[23, 136] In general, ACP is a highly unstable phase that hydrolyzes almost instantaneously to more stable phases. These amorphous clusters can serve as seeds during crystallization of HAP.[195] While unlike ACC, recent experimental studies found that ACP with little long range order has definite local atomic

microcrystalline order rather than a random network structure, and contains 10-20% wt tightly bound water.[221]

In vivo or synthetically, ACP may be stable for appreciable periods of time in aqueous solution[220] depending on the presence of additive molecules or ions, pH, ionic strength, and temperature.[87] For example, polyaspartate adsorbs strongly and reduced the rate of dissolution of amorphous phases. Moreover, the adsorbed macromolecules also block the surface nucleation sites during the crystal growth process.[222] In biological system, disordered ACP has been reported as a precursor phase of carbonated hydroxyapatite of blue sharks in chiton teeth[15] and zebrafish fin bony rays during bone maturation.[223] The transient ACP phase may conceivably be deposited inside the gap regions of collagen fibrils and also be delivered as extrafibrillar particles, as suggested in synthetic collagen mineralization.[224]

### **6.1.3 Control crystallization process of calcium phosphate**

Many important biominerals, such as bones and teeth, are composite materials being constructed from inorganic crystals and organic matrices/ molecules. These organic components have the ability to control crystallization processes and can be either insoluble, or soluble.[1, 225] These soluble additives can modify the crystallization pathway and change the particle number density and size, as well as morphology and polymorph.[128] Insoluble macromolecular matrices such as collagen or chitin[9] also control crystallization processes such as biomineralization and weathering by formation of a confined mineralisation environment.[128]

#### **6.1.3.1 Calcium Phosphate growth in the presence of Additives**

Considering the presence of additive in confinement in this chapter, the effect of polyaspartic acid (PAsp) on the crystallisation of calcium phosphate will be discussed. It is widely known that PAsp has the inhibit effect on transformation of calcium phosphate from the amorphous phase to crystalline.[31, 33] In the presence of PAsp, stable ACP clusters can be observed as colloidal species where PAsp chains are cross-linked to keep calcium phosphate as stable amorphous

intermediate.[31] It is also suggested that the size of the amorphous particles became larger in the presence of PAsp.[226] Additionally, PAsp has also been suggested to induce and stabilize the formation of OCP by the specific adsorption onto the hydrated layer of the the (100) and (010) faces of OCP.[227, 228] And PAsp was able to sufficiently inhibit the OCP growth by 20% by covering only 1% of the (100) face.[228] The morphology of OCP was also influenced by the adsorption of Pasp with formation of spheres and reducing its dimensions.[229, 230] Also the splitting of OCP crystals along their *c*-axis is prevented by the addition of PAsp, thus inhibit the transformation into HAP.[227] The adsorption effect of PAsp onto the (010) face of DCPD also indicated a dynamic adsorption/desorption equilibrium mechanism.[231] With the adsorption, DCPD were observed as leaf-like appearance with fragmented stripes.[232] Actually, not only the transformation from amorphous phase into HAP was inhibited in the presence of PAsp, the size of crystals was also decreased.[233] And the size of HAP continue decreased with increasing amounts of PAsp.[234] Interestingly, a “hollow snowball” of HAP was formed by transforming from ACP, composed of single crystal HAP platelets.[31] The crystals had a more spindle or needle-like shape and clusters of tiny crystals can also formed with a plate-like morphology.[235, 236]

### **6.1.3.2 Calcium Phosphate growth in Confinement**

As discussed above, confined volume is another key feature of deposition biominerals, especially for the precipitation of calcium phosphate in bones and teeth during biomineralization. The clear evidence is CaP platelets with 2-10 nm in thickness which can be formed in nanoscale gap regions of collagen in bone and dentin.[237, 238] And it is also shown that the surfaces became increasingly important with reduction in volume thus control the crystallization process[239] by providing an obvious effect on the nucleation and crystal growth pathway of both calcium carbonate and calcium sulfate.[119, 240]

Actually, there were lots of synthetic systems to investigate the effect of microenvironment on the precipitation of calcium phosphate. The frequently used system was reverse micelles that lead to control over the size, shape and phases of

CaP.[241] For example, nanofibers of calcium phosphate, approximately 2 nm in width and 300  $\mu\text{m}$  in length can be formed by using reverse micelles of calcium bis(2-ethylhexyl) phosphate through aggregation-based precipitation pathway.[242] The nanofibers of calcium phosphate can also be obtained in double-hydrophilic block copolymer aggregates which direct the growth and form nanoscaled calcium phosphate.[243] It is known that the cationic surfactant CTAB has been used to regulate the nucleation and crystal growth, which leading to form HAP nanoparticles with uniform morphologies and controllable size.[244] Interestingly, octacalcium phosphate (OCP) crystals can be formed in gelatin which were used as templates for the crystal growth and assemblies. OCP preferentially grew as thin plates elongated along their *c* axes with large (100) faces parallel to the sheets of gelatin films.[245] And the crosslinked gelatin, which serve as a nanoenvironment supported the transformation of HAP from ACP via an octacalcium phosphate intermediate.[246] And also spherulitic crystals of OCP can be formed in  $\text{Ca}(\text{NO}_3)_2\text{-(NH}_4)_2\text{HPO}_4$ -agar system consisting out of an assembly of plate-like crystallites or whiskers.[247]

## **6.2 Aims of this Project**

Calcium phosphate (CaP) precipitated within the crossed-cylinder apparatus with/without poly(aspartic acid) (PAsp) and the influence of the surface separations in confinement on the resulting various polymorphs CaP was investigated in this chapter. In order to gain further understanding of the influence of confined reaction volumes on CaP precipitation, the experiments were carried out here using a two crossed glass cylinders that immersed in CaP solutions at 37°C. The surface separations between the crossed-cylinders were investigated from  $\mu\text{m}$  to 100 nm. Therefore the system can provide controlled environment, enabling study of the effects of a constrained volume. PAsp also has sufficient effect on nucleation and crystal growth of CaP which induces and stabilizes amorphous calcium phosphate and OCP intermediate phase in the constrained volume.

## 6.3 Experimental

Calcium phosphate (CaP) was precipitated within the confines of the crossed-cylinder apparatus in the presence and absence of poly(aspartic acid) (PAsp), and the influence of the surface separations of confinement and the additive concentrations on the resulting particles was investigated.

### 6.3.1 Precipitation of Calcium Phosphate

According to the experiments by Olszta et al[30], 8.77g of NaCl, 6.61g of Tris-HCl and 0.96g of Tris-base (Sigma-Aldrich) was dissolved in 1L 18 M $\Omega$ /cm ultra-pure Millipore water for preparing the Tris-Slaine buffer solution. The pH of this buffer solution was measured as 7.68 at 25°C.

9 mM calcium chloride and 4.2 mM potassium hydrogen phosphate trihydrate were prepared by dissolving CaCl<sub>2</sub>·2H<sub>2</sub>O and K<sub>2</sub>HPO<sub>4</sub>·3H<sub>2</sub>O (Sigma-Aldrich), respectively, in the buffer stock solution. NaOH was used to adjust the pH of both solutions to 7.4 at 37°C.

Polyaspartic acid sodium salt solution (Poly-(alpha,beta)-DL-aspartic acid sodium salt Mw 2000 - 11000 Da) was added to K<sub>2</sub>HPO<sub>4</sub>·3H<sub>2</sub>O solution with a concentration range of 10  $\mu$ g/ml to 100  $\mu$ g/ml.

### 6.3.2 Crossed-Cylinder Experiment

To synthesise the CaP precipitates inside the confinement volume at various surface separations, the crossed-cylinder apparatus described in Chapter 5 was used. The crossed-cylinder glasses with TEM grid in the middle were immersed in the prepared CaP solution in a beaker. This was prepared by adding 50 mL buffered K<sub>2</sub>HPO<sub>4</sub>·3H<sub>2</sub>O solution with/without additive to 50 mL buffered CaCl<sub>2</sub>·2H<sub>2</sub>O solution. The solutions were then degassed under vacuum and left at 37°C in an oven for 3 hrs to 6 days. Precipitation was terminated by removing the holder from the solution and flushing the system with ethanol and drying with nitrogen gas while the surfaces were still in contact. The grid was rinsed with ethanol and dried with filter paper and the half cylinders then slowly separated.

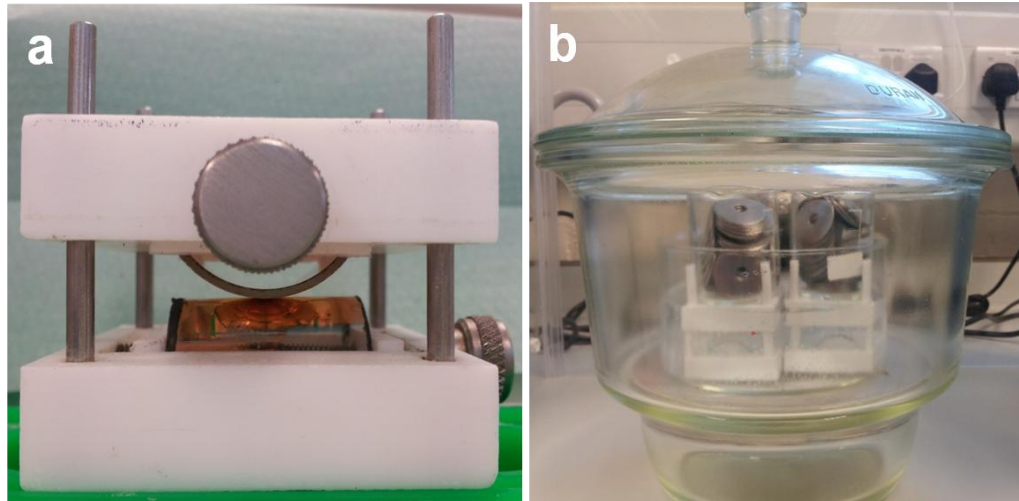


**Fig 6.1** a) Metal pieces are gradually placed on the top of the holder surface. b) Crossed-cylinder glasses with TEM grid were immersed in CaP solution in a beaker. After degassing, the beaker in a desiccator was placed at 37°C in an oven for 3 hrs to 6 days.

### 6.3.3 Control Experiment

Control experiments were performed where calcium phosphate was precipitated in bulk solution. Aqueous solutions of buffered 9 mM  $\text{CaCl}_2 \cdot 2\text{H}_2\text{O}$  solution and buffered 4.2 mM  $\text{K}_2\text{HPO}_4 \cdot 3\text{H}_2\text{O}$  solution were combined in a crystallization dish. Glass slides were placed at the base of the dish, and crystallization was allowed to proceed from the solution. For experiments carried out in the presence of the additive, this was introduced into the  $\text{K}_2\text{HPO}_4 \cdot 3\text{H}_2\text{O}$  solution prior to mixing with the calcium solution. The precipitates formed in bulk were then isolated by filtration through a 0.2  $\mu\text{m}$  filter membrane, washing with ethanol and air-drying and characterisation was performed using a range of techniques. Copper TEM grids were also dipped in the solution to observe precipitates using TEM, after which they were washed in ethanol and dried with filter paper.

### 6.3.4 Characterization Methods

The precipitates were imaged with Scanning Electron Microscopy (SEM) and Transmission Electron Microscopy (TEM) with associated Energy-Dispersive X-ray Analysis (EDX). For SEM, glass cylinders supporting calcium phosphate particles were mounted on SEM stubs using conducting carbon tape, which were then sputter-

coated with a 5 nm layer of Pt. All samples were examined using a Phillips XL-30 ESEM or a Leo 5000-SEM operating at 3 kV. The region on TEM grid around the contact point of the half-cylinders was found by identifying a region with scratches and devoid of precipitates using a Phillips Tecnai FEG-TEM operating at 200 kV. EDS was performed to determine the elemental composition and confirm the presence of phosphate and calcium.

## 6.4 Results

### 6.4.1 CaP precipitation in bulk solution

Control experiments were conducted in which calcium phosphate was precipitated from bulk solution in the absence and in the presence of additives. In bulk solution, amorphous calcium phosphate (ACP) was the main product after 1 hour from the calcium phosphate solution at 37 °C. The particle sizes of ACP were around 20 nm and the particles were characterised using TEM and EDX (shown in Fig 6.2a). After 2 hours, ACP particles were still observed. After 5 hours, all calcium phosphate had transformed into hydroxyapatite (HAP) as confirmed by TEM (shown in Fig 6.2d), Raman microscopy (Fig 6.3) and XRD (Fig 6.4).

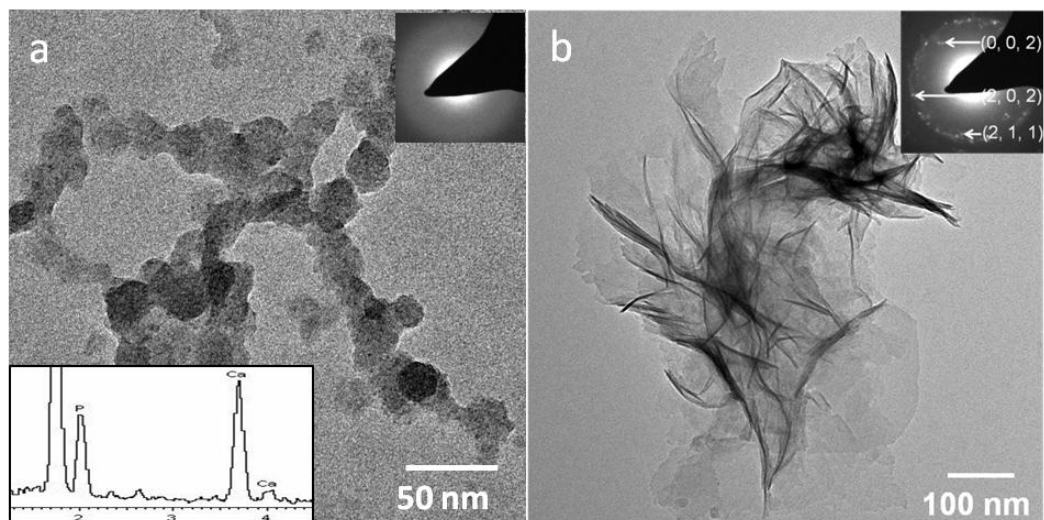


**Figure 6.2** TEM images, electron diffraction patterns and EDX data of CaP particles precipitated from a buffered solution of calcium phosphate in the absence of PAsp at 37 °C (a) After 1 h, most of the particles were amorphous phase and exhibit a Ca/P ratio of 1.15. And (b) after 5 hour, all the calcium phosphate precipitates were transformed to HPA.

As shown in Figure 6.3, the peaks in the Raman spectrum of the calcium phosphate precipitates were at  $961\text{ cm}^{-1}$ , which corresponds to the symmetric stretching mode (v1) of the tetrahedral  $\text{PO}_4$  group (P–O bond). The bending mode (v4) of the  $\text{PO}_4$  group (O–P–O bond) appears as a shift at  $590\text{ cm}^{-1}$ . Peaks at  $429\text{ cm}^{-1}$  and  $443\text{ cm}^{-1}$  correspond to the doubly degenerate bending mode (v2) of the  $\text{PO}_4$  group (O–P–O bond). The weak peak at  $1043\text{ cm}^{-1}$  is part of the triply degenerate asymmetric stretching mode (v3) of the  $\text{PO}_4$  group (P–O bond). This corresponds to HAP.[30] XRD was also confirmed that the precipitates of calcium phosphate were HAP (as shown in Fig 6.4).

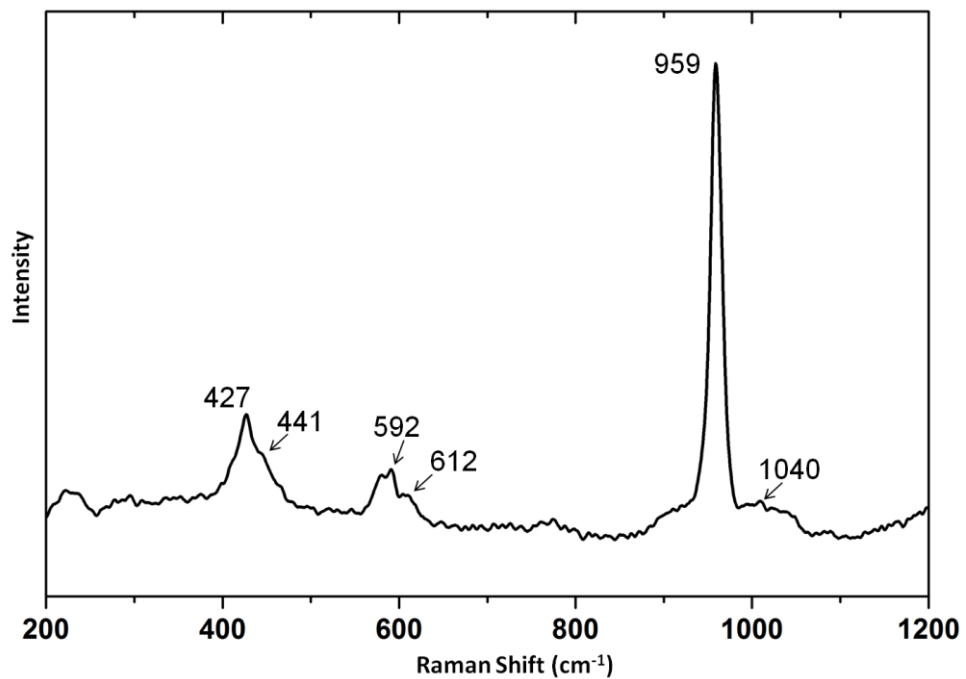


**Figure 6.3** Raman spectrum of CaP produced in bulk solution after 5 hrs at  $37\text{ }^{\circ}\text{C}$ . Analysis of the spectrum showed the produced material was HAP.

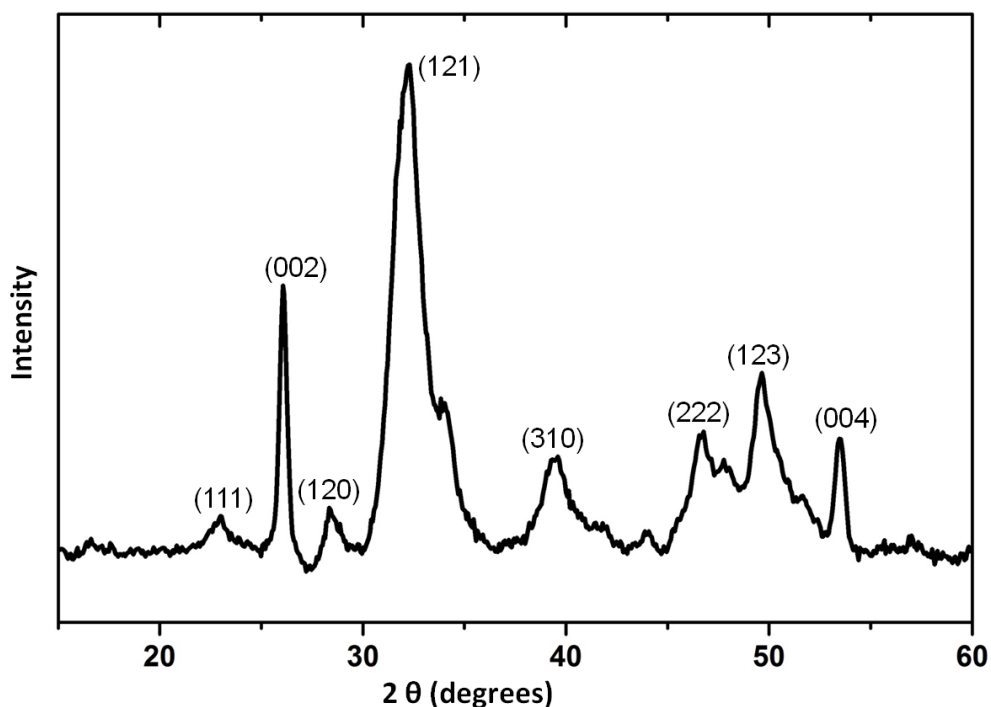


**Figure 6.4** The X-ray diffraction spectrum of calcium phosphate precipitates obtained in the bulk solution after 5 hrs at 37 °C, corresponding with HAP.

The effect of PAsp on the precipitation of calcium phosphate in bulk solution was also investigated. PAsp was added at concentrations of 10 µg/ml, where it had a marked inhibitory effect on the crystallization process, stabilizing the amorphous calcium phosphate phase. The precipitates formed over time were investigated using TEM. In the presence of 10 µg/ml PAsp after 1 day, most of the particles were amorphous calcium phosphate (Fig 6.5 a). While after 3 days, both amorphous nanoparticles and plate-like crystals can be observed. These thin plate-like crystals were shown as octacalcium phosphate (OCP) by diffraction patterns (shown in Fig 6.5b). While after 5 days, all the precipitates were crystals, shown as mixture of HAP and OCP. And 1 week after, all the crystals were HAP without any OCP anymore (shown in Fig 6.5d)

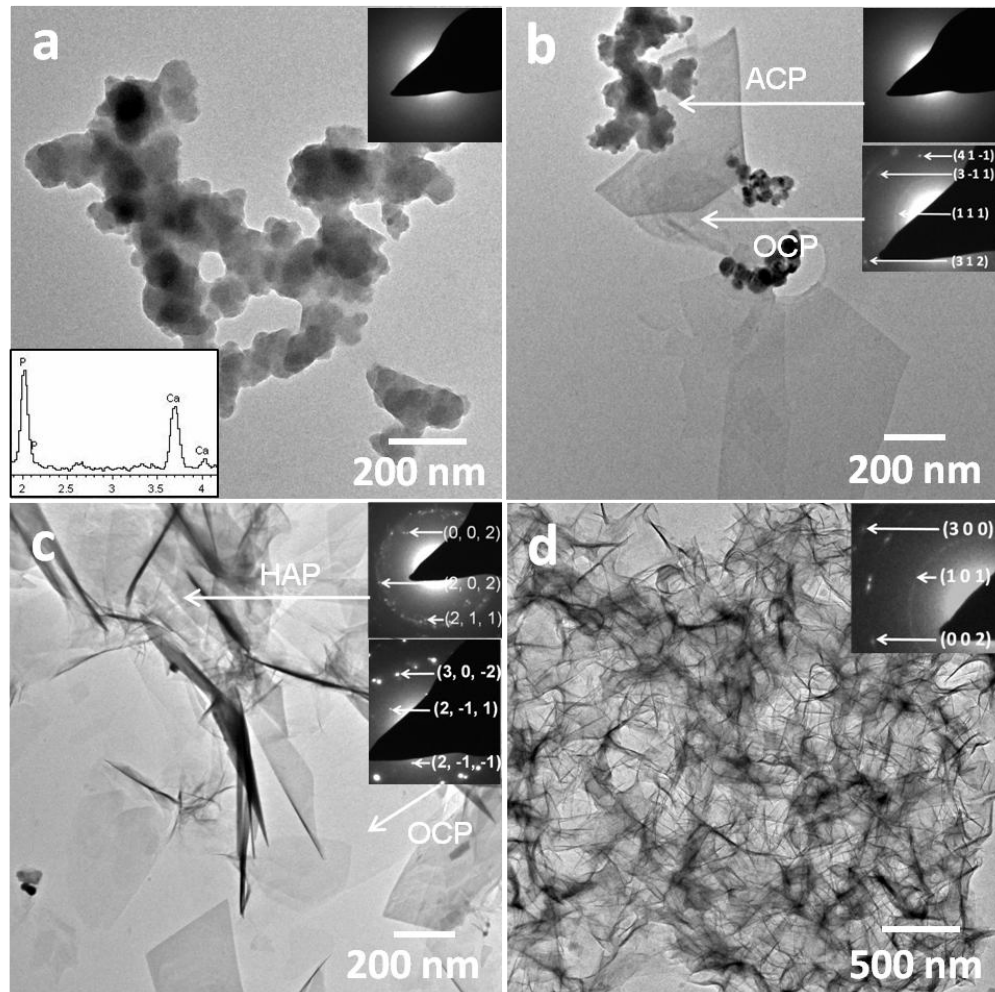


**Figure 6.5** TEM images of calcium phosphate precipitates in the presence of PAsp PAsp 10  $\mu\text{g/ml}$  at 37  $^{\circ}\text{C}$  after a) 1 day, shown as amorphous calcium phosphate crystals and was confirmed by electron diffraction. (b) After 3 days, nearly all the crystals were OCP and amorphous nanoparticles can still be observed. (c) After 5 days, all the precipitates were crystals and shown as mixture of OCP and HAP. And (d) after 1 week, both amorphous particles and OCP disappear and only HAP can be observed.

#### 6.4.2 CaP precipitation in Confinement in the absence of PAsp

The effect of confinement on calcium phosphate precipitation was investigated using the crossed-cylinder apparatus. The separation of the annular wedge between two half cylinder glasses in which calcium phosphate is precipitated were investigated from 5  $\mu\text{m}$  to 100 nm. Both TEM and SEM were used to characterize the particles between the cylinders at 37  $^{\circ}\text{C}$  after 3 days in the absence of additives.

When the surface separation ( $SS$ ) was greater than  $5\ \mu\text{m}$ , the crystals grew as clusters of micron-size, intergrown crystals with flower-like morphologies (Fig 6.6a). These were confirmed as HAP are thus identical to those produced in bulk solution. Closer to the contact point,  $SS = 2\ \mu\text{m}$ , normal HAP clusters were observed, although with lower density of crystals, as shown in Fig 6.6b. Marked changes in the CaP precipitates were observed at surface separations around  $1.5\ \mu\text{m}$ , where the crystals now appeared as  $1\ \mu\text{m}$  flattened clusters (Fig 6.6c). Electron diffraction (Fig 6.6d) confirmed that these crystals are still HAP, which is consistent with the crystal morphologies. Unlike HAP crystals precipitated in bulk, the morphologies of the HAP particles formed at  $SS = 1.5\ \mu\text{m}$  are affected by confinement.

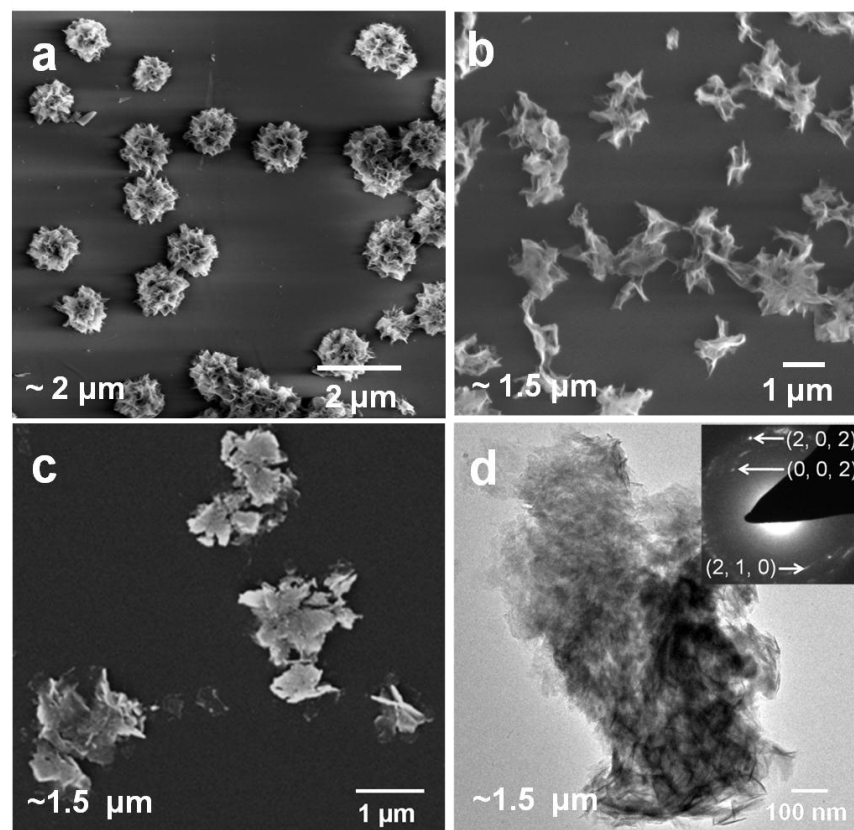


**Figure 6.6** SEM and TEM images of calcium phosphate precipitates in confinement at  $37\ ^\circ\text{C}$  after 3 days at surface separations of a)  $5\ \mu\text{m}$ , most of the precipitates were HAP as in bulk solution. b)  $2\ \mu\text{m}$ , calcium phosphate precipitates were still HAP with lower crystal density. c)  $1.5\ \mu\text{m}$ , plate-like calcium phosphate crystals were observed and d) electron diffraction was shown as HAP.

Further changes in the calcium phosphate precipitates were observed at smaller surface separations. In the region where  $SS = 1 \mu\text{m}$ , most of the precipitates appear as thin, plate-like crystals (Fig 6.7 a and b). Some of the large plates were several hundred nanometer in length, although some larger plates and aggregates of smaller plates were also present. As confirmed by electron diffraction in Figure 6.7c, these plate-like crystals were octacalcium phosphate (OCP). EDX (Fig 6.7d) showed very strong Ca and P peaks.

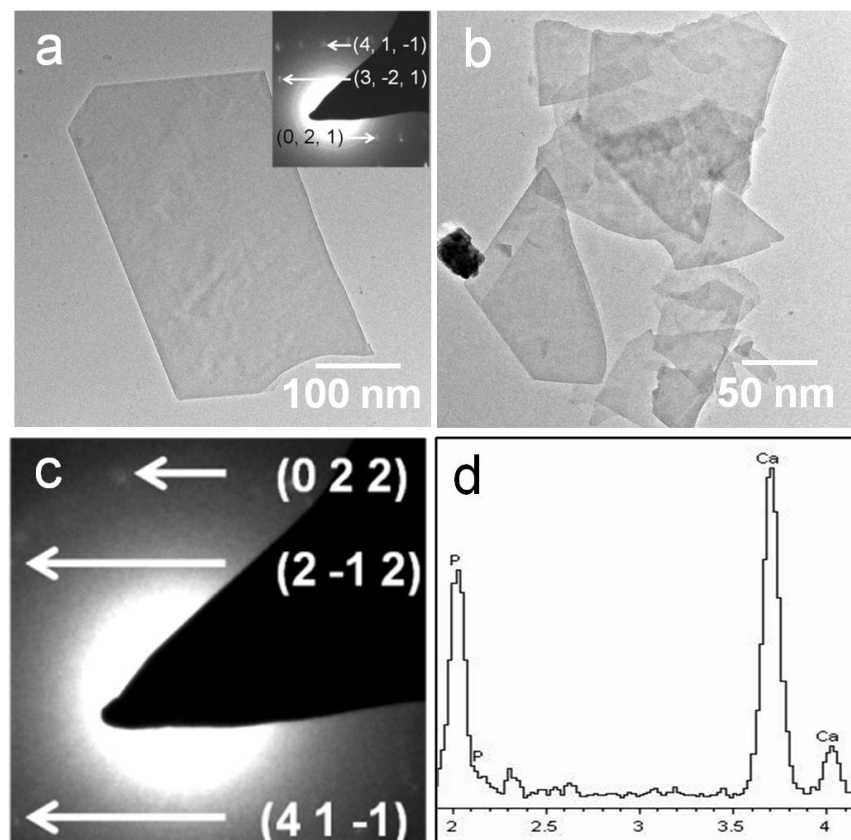


**Figure 6.7** TEM images of calcium phosphate precipitates in confinement at  $37\text{ }^\circ\text{C}$  after 3 days at surface separations of  $1\ \mu\text{m}$ . a) some of the precipitates were thin plate-like crystals, several hundred nanometer in length. b) some of the precipitates were aggregated smaller thin plates. c) Electron diffraction showed these thin plate-like crystals were OCP and d) EDX showed strong Ca and P peaks.

The edges and faces of the precipitated crystals also became progressively more irregular with increased confinement, as shown in Figures 6.8a and b, for  $SS = 0.5 \mu\text{m}$ . In this separation regime, nanospheres were also observed together with the plate-like crystals. These plate-like crystals were again OCP as observed at  $1 \mu\text{m}$  surface separation (shown in Fig 6.8c). The aggregates of 30-40 nm nanoparticles were shown to contain Ca and P using EDX and no evidence for crystallinity was found by selected area electron diffraction (Fig 6.8d).

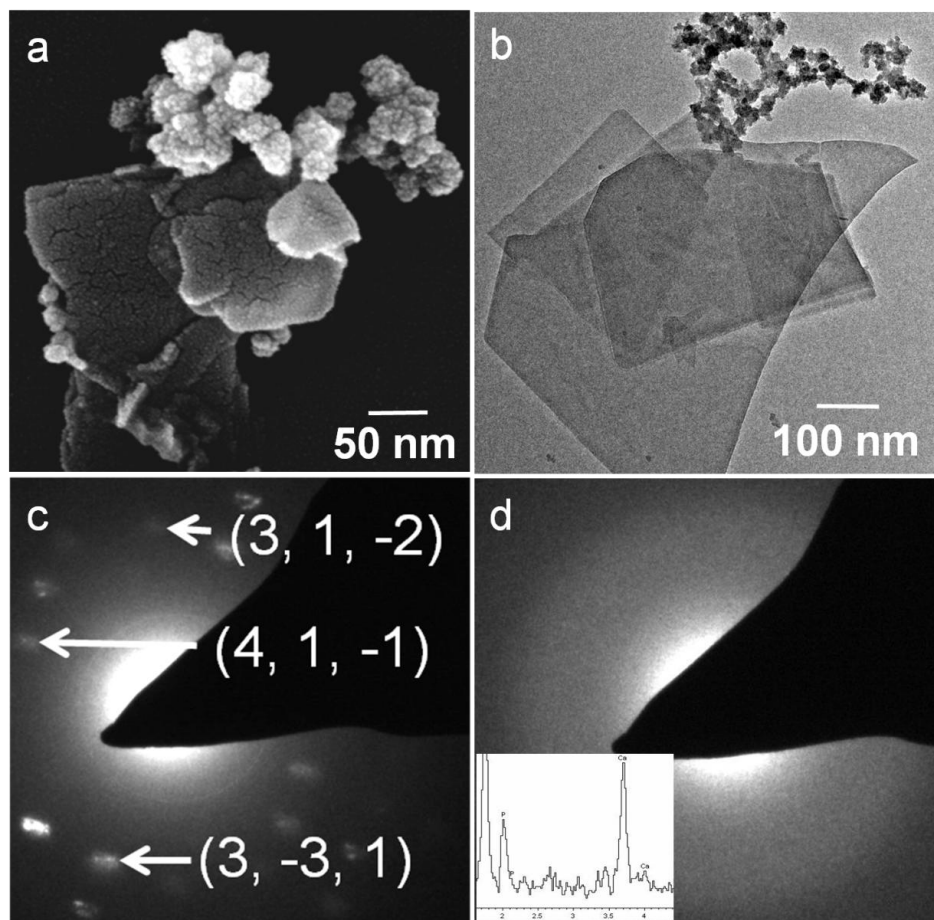


**Figure 6.8** SEM and TEM images of calcium phosphate precipitates in confinement at  $37 \text{ }^\circ\text{C}$  after 3 days at surface separations of  $0.5 \mu\text{m}$ . a) some of the precipitates were thin plate-like crystals, several hundred nanometer in length with nanoparticles, 30-50 nm in the diameter. b) corresponding TEM images of the same areas, similar particles. Electron diffraction showed c) these thin plate-like crystals were OCP and d) nanoparticles with no evidence for crystallinity and inserted EDX images showed Ca and P peaks.

Very close to the contact point, in the region where  $SS = 0.2 \mu\text{m}$ , all the precipitates were nanoparticles that were 30-50 nm in diameter (Fig 6.9 a and b). As confirmed by electron diffraction in Figure 6.9c, these nanoparticles were amorphous calcium phosphate and EDX (Fig 6.9d) showed Ca and P peaks. Interestingly, I emphasise that these amorphous particles were viewed after 3 days in nanometer scale separations, while this amorphous phase could not be found at all in bulk after 3 hours.

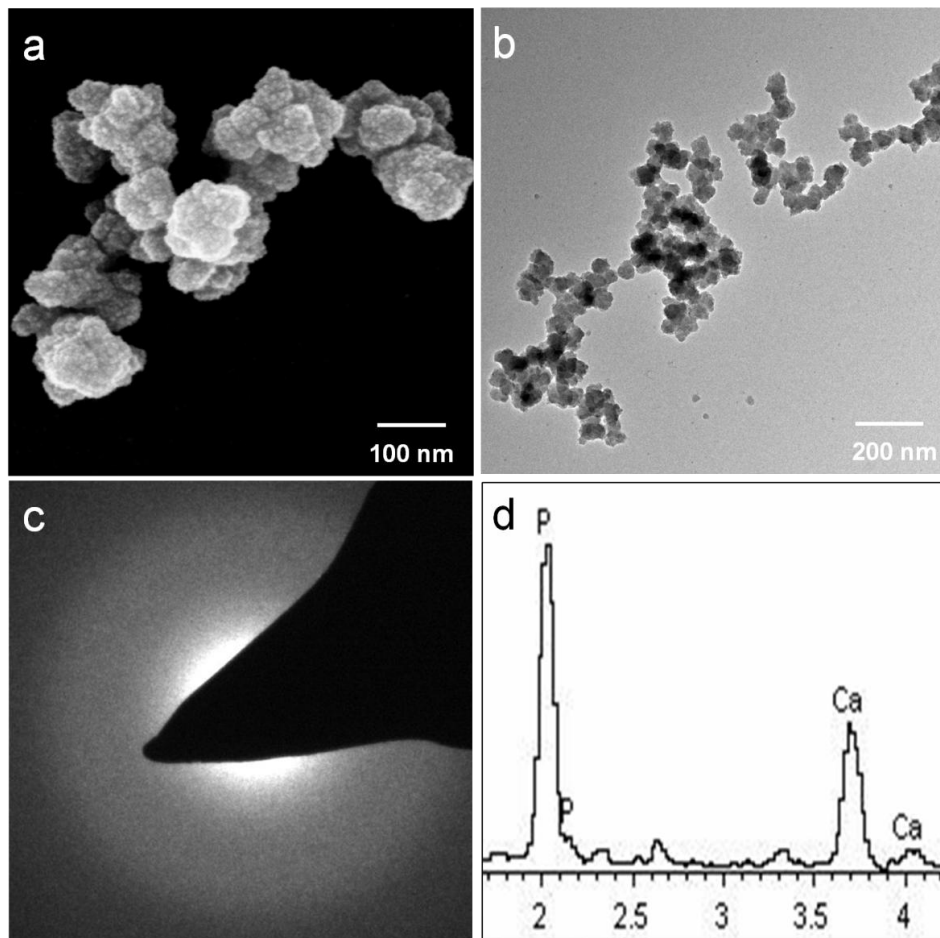


**Figure 6.9** SEM and TEM images of calcium phosphate precipitates in confinement at 37 °C after 3 days at surface separations of 0.2  $\mu\text{m}$ . a) All the precipitates were nanoparticles, 30-50 nm in the diameter. b) corresponding TEM images of the same areas, similar particles. c) Electron diffraction showed these nanoparticles with no evidence for crystallinity and d) EDX images showed Ca and P peaks.

### **6.4.3 CaP precipitation in Confinement in the presence of PAsp**

The combined effects of confined volumes and soluble additives were also investigated, with the goal of gaining insight into the possible role of the non-collagenous proteins in the mineralisation of collagen fibrils. Poly(aspartic acid) (PAsp) was selected as it has been considered an effective mimic of the non-collagenous proteins implicated in the mineralization of collagen with CaP and mineralisation of collagen fibrils to give structures comparable to native bone has been achieved by combining both components and using poly(aspartic acid) (PAsp) as an analogue of the non-collagenous proteins.[128] Control experiments conducted in bulk solution in the presence of  $10 \mu\text{g ml}^{-1}$  PAsp showed that this polymer inhibited crystallisation and stabilised ACP up to 3 days, such that crystallisation to HAP occurred within 5 days (as shown in Fig 6.5). An identical precipitation solution was then employed in the crossed cylinders apparatus, and samples were analysed after 1 week. In common with results obtained in the absence of PAsp, clusters of HAP crystals precipitated at surface separations of around  $5 \mu\text{m}$  and greater, as confirmed by TEM (shown as Fig6.10 a and b). Looking at smaller separations of  $SS = 2\text{-}5 \mu\text{m}$ , all the precipitates were still HAP while shown as flattened aggregates thin plates (shown Fig6.10c and d).

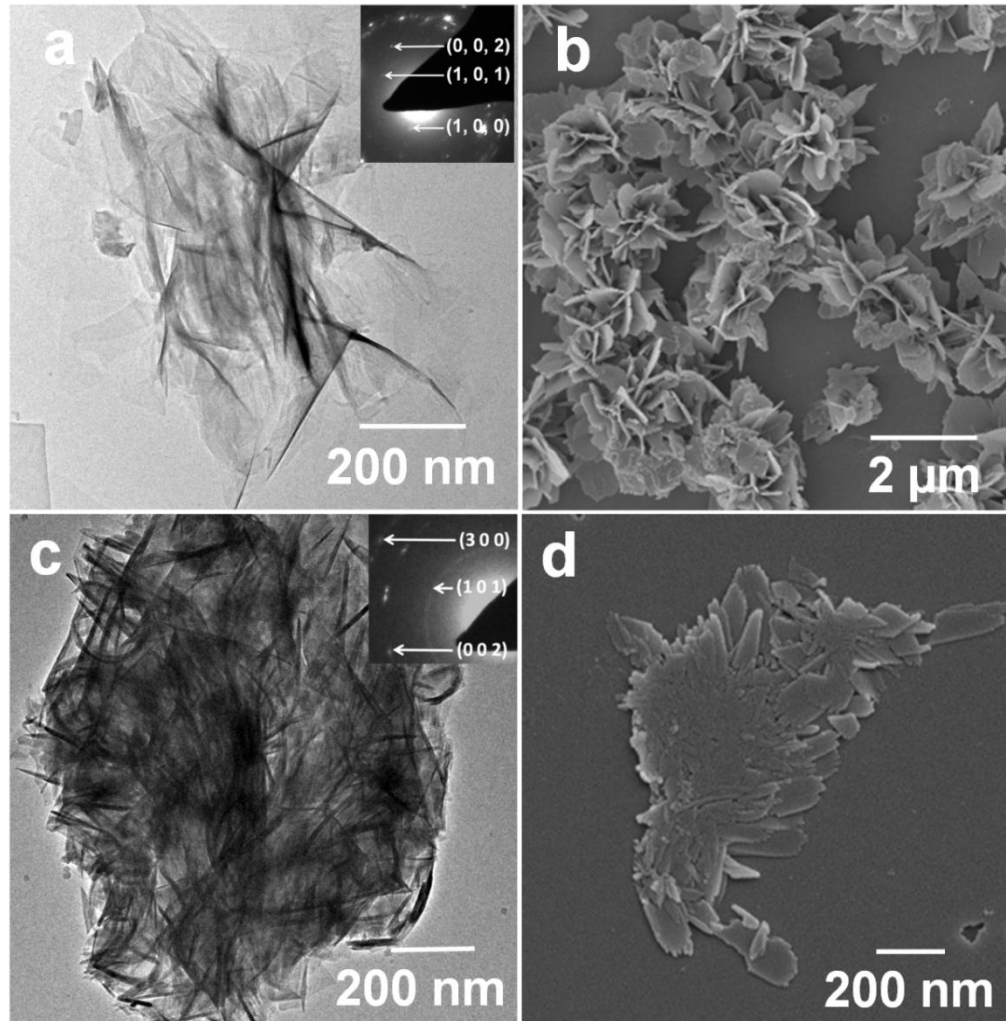


**Figure 6.10** TEM and SEM images of calcium phosphate precipitates formed in confinement at 37 °C after 1 week in the presence of 10 μm/mL PAsp at surface separations of a),b) above 5 μm, all the precipitates were HAP and c), d) at surface separations between 2-5 μm, calcium phosphate were shown as flattened aggregates.

Precipitation of CaP in confinement resulted in a marked stabilization of its metastable phases, as shown in Fig6.7 and Fig6.8. While thin, plate-like OCP crystals were found in confinement at  $SS = 1 \mu\text{m}$  after 3 days in the additive-free system, these plates were still observed and showed considerable stability (Fig 6.11a and b) after 1 week at  $SS = 1.5 \mu\text{m}$  in the presence of PAsp. Interestingly, aggregates of nanospheres were also observed at  $SS = 1 \mu\text{m}$  with each of the nanospheres being 20-30 nm in the diameter (Fig 6.11c and d). The EDX of these nanoparticle aggregates showed very strong Ca and P peaks and electron diffraction confirmed

that they were OCP. As far as we are aware, this structure of OCP were never been observed in bulk solution with/without additive.

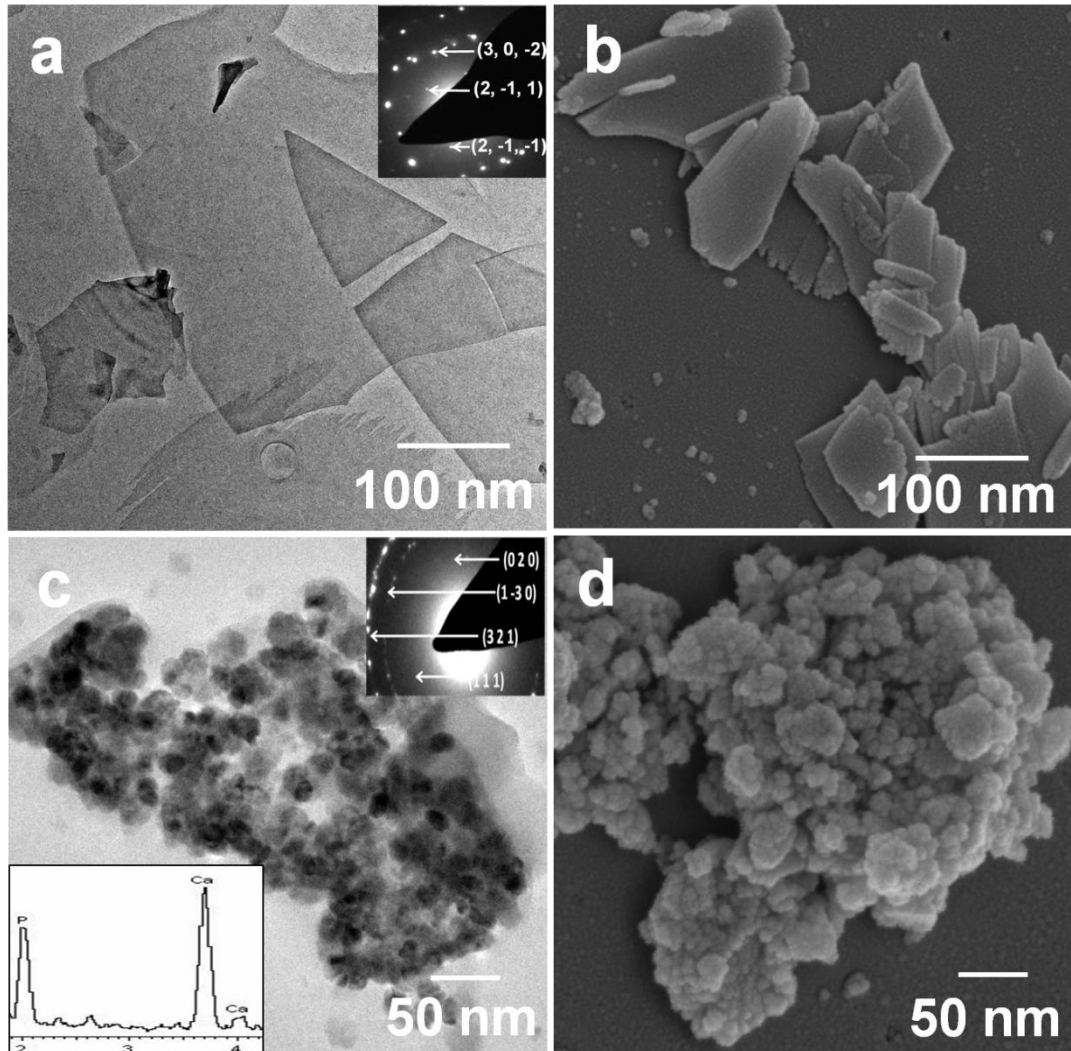


**Figure 6.11** TEM and SEM images of calcium phosphate precipitates in confinement at 37 °C after 1 week in the presence of 10 μm/mL PAsp at surface separations of a),b) 1.5 μm, all the precipitates were plate-like OCP and c), d) at surface separations of 1 μm, calcium phosphate were shown as agglomeration of nanospheres and electron diffraction showed them were OCP.

As highlighted before, PAsp has been shown to influence CaP precipitation and stabilise the amorphous phase.[31, 234] It is also suggested that with addition of PAsp, a “Polymer-Induced Liquid Precursor” (PILP) phase can be found, although this observation has been made based on infiltration into collagen fibers only.[30]

Actually, in the crossed-cylinder apparatus with addition of PAsp and a surface separation of 0.5  $\mu\text{m}$ , patches of an amorphous thin film were observed (Fig 6.12 a and b). Some areas of these aggregates were composed of nano-sized particles which were less than 20 nm in diameter. At a surface separation of 200 nm after 1 week, amorphous nanoparticles of around 20 nm in size were observed (Fig 6.12 c and d) which were quite stable and smaller in size than those grown in bulk solution in the presence of PAsp, or in confinement in the additive-free system. The experiments therefore demonstrate that in combination, confinement and additives can provide considerable stabilization of the metastable polymorphs of calcium phosphate.

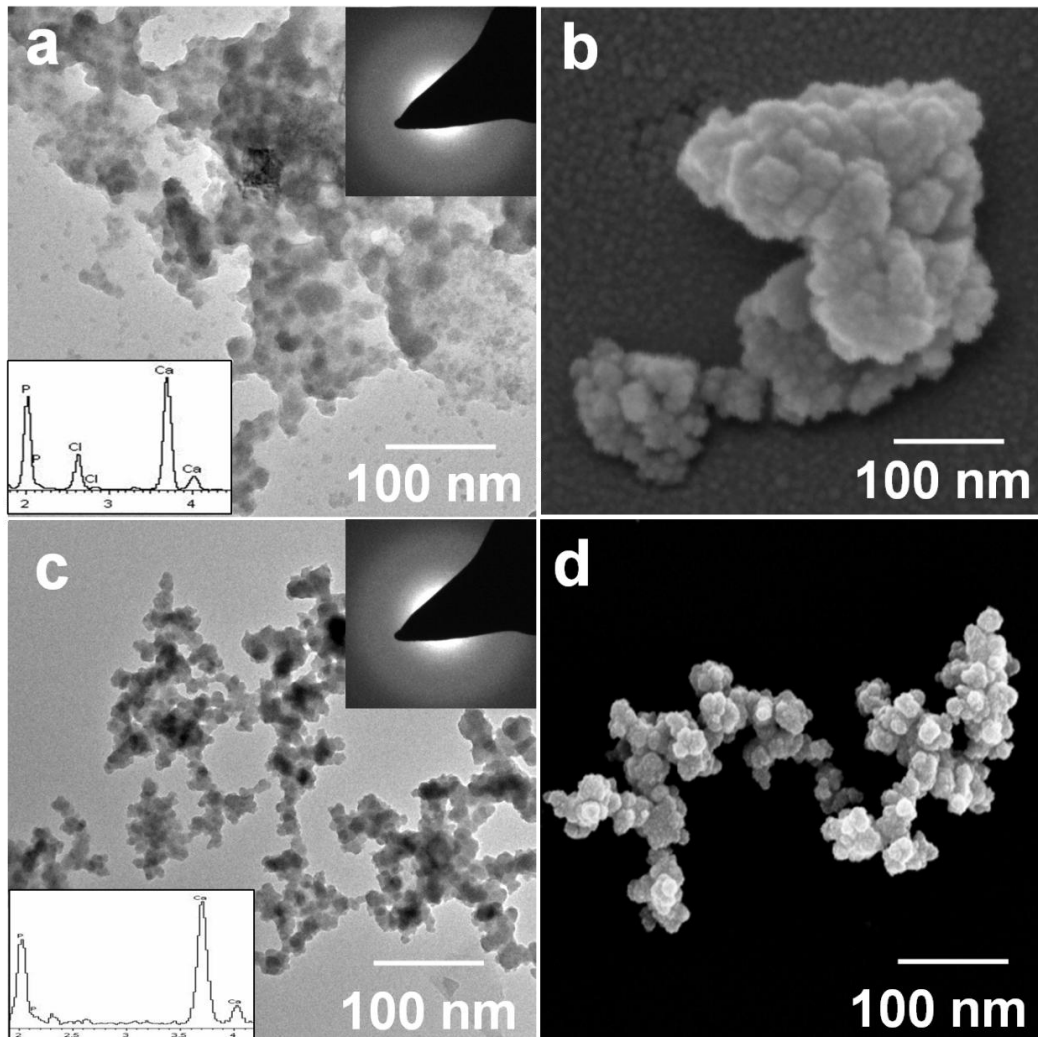


**Figure 6.12** TEM and SEM images of calcium phosphate precipitates in confinement at 37 °C after 1 week in the presence of 10 µm/mL PAsp at surface separations of a),b) 0.5 µm, all the precipitates were amorphous CaP, showed as thin films and c), d) at surface separations of 0.2 µm, calcium phosphate were shown as aggregations of nanospheres and electron diffraction showed no crystallinity.

## 6.5 Discussion

These results mentioned above demonstrated calcium phosphate precipitates were successfully growth in crossed-cylinder apparatus. Using this micro to nanoenvironment gave the precipitates not only HAP, but also OCP and amorphous calcium phosphate, which could be expected since this system allowed stabilizing the metastable and amorphous phases in confined volumes. In the presence of PAsp, the amorphous phase was stabilized for a longer time (6 days in 200 nm surface separation) compared with the results in the absence of additive that only 2 hour in bulk solution and 3 days in the same surface separation. ). This is also expected since it has been shown previously that the lifetime of ACP can be increased by the addition of soluble additive.[31]

Considering the precipitation of CaP in the absence of PAsp, comparison of the precipitates formed in the bulk solution with those which were produced in the crossed-cylinder apparatus, demonstrated that confinement in the surface separations used here from nanometers to 2 µm had significant effect on the precipitation of CaP, influencing the size, morphology, orientation, polymorphs and the rate of crystallization. By growing the precipitates in confinement at the surface separation of 1.5 µm, morphologically distinct plate-like HAP was generated, while only clusters of platelets of HAP were found in bulk solution. Both TEM and SEM images revealed the internal structure those comprising HAP platelets which suggested significant intergrowth in confinement. In addition to the effect on the morphology of HAP, a further very interesting effect of confinement was on the crystal polymorphs and the rate of crystallisation. Crystalline HAP was the unique product that found in additive-free bulk solutions after 3 days, while only hydrated amorphous CaP was observed at surface separation 200 nm after the same time. This

result was consistent with previous studies of calcium carbonate and calcium sulfate precipitation in crossed-cylinder apparatus, which demonstrated that both amorphous calcium carbonate (ACC) and amorphous calcium sulfate (ACS) is stabilised in an annular wedge when the surface separation is less than 200 nm.[119, 248] In this work the stabilisation of amorphous CaP provided a similar mechanism that there was a limitation contact of ACC or ACS particles with the solution resulting in its stabilisation in the centre of crossed-cylinders. Interestingly, the results also demonstrated that it was possible to form OCP in confinement. These thin plate-like OCP were entirely distinct from the crystal observed in bulk in control reactions. Similar results were also found when calcium phosphate was crystallised within crosslinked gelatin nanoparticles and gelatin films with sizes of hundreds of nanometer scale.[245, 246] This result again suggested the possible pathway that HAP was formed through an amorphous phase via an OCP intermediate. Many methods have also used to form similarly-sized OCP crystals as an intermediary phase, although the vast majority were formed under hydrothermal conditions and in the presence of organic additives.[128] The mechanisms of OCP to HAP has also been revealed by titration and high resolution TEM that both solid-state transformation and dissolve-reprecipitation can occur.[36, 249]

However, the greatest effect of confinement was surprisingly seen together with PAsp, that by addition of PAsp it was suggested to increase the stability of metastable and amorphous phase. Emanating from the observation that plate-like HAP can be formed in confinement in additive-free system, that was further supported in the presence of PAsp, which revealed that the plate-like HAP are more stable in a larger surface separation. And with the observation of thin plate-like OCP from TEM and SEM images, the plate-like HAP were thought to be formed by aggregation of plate-like OCP crystals. Furthermore, agglomerations of nanoparticles were also observed at the surface separation around 0.5 – 1  $\mu\text{m}$ , which shown as OCP crystals under diffraction. Here another possible precipitation pathway was provided that the transformation of OCP from aggregation of amorphous nanoparticles. Interestingly, amorphous thin films were formed in the half micrometer surface separation with addition of PAsp in confinement. It was never properly proved before that CaP is able to form thin films in confinement with additives. While in  $\text{Ca}^{2+}/\text{CO}_3^{2-}/\text{PAsp}$  system, it was believed that subsequent addition of carbonate ions resulted in the generation of amorphous calcium

carbonate, then forming precipitates with extraordinary morphologies such as films and fibers.[9, 38] And the precipitation of CaP to the nanometer sized gaps in collagen fibers provided a principal evidence that the amorphous films CaP could be formed into the collagen fibers by capillarity action.[250]

CaP precipitation is complex, with intermediate phases frequently forming prior to the thermodynamically favoured phase. HAP is the thermodynamically most stable phase from weakly acidic to basic conditions, but as it can be significantly slower to form than ACP or OCP, kinetic factors can support the formation of these polymorphs as intermediate species. Study of the transformation of OCP to HAP has suggested that this can occur either by a dissolution/ reprecipitation mechanism or by a solid-state transformation in which hydrolysis of an OCP unit cell leads to a two unit cell thick layer of HAP.[251] ACP in turn is highly unstable in solution, and has been considered to crystallise either via full dissolution/ reprecipitation, or possibly via dissociation into clusters rather than complete ionic solvation.

A recent detailed study of the mechanism of CaP precipitation in solutions supersaturated with HAP has shown that this process is based on the aggregation of calcium triphosphate complexes.[128] These complexes are initially present in the solution and subsequently aggregate into polymeric structures. Nucleation of ACP occurs through uptake of calcium ions to form post-nucleation clusters, which aggregation leads to their precipitation. Continued calcium uptake converts ACP into octacalcium phosphate (OCP) and ultimately HAP. That the precipitation process proceeds by an aggregation-based mechanism may provide an explanation for the significant effects of confinement – where stabilisation of the mesostable phases. OCP formation is affected by many solution factors including the pH, the concentrations of calcium and phosphate ions and the calcium to phosphate ratio. The observation of OCP as a precursor to HAP is strongly dependent on the solution pH, being more prevalent under neutral/ acidic conditions. The rate of crystallisation of ACP is well-recognised to strongly depend on variables including the pH, ionic strength, temperature and the presence of additives.[128]

Considering the relevance of these results to biomineralization processes, and the formation of bone in particular, much less is known about the mechanism of HAP

formation in vivo than in bulk solution, due to the significant problems associated with studying biomineralization processes. After many decades of debate, it is finally accepted that bone tissues can form via an ACP precursor phase, where this was determined by studying the forming cranial suture of a mouse[128] and the continuously forming fin bony rays of zebrafish.[128] That OCP can act as an intermediate between ACP and HAP during bone formation has also been widely discussed, but remains controversial.[128] In its support, the so-called central dark line observed by TEM in biogenic HAP has been attributed to a central OCP occlusion which may derive from the lattice mismatch between OCP and HAP.[128] OCP has also been observed in the forming cranial suture of a mouse using Raman spectroscopy, where it is notable that these samples were characterised without dehydration.[128]

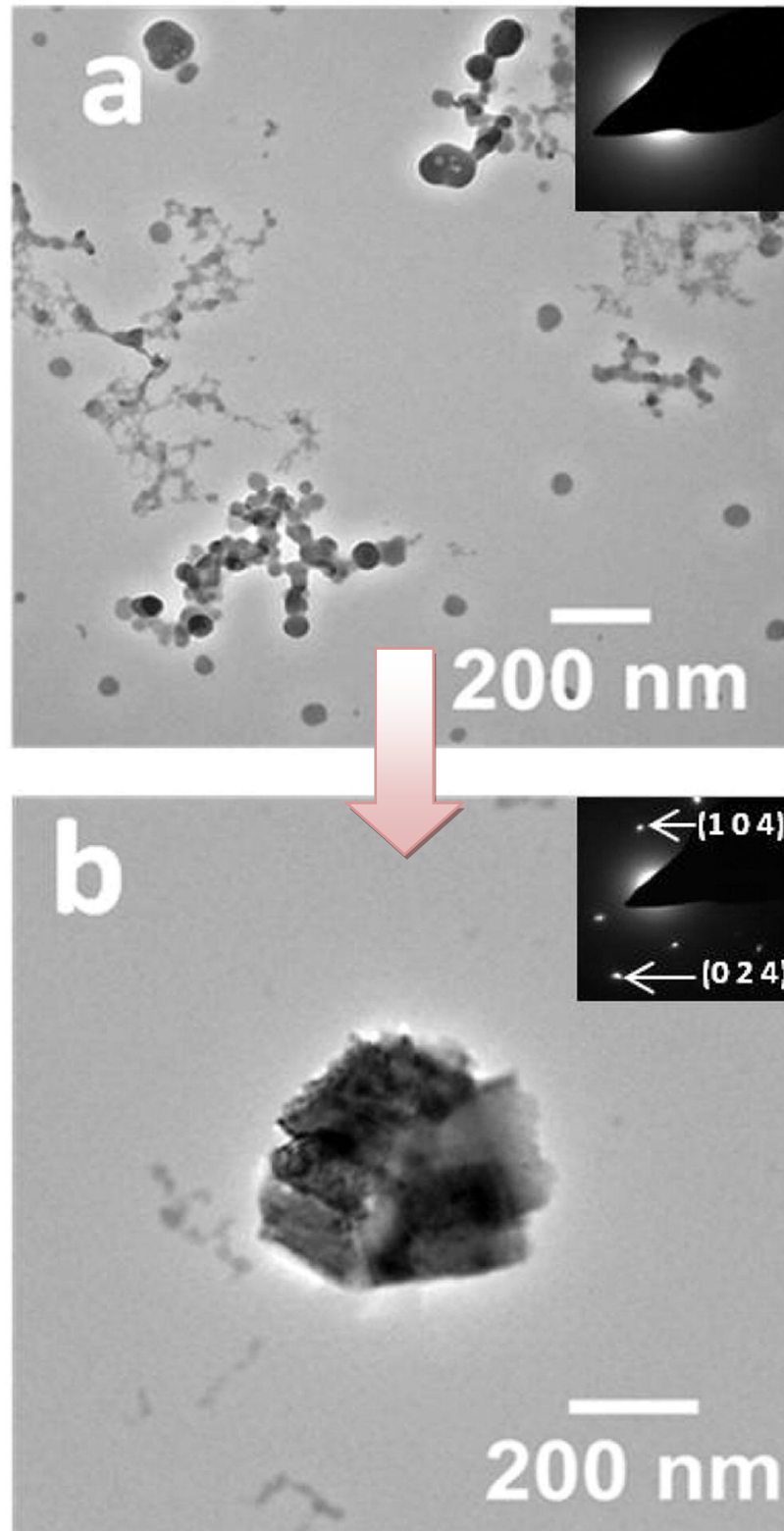
While the biological system is far more complex than the simple model system employed here, our results suggest that it is entirely possible that crystallization of ACP to HAP may occur via an OCP intermediate phase. Indeed, the degree of confinement offered by collagen fibrils is far greater than the modest values seen to provide significant stabilisation here. The mechanism of CaP precipitation in the biogenic system is therefore quite distinct from that observed here either in bulk solution or confinement, in the presence or absence of additives. Confinement therefore presents an alternative mechanism of stabilisation of ACP, where this could arise from a reduced ability of ACP to dissolve/ dissociate into clusters and to undergo subsequent structural reorganisation into a crystalline phase in a constrained reaction volume.

## **6.6 Summary**

The results showed that by the use of crossed-cylinder apparatus, it was successful to produce plate-like HAP, metastable OCP and amorphous calcium phosphate. Growing the crystals inside confinement had a large effect on the crystallisation rate, morphology and polymorph of the formed crystals. Plate-like HAP crystals comprising HAP platelets were generated and oriented with their *c*-axes along the

surface of the confinement. This morphology of HAP also provided a similar structure of mineralised collagen in bone and dentin. Furthermore this research also investigated the effect of additives. It was found that addition of PAsp had effect to stabilize OCP and ACP in confinement. It is thought this observation is due to the ability of PAsp to behave as an inhibitor in solution. The existence of amorphous thin films formed in the CaP/ PAsp system may suggest a specific interaction between the collagen matrix and ACP/PAsp precursor clusters[33] or PAsp molecules[252] which is responsible for an effective mineralisation.

## Chapter 7: A Turbidity Study of Calcium Carbonate Precipitation



This chapter investigates the nucleation pathways of  $\text{CaCO}_3$  in bulk solution in the presence and absence of additives, and how the presence of the amorphous precursor, ACC, is dependent on measurable quantities including solution concentrations and additive concentrations. The early growth stages of  $\text{CaCO}_3$  are investigated using UV-Vis spectrophotometry, where the transmitted intensity of light is related to the size of the crystal precipitates. To investigate this further, particles were collected during in situ spectrophotometry measurements and were analyzed using Raman spectroscopy to determine polymorphism, and TEM to determine the degree of crystallinity. By relating the transmitted intensity with reaction time during crystallization, it was possible to determine the solution composition at a given time, and thus to determine the nucleation pathway. These results also demonstrated that addition of  $\text{Mg}^{2+}$  or polyacrylic acid can efficiently stabilise ACC with respect to the crystalline polymorphs, retarding crystallisation.

## **7.1 Introduction**

The high abundance and rich polymorphism of calcium carbonate is such that it has received considerable interest from many researchers in many branches of science. For example, the mechanical properties of calcium carbonate biominerals have long fascinated, and frequently exceed all expectation for such a traditionally poor engineering material.[253] It also has been widely used as a model mineral in biomimetic experiments, leading to increased understanding of the mechanisms of biogenic control over mineral polymorph, orientation, and morphology.[2] Calcium carbonate can precipitate as six distinct polymorphs and hydrates: calcite, aragonite, vaterite, calcium carbonate hexahydrate, calcium carbonate monohydrate and amorphous calcium carbonate. A polymorph is defined as a substance or compound that has the ability to exist in different crystalline forms.[62] The arrangement of atoms within each polymorph is different, leading to different crystal structures and hence different physical properties between polymorph, although they are identical in chemical composition.

### **7.1.1 Three main crystalline polymorph of Calcium Carbonate**

Calcite is the main constituent of most limestones and sedimentary rocks, and is also the main component of the shells of many organisms.[254] Under ambient conditions, calcite is an abundant carbonate mineral, being somewhat more stable than aragonite.[255] In the calcified biological systems, calcium carbonate has been found predominantly as calcite and aragonite and less commonly as vaterite and amorphous calcium carbonate. Aragonite, which has similar thermodynamic stabilities to calcite under standard conditions of temperature and pressure, is also common in biological and geological samples.[256] The difference in standard free energy for calcite-aragonite is  $1.14 \pm 0.01$  kJ/mol[62], therefore aragonite is considered as metastable with respect to calcite and will eventually transform into calcite under ambient conditions. The crystal lattice of aragonite differs from that of calcite, resulting in a different crystal shape, an orthorhombic system with acicular crystals. Vaterite is the least stable anhydrous crystalline polymorph of  $\text{CaCO}_3$  under standard conditions[256]. The unit cell of vaterite is described as hexagonal with the loosely packed structure. This metastable polymorph of  $\text{CaCO}_3$  is less dense than calcite and under standard conditions, would gradually transform into the more stable calcite or aragonite.

### **7.1.2 Amorphous Calcium Carbonate**

Crystalline minerals have a strong tendency to adopt shapes that reflect the molecular interactions and the symmetry within their structure. They can also show poor mechanical properties due to the anisotropy of the crystals. An alternative to using crystalline materials would be to use an amorphous mineral, as it is isotropic in polarized light and does not diffract X-rays; hence it is described as being amorphous.  $\text{CaCO}_3$  also exists as a highly unstable amorphous phase, amorphous calcium carbonate (ACC), which is known to act as a precursor phase during biomineralization. ACC may be more widely distributed, but it is difficult to detect when associated with a crystalline form. Therefore its presence may well have been overlooked in many mineralized tissues. Much interest in ACC stems from its potential in materials synthesis – as is beautifully illustrated by the use of ACC in living organisms. For example, in the moult cycle of a terrestrial isopod, it has been demonstrated that ACC can act as a temporary storage site.[256] Another advantage

of ACC is its mechanical properties as it does not have any intrinsic fracture planes.[2] As it has no preferred morphology, it means that it is more easily to mould into more intricate structures than crystalline materials. [257]

Mineralization in sea urchin larvae represents the first example in biology of ACC acting as a transient precursor to calcite.[50] In sea urchins, crystal growth occurs within a membrane delineated compartment. Within this compartment, ACC addition grows gradually to form the mineral deposit and then transforms into an oriented single crystal of calcite. As compared with the crystalline component, ACC is present in relatively large amounts during the first stages of spicule growth, and the proportion of ACC decreases on aging of the spicule. The transformation process of biogenic ACC is much slower than for synthetic ACC but is also significantly faster than the crystallization of dried spicules isolated from the larvae. This suggests that crystallization *in vivo* must be mediated by organism.[257] Much attention has been focused on the importance of biologically active molecules such as proteins in stabilizing and controlling the crystallization of ACC,[258, 259] while recent experiments have suggested that physical confinement can also cause stabilisation without the involvement of additives.[240, 260] A considerable amount of work has been done on precipitation in the  $\text{CaCO}_3$  system and several very elegant experimental studies have focused on the early stages of the nucleation of ACC,[78, 153, 261-264] while many computer simulations have studied the crystallisation of ACC.[265-269]

### **7.1.3 Calcium Carbonate in Industry and Biomineralization**

As nature is adept at controlling mineralization processes to produce crystals with remarkable morphologies and mechanical properties, calcium carbonate, one of the most common biominerals, has received considerable attention[225]. Ideas from biomineralization can also be used to apply of identified strategies to control the precipitation synthetically.

As discussed above, there are six polymorphs of calcium carbonate minerals and some mineralized tissues may contain several of the calcium carbonate polymorphs at differences locations. Of these, calcite and aragonite are very widespread in living organisms, and mollusk shells contain both calcitic and aragonitic layers in different locations.[270]. In contrast, vaterite is rare in nature, being detected as a minor

component of only a few biomineralized structure, and not in geological samples [225]. Some investigations have shown that vaterite can naturally occur with organic tissue, gallstones, urinary calculi, microbial biscuits, otoliths and eggshells of turtle[271-275]. ACC in biological system was principally observed in one taxon, the crustaceans, such as crabs, lobster etc., where it is widely distributed.[276] In this case, its high solubility is beneficial in its use as a temporary storage as some minerals need to be dissolved periodically during the molting phase.[277] With its isotropic mechanical properties, ACC also used for structural purposes to stiffen the exoskeletal cuticle. [278] As an amorphous early stage, ACC also functions as a transient precursor phase prior to the formation of aragonite in the larvae of molluscan bivalves [279] and calcitic spicules of mature sea urchin larvae. [280]

Industrially, calcium carbonate is the most important filler for plastics and it is also widely used in rubber and paints. Calcium carbonate is, in fact, much more than “chalk” (as it is universally described in the plastic industry). In plastics, it is used mainly in PVC, both flexible and rigid. Coarser particles are mainly used, but as compound specifications become more exacting fine-particles stearic acid-coated grades are used for better mechanical and processing properties. Calcium carbonate particles are used to aid in pigmentation and can also assist gloss as an extender in paints, including compensating for loss of gloss where lead stabilizers have been replaced by calcium/zinc systems. It is also used as a mild abrasive in cleaning products, adhesives, and pharmaceuticals and many household products[281]. It is also a major problem in the formation of limescale in and domestic water heaters and pipes. Some toilet cleaners have a weak acid in them to remove the limescale as carbon dioxide.

#### **7.1.4 Influence of Metal ions and Organic Molecules in CaCO<sub>3</sub> precipitation**

The role of ACC as a transient amorphous precursor phase is now well established, where the most stable end product (with higher thermal stability), such as calcite is transformed from ACC with lower thermal stability. Unstable intermediate phases can often be stabilized in the presence of additives.

#### 7.1.4.1 Influence of metal ions on CaCO<sub>3</sub> precipitation

In the simplest case, metal ions which are readily accommodated by the calcite crystal lattice can control the polymorph and structure of crystal formation. Alkali metal ions incorporation into calcium carbonate has been of interest to geochemists, where these occupy interstitial positions in the calcite structure, causing distortion of the surface structure.[282] Therefore, the transformation of aragonite or vaterite to calcite was retarded. The habit of the precipitated calcium carbonate was also affected by the addition of Li<sup>+</sup> ions. Adsorption of Li<sup>+</sup> ions on the crystal surface may lead to aragonite with well-defined outgrowths, consisting of six prismatic side faces truncated by relatively large and flat pseudo-hexagonal end-faces.[283] The precipitation pathway of calcium carbonate has also been affected by the other divalent metal ions which can partially replace the Ca<sup>2+</sup> ions in calcite or aragonite. Fe<sup>2+</sup> ions is a common substitution for some Ca-based minerals, at levels of 5-10 mol% in natural samples. Some synthesised calcite contains up to 16 mol% manganese, while in nature samples can contain up to 50% Mn.[284] The adsorption reaction of Cd<sup>2+</sup> involves two steps. The first step involves a fast adsorption reaction to form a layer of Cd<sup>2+</sup> ions on the surface of calcite. The second step is the process of formation of a new crystalline material, which contains a disordered hydrated surface layer of a mixture of Cd<sup>2+</sup> and Ca<sup>2+</sup> carbonate. [285] Barium, having an ionic radius similar to Ca<sup>2+</sup>, preferentially incorporates into aragonite rather than calcite. In natural materials, such as corals, aragonite contains 8-15 ppm Ba<sup>2+</sup> while the ratio in calcite is only to 1-3 ppm. [286] Strontium has a similar effect to Ba<sup>2+</sup> but is a much more important chemical substitute in aragonite. Sr<sup>2+</sup> is generally considered to substitute for Ca<sup>2+</sup> ions in the orthorhombic aragonite lattice, and to suppress the transformation to calcite.[287]

It has been well established that the Mg<sup>2+</sup> ion has a significant effect on the precipitation of CaCO<sub>3</sub>. When present in sufficient concentrations, it generally results in aragonite, rather than the more stable calcite.[51, 52, 288, 289] It was also indicated that the transformation from aragonite to calcite which occurs in low-temperature via dissolution-reprecipitation, was inhibited in the presence of Mg<sup>2+</sup>. [290, 291] A commonly accepted explanation of these observations is that Mg<sup>2+</sup> ion is more strongly hydrated than Ca<sup>2+</sup> and is more strongly adsorbed to the surface of growing calcite crystals. [52, 54] The calcite which contains Mg in its structure is also thermodynamically destabilized relative to aragonite.[292] An alternate

explanation is that dehydration of the  $Mg^{2+}$  ion prior to incorporation in the calcite lattice creates a barrier to the growth of calcite nuclei.[293, 294] It suggests that  $Mg^{2+}$  inhibits calcite nucleation and/or crystal growth, and as a result, aragonite is kinetically 'stabilized' and precipitates faster than calcite. [295] It is also shown that when magnesian calcite is produced via a partially stabilized amorphous precursor phase, they contain as much as 21 mol% magnesium within the calcitic structure, and could additionally provide a route to morphology control. [57, 225] It is also well known that the addition of magnesium can lead to the formation of spicular aragonite crystals rather than rhombohedral calcite.[81]

#### **7.1.4.2 Influence of organic molecules on $CaCO_3$ precipitation**

Due to the importance of calcium carbonate precipitation in geology, the chemical industry and water treatment, manipulation of variables including supersaturation, reactant flow rates, temperatures and pressure were used to calcium carbonate crystallization.[225] Inspired by biological systems, organic molecules as additives are used to control crystal growth. In the simplest cases, malic acid and citric acid can be effective in influencing the morphology of growing crystals, and resulted in calcite elongated along the *c*-axis.[81] The studies have also shown that acidic peptides, and in particular aspartic acid, possesses a terminal carboxyl group that binds to Ca affect calcium carbonate precipitation through stereochemical recognition. The carboxyl group cannot rotate freely to optimize coordination.[82] In supersaturated solutions, acidic acid can also alter the equilibrium thermodynamics of calcite growth surface by stabilizing the vaterite polymorph through chemical and structural affinity to this mineral phase.[296, 297] Amino acids, such as alanine, glycine, lysine, polyglycine, polymethionine and polylysine also stabilize vaterite polymorph.[83] Some amino acids with more complicated sequences, such as a peptide or protein is expressed as a fusion with a coat protein of a bacteriophage in biomineral forming system, have also been shown to strongly adsorb on calcium carbonate. These findings have implications for transformation from hollow sphere vaterite to rhombic calcite via a solution-mediated process.[298, 299]

In the bio-inspired systems, polymers with complex sequences have also been used to control the nucleation and growth of calcium carbonate crystals. In many cases,

polymeric systems containing aspartic acid and glutamic acid have been used to alter calcium carbonate precipitation because they are components present in several natural shell-forming systems.[50] Some common partial sequences of amino acids and polypeptide have also been identified to control the polymorph and morphology of calcium carbonate. The peptide containing an array of aspartyl residues can bind to specific face of calcite producing at least three different shapes of calcite depending on peptide conformation and solution conditions.[300] Lysozyme-calcite system was also used to explain the interactions between proteins and mineral surfaces. The habit of calcite crystals was modified and the degree of modification changes with protein concentrations. By the preferential adsorption of lysozyme, the typical rhombohedral calcite crystals was modified by the expression of (1 1 0) faces. And the growth of (1 0 0), and finally (0 0 1) faces was sequentially inhibited with increasing lysozyme concentration, demonstrating that the protein favoured and controlled the nucleation on the calcite substrate. [301] Collagen has a similar morphological effect on calcite growth to inhibit the specific crystal planes. The effect also becomes more pronounced with increased concentration. Collagen incorporated into the calcite planes randomly to induce new crystal planes with higher collagen density. These slower growing planes changed the morphology of calcite, from rhombohedral crystals to spherulitic crystal aggregates.[302]

In the presence of soluble macromolecules extracted from coralline algae, amorphous calcium carbonate has been stabilized, and almost no aragonite forms.[57] Thus, in some cases, synthetic polymers which can mimic macromolecules in biological system have also been added to alter calcium carbonate precipitation, instead of proteins in the biological system. Simple anionic polymers, such as poly(acrylic acid), which was used to inhibit crystallization, affect the crystal mean size, morphology and polymorphs. [303-305] According to the amount of PAA added, well-defined rhombohedral, rectangular, irregular-shaped round particles, and twinned calcium carbonate crystals with smooth surfaces were obtained with increased polymer concentrations.[306] Another polymer additive, polystyrene sulfonate, inhibits the nucleation and growth in all directions of precipitated calcium carbonate, leading to modification the crystal structure and morphology. At moderate concentrations, spherical calcium carbonate particles were obtained. Further, the vaterite unstable phase was stabilized first can then transformed to calcite.[307]

CaCO<sub>3</sub> is typically precipitated *in vivo* in the presence of both organic molecules and magnesium. When additives, such as macromolecules extracted from sea urchin, mollusk, sponge[308, 309] and coccoliths[310] are induced to the high-magnesium-bearing solution, the final morphology of calcite was modified by promoting Mg-incorporation with calcite nuclei[53] and the amorphous phase was further stabilized.[81]

### **7.1.5 Ultraviolet–visible spectroscopy to study the Precipitation of CaCO<sub>3</sub>**

Turbidimetry was used to study the nucleation pathway of CaCO<sub>3</sub> in bulk solution and the transformation of the early stage precursor, ACC, from mixtures of CaCl<sub>2</sub> and Na<sub>2</sub>CO<sub>3</sub> solutions. In this experiment, Ultraviolet–visible spectroscopy (UV-Vis) was used as a simple technique to study the precipitation pathway of calcium carbonate.

The time which elapses between the onset of the formation of supersaturation and the formation of critical nuclei or embryos is defined as the true induction period. However, as highlighted by Sohnel and Mullin,[311] it is not possible to experimentally measure the real induction period because no method has yet been devised for the detection of critical nuclei. It is accepted that the time elapsing between the moment when liquid movement ceases and the first change in turbidity is recorded as the induction period,  $t_{ind}$ . Recently the induction time has also been defined as the time elapsing between the attainment of supersaturation and the appearance of the first crystals[150]. Various materials, including calcium oxalate,[312] barium sulphate[313, 314] magnesium hydroxide, magnesium ammonium phosphate[314, 315] and dimethylglyoxime.[316] were investigated using the same method to study their precipitation pathway. Another study also considered the precipitation of calcium carbonate using light scattering and reported that amorphous calcium carbonate was stable at early stage and the induction time was also longer with polymer additives.[317]. Similarly, time resolved static light scattering was also used to analyse the nucleation and growth of ACC.[318]

For spectrophotometry measurements, the nucleation point of precipitates is succeeded by a fall in transmitted intensity of light passing through the solution due

to Rayleigh scattering from the surfaces of small particles. The induction period is inversely proportional to the nucleation rate,  $J$

$$t_{ind} = \frac{1}{J} \quad (\text{equation 7.1})$$

According to the Beer-Lambert Law, the transmitted intensity,  $I$ , of light through a solution is related to the reflected areas of the particles in unit volume of suspension,  $A_p$ , the path length of light in solution,  $L$ , and to the intensity of light transmitted through reference sample,  $I_0$ . [319]

$$\ln \frac{I_0}{I} = A_p L \quad (\text{equation 7.2})$$

The above equation is dependent on three assumptions; 1) the absorbing particles act independently of each other, regardless of density, 2) absorption is uniform throughout the sample and 3) absorption is the only interaction between the incident radiation and the solutes. Thus, for a fixed path length, UV-Vis spectroscopy can be used to determine the concentration of the absorber in a solution. It is necessary to know how quickly the turbidity changes with concentrations of samples.

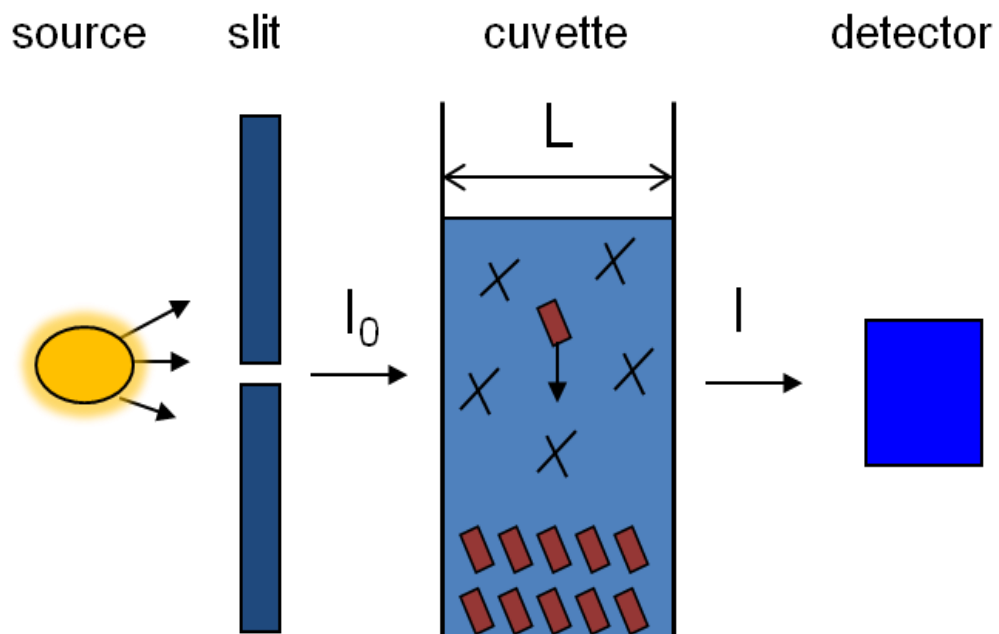


**Figure 7.1** Schematic diagram showing the spectrophotometry cuvette, with the transmitted intensity,  $I$ , related to the initial intensity,  $I_0$  by the path length,  $L$ , and the effective cross-section of the particles.

A few reports have described the use of turbidity studies of crystal precipitation to investigate crystallization procedures, the induction time,[311, 320, 321] and crystal growth rates in moderately supersaturated  $\text{CaCO}_3$  solutions.[322-324] However, with one exception, [311] there are no studies which have used this method to follow the conversion between the different polymorph of  $\text{CaCO}_3$ . Here we explore the possibility of using an extremely simple and seldom used experimental method – turbidimetry to investigate calcium carbonate precipitation from solution of low/moderate supersaturated solution. It will be shown later in this chapter that amorphous calcium carbonate particles are smaller than calcite particles and are produced with a higher nucleation density. Therefore, a solution which contains a higher number of ACC nanoparticles will have significantly more scattering centres than a solution only containing calcite. This makes it possible to investigate the transformations of calcium carbonate as a function of time. This chapter also considers the nucleation of calcium carbonate from bulk solution with and without  $\text{Mg}^{2+}$  and PAA additives.

## 7.2 Aims

The experiments were carried out here using turbidimetry and electron microscopy to study the nucleation pathway of  $\text{CaCO}_3$  in bulk solution and the transformation of the early stage precursor, ACC, from mixtures of  $\text{CaCl}_2$  and  $\text{Na}_2\text{CO}_3$  solutions of concentrations in the range of 2 to 10 mM. The change in turbidity with time and concentration is related to the precipitation and aggregation of ACC, its crystallisation to calcite (and occasionally vaterite) and the sedimentation of the growing crystals. Particles collected during the in situ spectrophotometry measurements were analysed using Raman spectroscopy to determine polymorphism, and TEM to determine the particle size distributions and relative degree of crystallinity. In order to gain further understanding, the influence of the important additives  $\text{Mg}^{2+}$  and poly(acrylic acid) was also investigated. Addition of  $\text{Mg}^{2+}$  or polyacrylic acid, which are known to stabilise ACC with respect to crystallisation, retards the entire process.

## 7.3 Experimental

### 7.3.1 Materials

CaCO<sub>3</sub> was precipitated by the double decomposition method from metastable solutions by mixing 0.5 ml each of equimolar aqueous solutions (Milli-Q water, resistivity = 18.2 MΩcm<sup>-1</sup>) of CaCl<sub>2</sub>·2H<sub>2</sub>O (pH = 6.0) and Na<sub>2</sub>CO<sub>3</sub> (pH = 11.4) (both Sigma-Aldrich), directly in 2 ml Plasticband Perspex spectrophotometer cuvettes. Both of the solutions were freshly made in Milli-Q water and pre-equilibrated with atmospheric CO<sub>2</sub>. The solubility of the different polymorphs of CaCO<sub>3</sub> depends on a series of equilibria between atmospheric carbon dioxide, hydrogen ions and added carbonate ions, and also on the concentration of inert background electrolyte (here NaCl).[325, 326] However, the evolution of turbidity with time and concentration was very similar thus suggesting that equilibration occurs relatively rapidly on mixing and exposure of the solutions to the atmosphere.

### 7.3.2 Precipitation of Calcium Carbonate

The final concentrations of calcium carbonate solutions were from 2-10 mM. The mixing time in the cuvettes before inserted into the UV instrument was less than 5 seconds. Solutions with final concentrations of 50 and 100 mM were prepared for inspection and Raman microscopy only. In the additive experiments, different concentrations of MgCl<sub>2</sub>·6H<sub>2</sub>O (Sigma-Aldrich) were combined in equal volumes with CaCl<sub>2</sub> solutions, gives final concentration of Mg<sup>2+</sup> from 2.5-10 mM solutions before mixing this solution with Na<sub>2</sub>CO<sub>3</sub>. For the soluble polymer additive experiment, polyacrylic acid (PAA, MW = 8000, Sigma-Aldrich) was used to prepared 1 µg/ml stock solution. The stock solution was added to the CaCl<sub>2</sub> solution prior to mixing with the Na<sub>2</sub>CO<sub>3</sub> solution of the same concentration. The saturation ratio *S* were often used to describe the solution conditions, such as induction times of CaCO<sub>3</sub> solutions. Using the Güntelberg equation[327] we estimate that the thermodynamic supersaturation values *S<sub>a</sub>* (including activity coefficients) with respect to calcite in this study range from about 2 at 2 mM to ca. 8 at 10 mM. The supersaturation ratios with respect to ACC are lower and should vary from about 1 to 4 over the same range, using the solubility of 1.7 mM for ACC as determined by Brečević and Nielsen.[328]

### 7.3.3 Characterization Methods

The turbidity measurement were obtained using a Perkin-Elmer Lambda UV-Vis system, operating in a time-drive mode ( $\lambda = 500$  nm, exposure time = 1s). The transmitted intensity,  $I$ , was recorded as a function of base intensity,  $I_0$ , where  $I_0$  was measured through an empty cuvette over a time period of 20 mins. A control experiment showed that  $I/I_0$  was constant between 300 and 700 nm, and approximately 20% lower from 200 to 300 nm (as shown in Fig 7.2). Monochromatic light of 500 nm wavelength was chosen since the empty cuvette did not absorb significantly at this wavelength, yet over 90% of the light was absorbed by 5 mM  $\text{CaCO}_3$  solution 30s after mixing.

Transmission electron microscopy (TEM) images were obtained using FEI Tecnai TF20 FEGTEM fitted with Oxford Instruments INCA 350 EDX system/80mm X-Max SDD detector and Gatan Orius SC600A CCD camera operating at 200 kV. TEM images were taken for  $\text{CaCO}_3$  particles extracted from solution after short growth periods of 15s, 1 minute and 5 minutes, at concentrations of  $[\text{Ca}^{2+}] = 5$  and 10 mM.  $\text{CaCO}_3$  precipitates were collected on carbon/Formvar-coated Cu TEM grids (50  $\mu\text{m}$  mesh) by immersing the grids in 10 ml of metastable solution for 2 s, rinsing them with ethanol and drying at room temperature.

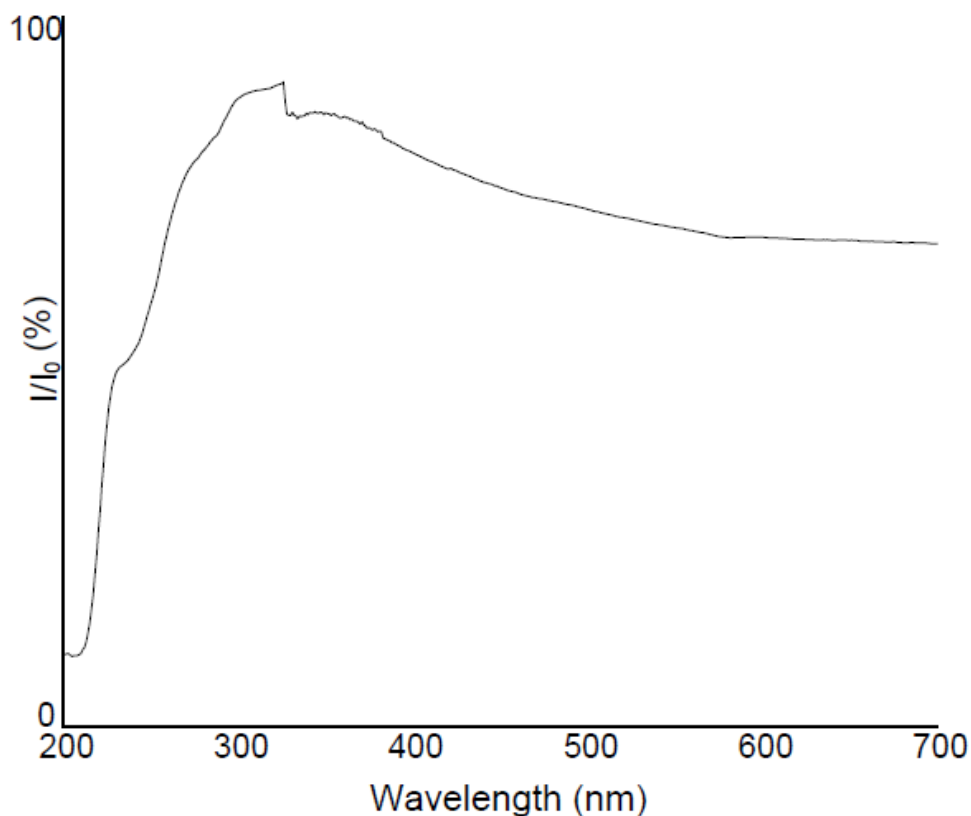


**Fig 7.2** UV-Vis absorption over 200-700 nm, measured for  $[\text{Ca}^{2+}] = 5 \text{ mM}$  solution 30 s after mixing. A wavelength of  $\lambda = 500 \text{ nm}$  was used for the Spectrophotometry measurements.

## 7.4 Results

### 7.4.1 Precipitation of Calcium Carbonate in Additive-Free Bulk Solution

The precipitation pathway of calcium carbonate in solution at early reaction times was measured by using solution turbidity, shown in Fig 7.3. Percentage transmission  $I/I_0$  for solutions with  $\text{CaCO}_3$  concentrations in the range of 2-10 mM was measured as a function of time. The changes in light transmission showed that the reaction proceeds increasingly fast at higher concentrations, such as above 4 mM concentration, while there is no experimentally significant change in light transmission at 2 mM solution. All experiments were repeated at least five times, and although there were small differences in the precise shape of the curves, the manner in which the light transmission fell and then recovered with time, and how the light transmission evolved with concentration, was identical in all cases.

Figure 7.3 shows the transmission-time plots for additive-free solutions in the range of 2-10 mM. It was observed that the supersaturated  $\text{CaCO}_3$  solutions, prepared using the double decomposition method, solutions in the concentration range 2.5 – 3 mM, exhibited a slight decrease in transmission. This could be recorded using the spectrometer but was not perceptible to the naked eye. In contrast, turbidity was clearly visible at initial  $\text{Ca}^{2+}$  concentrations of 4 – 10 mM (and indeed at the higher concentrations of 50 mM and 100 mM which were also inspected). The induction periods were shorter than the experimental initiation times at higher concentrations, suggesting that the onset of nucleation occurs within the first few seconds. Transmission minimum occurred between 100 and 200s with the largest turbidity observed at  $[\text{Ca}^{2+}] = 10 \text{ mM}$ .

In the concentration range 6 – 10 mM, the turbidities measured were less than 10% in transmission. After a lapse ranging between 0 s and 1500 s, depending on the concentration, the final solutions cleared up.. During this experiment, the solution initially turns cloudy before clearing as the solution converts to calcite and settles at the bottom of the cuvettes. The transmission then recovers more quickly at higher concentrations (after about 300 s at 10 mM) and the turbidity persisted for the longest time (ca. 1000 s) at concentrations of 4.5 – 6 mM. After the measurements, significant amounts of what appeared to be calcite crystals were extracted from the bottom of the cuvettes.

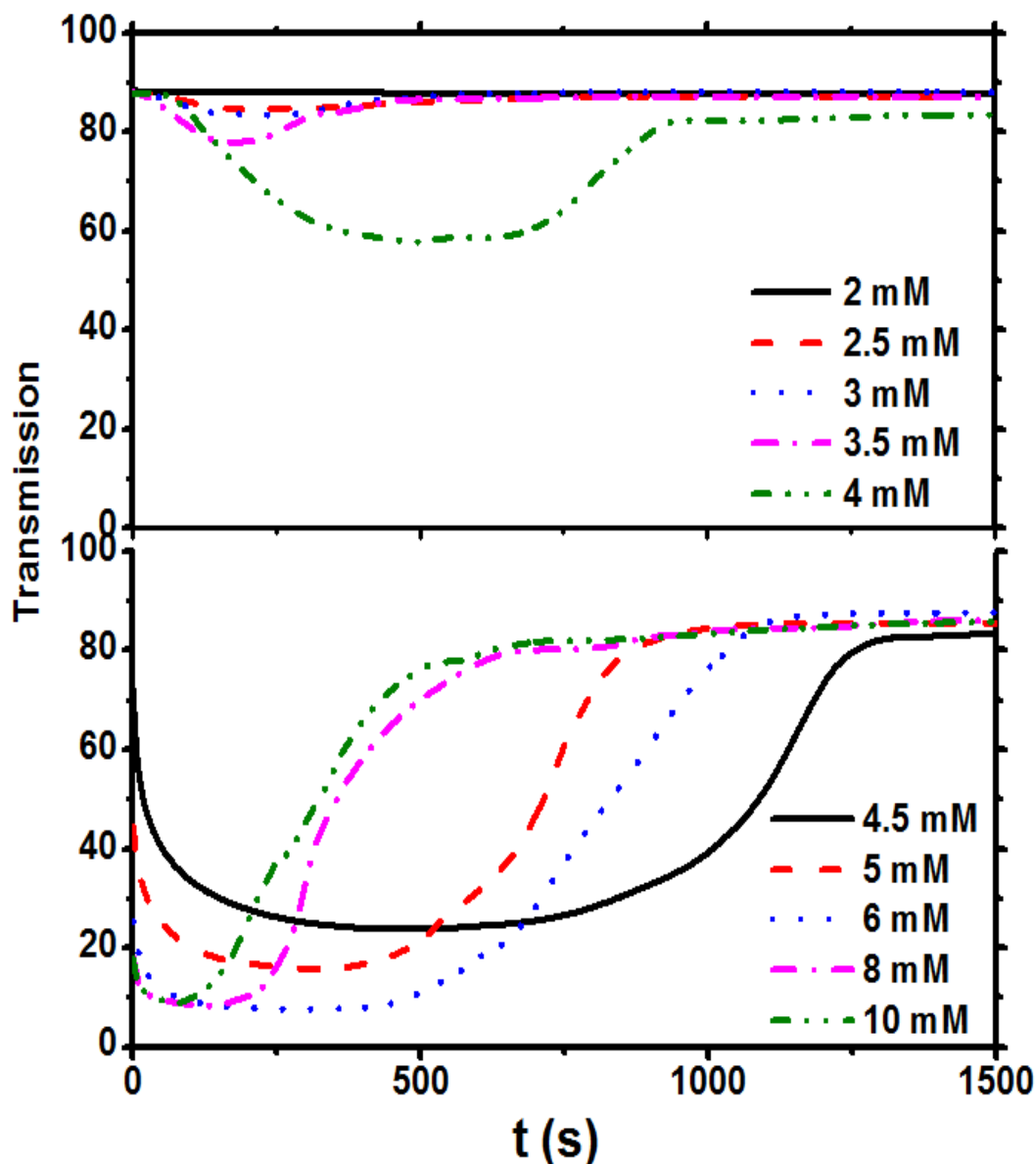


**Figure 7.3** Percentage transmitted light intensity as a function of time after mixing in solutions of 2-10 mM initial  $\text{Ca}^{2+}$  concentration. At 2 mM  $\text{Ca}^{2+}$  there was no increase in turbidity; at 2.5 - 3.5 mM there was a slight initial decrease in transmission, which became increasingly sharp at concentrations of 4 mM and above. The recovery of transmission became faster at concentrations above 5-6 mM.

In situ pH measurements were carried out as a function of time for  $\text{CaCO}_3$  solution concentrations of  $[\text{Ca}^{2+}] = 2.5 \text{ mM}$  and  $[\text{Ca}^{2+}] = 10 \text{ mM}$  (shown in Fig 7.4). For  $\text{CaCl}_2$  solutions (initial pH = 6.9), there was a sharp, instantaneous increase in pH after 30 s upon the addition of  $\text{Na}_2\text{CO}_3$  solution, rising to 9.9 and 10.5 for 2.5 mM

and 10 mM concentrations respectively. Interestingly, the time scale for the appearance of the maximum pH depended on the concentrations, appearing after 300 s for 2.5 mM and 100 s for 10 mM solution. For the 2.5 mM and 10 mM  $\text{CaCO}_3$  solutions, there was an approximate correlation in time periods for the maximum pH and maximum turbidity. After 300 s reaction time, both of the sharp rise proceeded a gradual, attributed to the fall in free  $\text{Ca}^{2+}$  and  $\text{CO}_3^{2-}$  ions during precipitation.

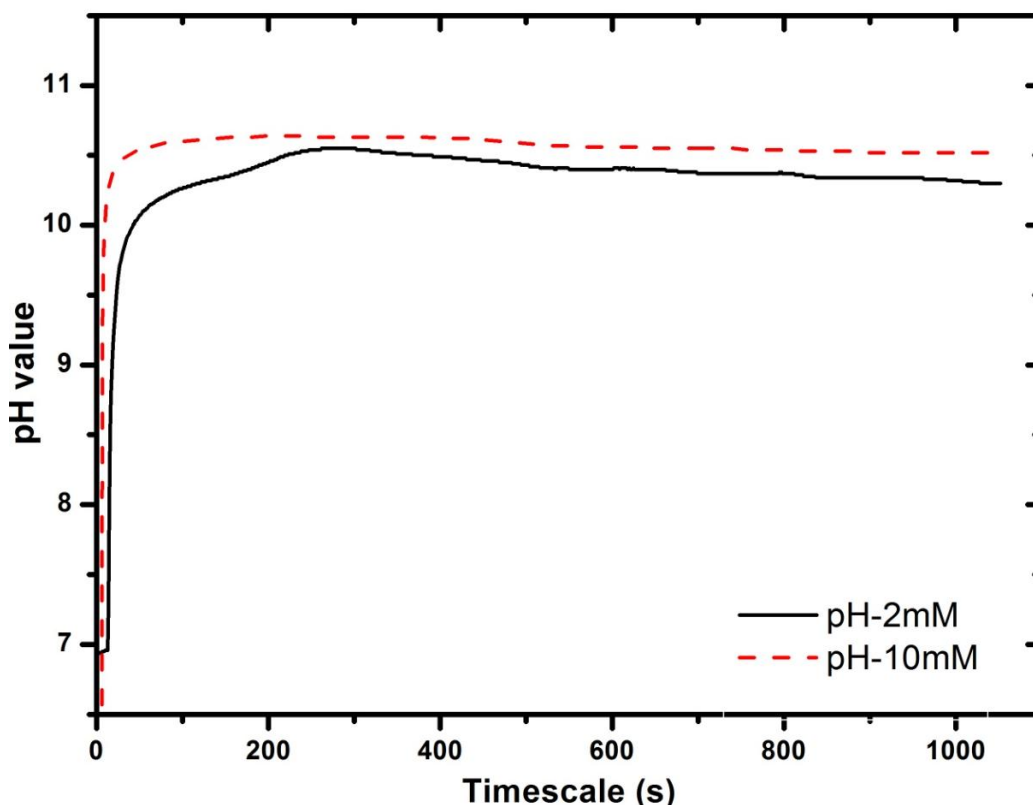


**Figure 7.4** The changes of pH as a function of time, for  $\text{CaCO}_3$  solution concentrations of 2.5 mM (solid line) and 10 mM (dash line).

The precipitates formed in the reactions were also studied with Raman microscopy and TEM in order to correlate the changes in turbidity with the phenomena occurring in the solution. Figure 7.5 shows Raman spectra of particles filtered out of solution with a 200 nm track-etch membrane filter after growth periods of 15 s, 1, 2, and 5 min in 2.5 in 10 mM solutions. All of the precipitates extracted from the 2.5 mM solutions at all times were calcite, which is consistent with the reference (not shown in Fig 7.5a). Comparable results were obtained for the precipitates formed in solutions of concentrations of  $[\text{Ca}^{2+}] = 10$  mM (shown in Fig 7.5b). Raman spectra

of particles collected from the 10 mM solution after 15 s were characteristic of ACC, as shown by a 9-fold broadening of the  $1085\text{ cm}^{-1}$  ( $\nu_1$ , internal  $\text{CO}_3^{2-}$  symmetric stretch mode), an absence of the  $711\text{ cm}^{-1}$   $\nu_4$   $\text{CO}_3^{2-}$  symmetric bending mode, and a broad peak in the range of  $140\text{--}220\text{ cm}^{-1}$  (translational lattice mode).[329] After 1 min, calcite-like features began to appear, and the particles again had Raman spectra with features associated with both calcite and ACC, with all the expected Raman active modes visible and a sharpening of the  $1085\text{ cm}^{-1}$  mode. There is no increase in absolute intensity of the  $1085\text{ cm}^{-1}$  carbonate bending mode which was observed between 2 and 5 minutes at this concentration.

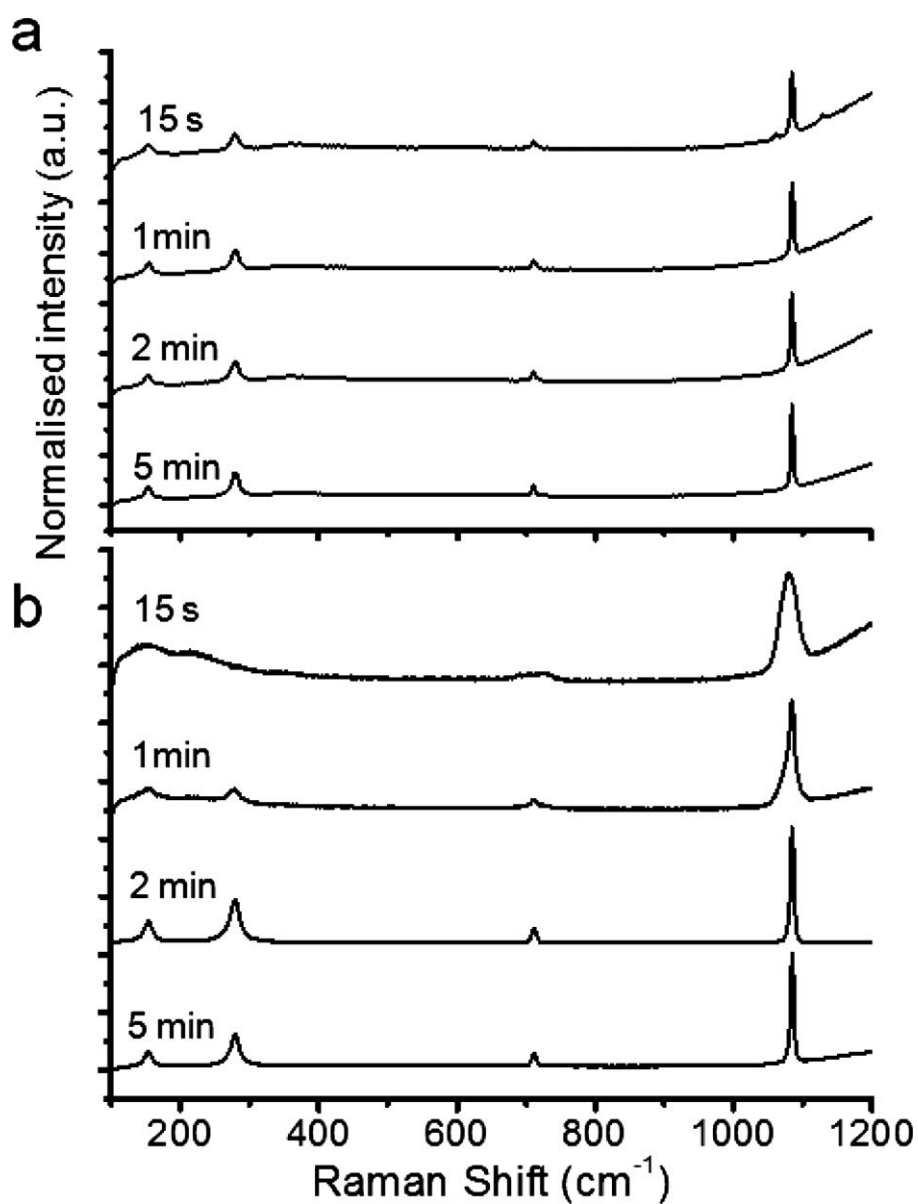


**Figure 7.5** Normalized Raman spectra of CaCO<sub>3</sub> precipitates extracted from solutions after varying growth periods. (a) All particles extracted from 2.5 mM Ca<sup>2+</sup> were apparently calcite. (b) Particles obtained from 10 mM Ca<sup>2+</sup> after 15 s showed spectra with a broad hump at 100–200 cm<sup>-1</sup> and a broad peak centred at 1085 cm<sup>-1</sup>, characteristic of ACC. After 2 min the spectra of the particles were consistent with calcite while after 1 min intermediate spectra were obtained.

Samples for TEM were prepared from 2.5, 3.5 and 5 mM reaction solutions after 10, 15 s, 1 min, 2 min, and 5 min growth time and typical images of selected samples are shown in Figure 7.6 together with corresponding electron diffraction patterns. TEM images showed the characteristic ACC particles reported in previous studies,[328, 330-332] which were either isolated or aggregated (Figure 7.6a and f). The size of the ACC particles varied from about 10 to 100 nm at 2.5 and 3.5 mM, with most about 30 nm in diameter. At 5 mM the particles were larger, being on average about 100 nm in diameter (Figure 7.6f), but were occasionally up to 300 nm. Electron diffraction patterns confirmed their amorphous nature, with diffuse rings rather than the sharp rings and spots observed from comparably sized synthetic calcite particles (not shown). At the two lower concentrations there were also small numbers of large particles, which were morphologically similar to calcite after 5 min in 2.5 mM (Figure 7.6b) and after 1 min (Figure 7.6d) at 3.5 mM. On average, the ACC particles tended to aggregate with time (Figure 7.6f). Curiously, there appeared to be fewer clear signs of crystalline structures at 5 mM (Figure 7.6e), although this was not further investigated. SEM images confirmed the presence of large crystals (diameter over 1 μm) with vaterite- and calcite-like morphologies after 1 min at 2.5 and 3.5 mM (not shown), while at 5 mM such crystals were first seen after 2 min. At 50 mM and 100 mM Ca<sup>2+</sup> the precipitate appeared to be initially mainly vaterite, in agreement with many literature results.[333-335]

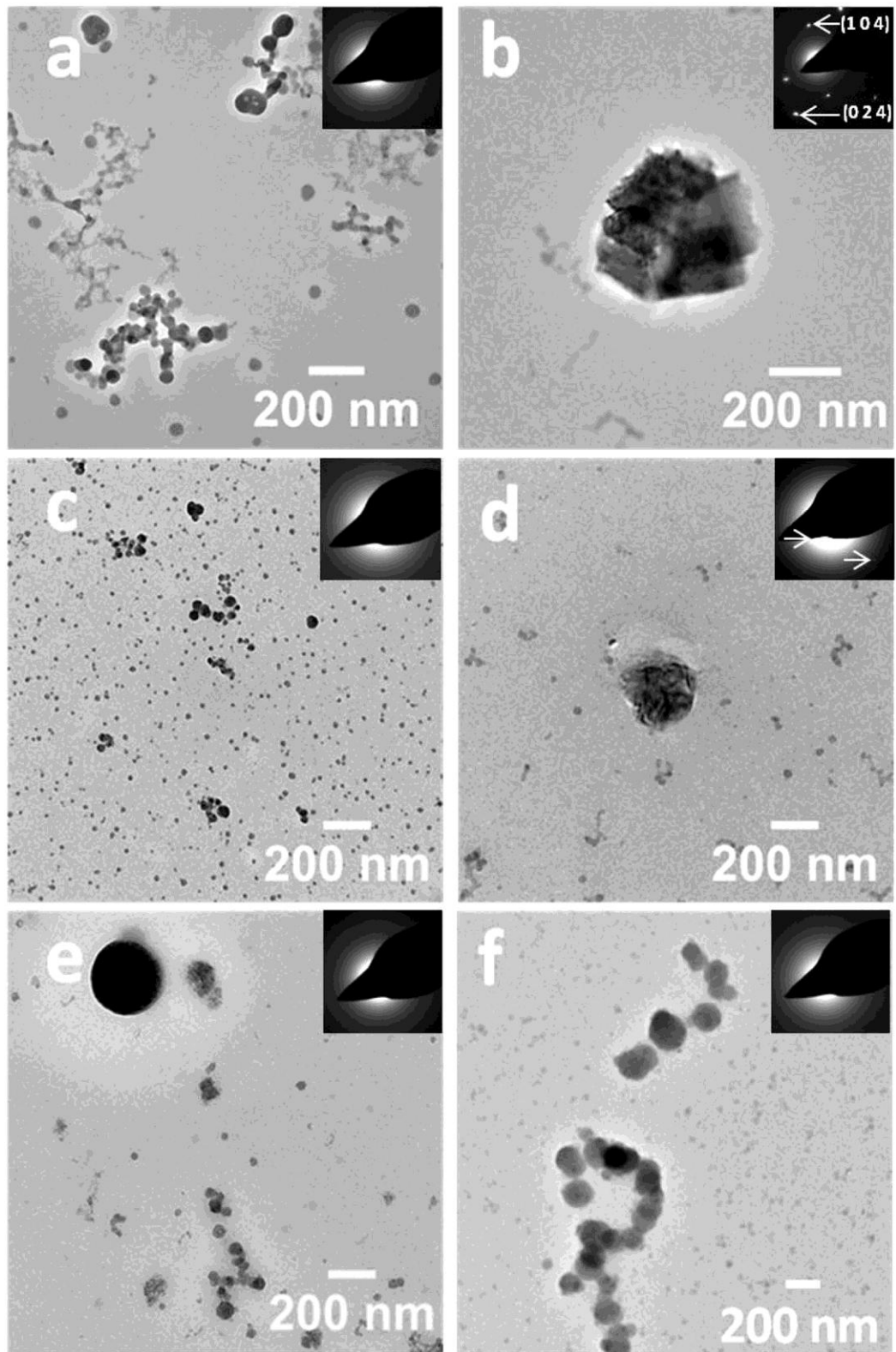


**Figure 7.6** TEM images of CaCO<sub>3</sub> precipitates from solutions of concentration (a) 2.5 mM Ca<sup>2+</sup> after 15 s, (b) 2.5 mM Ca<sup>2+</sup> after 5 min, (c) 3.5 mM Ca<sup>2+</sup> after 15 s, (d) 3.5 mM Ca<sup>2+</sup> after 1 min, (e) 5 mM Ca<sup>2+</sup> after 1 min and (f) 5 mM Ca<sup>2+</sup> after 5 min.

### 7.4.2 Precipitation of $\text{CaCO}_3$ in the Presence of $\text{Mg}^{2+}$

Additives are frequently used to control features such as the polymorph, size and morphology of calcium carbonate precipitates and have been widely employed to stabilise ACC.[9, 336-338] We therefore studied  $\text{CaCO}_3$  precipitation in the presence of two additives which are widely used to increase the lifetime of ACC,  $\text{Mg}^{2+}$  and poly(acrylic acid) (PAA) and used turbidity measurements to investigate how these additives alter the precipitation process. Precipitation of  $\text{CaCO}_3$  in the presence of  $\text{Mg}^{2+}$  led to significant differences in the time evolution of the turbidity.

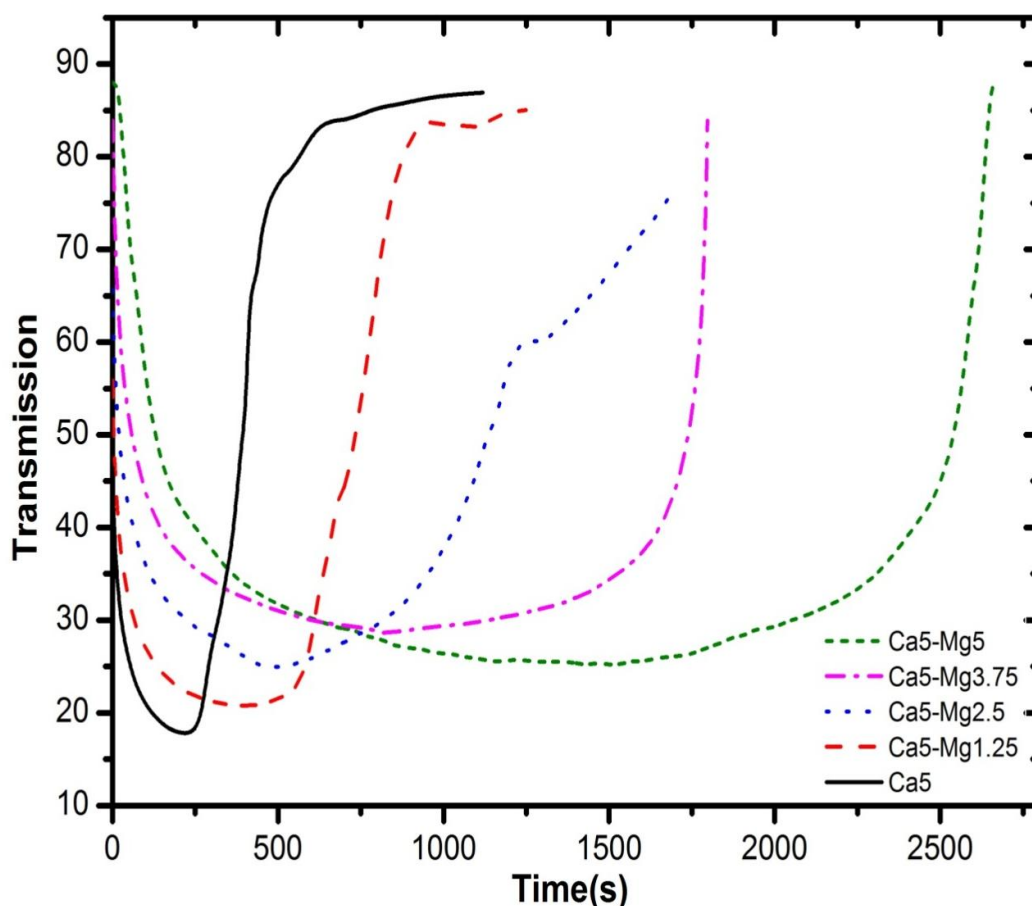


**Fig. 7.7** Percentage transmitted light intensity of  $[\text{Ca}^{2+}] = 5 \text{ mM}$  as a function of time in the presence of Mg additives. A clear progression in initial gradient, maximum turbidity period and recovery time is apparent with increased additive concentration.

For a  $\text{CaCO}_3$  solution concentration of 5 mM, the induction time and recovery period changed with the  $\text{Mg}^{2+}$  additive (shown in Fig 7.7). Obviously, the induction time and recovery period is systematically changed with increasing the Ca: Mg ratio, and ACC formed with a higher magnesium concentrations was significantly more stable than low magnesium ACC. When the ratio of Mg: Ca = 1:2, the induction time is nearly 1100s, which is 500s longer than the solution with no  $\text{Mg}^{2+}$  at the same concentration. At the higher Mg ratio of Mg: Ca = 1:1, both induction time and recovery period are much longer than in the control sample, with the induction period being as long as 2750 s (shown in Table 7.1). These results provide evidence that ACC is more stable with increase in the  $\text{Mg}^{2+}$  ratio. A delayed onset of turbidity and an increased lifetime at a solution concentration of 10 mM has a similar trend as a solution concentration of 5 mM with varying  $\text{Mg}^{2+}$  ratio (shown in Fig 7.8).

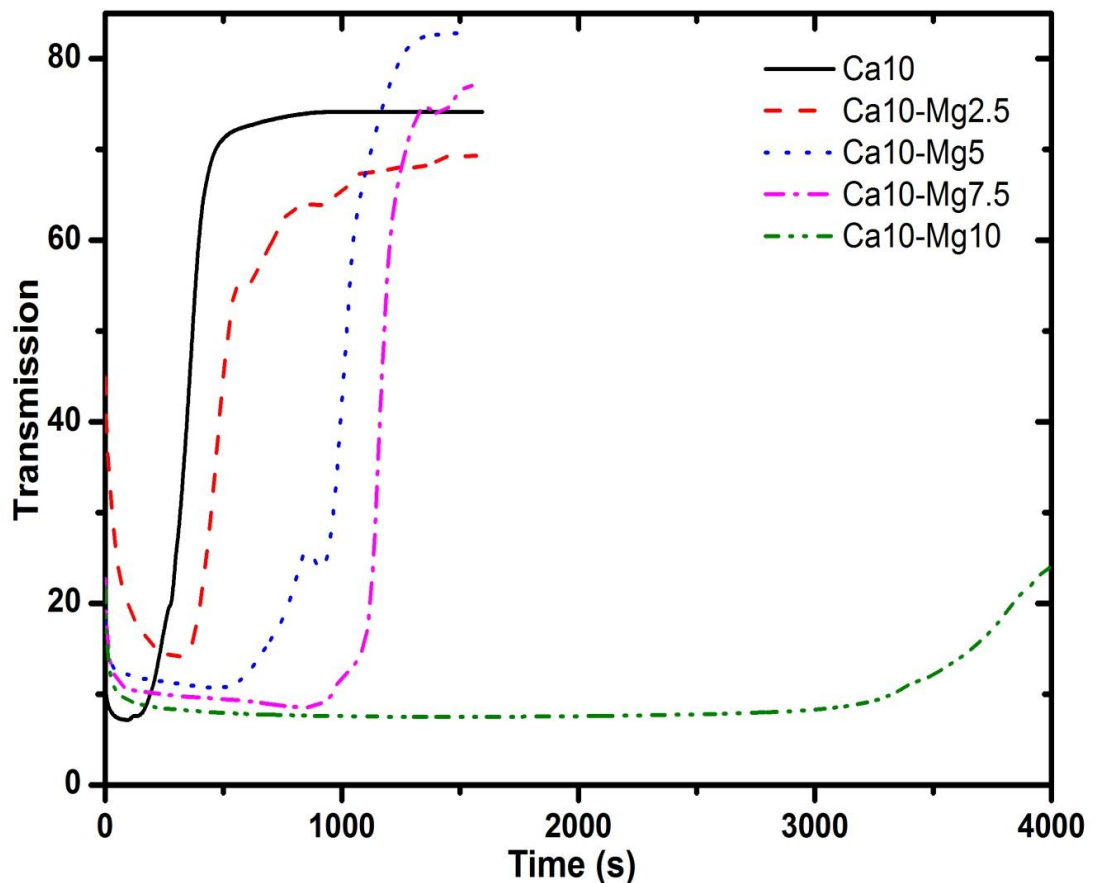


**Fig. 7.8** Percentage transmitted light intensity of  $[\text{Ca}^{2+}] = 10$  mM as a function of time in the presence of Mg additives. A clear progression in initial gradient, maximum turbidity period and recovery time is apparent with increased additive concentration.

**Table 7.1** Time of maximum rate of recovery of light transmission as a function of mole fraction of  $Mg^{2+}$  for 5 mM and 10 mM  $Ca^{2+}$  concentrations.

<b><math>Mg^{2+}</math> concentrations (mM)</b>	<b>Recovery time (s) at <math>[Ca^{2+}]</math> = 5 mM</b>	<b>Recovery time (s) at <math>[Ca^{2+}]</math> = 10 mM</b>
0	600	250
1.25	770	-
2.5	1100	400
3.75	1750	-
5	2750	1000
7.5	-	1200
10	-	4500

ACC is still more stable when formed at higher Mg: Ca ratio solutions. When the solution concentration is  $[Ca^{2+}] = 10\text{mM}$  plus  $[Mg^{2+}] = 10\text{mM}$ , the induction time of ACC is the longest at approximately 4500s, together with the longest recovery time. This reveals that ACC is of the more stable in higher  $Mg^{2+}$  ratio solutions. Further increasing  $Mg^{2+}$ , e.g., at  $[Ca^{2+}] = 10\text{mM}$  plus  $[Mg^{2+}] = 20\text{mM}$ , lead to excessive turbidity in the solution that precluded a full analysis using the UV-Vis method. Figure 7.9 shows the time at which the light transmission recovers most rapidly (after the turbidity maximum) as a function of  $Mg^{2+}$  mole fraction from 0 to 0.50, at both 5 and 10 mM  $Ca^{2+}$  concentration.

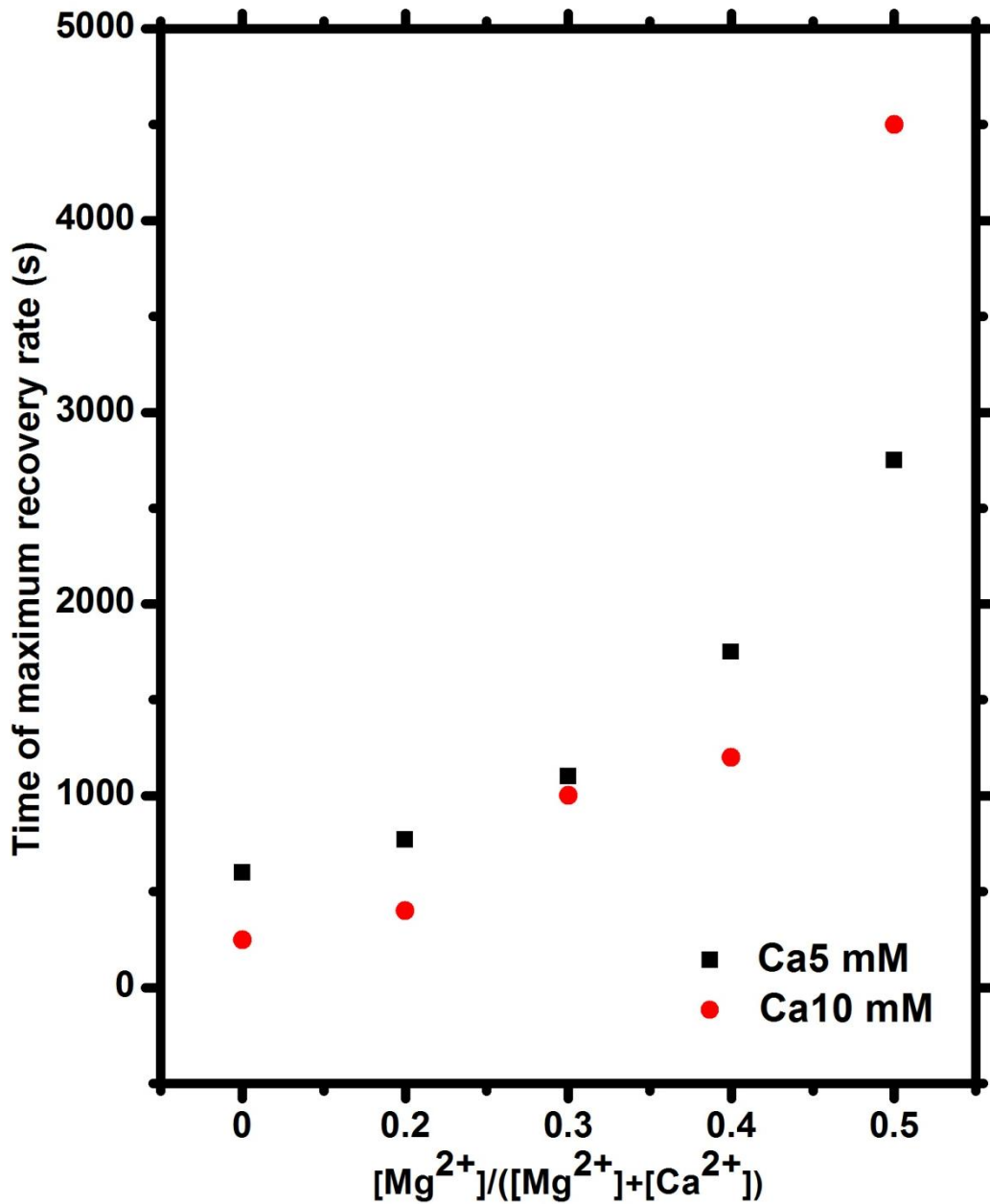


**Figure 7.9** Time of maximum rate of recovery of light transmission as a function of mole fraction of  $\text{Mg}^{2+}$  for 5 mM and 10 mM  $\text{Ca}^{2+}$  concentrations. The period of high turbidity increases with  $\text{Mg}^{2+}$  concentration, suggesting that it acts to delay the conversion of ACC to calcite.

#### 7.4.3 Precipitation of $\text{CaCO}_3$ in the Presence of PAA

Previous literature has described the precipitation of calcium carbonate particles with various shapes by the reaction of sodium carbonate with calcium chloride in the presence of PAA at room temperature. When the amount of PAA is less than 1  $\mu\text{g}/\text{ml}$ , well-defined rhombohedral and rectangular crystals were obtained. However,

when the concentration of PAA exceeds 2  $\mu\text{g/ml}$ , large irregular round particles were obtained. This is because of the strong interaction between the carboxylic acid groups of PAA and the crystallizing  $\text{CaCO}_3$ , which effectively suppressed crystal growth. As shown in Fig 7.10a, in the presence of 2.5  $\mu\text{g/ml}$  PAA in 5 mM calcium carbonate solution, all the precipitates were 2  $\mu\text{m}$  calcite particles after 20 mins with spherical shapes. With higher concentrations of PAA, such as 5  $\mu\text{g/ml}$ , most of the particles were still amorphous nanospheres, 200 nm in diameter, after 20 min (shown in Fig 7.10b)

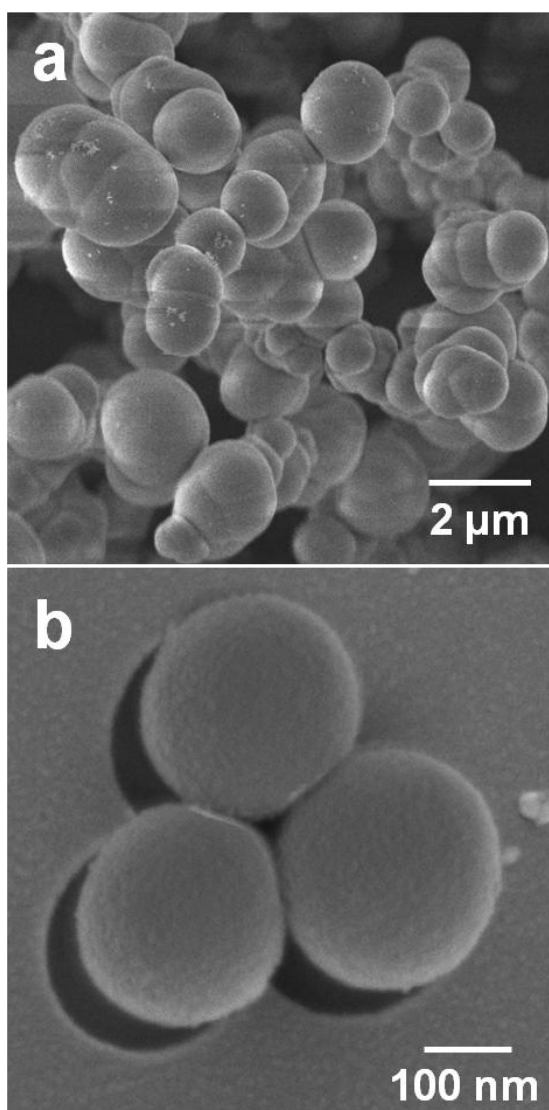


**Fig. 7.10** SEM images of  $\text{CaCO}_3$  precipitates from 5 mM calcium carbonate solutions after 20 mins in the presence of PAA a) 2.5  $\mu\text{g/ml}$ , which shown large irregular shaped round particles and b) 5  $\mu\text{g/ml}$ , as shown amorphous nanoparticles.

For 5 mM calcium carbonate solution, the induction time and recovery period also increased with increasing the concentration of PAA (shown in Fig 7.11). When the concentration of PAA exceeded 5  $\mu\text{g/ml}$ , a obvious delayed onset of turbidity and an increased lifetime of ACC was observed. The recovery time at this concentration was nearly 1 hour (shown in Table7.2). For 10 mM calcium carbonate solution, changes in the induction time and recovery period showed a similar delay.

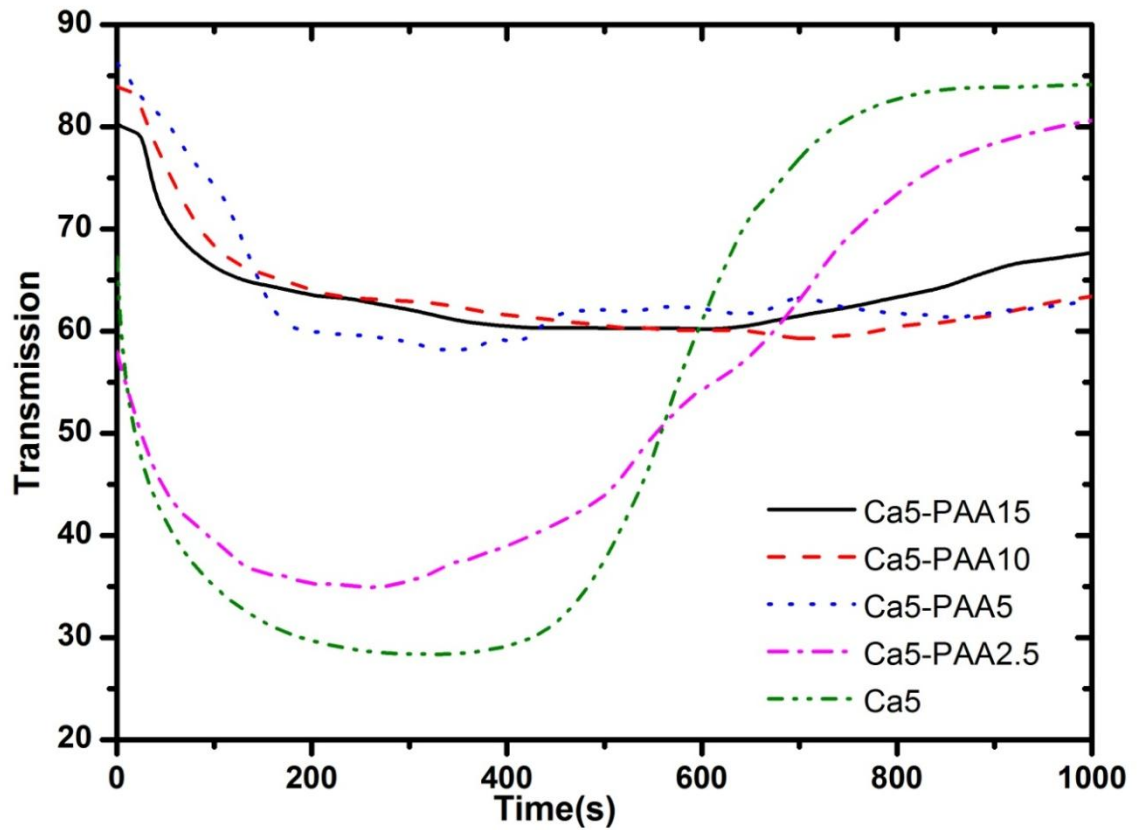


**Fig. 7.11** Percentage transmitted light intensity of  $[\text{Ca}^{2+}] = 5 \text{ mM}$  as a function of time in the presence of PAA additives. A clear progression in initial gradient, maximum turbidity period and recovery time is apparent with increased additive concentrations.

**Table 7.2** Time of maximum rate of recovery of light transmission as a function of mole fraction of PAA for 5 mM and 10 mM  $\text{Ca}^{2+}$  concentrations.

<b>PAA concentrations (<math>\mu\text{g/ml}</math>)</b>	<b>Recovery time (s) at <math>[\text{Ca}^{2+}] = 5 \text{ mM}</math></b>	<b>Recovery time (s) at <math>[\text{Ca}^{2+}] = 10 \text{ mM}</math></b>
0	600	250
1.25	700	-
2.5	1000	450
3.75	1500	-
5	3000	900
7.5	-	1200
10	-	2500

Addition of PAA in the concentration range 1.4 – 10  $\mu\text{g/ml}$  was also used to calculate the recovery time for both the 5 mM and 10 mM calcium carbonate concentrations (shown in Fig 7.12). ACC is also more stable when formed at higher PAA: Ca ratios. When the solution concentration is  $[\text{Ca}^{2+}] = 5 \text{ mM}$  plus  $[\text{PAA}] = 5 \mu\text{g/mL}$ , the induction time of ACC is the longest at approximately 3000s, together with the longest recovery time. When the solution concentration is  $[\text{Ca}^{2+}] = 10 \text{ mM}$  plus  $[\text{PAA}] = 10 \mu\text{g/mL}$ , the induction time of ACC is 2500s, which is 500s shorter than the same ratio solution of PAA:Ca = 1 but  $[\text{Ca}^{2+}] = 5 \text{ mM}$ . These results provide evidence that ACC is more stable at lower  $\text{Ca}^{2+}$  concentrations with the same  $\text{Ca}^{2+}$  to PAA ratio.

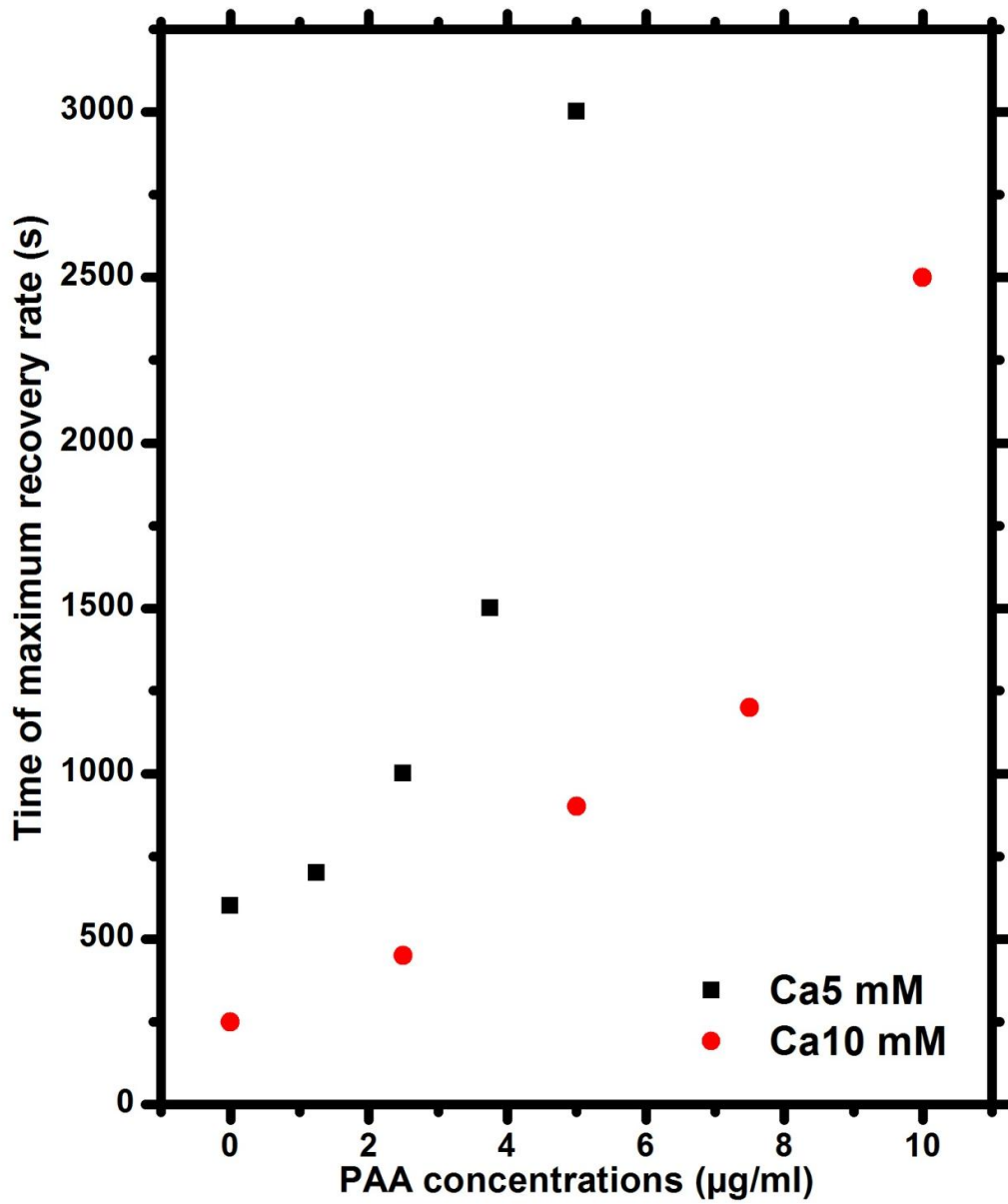


**Figure 7.12** Time of maximum rate of recovery of light transmission as a function of added amount of poly(acrylic acid) (PAA) for 5 mM and 10 mM  $\text{Ca}^{2+}$  concentrations. The period of high turbidity increases with PAA concentration, suggesting that like  $\text{Mg}^{2+}$  it acts to delay the conversion of ACC to calcite.

## 7.5 Discussion

The results in this chapter present evidence for the formation of a transient amorphous precursor phase during the precipitation of calcium carbonate particles

from bulk supersaturated solution. Actually, the factors governing the turbidity of a suspension are complex as the transmission is affected by particle size and particle density, the refractive index of the particles and their shape as well as the degree of polydispersity.[339] Here we have not attempted any quantitative interpretation of the turbidity data. However, it was possible to relate the transmitted light intensity to the observations made by TEM and Raman in order to discuss the evolution of the system after precipitation.

For solution concentrations of  $[Ca^{2+}] = 2.5$  mM and above, the turbidity measurements show that there is increasingly rapid precipitation of ACC, which is in agreement with many literature observations.[328, 331, 332] Also the induction times obtained from 3 mM ( $S_a \approx 3$ ) solution (shown in Fig 7.3) by conductivity and turbidity measurements are 100 s which are in semi-quantitative agreement with the literature. [311, 323, 340] As the concentration increases above 4 – 5 mM, the turbidity peaks appears later and the recovery of transmission occurs more slowly. The longer induction time and large increase in initial turbidity at this concentration range suggests a lower nucleation rate of ACC particles which is easily rationalised by considering that the maximum possible amount of ACC precipitated varies from 0.3 mM at 2 mM to 8.3 mM at 10 mM – an increase by a factor of almost 30 – since the solubility of ACC is 1.7 mM.[328]. These findings also correlated with the TEM measurements, which still showed irregular amorphous particles after 5 min in the 5 mM solution (shown in Fig 7.6 e and f). When the concentration of calcium carbonate solution increased to 10 mM ( $S_a \approx 8$ ), the induction times decreased to several seconds,[311] with the ratio  $I/I_0$  falling to less than 10%. And both Raman and TEM measurements confirmed that the existence of ACC particles after this growth period (shown in Fig 7.5 and 7.6). These findings were also in agreement with theoretical models that reported an increase in the ACC nucleation rate with an increasing degree of supersaturation.[78] At a solution concentration of 4.5 mM, there was minimal particle aggregation, whereas at 10 mM solution, there was a high degree of particles aggregation, resulting in a short lifetime of the amorphous precursor phase.

In the case of  $CaCO_3$  precipitating in solution, the situation is complicated by the sedimentation of calcite particles upon growth to a certain size. Whitmer and Luijten

described the relative importance of Brownian motion and the rate of sedimentation under gravity.[341] For spherical particles, the dimensionless Peclet number  $Pe$  of a suspension is briefly described by:

$$Pe = \frac{4\pi\Delta\rho r^4}{3kT} \quad (\text{equation 7.3})$$

Where  $r$  is the radius of the particle and  $\Delta\rho$  is the effective density, i.e. the difference in density between particle and medium. Upon reaching a certain size, the particles will sediment at a terminal velocity, where the weight of the particle is equal to the drag force acting upon it.[314] For  $Pe < 1$  Brownian motion dominates and gravitational sedimentation is unimportant, whereas particles with  $Pe > 1$  will settle under gravity. For the effective density of ACC  $\Delta\rho \approx 620 \text{ kgm}^{-3}$  and  $\Delta\rho \approx 1760 \text{ kgm}^{-3}$  for calcite,[78] the critical value of  $r$  at 22 °C is hence about 0.9  $\mu\text{m}$  for ACC and about 0.8  $\mu\text{m}$  for calcite. This estimate means that ACC with  $r \leq 0.15 \mu\text{m}$  will not sediment, whereas calcite crystals will settle as they grow into the micrometer size regime. Actually, at the concentration of 2.5 mM solution, there are two particles types: ACC and calcite. Due to their small size ( $r \leq 0.15 \mu\text{m}$ ) and lower density, the ACC particles will not readily sediment, and it is assumed that sedimentation occurs only for calcite crystals with micrometer size after 1 min.

The Raman measurements also suggested an increased degree of crystallinity after a 1 minute growth period. However, only ACC particles, which do not settle, were observed using TEM or SEM after this time period (Fig 7.6 a, c and e). In contrast, calcite particles were observed at solution concentrations of 2.5 mM after 1 min under Raman, which is indicative of the conversion of ACC into calcite. However, it is difficult to prove to what extent this may be influenced by the sample collecting procedure. The Raman spectra of precipitates from all concentrations were indistinguishable from reference calcite after 5 mins growth period, although TEM measurements after 5 mins suggested that there was still a high number density of amorphous particles.

The relative magnitude of an attractive van der Waals force and a repulsive electrical double-layer force [342] i.e. the DLVO theory of colloidal stability, are normally the significant parameters to determine the stability of a colloidal

dispersion which formed by nano-sized ACC spheres. Actually, in this case, the electrostatic stabilisation can be negligible because the surface potential of ACC is low (10-15 mV) which is likely to be close to that of calcite. [343-345] This compares with the large van der Waals (quantified by the magnitude of the Hamaker constant, which would be close to that of calcite, or  $2.2 \times 10^{-20}$  J), [346]. The attraction leads to the aggregation of particles which is suggested by the images.

The results shown above described the aggregation and growth pathway of ACC transformed to calcite (or vaterite) when the size of amorphous particles exceeded 100 nm. Thereafter, the crystals grow rapidly to micron-sized after 1 min even at the lower concentrations and then settle. The combination of sedimentation of larger crystals and dissolution of unstable ACC particles/aggregates as the solution concentration falls leads to the clearing of the mixed solution with time. It should also be noted that despite the very obvious differences in turbidity of the 2.5 mM and 5 mM solutions (the 2.5 mM shows only very slight turbidity which could not be observed with the naked eye, while the turbidity in the 5 mM solution is easily seen) and the lifetime of ACC (the 2.5 mM shows short-lived amorphous phase, while in 5 mM solution, ACC still exists after 10 mins) the pathways of crystallisation in the two systems appear to be quite similar. These results also showed the appearance of calcite may take slightly longer at the higher concentrations (such as calcite can be observed in 5 mins at 2.5 mM-3.5 mM solutions ) but it is difficult to be certain in view of the nature of the sample extraction. However, there is a similar conclusion that the calcite can appear earlier at lower concentration with a large excess of  $\text{CO}_3^{2-}$  in 0.1 M NaCl solution. [330] That the solution clears more quickly at higher concentrations can be attributed to faster sedimentation of more rapidly growing crystals, as well as dissolution of ACC.

A detectable increase in turbidity is found at 2.5 mM, which is equivalent to 40 % supersaturation with respect to ACC, and almost 3 times the supersaturation with respect to calcite. It is hence suggested that homogeneous nucleation of ACC occurs concurrently with heterogeneous nucleation of calcite (on foreign particles). This is due to the transformation of nano-sized ACC particles to 200 nm crystals (as shown in Fig 7.6b and d), in the presence of micron-sized calcite and vaterite crystals at the

same time as ACC. As different crystallization pathways (including homogeneous and heterogeneous nucleation) operate at one and the same concentration therefore casts doubt on the use of induction times to distinguish between different nucleation mechanisms at different concentrations.[323, 347]

The presence of  $Mg^{2+}$  also leads to a longer lifetime of ACC. This is caused by an inhibition of calcite growth, arising from the energy barrier for dehydration of  $Mg^{2+}$  relative to  $Ca^{2+}$  [32, 348, 349]. The elapsed time of maximum turbidity shown in Fig 6.8 and 6.9 indeed relates to magnesium concentrations. It is suggested that the magnesium ions slow the onset of  $CaCO_3$  precipitation, with the large recovery lag period at higher magnesium ion concentrations which also implying a stabilisation of smaller particles, such as ACC. Poly(acrylic acid) is also recognised to stabilise ACC, and in the concentration regime employed here (from 1.25 to 10  $\mu g/ml$ ) forms a so-called Polymer Induced Liquid Precursor (PILP) phase, which comprises a hydrated calcium-carbonate-polymer species. This then transforms to ACC before crystallising to calcite or vaterite. Again, as in the addition of  $Mg^{2+}$ , the changes in the turbidity of the reaction solution are consistent with this process, with the poly(acrylic acid) causing a delay in the development of turbidity, and an increased lifetime of ACC.

## 7.6 Summary

The results presented showed that the initial development of turbidity (with decreasing the transmission) can be related to the formation of isolated amorphous precursors, nano-sized ACC particles. The subsequent of increasing turbidity with time can be attributed to the transformation or/and aggregation of calcite or vaterite.

The turbidity results also suggest that calcite precipitates directly in the absence of an ACC precursor phase below 2 mM reaction solutions, while ACC can be observed in solutions concentrations of 2.5 mM and above. With increase in the solution concentrations from 2.5 mM to 10 mM, the turbidity increases with the presence of ACC, before decreasing with time.

The maximum value of turbidity corresponding to 10% transmission is achieved from a 6 mM concentration after approximately 4 mins and then can be observed for

all of the higher concentration solutions (including 8 mM and 10 mM solutions). The increase in turbidity values and the lifetime of the turbidity between concentrations of 2.5 and 4.5 mM solution suggested that there are two possible parallel crystallization pathways; the formation of calcite crystals can be obtained both directly from solution, and via crystallization of amorphous precursor phase. The precipitation pathway via ACC increases in dominance with the solution concentration until it becomes the exclusive mechanism that results in its increased lifetime. However, increase in the solution concentration also leads to more rapid ACC aggregation and crystallization, which reduces the lifetime of the turbidity. The lifetime of ACC also increased with the addition of  $Mg^{2+}$  or PAA inhibitors.

## Chapter 8 Final Conclusion and Future Work

The work of this thesis presents evidence for the formation of three minerals, calcium sulfate, calcium phosphate and calcium carbonate. A transient amorphous precursor phase was formed during the precipitation of these minerals. The precipitations of these crystals were considered in a variety of different systems, aiming to further understand the crystallization pathways.

In Chapter 3, the production of calcium sulfate was demonstrated by precipitation of calcium sulfate in 15 mM solution and isolated its early stages. Hemihydrate nanorods were obtained as the precursor phase of gypsum in the room temperature. This was the first finding of precipitation of hemihydrate at ambient conditions. Interestingly, amorphous nanoparticles was also observed and characterized to be amorphous calcium sulfate (ACS) under TEM. It has been overlooked for year because of the short lifetime and unstable property. Then this was the first report about the existence of ACS as the precursor phase of gypsum via hemihydrate intermediate. Complete characterisation of these processes also investigated by using Cryo-TEM and Titration under the solubility level. The observed hemihydrate formation in the “forbidden region” was also attributed a size dependent surface enthalpy of hemihydrate which makes this mineral phase more stable than gypsum at lower particle size and lower concentrations.

Growing calcium sulfate in the presence of additives demonstrated that both morphology and polymorph of  $\text{CaSO}_4$  can be under control of additives. Although our experimental set-up was simple, the results showed that the growth of gypsum was effectively inhibited in the addition of PAA, Mg ions and sodium triphosphate. In retarding the precipitation, and producing both ACS and hemihydrate with considerably longevity, additives can therefore be used as an effective means for synthesizing these metastable phases. Indeed, it matches with previous hypotheses that stabilized calcium hemihydrate can also be formed as a biomineral within deep-sea medusae [141, 198].

The stabilization of the metastable phases using additives also facilitates investigation of the crystallization mechanism that the oriented aggregation of hemihydrate nanorods into needle-like gypsum can be transformed through aggregation-based pathway.

The work in this thesis considered the formation and transformation mechanisms of  $\text{CaSO}_4$ . However, the methods developed here are well suited to study the crystallization of a range of inorganic materials. Calcium oxalate, in particular calcium oxalate monohydrate is an important biomaterial, widely present in kidney stone. The crossed-cylinder apparatus in the absence or presence of additives in Chapter 5 and Chapter 6 present an ideal model to investigate how small volume influence the mineral formation over a continuous range. As amorphous calcium carbonate, amorphous calcium sulfate and amorphous calcium phosphate were observed within confined geometries around the region of contact, and it would be a point of interest to determine whether amorphous calcium oxalate exist as an early stage in calcium oxalate crystallization.

Furthermore, the technique developed to study crystallization within small volumes perhaps presents the largest scope for development of studying crystallization pathway. By precipitation the sample in a micro-droplets, from micron to nanometer scales, in-situ nucleation statistics could be observed under high resolution camera. Furthermore, both oil-solution or agar-solution micro-fluidic system can be used in Polydimethylsiloxane (PDMS) chips. Since amorphous phase is isotropic, it can be readily distinguished from crystals under crossed-polarisers, enabling realtime monitoring of polymorphic transformations.

## List of References

1. Mann, S., *Biom mineralization: principles and concepts in bioinorganic materials chemistry*. 2001: Oxford University Press, USA.
2. Tang, Z., et al., *Nanostructured artificial nacre*. *Nature Materials*, 2003. **2**(6): p. 413-418.
3. Hardikar, V.V. and E. Matijevi, *Influence of ionic and nonionic dextrans on the formation of calcium hydroxide and calcium carbonate particles*. *Colloids and Surfaces A: Physicochemical and Engineering Aspects*, 2001. **186**(1-2): p. 23-31.
4. Lowenstam, H.A. and S. Weiner, *On biomineralization*. 1989: Oxford University Press, USA.
5. Bazylinski, D. and R. Frankel, *Biologically controlled mineralization in prokaryotes*. *Reviews in Mineralogy and Geochemistry*, 2003. **54**(1): p. 217.
6. Kim, Y.-Y., et al., *An artificial biomineral formed by incorporation of copolymer micelles in calcite crystals*. *Nature Materials*, 2011. **10**(11): p. 890-896.
7. Furby, E., Glueckau, E., and L.A. McDonald, *SOLUBILITY OF CALCIUM SULPHATE IN SODIUM CHLORIDE AND SEA SALT SOLUTIONS*. *Desalination*, 1968. **4**(2): p. 264-&.
8. Kuang, D.B., et al., *Preparation of inorganic salts (CaCO<sub>3</sub>, BaCO<sub>3</sub>, CaSO<sub>4</sub>) nanowires in the Triton X-100/cyclohexane/water reverse micelles*. *Journal of Crystal Growth*, 2002. **244**(3-4): p. 379-383.
9. Gower, L.B., *Biomimetic model systems for investigating the amorphous precursor pathway and its role in biomineralization*. *Chemical reviews*, 2008. **108**(11): p. 4551-4627.
10. Grieshaber, E., et al., *Amorphous calcium carbonate in the shell material of the brachiopod *Megerlia truncata**. *European Journal of Mineralogy*, 2009. **21**(4): p. 715-723.
11. Herrero, J., O. Artieda, and W.H. Hudnall, *Gypsum, a Tricky Material*. *Soil Science Society of America Journal*, 2009. **73**(6): p. 1757-1763.
12. Kashchiev, D., *Nucleation*. 2000, Oxford: Butterworth-Heinemann.
13. Kashchiev, D. and G.M. van Rosmalen, *Review: Nucleation in solutions revisited*. *Crystal Research and Technology*, 2003. **38**(7-8): p. 555-574.
14. Beniash, E., et al., *Amorphous calcium carbonate transforms into calcite during sea urchin larval spicule growth*. *Proceedings of the Royal Society of London Series B-Biological Sciences*, 1997. **264**(1380): p. 461-465.
15. Rees, G.D., et al., *Formation and morphology of calcium sulfate nanoparticles and nanowires in water-in-oil microemulsions*. *Langmuir*, 1999. **15**(6): p. 1993-2002.
16. Wang, Y.-W., et al., *A new precipitation pathway for calcium sulfate dihydrate (gypsum) via amorphous and hemihydrate intermediates*. *Chemical Communications*, 2012. **48**(4): p. 504-506.
17. Kim, Y.Y., et al., *Substrate-directed formation of calcium carbonate fibres*. *Journal of Materials Chemistry*, 2009. **19**(3): p. 387-398.

18. Addadi, L., S. Raz, and S. Weiner, *Taking advantage of disorder: amorphous calcium carbonate and its roles in biomineralization*. *Advanced Materials*, 2003. **15**(12): p. 959-970.
19. Weiner, S., L. Addadi, and H.D. Wagner, *Materials design in biology*. *Materials Science and Engineering: C*, 2000. **11**(1): p. 1-8.
20. Meldrum, F.C. and H. Co Ifen, *Controlling mineral morphologies and structures in biological and synthetic systems*. *Chemical reviews*, 2008. **108**(11): p. 4332-4432.
21. Wilbur, K.M. and N. Watabe, *Experimental studies on calcification in molluscs and the alga *Coccolithus huxleyi**. *Annals of the New York Academy of Sciences*, 1963. **109**(1): p. 82-112.
22. Herman, A., L. Addadi, and S. Weiner, *Interactions of sea-urchin skeleton macromolecules with growing calcite crystals—a study of intracrystalline proteins*. 1988.
23. Lioliou, M.G., et al., *Calcium sulfate precipitation in the presence of water-soluble polymers*. *Journal of colloid and interface science*, 2006. **303**(1): p. 164-170.
24. Jackson, A., J. Vincent, and R. Turner, *The mechanical design of nacre*. *Proceedings of the Royal society of London. Series B. Biological sciences*, 1988. **234**(1277): p. 415-440.
25. Currey, J., *Mechanical properties of mother of pearl in tension*. *Proceedings of the Royal society of London. Series B. Biological sciences*, 1977. **196**(1125): p. 443-463.
26. Jackson, A., J. Vincent, and R. Turner, *Comparison of nacre with other ceramic composites*. *Journal of Materials Science*, 1990. **25**(7): p. 3173-3178.
27. Osterwalder, N., et al., *Preparation of nano-gypsum from anhydrite nanoparticles: Strongly increased Vickers hardness and formation of calcium sulfate nano-needles*. *Journal of Nanoparticle Research*, 2007. **9**(2): p. 275-281.
28. Cölfen, H. and S. Mann, *Higher Order Organization by Mesoscale Self Assembly and Transformation of Hybrid Nanostructures*. *Angewandte Chemie International Edition*, 2003. **42**(21): p. 2350-2365.
29. Klepetsanis, P.G. and P.G. Koutsoukos, *Kinetics of calcium sulfate formation in aqueous media: effect of organophosphorus compounds*. *Journal of Crystal Growth*, 1998. **193**(1-2): p. 156-163.
30. Kuntze, R.A., *RETARDATION OF CRYSTALLIZATION OF CALCIUM SULPHATE DIHYDRATE*. *Nature*, 1966. **211**(5047): p. 406-&.
31. Liu, S.T. and Nancolla.Gh, *LINEAR CRYSTALLIZATION AND INDUCTION-PERIOD STUDIES OF GROWTH OF CALCIUM SULFATE DIHYDRATE CRYSTALS*. *Talanta*, 1973. **20**(2): p. 211-216.
32. Loste, E., et al., *The role of magnesium in stabilising amorphous calcium carbonate and controlling calcite morphologies*. *Journal of Crystal Growth*, 2003. **254**(1-2): p. 206-218.
33. Lou, W.B., B.H. Guan, and Z.B. Wu, *Dehydration behavior of FGD gypsum by simultaneous TG and DSC analysis*. *Journal of Thermal Analysis and Calorimetry*, 2011. **104**(2): p. 661-669.

34. Meldrum, F.C. and H. Colfen, *Controlling Mineral Morphologies and Structures in Biological and Synthetic Systems*. Chemical reviews, 2008. **108**(11): p. 4332-4432.
35. Niederberger, M. and H. Cölfen, *Oriented attachment and mesocrystals: Non-classical crystallization mechanisms based on nanoparticle assembly*. Physical Chemistry Chemical Physics, 2006. **8**(28): p. 3271-3287.
36. Nancollas, G.H., M.M. Reddy, and F. Tsai, *CALCIUM SULFATE DIHYDRATE CRYSTAL-GROWTH IN AQUEOUS-SOLUTION AT ELEVATED-TEMPERATURES*. Journal of Crystal Growth, 1973. **20**(2): p. 125-134.
37. Ostroff, A.G., *Conversion of gypsum to anhydrite in aqueous salt solutions*. Geochim. Cosmochim. Acta., 1964. **28**: p. 1363-1372.
38. Pina, C.M., *Nanoscale dissolution and growth on anhydrite cleavage faces*. Geochimica Et Cosmochimica Acta, 2009. **73**(23): p. 7034-7044.
39. Sigel, A., H. Sigel, and R.K. Sigel, *Biom mineralization: from nature to application*. 2008: Wiley.
40. MacDonald, G.J.F., *Anhydrite-gypsum equilibrium relations*. Amer. J. Sci., 1953. **251**: p. 884-898.
41. Colfen, H. and M. Antonietti, *Mesocrystals: Inorganic superstructures made by highly parallel crystallization and controlled alignment*. Angewandte Chemie-International Edition, 2005. **44**(35): p. 5576-5591.
42. Mahmoud, M.H.H., et al., *Crystal modification of calcium sulfate dihydrate in the presence of some surface-active agents*. Journal of Colloid and Interface Science, 2004. **270**(1): p. 99-105.
43. Mullin, J.W., *Crystallization*. Fourth ed. 2001, Oxford: Butterworth-Heinemann.
44. Hamilton, B.D., et al., *Manipulating Crystal Growth and Polymorphism by Confinement in Nanoscale Crystallization Chambers*. Acc. Chem. Res., 2012. **45**(3): p. 414-423.
45. Meldrum, F.C. and H. Colfen, *Controlling Mineral Morphologies and Structures in Biological and Synthetic Systems*. Chem. Revs., 2008. **108**(11): p. 4332-4432.
46. Charola, A.E., J. Puhlinger, and M. Steiger, *Gypsum: a review of its role in the deterioration of building materials*. Environ. Geol., 2007. **52**(2): p. 207-220.
47. Goldsmith, J.R., D.L. Graf, and O.I. Joensuu, *The occurrence of magnesian calcites in nature*. Geochimica Et Cosmochimica Acta, 1955. **7**(5): p. 212-230.
48. Weber, J.N., *Incorporation of strontium into reef coral skeletal carbonate*. Geochimica Et Cosmochimica Acta, 1973. **37**(9): p. 2173-2190.
49. Bischoff, W.D., F.T. Mackenzie, and F.C. Bishop, *Stabilities of synthetic magnesian calcites in aqueous solution: Comparison with biogenic materials*. Geochimica Et Cosmochimica Acta, 1987. **51**(6): p. 1413-1423.
50. Butler, M.F., et al., *Calcium carbonate crystallization in the presence of biopolymers*. Crystal Growth & Design, 2006. **6**(3): p. 781-794.

51. Lippmann, F., *Sedimentary carbonate minerals*. 1973: Springer Verlag.
52. Mucci, A. and J.W. Morse, *The incorporation of Mg<sup>2+</sup> and Sr<sup>2+</sup> into calcite overgrowths: influences of growth rate and solution composition*. *Geochimica Et Cosmochimica Acta*, 1983. **47**(2): p. 217-233.
53. Falini, G., et al., *Control of aragonite or calcite polymorphism by mollusk shell macromolecules*. *Science*, 1996. **271**(5245): p. 67-69.
54. Fernandez-Diaz, L., et al., *The role of magnesium in the crystallization of calcite and aragonite in a porous medium*. *Journal of Sedimentary Research*, 1996. **66**(3): p. 482-491.
55. Nancollas, G.H. and K. Sawada, *Formation of scales of calcium carbonate polymorphs: The influence of magnesium ion and inhibitors*. *Journal of Petroleum Technology*, 1982. **34**(3): p. 645-652.
56. Falini, G., et al., *Oriented crystallization of vaterite in collagenous matrices*. *Chemistry- A European Journal*, 1998. **4**(6): p. 1048-1052.
57. Raz, S., S. Weiner, and L. Addadi, *Formation of High-Magnesian Calcites via an Amorphous Precursor Phase: Possible Biological Implications*. *Advanced Materials*, 2000. **12**(1): p. 38-42.
58. Cöelfen, H. and M. Antonietti, *Mesocrystals and nonclassical crystallization*. 2008: Wiley. com.
59. Levi, Y., et al., *Control Over Aragonite Crystal Nucleation and Growth: An In Vitro Study of Biomineralization*. *Chemistry – A European Journal*, 1998. **4**(3): p. 389-396.
60. Aizenberg, J., A.J. Black, and G.H. Whitesides, *Oriented growth of calcite controlled by self-assembled monolayers of functionalized alkanethiols supported on gold and silver*. *Journal of the American Chemical Society*, 1999. **121**(18): p. 4500-4509.
61. Damien, C. and J. Parsons, *Bone graft and bone graft substitutes: a review of current technology and applications*. *Journal of Applied Biomaterials*, 2004. **2**(3): p. 187-208.
62. Reeder, R. and D. Barber, *Carbonates: mineralogy and chemistry*. 1983: Mineralogical Society of America Washington, DC;.
63. Deer, W. and H. HOWIE, A. and Zussman, J., 1974, *An Introduction to the Rock Forming Minerals*, Longman, London.
64. Shiraga, H., et al., *Inhibition of calcium oxalate crystal growth in vitro by uropontin: another member of the aspartic acid-rich protein superfamily*. *Proceedings of the National Academy of Sciences*, 1992. **89**(1): p. 426-430.
65. Königsberger, E. and L. Königsberger, *Biomineralization: medical aspects of solubility*. 2006: J. Wiley.
66. Young, J.R., et al., *Crystal assembly and phylogenetic evolution in heterococcoliths*. *Nature*, 1992. **356**(6369): p. 516-518.
67. Brown, W.E., et al., *CRYSTALLOGRAPHY OF OCTACALCIUM PHOSPHATE*. *Journal of the American Chemical Society*, 1957. **79**(19): p. 5318-5319.
68. Weissman, I.L., *Stem cells: units of development, units of regeneration, and units in evolution*. *Cell*, 2000. **100**(1): p. 157-168.
69. Weiss, I.M., et al., *Mollusc larval shell formation: amorphous calcium carbonate is a precursor phase for aragonite*. *Journal of Experimental Zoology*, 2002. **293**(5): p. 478-491.

70. Mann, S., *Biomineralization: principles and concepts in bioinorganic materials chemistry*. Vol. 5. 2001: Oxford University Press on Demand.
71. Anderson, H.C., *Molecular biology of matrix vesicles*. Clinical orthopaedics and related research, 1995. **314**: p. 266-280.
72. Anderson, H.C., *Vesicles associated with calcification in the matrix of epiphyseal cartilage*. The Journal of cell biology, 1969. **41**(1): p. 59-72.
73. Arias, J.L. and M.S. Fernández, *Biomimetic processes through the study of mineralized shells*. Materials Characterization, 2003. **50**(2-3): p. 189-195.
74. Davey, R.J. and J.W. Mullin, *Growth of the {101} faces of ammonium dihydrogen phosphate crystals in the presence of ionic species*. Journal of Crystal Growth, 1974. **23**(2): p. 89-94.
75. De Yoreo, J.J. and P.G. Vekilov, *Principles of crystal nucleation and growth*. Reviews in Mineralogy and Geochemistry, 2003. **54**(1): p. 57-93.
76. Berman, A., et al., *Biological control of crystal texture: a widespread strategy for adapting crystal properties to function*. Science, 1993. **259**(5096): p. 776-779.
77. Kim, Y.-Y., et al., *An artificial biomineral formed by incorporation of copolymer micelles in calcite crystals*. Nat Mater, 2011. **10**(11): p. 890-896.
78. Bolze, J., et al., *Formation and growth of amorphous colloidal CaCO<sub>3</sub> precursor particles as detected by time-resolved SAXS*. Langmuir, 2002. **18**(22): p. 8364-8369.
79. Albeck, S., et al., *Interactions of various skeletal intracrystalline components with calcite crystals*. Journal of the American Chemical Society, 1993. **115**(25): p. 11691-11697.
80. Grases, F., C. Genestar, and A. Millán, *The influence of some metallic ions and their complexes on the kinetics of crystal growth of calcium oxalate*. Journal of Crystal Growth, 1989. **94**(2): p. 507-512.
81. Meldrum, F.C. and S.T. Hyde, *Morphological influence of magnesium and organic additives on the precipitation of calcite*. Journal of Crystal Growth, 2001. **231**(4): p. 544-558.
82. Orme, C., et al., *Formation of chiral morphologies through selective binding of amino acids to calcite surface steps*. Nature, 2001. **411**(6839): p. 775-779.
83. Manoli, F., et al., *The effect of aminoacids on the crystal growth of calcium carbonate*. Journal of Crystal Growth, 2002. **236**(1-3): p. 363-370.
84. Boanini, E., et al., *Nanocomposites of hydroxyapatite with aspartic acid and glutamic acid and their interaction with osteoblast-like cells*. Biomaterials, 2006. **27**(25): p. 4428-4433.
85. Chutipongtanate, S., S. Chaiyarit, and V. Thongboonkerd, *Citrate, not phosphate, can dissolve calcium oxalate monohydrate crystals and detach these crystals from renal tubular cells*. European Journal of Pharmacology. **689**(1-3): p. 219-225.
86. Wang, L. and G. Nancollas, *Calcium orthophosphates: crystallization and dissolution*. Chem. Rev, 2008. **108**(11): p. 4628-4669.

87. Somasundaran, P. and B. Markovic, *Interfacial properties of calcium phosphate*. Calcium phosphate in biological and industrial system, 1998: p. 85–101.
88. Daculsi, G., et al., *Formation of carbonate-apatite crystals after implantation of calcium phosphate ceramics*. Calcified tissue international, 1990. **46**(1): p. 20-27.
89. Russell, P., et al., *Photonic-crystal fibres and photonic-crystal fibre devices*, 2002, Google Patents.
90. Zhou, H.X., G.N. Rivas, and A.P. Minton, *Macromolecular crowding and confinement: Biochemical, biophysical, and potential physiological consequences*, in *Annual Review of Biophysics*. 2008, Annual Reviews: Palo Alto. p. 375-397.
91. Yunoki, S., et al., *Control of pore structure and mechanical property in hydroxyapatite/collagen composite using unidirectional ice growth*. Materials Letters, 2006. **60**(8): p. 999-1002.
92. Kennedy, M.T., et al., *Cryo-transmission electron microscopy confirms controlled synthesis of cadmium sulfide nanocrystals within lecithin vesicles*. Chemistry of Materials, 1998. **10**(8): p. 2116-2119.
93. Doi, Y., et al., *Inhibition of seeded growth of enamel apatite crystals by amelogenin and amelotin proteins in vitro*. Journal of Dental Research, 1984. **63**(2): p. 98-105.
94. Eanes, E. and A. Hailer, *Liposome-mediated calcium phosphate formation in metastable solutions*. Calcified tissue international, 1985. **37**(4): p. 390-394.
95. Heywood, B.R. and E.D. Eanes, *An ultrastructural study of calcium phosphate formation in multilamellar liposome suspensions*. Calcified tissue international, 1987. **41**(4): p. 192-201.
96. Eanes, E.D., et al., *Proteoglycan inhibition of calcium phosphate precipitation in liposomal suspensions*. Glycobiology, 1992. **2**(6): p. 571-578.
97. Kuang, D., et al., *Preparation of inorganic salts (CaCO<sub>3</sub>, BaCO<sub>3</sub>, CaSO<sub>4</sub>) nanowires in the Triton X-100/cyclohexane/water reverse micelles*. Journal of Crystal Growth, 2002. **244**(3-4): p. 379-383.
98. Zhang, R. and P.X. Ma, *Poly( $\alpha$ -hydroxyl acids)/hydroxyapatite porous composites for bone- tissue engineering. I. Preparation and morphology*. Journal of Biomedical Materials Research, 1999. **44**(4): p. 446-455.
99. Mikos, A.G., et al., *Preparation and characterization of poly(l-lactic acid) foams*. Polymer, 1994. **35**(5): p. 1068-1077.
100. Borden, M., M. Attawia, and C.T. Laurencin, *The sintered microsphere matrix for bone tissue engineering: In vitro osteoconductivity studies*. Journal of Biomedical Materials Research, 2002. **61**(3): p. 421-429.
101. Mooney, D.J., et al., *Novel approach to fabricate porous sponges of poly(d,l-lactic-co-glycolic acid) without the use of organic solvents*. Biomaterials, 1996. **17**(14): p. 1417-1422.
102. Williams, D.F., *Biocompatibility of clinical implant materials*. Vol. 1. 1981: CRC press Boca Raton, Florida.
103. Ramay, H.R. and M. Zhang, *Preparation of porous hydroxyapatite scaffolds by combination of the gel-casting and polymer sponge methods*. Biomaterials, 2003. **24**(19): p. 3293-3302.

104. Tian, J. and J. Tian, *Preparation of porous hydroxyapatite*. Journal of Materials Science, 2001. **36**(12): p. 3061-3066.
105. Park, R.J. and F.C. Meldrum, *Shape-constraint as a route to calcite single crystals with complex morphologies*. Journal of Materials Chemistry, 2004. **14**(14): p. 2291-2296.
106. Goh, L., et al., *A stochastic model for nucleation kinetics determination in droplet-based microfluidic systems*. Crystal Growth & Design, 2010. **10**(6): p. 2515-2521.
107. Sanjoh, A. and T. Tsukihara, *Spatiotemporal protein crystal growth studies using microfluidic silicon devices*. Journal of Crystal Growth, 1999. **196**(2): p. 691-702.
108. Squires, T.M. and S.R. Quake, *Microfluidics: Fluid physics at the nanoliter scale*. Reviews of modern physics, 2005. **77**(3): p. 977.
109. Hansen, C.L., M.O. Sommer, and S.R. Quake, *Systematic investigation of protein phase behavior with a microfluidic formulator*. Proceedings of the National Academy of Sciences of the United States of America, 2004. **101**(40): p. 14431-14436.
110. Hansen, C.L., et al., *A microfluidic device for kinetic optimization of protein crystallization and in situ structure determination*. Journal of the American Chemical Society, 2006. **128**(10): p. 3142-3143.
111. Wolf, S.E., et al., *Early homogenous amorphous precursor stages of calcium carbonate and subsequent crystal growth in levitated droplets*. Journal of the American Chemical Society, 2008. **130**(37): p. 12342-12347.
112. Lee, A.Y., I.S. Lee, and A.S. Myerson, *Factors affecting the polymorphic outcome of glycine crystals constrained on patterned substrates*. Chemical engineering & technology, 2006. **29**(2): p. 281-285.
113. Lee, I.S., et al., *Concomitant crystallization of glycine on patterned substrates: The effect of pH on the polymorphic outcome*. Crystal Growth and Design, 2008. **8**(1): p. 108-113.
114. Stephens, C.J., et al., *Early Stages of Crystallization of Calcium Carbonate Revealed in Picoliter Droplets*. Journal of the American Chemical Society, 2011. **133**(14): p. 5210-5213.
115. Martin, C.R., *Membrane-Based Synthesis of Nanomaterials*. Chemistry of Materials, 1996. **8**(8): p. 1739-1746.
116. Loste, E., et al., *Precipitation of Calcium Carbonate in Confinement*. Advanced Functional Materials, 2004. **14**(12): p. 1211-1220.
117. Loste, E. and F.C. Meldrum, *Control of calcium carbonate morphology by transformation of an amorphous precursor in a constrained volume*. Chemical Communications, 2001(10): p. 901-902.
118. Stephens, C.J., et al., *Amorphous Calcium Carbonate is Stabilized in Confinement*. Advanced Functional Materials. **20**(13): p. 2108-2115.
119. Wang, Y.W., H.K. Christenson, and F.C. Meldrum, *Confinement Leads to Control over Calcium Sulfate Polymorph*. Advanced Functional Materials, 2013.
120. Aizenberg, J., et al., *Direct fabrication of large micropatterned single crystals*. Science, 2003. **299**(5610): p. 1205-1208.

121. Song, X.Y., et al., *Preparation of different morphologies of calcium sulfate in organic media*. Journal of Materials Chemistry, 2003. **13**(7): p. 1817-1821.
122. Moriarty, P., *Nanostructured materials*. Reports on Progress in Physics, 2001. **64**(3): p. 297-381.
123. Williams, D.B. and C.B. Carter, *Transmission electron microscopy: a textbook for materials science*. 2009: Springer.
124. Sawant, P.D. and A. Niranjane, *Formation of nanoparticles of sparingly soluble salts (CaSO<sub>4</sub> and CaSO<sub>4</sub> : Dy) using liquid-liquid separation method and application for detection of alpha-radiations*. Micro & Nano Letters, 2006. **1**(2): p. 108-111.
125. Li, M., H. Colfen, and S. Mann, *Morphological control of BaSO<sub>4</sub> microstructures by double hydrophilic block copolymer mixtures*. Journal of Materials Chemistry, 2004. **14**(14): p. 2269-2276.
126. Li, M. and S. Mann, *Emergence of morphological complexity in BaSO<sub>4</sub> fibers synthesized in AOT microemulsions*. Langmuir, 2000. **16**(17): p. 7088-7094.
127. Friedrich, H., et al., *Imaging of Self-Assembled Structures: Interpretation of TEM and Cryo-TEM Images*. Angewandte Chemie-International Edition, 2010. **49**(43): p. 7850-7858.
128. !!! INVALID CITATION !!!
129. Van Driessche, A., et al., *The role and implications of bassanite as a stable precursor phase to gypsum precipitation*. Science, 2012. **336**(6077): p. 69-72.
130. Paul, H. and A. Nico, *Stabilization of amorphous calcium carbonate by controlling its particle size*. Nanoscale, 2010. **2**(11): p. 2436-2439.
131. Navrotsky, A., *Energetic clues to pathways to biomineralization: Precursors, clusters, and nanoparticles*. Proceedings of the National Academy of Sciences of the United States of America, 2004. **101**(33): p. 12096-12101.
132. Austin, A.E., et al., *PRECIPITATION OF CALCIUM-SULFATE FROM SEA-WATER AT HIGH-TEMPERATURES*. Desalination, 1975. **16**(3): p. 331-344.
133. Kirfel, A. and G. Will, *Charge density in anhydrite CaSO<sub>4</sub> from X-ray and neutron diffraction Measurements*. Acta Crystallogr., 1980. **B36**: p. 2881-2890.
134. Hanic, F., *Kinetics of the thermal decomposition of CaSO<sub>4</sub> in air*. Br. Ceram. Trans. J., 1985. **84**: p. 22-25.
135. Wirsching, F., *Calcium Sulfate*, in *Ullmann's Encyclopedia of Industrial Chemistry*. 2000, Wiley-VCH Verlag GmbH & Co. KGaA.
136. Luo, K.B., et al., *Influence of temperature and solution composition on the formation of calcium sulfates*. Particuology. **8**(3): p. 240-244.
137. Charola, A.E., J. Puhlinger, and M. Steiger, *Gypsum: a review of its role in the deterioration of building materials*. Environmental Geology, 2007. **52**(2): p. 207-220.
138. Beniash, E., L. Addadi, and S. Weiner, *Cellular control over spicule formation in sea urchin embryos: A structural approach*. Journal of Structural Biology, 1999. **125**(1): p. 50-62.
139. Brecevic, L. and A.E. Nielsen, *SOLUBILITY OF AMORPHOUS CALCIUM-CARBONATE*. Journal of Crystal Growth, 1989. **98**(3): p. 504-510.

140. Gruver, R.M., *Differential Thermal-Analysis Studies of Ceramic Materials: III, Characteristic Heat Effects of Some Sulfates*. Journal of the American Ceramic Society, 1951. **34**(11): p. 353-357.
141. Becker, A., et al., *Calcium sulfate hemihydrate is the inorganic mineral in statoliths of Scyphozoan medusae (Cnidaria)*. Dalton Transactions, 2005(8): p. 1545-1550.
142. Chapman, D.M., *X-RAY-MICROANALYSIS OF SELECTED COELENTERATE STATOLITHS*. Journal of the Marine Biological Association of the United Kingdom, 1985. **65**(3): p. 617-627.
143. Ching, W. and McCartne, E., *USE OF A MEMBRANE ELECTRODE TO STUDY CRYSTALLIZATION OF CALCIUM SULFATE FROM AQUEOUS-SOLUTION .1. RELATION BETWEEN CALCIUM-ION ACTIVITY AND CRYSTALLIZATION RATE*. Journal of Applied Chemistry and Biotechnology, 1973. **23**(6): p. 441-450.
144. Kraus, W. and G. Nolze, *PowderCell for Windows*, 1999, Federal Institute for Materials Research and Testing: Berlin.
145. Clarkson, J.R., T.J. Price, and C.J. Adams, *ROLE OF METASTABLE PHASES IN THE SPONTANEOUS PRECIPITATION OF CALCIUM-CARBONATE*. Journal of the Chemical Society-Faraday Transactions, 1992. **88**(2): p. 243-249.
146. Freyer, D., *Untersuchungen zur Phasenbildung und -stabilität im System Na<sub>2</sub>SO<sub>4</sub>-CaSO<sub>4</sub>-H<sub>2</sub>O*, in *Fakultät für Chemie und Physik 2000*, Technische Universität Bergakademie Freiberg: Freiberg. p. 200.
147. Oetzel, M., *Untersuchung der Phasenbeziehungen im System CaSO<sub>4</sub>-H<sub>2</sub>O*, in *Fakultät für Bergbau, Hüttenwesen und Geowissenschaften 1999*, Rheinisch-Westfälische Technische Hochschule Aachen: Aachen. p. 219.
148. Ludwig, U. and N.B. Singh, *Hydration of hemihydrate of gypsum and its supersaturation*. Cement and Concrete Research, 1978. **8**(3): p. 291-299.
149. Dorozhkin, S.V., *Amorphous calcium (ortho)phosphates*. Acta Biomaterialia, 2010. **6**(12): p. 4457-4475.
150. Klepetsanis, P.G., E. Dalas, and P.G. Koutsoukos, *Role of temperature in the spontaneous precipitation of calcium sulfate dihydrate*. Langmuir, 1999. **15**(4): p. 1534-1540.
151. Packter, A., *The precipitation of calcium sulphate dihydrate from aqueous solution: Induction periods, crystal numbers and final size*. Journal of Crystal Growth, 1974. **21**(2): p. 191-194.
152. Erdemir, D., A.Y. Lee, and A.S. Myerson, *Nucleation of Crystals from Solution: Classical and Two-Step Models*. Accounts of Chemical Research, 2009. **42**(5): p. 621-629.
153. Pouget, E.M., et al., *The Initial stages of template-controlled CaCO<sub>3</sub> formation revealed by cryo-TEM*. Science, 2009. **323**(5920): p. 1455-1458.
154. Freyer, D. and W. Voigt, *Crystallization and phase stability of CaSO<sub>4</sub> and CaSO<sub>4</sub>-based salts*. Monatshefte Fur Chemie, 2003. **134**(5): p. 693-719.
155. Sarma, L.P., P.S.R. Prasad, and N. Ravikumar, *Raman spectroscopic study of phase transitions in natural gypsum*. Journal of Raman Spectroscopy, 1998. **29**(9): p. 851-856.

156. Society, A.C., *Reagent Chemicals: Specifications and Procedures: American Chemical Society Specifications, Official from January 1, 2006*. 2006: American Chemical Society.
157. Tiemann, H., et al., *Calcium sulfate hemihydrate in statoliths of deep-sea medusae*. Journal of the Chemical Society-Dalton Transactions, 2002(7): p. 1266-1268.
158. Karni, J. and E.Y. Karni, *Gypsum in construction: origin and properties*. Materials and Structures, 1995. **28**(2): p. 92-100.
159. Blaine, S., *Accelerating the hydration of calcium sulfate hemihydrate via high energy mixing*. Materials and Structures, 1997. **30**(6): p. 362-365.
160. Lewry, A.J. and J. Williamson, *The setting of gypsum plaster*. Journal of Materials Science, 1994. **29**(23): p. 6085-6090.
161. Ridge, M.J. and G.A. King, *Hydration of calcium sulphate hemihydrate in the presence of calcium hydroxide*. Journal of Applied Chemistry and Biotechnology, 1977. **27**(1): p. 125-136.
162. Amjad, Z., *Scale inhibition in desalination applications: an overview*. CORROSION 96, 1996.
163. Smith, B.R. and Alexande.Ae, *EFFECT OF ADDITIVES ON PROCESS OF CRYSTALLIZATION .2. FURTHER STUDIES ON CALCIUM SULPHATE (1)*. Journal of colloid and interface science, 1970. **34**(1): p. 81-&.
164. Badens, E., S. Veessler, and R. Boistelle, *Crystallization of gypsum from hemihydrate in presence of additives*. Journal of Crystal Growth, 1999. **198**: p. 704-709.
165. Demadis, K.D. and P. Lykoudis, *Chemistry of Organophosphonate Scale Growth Inhibitors: 3. Physicochemical Aspects of 2-Phosphonobutane-1,2,4-Tricarboxylate (PBTC) And Its Effect on CaCO<sub>3</sub> Crystal Growth*. Bioinorganic Chemistry and Applications, 2005. **3**(3-4): p. 135-149.
166. Amjad, Z., *Calcium Sulfate Dihydrate (Gypsum) Scale Formation on Heat Exchanger Surfaces: The Influence of Scale Inhibitors*. J. Coll. Int. Sci., 1988. **123**(2): p. 523-536.
167. Leung, W.H. and G.H. Nancollas, *Nitrilotri (methylenephosphonic acid) adsorption on barium sulfate crystals and its influence on crystal growth*. Journal of Crystal Growth, 1978. **44**(2): p. 163-167.
168. Liu, S.-T. and G.H. Nancollas, *The crystal growth of calcium sulfate dihydrate in the presence of additives*. Journal of colloid and interface science, 1973. **44**(3): p. 422-429.
169. Clifton, J.R., *THERMAL-ANALYSIS OF CALCIUM SULFATE DIHYDRATE AND SUPPOSED ALPHA AND BETA FORMS OF CALCIUM SULFATE HEMIHYDRATE FROM 25 TO 500 DEGREES C*. Journal of Research of the National Bureau of Standards Section a-Physics and Chemistry, 1972. **A 76**(1): p. 41-&.
170. Dumazer, G., A. Smith, and A. Lemarchand, *Master Equation Approach to Gypsum Needle Crystallization*. Journal of Physical Chemistry C, 2010. **114**(9): p. 3830-3836.
171. Hamdona, S.K. and U.A. Al Hadad, *Crystallization of calcium sulfate dihydrate in the presence of some metal ions*. Journal of Crystal Growth, 2007. **299**(1): p. 146-151.

172. Sayan, P., S. Titiz-Sargut, and B. Avci, *Effect of trace metals on reactive crystallization of gypsum*. Crystal Research and Technology, 2007. **42**(10): p. 961-970.
173. Rashad, M.M., et al., *Crystallization of calcium sulfate dihydrate under simulated conditions of phosphoric acid production in the presence of aluminum and magnesium ions*. Journal of Crystal Growth, 2004. **267**(1-2): p. 372-379.
174. Freyer, D., et al., *Thermal behaviour and crystal structure of sodium-containing hemihydrates of calcium sulfate*. Monatshefte Fur Chemie, 1999. **130**(10): p. 1179-1193.
175. Tang, M.L., X.D. Shen, and H. Huang, *Influence of alpha-calcium sulfate hemihydrate particle characteristics on the performance of calcium sulfate-based medical materials*. Mater. Sci. Eng. C, 2010. **30**(8): p. 1107-1111.
176. Miyajima, T., M. Mori, and S. Ishiguro, *Analysis of complexation equilibria of polyacrylic acid by a Donnan-based concept*. Journal of colloid and interface science, 1997. **187**(1): p. 259-266.
177. Huber, K., *Calcium-induced shrinking of polyacrylate chains in aqueous solution*. The Journal of Physical Chemistry, 1993. **97**(38): p. 9825-9830.
178. Rivas, B.L., E.D. Pereira, and I. Moreno-Villoslada, *Water-soluble polymer-metal ion interactions*. Progress in Polymer Science, 2003. **28**(2): p. 173-208.
179. Wang, Y.-W., et al., *A new precipitation pathway for calcium sulfate dihydrate (gypsum) via amorphous and hemihydrate intermediates*. Chem. Commun., 2012. **48**(4): p. 504-506.
180. Mandal, P.K. and T.K. Mandal, *Anion water in gypsum (CaSO<sub>4</sub>·2H<sub>2</sub>O) and hemihydrate (CaSO<sub>4</sub>·1/2H<sub>2</sub>O)*. Cement and Concrete Research, 2002. **32**(2): p. 313-316.
181. Nakamoto, K., *Infrared and Raman spectra of inorganic and coordination compounds*. 1978: Wiley Online Library.
182. Sansonetti, J.E., et al. *Handbook of basic atomic spectroscopic data*. 2003; Available from: <http://physics.nist.gov/PhysRefData/Handbook/index.html>.
183. Titiz-Sargut, S., P. Sayan, and B. Avci, *Influence of citric acid on calcium sulfate dihydrate crystallization in aqueous media*. Crystal Research and Technology, 2007. **42**(2): p. 119-126.
184. Kushnir, J., *Geochim. Cosmochim. Acta*, 1980. **44**: p. 1471-1482.
185. Cabrera, N. and D.A. Vermilyea, *The Growth of Crystals from Solution*, 1958: p. 393-410.
186. Weijnen, M.P.C., G.M. van Rosmalen, and P. Bennema, *The adsorption of additives at the gypsum crystal surface: A theoretical approach: II. Determination of the surface coverage required for growth inhibition*. Journal of Crystal Growth, 1987. **82**(3): p. 528-542.
187. Weijnen, M.P.C. and G.M. Van Rosmalen, *Adsorption of phosphonates on gypsum crystals*. Journal of Crystal Growth, 1986. **79**(1-3): p. 157-168.
188. Guan, B.H., L.C. Yang, and Z.B. Wu, *Effect of Mg<sup>2+</sup> ions on the Nucleation Kinetics of Calcium Sulfate in Concentrated Calcium Chloride Solutions*. Industrial & Engineering Chemistry Research, 2010. **49**(12): p. 5569-5574.

189. Smith, B.R. and F. Sweett, *CRYSTALLIZATION OF CALCIUM SULFATE DIHYDRATE*. J. Coll. Int. Sci., 1971. **37**(3): p. 612-&.
190. Ahmed, S.B., et al., J. Phys. IV, 2004: p. 141-147.
191. Dogan, O., E. Akyol, and M. Oner, *Polyelectrolytes inhibition effect on crystallization of gypsum*. Crystal Research and Technology, 2004. **39**(12): p. 1108-1114.
192. Lioliou, M.G., et al., *Calcium sulfate precipitation in the presence of water-soluble polymers*. J. Coll. Int. Sci., 2006. **303**(1): p. 164-170.
193. Badens, E., S. Veessler, and R. Boistelle, *Crystallization of gypsum from hemihydrate in presence of additives*. J. Cryst. Growth, 1999. **198**: p. 704-709.
194. Boisvert, J.P., et al., *Hydration of calcium sulfate hemihydrate (CaSO<sub>4</sub> center dot 1/2H<sub>2</sub>O) into gypsum (CaSO<sub>4</sub> center dot 2H<sub>2</sub>O). The influence of the sodium poly(acrylate)/surface interaction and molecular weight*. J. Cryst. Growth, 2000. **220**(4): p. 579-591.
195. Singh, N.B. and B. Middendorf, *Calcium sulphate hemihydrate hydration leading to gypsum crystallization*. Progress in Crystal Growth and Characterization of Materials, 2007. **53**(1): p. 57-77.
196. Van Driessche, A.E.S., et al., *The Role and Implications of Bassanite as a Stable Precursor Phase to Gypsum Precipitation*. Science, 2012. **336**(6077): p. 69-72.
197. Yuwono, V.M., et al., *Oriented Aggregation: Formation and Transformation of Mesocrystal Intermediates Revealed*. J. Am. Chem. Soc., 2010. **132**(7): p. 2163-2165.
198. Tiemann, H., et al., *Calcium sulfate hemihydrate in statoliths of deep-sea medusae*. J. Chem. Soc. Dalton Trans., 2002(7): p. 1266-1268.
199. Shih, W.Y., et al., *Morphometric characterization of calcium sulfate dihydrate (gypsum) scale on reverse osmosis membranes*. Journal of Membrane Science, 2005. **252**(1-2): p. 253-263.
200. Kong, B., et al., *Synthesis of  $\bar{1}\pm$ -calcium sulfate hemihydrate submicron-rods in water/n-hexanol/CTAB reverse microemulsion*. Colloids and Surfaces A: Physicochemical and Engineering Aspects, (0).
201. Stephens, C.J., et al., *Biom mineralization: Amorphous Calcium Carbonate is Stabilized in Confinement (Adv. Funct. Mater. 13/2010)*. Advanced Functional Materials. **20**(13): p. n/a-n/a.
202. Christenson, H.K., Coll. Surf. A, 1997. **123-124**: p. 355.
203. Kovács, T. and H.K. Christenson, *A two-step mechanism for crystal nucleation without supersaturation* Faraday Discuss., 2012. **159**: p. 123-138.
204. Kovács, T., F.C. Meldrum, and H.K. Christenson, *Crystal Nucleation without Supersaturation*. J. Phys. Chem. Lett 2012. **3**: p. 1602-1606.
205. Wang, Y.-W. and F.C. Meldrum, *Additives Stabilize Calcium Sulfate Hemihydrate (Bassanite) in Solution*. J. Mater. Chem., 2012. **22**(41): p. 22055-22062.
206. Saha, A., et al., *New Insights into the Transformation of Calcium Sulfate Hemihydrate to Gypsum Using Time-Resolved Cryogenic Transmission Electron Microscopy*. Langmuir, 2012. **28**(30): p. 11182-11187.

207. Chung, S.-Y., et al., *Multi-phase transformation and Ostwald's rule of stages during crystallization of a metal phosphate*. Nature Physics, 2009. **5**: p. 68-72.
208. ten Wolde, P.R. and D. Frenkel, *Homogeneous nucleation and the Ostwald step rule*. Phys. Chem. Chem. Phys., 1999. **1**: p. 2191-2196.
209. Mathur, A., P. Sharma, and R.C. Cammarata, *Negative surface energy - clearing up confusion*. Nat. Mater., 2005. **4**: p. 186.
210. Ha, J.M., et al., *Polymorph selectivity under nanoscopic confinement*. J. Am. Chem. Soc., 2004. **126**(11): p. 3382-3383.
211. Beiner, M., et al., *Manipulating the crystalline state of pharmaceuticals by nanoconfinement*. Nano Letters, 2007. **7**(5): p. 1381-1385.
212. Stephens, C.J., et al., *Amorphous Calcium Carbonate is Stabilized in Confinement*. Adv. Func. Mater., 2010. **20**(13): p. 2108-2115.
213. Tiemann, H., et al., *Calcium sulfate hemihydrate (bassanite) statoliths in the cubozoan Carybdea sp.* Zool. Anzeiger, 2006. **245**(1): p. 13-17.
214. Ahmi, F. and A. Gadri, *Kinetics and morphology of formed gypsum\**. Desalination, 2004. **166**: p. 427-434.
215. Mann, S., J. Webb, and R.J.P. Williams, *Biom mineralization: chemical and biochemical perspectives*. 1989: John Wiley & Sons.
216. Sarig, S. and J.W. Mullin, *Effect of trace impurities on calcium sulphate precipitation*. Journal of Chemical Technology and Biotechnology, 1982. **32**(4): p. 525-531.
217. Kamhi, S.R., *On the structure of vaterite CaCO<sub>3</sub>*. Acta Crystallographica, 1963. **16**(8): p. 770-772.
218. Schonenberger, C., et al., *Domain structure of self-assembled alkanethiol monolayers on gold*. Journal of Physical Chemistry, 1995. **99**(10): p. 3259-3271.
219. Lee, S.K., M.K. Lee, and H. Lee, *Surfactant-Free Synthesis of CaSO Nanorod/Nanowire by Electrochemical Deposition*. Journal of The Electrochemical Society. **157**: p. K43.
220. Liu, S.T. and G.H. Nancollas, *The kinetics of crystal growth of calcium sulfate dihydrate*. Journal of Crystal Growth, 1970. **6**(3): p. 281-289.
221. Lee, S.K., M.K. Lee, and H. Lee, *Surfactant-Free Synthesis of CaSO<sub>4</sub> Nanorod/Nanowire by Electrochemical Deposition*. Journal of The Electrochemical Society. **157**(3): p. K43-K46.
222. Alimi, F. and A. Gadri, *Kinetics and morphology of formed gypsum*. Desalination, 2004. **166**(1-3): p. 427-434.
223. Mahamid, J., et al., *Amorphous calcium phosphate is a major component of the forming fin bones of zebrafish: Indications for an amorphous precursor phase*. Proceedings of the National Academy of Sciences, 2008. **105**(35): p. 12748-12753.
224. Smith, B. and F. Sweett, *The crystallization of calcium sulfate dihydrate*. Journal of colloid and interface science, 1971. **37**(3): p. 612-618.
225. Meldrum, F., *Calcium carbonate in biomineralisation and biomimetic chemistry*. International Materials Reviews, 2003. **48**(3): p. 187-224.
226. Nudelman, F., et al., *The role of the amorphous phase on the biomimetic mineralization of collagen*. Faraday Discussions, 2012. **159**: p. 357-370.

227. Bigi, A., et al., *Interaction of acidic poly-amino acids with octacalcium phosphate*. Journal of inorganic biochemistry, 2003. **95**(4): p. 291-296.
228. Burke, E., et al., *Influence of polyaspartic acid and phosphophoryn on octacalcium phosphate growth kinetics*. Colloids and Surfaces B: Biointerfaces, 2000. **17**(1): p. 49-57.
229. Bigi, A., et al., *Morphological and structural modifications of octacalcium phosphate induced by poly-L-aspartate*. Crystal Growth & Design, 2004. **4**(1): p. 141-146.
230. Bigi, A., et al., *Morphosynthesis of Octacalcium Phosphate Hollow Microspheres by Polyelectrolyte - Mediated Crystallization*. Angewandte Chemie, 2002. **114**(12): p. 2267-2270.
231. Peytcheva, A. and M. Antonietti, "*Carving on the Nanoscale*": *Polymers for the Site - Specific Dissolution of Calcium Phosphate*. Angewandte Chemie International Edition, 2001. **40**(18): p. 3380-3383.
232. Sikirić, M.D. and H. Füreidi-Milhofer, *The influence of surface active molecules on the crystallization of biominerals in solution*. Advances in Colloid and Interface Science, 2006. **128**: p. 135-158.
233. Tsortos, A. and G.H. Nancollas, *The role of polycarboxylic acids in calcium phosphate mineralization*. Journal of colloid and interface science, 2002. **250**(1): p. 159-167.
234. Liu, S.T. and Nancolla.Gh, *CRYSTAL-GROWTH OF CALCIUM SULFATE DIHYDRATE IN PRESENCE OF ADDITIVES*. Journal of Colloid and Interface Science, 1973. **44**(3): p. 422-429.
235. Schweizer, S. and A. Taubert, *Polymer - Controlled, Bio - Inspired Calcium Phosphate Mineralization from Aqueous Solution*. Macromolecular bioscience, 2007. **7**(9 - 10): p. 1085-1099.
236. Diegmüller, J.J., X. Cheng, and O. Akkus, *Modulation of hydroxyapatite nanocrystal size and shape by polyelectrolytic peptides*. Crystal Growth & Design, 2009. **9**(12): p. 5220-5226.
237. Traub, W., T. Arad, and S. Weiner, *Three-dimensional ordered distribution of crystals in turkey tendon collagen fibers*. Proceedings of the National Academy of Sciences, 1989. **86**(24): p. 9822-9826.
238. Landis, W., et al., *Mineral and organic matrix interaction in normally calcifying tendon visualized in three dimensions by high-voltage electron microscopic tomography and graphic image reconstruction*. Journal of Structural Biology, 1993. **110**(1): p. 39-54.
239. Christenson, H.K., *Confinement effects on freezing and melting*. Journal of Physics-Condensed Matter, 2001. **13**(11): p. R95-R133.
240. Stephens, C.J., et al., *Amorphous calcium carbonate is stabilized in confinement*. Advanced Functional Materials, 2010. **20**(13): p. 2108-2115.
241. Singh, S., et al., *Synthesis of nanocrystalline calcium phosphate in microemulsion—effect of nature of surfactants*. Journal of colloid and interface science, 2008. **319**(1): p. 322-329.
242. Sadasivan, S., D. Khushalani, and S. Mann, *Synthesis and shape modification of organo-functionalised silica nanoparticles with ordered mesostructured interiors*. Journal of Materials Chemistry, 2003. **13**(5): p. 1023-1029.

243. Antonietti, M., et al., *Inorganic/Organic Mesostructures with Complex Architectures: Precipitation of Calcium Phosphate in the Presence of Double - Hydrophilic Block Copolymers*. Chemistry-a European Journal, 1998. **4**(12): p. 2493-2500.
244. Wang, Y., et al., *Hydrothermal synthesis of hydroxyapatite nanopowders using cationic surfactant as a template*. Materials Letters, 2006. **60**(12): p. 1484-1487.
245. Falini, G., M. Gazzano, and A. Ripamonti, *Control of the architectural assembly of octacalcium phosphate crystals in denatured collagenous matrices*. Journal of Materials Chemistry, 2000. **10**(2): p. 535-538.
246. Ethirajan, A., et al., *Biomimetic hydroxyapatite crystallization in gelatin nanoparticles synthesized using a miniemulsion process*. Advanced Functional Materials, 2008. **18**(15): p. 2221-2227.
247. Teshima, K., et al., *Morphologically controlled fibrous spherulites of an apatite precursor biocrystal*. Crystal Growth and Design, 2008. **9**(2): p. 650-652.
248. Han, T.Y.J. and J. Aizenberg, *Calcium Carbonate Storage in Amorphous Form and Its Template-Induced Crystallization*. Chemistry of Materials, 2007. **20**(3): p. 1064-1068.
249. Wang, L.J. and G.H. Nancollas, *Calcium Orthophosphates: Crystallization and Dissolution*. Chemical reviews, 2008. **108**(11): p. 4628-4669.
250. Cheng, X., et al., *Biomimetic synthesis of calcite films by a polymer-induced liquid-precursor (PILP) process:: 1. Influence and incorporation of magnesium*. Journal of Crystal Growth, 2007. **307**(2): p. 395-404.
251. Wang, L.J. and G.H. Nancollas, *Calcium Orthophosphates: Crystallization and Dissolution*. Chem. Revs., 2008. **108**(11): p. 4628-4669.
252. Rengarajan, G., et al., *Stabilization of the amorphous state of pharmaceuticals in nanopores*. Journal of Materials Chemistry, 2008. **18**(22): p. 2537-2539.
253. Deer, W., R. Howie, and J. Zussman, *An introduction to the rock forming minerals*, 528 p, 1966, Longman Group Ltd., London.
254. Ulman, A., *Formation and structure of self-assembled monolayers*. Chemical reviews, 1996. **96**(4): p. 1533-1554.
255. Gower, L., *ChemInform Abstract: Biomimetic Model Systems for Investigating the Amorphous Precursor Pathway and Its Role in Biomineralization*. ChemInform, 2009. **40**(5).
256. Aizenberg, J., et al., *Factors involved in the formation of amorphous and crystalline calcium carbonate: a study of an ascidian skeleton*. Journal of the American Chemical Society, 2002. **124**(1): p. 32-39.
257. Titiloye, J.O., et al., *Predicting the influence of growth additives on the morphology of ionic crystals*. Journal of the Chemical Society, Chemical Communications, 1991(20): p. 1494-1496.
258. Aizenberg, J., et al., *Factors Involved in the Formation of Amorphous and Crystalline Calcium Carbonate: A Study of an Ascidian Skeleton*. J. Amer. Chem. Soc., 2002. **124**(1): p. 32-39.
259. Sato, A., et al., *Glycolytic intermediates induce amorphous calcium carbonate formation in crustaceans*. Nature Chemical Biology, 2011. **7**(4): p. 197-199.

260. Stephens, C.J., et al., *Early Stages of Crystallisation of Calcium Carbonate Revealed in Picolitre Droplets*. J. Am. Chem. Soc., 2011.
261. Gebauer, D., A. Völkel, and H. Cölfen, *Stable prenucleation calcium carbonate clusters*. Science, 2008. **322**: p. 1819-1822.
262. Liu, J., et al., *Evaluation of the Particle Growth of Amorphous Calcium Carbonate in Water by Means of the Porod Invariant from SAXS*. Langmuir, 2010. **26**(22): p. 17405-17412.
263. Nudelman, F., et al., *Stabilization of amorphous calcium carbonate by controlling its particle size*. Nanoscale, 2010. **2**(11): p. 2436-2439.
264. Rieger, J., J. Thieme, and C. Schmidt, *Study of precipitation reactions by X-ray microscopy: CaCO<sub>3</sub> precipitation and the effect of polycarboxylates*. Langmuir, 2000. **16**(22): p. 8300-8305.
265. Quigley, D. and P.M. Rodger, *Free energy and structure of calcium carbonate nanoparticles during early stages of crystallisation*. J. Chem. Phys, 2008. **128**: p. 221101.
266. Tribello, G.A., et al., *A Molecular Dynamics Study of the Early Stages of Calcium Carbonate Growth*. J. Phys. Chem. B, 2009. **113**: p. 11680-11687.
267. Raiteri, P. and J.D. Gale, *Water is the Key to Nonclassical Nucleation of Amorphous Calcium Carbonate*. J. Am. Chem. Soc., 2010. **132**: p. 17623-17634.
268. Michel, F.M., et al., *Structural Characteristics of Synthetic Amorphous Calcium Carbonate*. Chem. Mater, 2008. **20**: p. 4720-4728.
269. Goodwin, A.L., et al., *Nanoporous Structure and Medium-Range Order in Synthetic Amorphous Calcium Carbonate*. Chemistry of Materials, 2010. **22**(10): p. 3197-3205.
270. Belcher, A.M., et al., *Control of crystal phase switching and orientation by soluble mollusc-shell proteins*. 1996.
271. Oliveira, A.M., et al., *Vaterite, calcite, and aragonite in the otoliths of three species of piranha*. Naturwissenschaften, 1996. **83**(3): p. 133-135.
272. Palchik, N.A. and T.N. Moroz, *Polymorph modifications of calcium carbonate in gallstones*. Journal of Crystal Growth, 2005. **283**(3-4): p. 450-456.
273. Meenakshi, V.R., P.L. Blackwelder, and N. Watabe, *Studies on the formation of calcified egg-capsules of ampullarid snails*. Calcified Tissue Research, 1974. **16**(1): p. 283-291.
274. Giralt, S., R. Julia, and J.A.N. Klerkx, *Microbial biscuits of vaterite in lake issyk-kul (Republic of Kyrgyzstan)*. Journal of Sedimentary Research, 2001. **71**(3): p. 430-435.
275. Prien, E.L. and C. Frondel, *Studies in urolithiasis; the composition of urinary calculi*. The Journal of urology, 1947. **57**(6): p. 949-994.
276. Vinogradov, A.P., *The elementary chemical composition of marine organisms*. 1953.
277. GREENAWAY, P., *Calcium balance and moulting in the Crustacea*. Biological Reviews, 1985. **60**(3): p. 425-454.
278. Ashby, M., et al., *The mechanical properties of natural materials. I. Material property charts*. Proceedings: Mathematical and Physical Sciences, 1995. **450**(1938): p. 123-140.

279. Currey, J.D., et al., *Mechanical properties of nacre and highly mineralized bone*. Proceedings of the Royal Society of London. Series B: Biological Sciences, 2001. **268**(1462): p. 107-111.
280. Wang, R.Z., et al., *Observations of damage morphologies in nacre during deformation and fracture*. Journal of Materials Science, 1995. **30**(9): p. 2299-2304.
281. Murphy, J., *Additives for plastics handbook*. 2001: Elsevier Science.
282. Okumura, M. and Y. Kitano, *Coprecipitation of alkali metal ions with calcium carbonate*. Geochimica Et Cosmochimica Acta, 1986. **50**(1): p. 49-58.
283. Sims, S.D., J.M. Didymus, and S. Mann, *Habit modification in synthetic crystals of aragonite and vaterite*. J. Chem. Soc., Chem. Commun., 1995(10): p. 1031-1032.
284. Chang, L.L., et al., *Non-silicates: sulphates, carbonates, phosphates, halides*. Vol. 5. 1998: Geological Society Pub House.
285. Davis, J.A., C.C. Fuller, and A.D. Cook, *A model for trace metal sorption processes at the calcite surface: Adsorption of Cd<sup>2+</sup> and subsequent solid solution formation*. Geochimica Et Cosmochimica Acta, 1987. **51**(6): p. 1477-1490.
286. Pingitore Jr, N.E. and M.P. Eastman, *Barium partitioning during the transformation of corals from aragonite to calcite*. Chemical Geology, 1985. **48**(1-4): p. 183-187.
287. Reeder, R.J., *Crystal chemistry of the rhombohedral carbonates*. Reviews in Mineralogy and Geochemistry, 1983. **11**(1): p. 1-47.
288. Kitano, Y., *The behavior of various inorganic ions in the separation of calcium carbonate from a bicarbonate solution*. Bulletin of the Chemical Society of Japan, 1962. **35**(12): p. 1973-1980.
289. Falini, G., et al., *Biomimetic crystallization of calcium carbonate polymorphs by means of collagenous matrices*. Chemistry-a European Journal, 1997. **3**(11): p. 1807-1814.
290. Taft, W.H., *Physical chemistry of formation of carbonates*. Developments in sedimentology B, 1967. **9**: p. 151-167.
291. Bischoff, J. and W. Fyfe, *Catalysis, inhibition, and the calcite-aragonite problem;[Part] 1, The aragonite-calcite transformation*. American Journal of Science, 1968. **266**(2): p. 65-79.
292. Winland, H.D., *Stability of calcium carbonate polymorphs in warm, shallow seawater*. Journal of Sedimentary Research, 1969. **39**(4).
293. Falini, G., M. Gazzano, and A. Ripamonti, *Magnesium calcite crystallization from water-alcohol mixtures*. Chemical Communications, 1996(9): p. 1037-1038.
294. White, D.J. and G.H. Nancollas, *The kinetics of dissolution of calcium oxalate monohydrate; a constant composition study*. Journal of Crystal Growth, 1982. **57**(2): p. 267-272.
295. Bischoff, J.L., *Kinetics of calcite nucleation: magnesium ion inhibition and ionic strength catalysis*. Journal of Geophysical Research, 1968. **73**(10): p. 3315-3322.
296. Teng, H.H., et al., *Thermodynamics of Calcite Growth: Baseline for Understanding Biomineral Formation*. Science, 1998. **282**(5389): p. 724-727.

297. Malkaj, P. and E. Dalas, *Calcium Carbonate Crystallization in the Presence of Aspartic Acid*. *Crystal Growth & Design*, 2004. **4**(4): p. 721-723.
298. Smith, G.P. and V.A. Petrenko, *Phage display*. *Chemical reviews*, 1997. **97**(2): p. 391-410.
299. Li, C., G.D. Botsaris, and D.L. Kaplan, *Selective in Vitro Effect of Peptides on Calcium Carbonate Crystallization*. *Crystal Growth & Design*, 2002. **2**(5): p. 387-393.
300. DeOliveira, D.B. and R.A. Laursen, *Control of Calcite Crystal Morphology by a Peptide Designed To Bind to a Specific Surface*. *Journal of the American Chemical Society*, 1997. **119**(44): p. 10627-10631.
301. Jimenez-Lopez, C., et al., *Influence of lysozyme on the precipitation of calcium carbonate: a kinetic and morphologic study*. *Geochimica Et Cosmochimica Acta*, 2003. **67**(9): p. 1667-1676.
302. Shen, F.H., Q.L. Feng, and C.M. Wang, *The modulation of collagen on crystal morphology of calcium carbonate*. *Journal of Crystal Growth*, 2002. **242**(1-2): p. 239-244.
303. Ouhenia, S., et al., *Synthesis of calcium carbonate polymorphs in the presence of polyacrylic acid*. *Journal of Crystal Growth*, 2008. **310**(11): p. 2832-2841.
304. Kato, T., *Polymer/Calcium Carbonate Layered Thin - Film Composites*. *Advanced Materials*, 2000. **12**(20): p. 1543-1546.
305. Zhang, S.K. and K.E. Gonsalves, *Influence of the chitosan surface profile on the nucleation and growth of calcium carbonate films*. *Langmuir*, 1998. **14**(23): p. 6761-6766.
306. Yu, J., et al., *Effects of PAA additive and temperature on morphology of calcium carbonate particles*. *Journal of Solid State Chemistry*, 2004. **177**(3): p. 681-689.
307. Jada, A. and A. Verraes, *Preparation and microelectrophoresis characterisation of calcium carbonate particles in the presence of anionic polyelectrolyte*. *Colloids and Surfaces A: Physicochemical and Engineering Aspects*, 2003. **219**(1-3): p. 7-15.
308. Albeck, S., L. Addadi, and S. Weiner, *Regulation of Calcite Crystal Morphology by Intracrystalline Acidic Proteins and Glycoproteins*. *Connective Tissue Research*, 1996. **35**(1-4): p. 365-370.
309. Aizenberg, J., et al., *Intracrystalline Macromolecules are Involved in the Morphogenesis of Calcitic Sponge Spicules*. *Connective Tissue Research*, 1996. **34**(4): p. 255-261.
310. Didymus, J.M., et al., *Influence of low-molecular-weight and macromolecular organic additives on the morphology of calcium carbonate*. *Journal of the Chemical Society, Faraday Transactions*, 1993. **89**(15): p. 2891-2900.
311. Söhnel, O. and J.W. Mullin, *Precipitation of Calcium Carbonate*. *J. Cryst. Growth*, 1982: p. 239-250.
312. Baumann, J., et al., *Nucleation and aggregation of calcium oxalate in whole urine; spectrophotometric sedimentation analysis: a new approach to study the aggregation of calcium oxalate dihydrate*. *Urological Research*, 2000. **28**(3): p. 147-154.

313. Carosso, P.A. and E. Pelizzetti, *A stopped-flow technique in fast precipitation kinetics—The case of barium sulphate*. Journal of Crystal Growth, 1984. **68**(2): p. 532-536.
314. Gunn, D. and M. Murthy, *Kinetics and mechanisms of precipitations*. Chemical Engineering Science, 1972. **27**(6): p. 1293-1313.
315. Gunn, D.J., *Mechanism for the formation and growth of ionic precipitates from aqueous solution*. Faraday Discuss. Chem. Soc., 1976. **61**: p. 133-140.
316. Kozlovskii, M., H. Wakita, and I. Masuda, *Analyses of precipitation processes of bis (dimethylglyoximato) Ni (II) and related complexes*. Journal of Crystal Growth, 1983. **61**(2): p. 377-382.
317. Faatz, M., F. Gröhn, and G. Wegner, *Amorphous calcium carbonate: synthesis and potential intermediate in biomineralization*. Advanced Materials, 2004. **16**(12): p. 996-1000.
318. Liu, J., J. Rieger, and K. Huber, *Analysis of the Nucleation and Growth of Amorphous CaCO<sub>3</sub> by Means of Time-Resolved Static Light Scattering*. Langmuir, 2008. **24**(15): p. 8262-8271.
319. Zijlstra, W.G., A. Buursma, and O.W. Van Assendelft, *Visible and near infrared absorption spectra of human and animal haemoglobin: determination and application*. 2000: Vsp.
320. Brečević, L. and H. Füredi-Milhofer, *Precipitation of Calcium Phosphate from Electrolyte Solutions II. The Formation and Transformation of the Precipitates*. Calc. Tiss. Res., 1972. **10**: p. 82-90.
321. Hess, B., et al., *Simultaneous Measurements of Calcium Oxalate Crystal Nucleation and Aggregation: Impact of Various Modifiers*. Urol. Res., 1995. **23**: p. 231-238.
322. Chien, W.C., C.-C. Lee, and C.Y. Tai, *Heterogeneous Nucleation rate of calcium Carbonate Derived from Induction Period*. Industrial & Engineering Chemistry Research, 2007. **46**: p. 6435-6441.
323. Chien, W.-C., C.Y. Tai, and J.-P. Hsu, *The Induction Period of the CaCl<sub>2</sub>-Na<sub>2</sub>CO<sub>3</sub> System: Theory and Experiment*. J. Chem. Phys., 1999. **111**: p. 2657-2664.
324. Chien, Y.C., et al., *Ultrastructural matrix-mineral relationships in avian eggshell, and effects of osteopontin on calcite growth in vitro*. Journal of Structural Biology, 2008. **163**(1): p. 84-99.
325. Johnston, J. and E.D. Williamson, *The Complete Solubility Curve of Calcium Carbonate*. J. Am. Chem. Soc., 1916. **38**: p. 975-983.
326. Miller, J.P., *A Portion of the System Calcium Carbonate-Carbon Dioxide-Water with Geological Implications*. Am. J. Sci., 1952. **250**: p. 161-203.
327. Söhnel, O. and J.W. Mullin, *A method for the Determination of Precipitation Induction Times*. J. Cryst. Growth, 1978. **44**: p. 377-382.
328. Brečević, L. and A.E. Nielsen, *Solubility of amorphous calcium carbonate*. J. Crystal Growth, 1989. **98**: p. 504-510.
329. Raz, S., et al., *Stable Amorphous Calcium Carbonate Is the Main Component of the Calcium Storage Structures of the Crustacean *Orchestia cavimana**. Biological Bulletin, 2002. **203**(3): p. 269-274.
330. Clarkson, J.R., T.J. Price, and C.J. Adams, *Role of metastable phases in the spontaneous precipitation of calcium carbonate*. J. Chem. Soc. Faraday Trans., 1992. **88**: p. 243-249.

331. Rieger, J., et al., *Precursor structures in the crystallization/precipitation processes of CaCO<sub>3</sub> and control of particle formation by polyelectrolytes*. Faraday Discuss., 2007. **136**: p. 265-277.
332. Ogino, T., T. Suzuki, and K. Sawada, *The formation and transformation mechanism of calcium carbonate in water*. Geochim. Cosmochim. Acta, 1987. **51**: p. 2757-2767.
333. Andreassen, J.-P., *Formation mechanism and morphology in precipitation of vaterite - nano-aggregation or crystal growth?* J. Crystal Growth, 2005. **274**: p. 256-264.
334. Shen, Q., et al., *Properties of amorphous calcium carbonate and the template action of vaterite spheres*. J. Phys. Chem. B, 2006. **110**: p. 2994-3000.
335. Rodriguez-Blanco, J.D., S. Shaw, and L.G. Benning, *The kinetics and mechanisms of amorphous calcium carbonate (ACC) crystallization to calcite, via vaterite*. Nanoscale, 2011. **3**: p. 265-271.
336. Gebauer, D., et al., *Influence of Selected Artificial Peptides on Calcium Carbonate Precipitation - A Quantitative Study*. Crystal Growth & Design, 2009. **9**(5): p. 2398-2403.
337. Lam, R.S.K., et al., *Synthesis-dependent structural variations in amorphous calcium carbonate*  
CrystEngComm, 2007 **9**: p. 1226-1236.
338. Oaki, Y., et al., *Nanosegregated Amorphous Composites of Calcium Carbonate and an Organic Polymer*. Advanced Materials, 2008. **20**(19): p. 3633-+.
339. Melik, D.H. and H.S. Fogler, *Turbidimetric Determination of Particle Size Distributions of Colloidal Systems*. J. Colloid Interface Sci., 1983. **92**: p. 161-180.
340. Tai, C.Y., W.C. Chien, and J.P. Hsu, *Induction Period of CaCO<sub>3</sub> Interpreted by the Smoluchowski's Coagulation Theory*. AIChE Journal, 2005. **51**: p. 480-486.
341. Whitmer, J.K. and E. Luijten, *Sedimentation of Aggregating Colloids*. J. Chem. Phys., 2011. **134**: p. 034510.
342. Israelachvili, J.N., *Intermolecular and Surface Forces*. 2nd ed. 1992, San Diego: Academic Press.
343. Donnet, M., et al., *Contribution of Aggregation to the Growth Mechanism of Seeded Calcium Carbonate Precipitation in the Presence of Polyacrylic Acid*. J. Phys. Chem. B, 2010. **114**: p. 12058-12067.
344. Donnet, M., P. Bowen, and J. Lemaitre, *A Thermodynamic Solution Model for Calcium Carbonate: Towards an Understanding of Multi-Equilibria Precipitation Pathways*. J. Colloid Interface Sci., 2009. **340**: p. 218-224.
345. Thompson, D.W. and P.G. Pownall, *Surface Electrical Properties of Calcite*. J. Colloid Interface Sci., 1989. **131**: p. 74-82.
346. Hough, D.B. and L.R. White, *The Calculation of Hamaker Constants from Lifshitz Theory with Applications to Wetting Phenomena*. Adv. Colloid Interface Sci., 1981. **14**: p. 3-41.
347. Söhnel, O. and J.W. Mullin, *Interpretation of Crystallization Induction Periods*. J. Colloid Interface Sci., 1988. **123**: p. 43-50.

348. Long, X., Y.R. Ma, and L.M. Qi, *In Vitro Synthesis of High Mg Calcite under Ambient Conditions and Its Implication for Biomineralization Process*. *Crystal Growth & Design*, 2011. **11**(7): p. 2866-2873.
349. Astilleros, J.M., L. Fernandez-Diaz, and A. Putnis, *The role of magnesium in the growth of calcite: An AFM study*. *Chemical Geology*, 2010. **271**(1-2): p. 52-58.